Interface Engineering for Oxide Electronics:

Tuning electronic properties by atomically controlled growth

Cover: Combined picture of the atomically controlled growth process consisting of a schematic image of the pulsed laser deposition process with reflection high-energy electron diffraction monitoring (top left), a RHEED intensity analysis during layer-by-layer growth (bottom right), a schematic image of the atomic stacking sequence at a perovskite interface (top right) and an atomic force micrograph of a surface with unit cell height terrace steps (bottom left). The background displays a high-resolution transmission electron micrograph of a $[(LaAlO_3)_{10}/(SrTiO_3)_{11}]_{10}$ superlattice.

Ph.D. committee

Chairman and secretary
Prof. Dr. A. Bliek (University of Twente)

Supervisors
Prof. Dr. Ir. J.W.M. Hilgenkamp (University of Twente)
Prof. Dr. Ing. D.H.A. Blank (University of Twente)

Assistant supervisor
Dr. Ing. A.J.H.M. Rijnders (University of Twente)

Members
Prof. Dr. H.Y. Hwang (University of Tokyo, Japan)
Prof. Dr. J. Aarts (University of Leiden)
Dr. Y.W. Ponomarev (IMEC, Belgium)
Prof. Dr. H. Rogalla (University of Twente)
Prof. Dr. Ir. H.J.W. Zandvliet (University of Twente)

The research described in this thesis was performed in the Faculty of Science & Technology and the MESA$^+$ Research Institute at the University of Twente. The project is part of the research programme of the Dutch Foundation for Fundamental Research on Matter (FOM), financially supported by the Netherlands Organization for Scientific Research (NWO), and Philips Research.

M. Huijben
Interface Engineering for Oxide Electronics:
Tuning electronic properties by atomically controlled growth,
Ph.D. thesis University of Twente, Enschede, The Netherlands.

ISBN: 90-365-2351-6

Printed by Wöhrmann Print Service, The Netherlands

© M. Huijben, 2006

INTERFACE ENGINEERING FOR OXIDE ELECTRONICS:
TUNING ELECTRONIC PROPERTIES BY ATOMICALLY CONTROLLED GROWTH

PROEFSCHRIFT

ter verkrijging van
de graad van doctor aan de Universiteit Twente,
op gezag van de rector magnificus,
prof. dr. W.H.M. Zijm,
volgens besluit van het College voor Promoties
in het openbaar te verdedigen
op vrijdag 28 april 2006 om 16.45 uur

door

Mark Huijben

geboren op 22 februari 1978
te Groningen

Dit proefschrift is goedgekeurd door de promotores

Prof. Dr. Ir. J.W.M. Hilgenkamp
Prof. Dr. Ing. D.H.A. Blank

en de assistent-promotor

Dr. Ing. A.J.H.M. Rijnders

Contents

1 Introduction **1**

1.1 Motivation 1
1.2 Outline of the thesis 2
1.3 References 3

2 Carrier doping in strongly correlated electron systems **5**

2.1 Introduction 5
2.2 Strongly correlated electron systems 6
2.3 Carrier doping in transition-metal oxides 8
2.3.1 Control of metal-insulator transitions 8
2.3.2 Metal-insulator phenomena in 3d transition-metal oxides 9
2.4 Carrier doping in high-T_c superconductors 13
2.5 Electric field induced carrier doping 14
2.6 Concluding remarks 16
2.7 References 17

3 Fabrication and characterization of oxide thin films **21**

3.1 Introduction 21
3.2 Thin film growth by pulsed laser deposition 22
3.2.1 Principles of the deposition process 22
3.2.2 Pulsed laser deposition setup 25
3.2.3 Growth monitoring by reflection high-energy electron diffraction 26
3.3 Thin film structure analysis 32
3.3.1 Scanning probe microscopy 33
3.3.2 Scanning electron microscopy 33
3.3.3 X-ray diffraction 34
3.3.4 Transmission electron microscopy 35

3.3.5 Rutherford backscattering spectrometry ... 36
3.4 Electronic transport analysis ... 36
3.4.1 Temperature dependent conductivity measurements ... 37
3.4.2 Hall effect measurements ... 37
3.4.3 UV-Vis spectrophotometry measurements ... 37
3.4.4 Probing station ... 38
3.5 Concluding remarks ... 39
3.6 References ... 40

4 Carrier doping control in $La_{2-x}Sr_xCuO_{4+\delta}$ ultrathin films 43

4.1 Introduction ... 43
4.2 Initial growth at the substrate surface ... 45
4.3 Epitaxial strain ... 49
4.4 Carrier doping dependence of the superconducting properties ... 51
4.5 Ultrathin superconducting films ... 53
4.6 Vortex lattice imaging ... 55
4.7 Towards electric field modulated carrier doping ... 60
4.7.1 Theoretical aspects of superconducting field effect devices ... 60
4.7.2 High quality Al_2O_3 gate dielectric by interval annealing ... 61
4.7.3 Field effect device fabrication ... 64
4.8 Conclusions ... 68
4.9 References ... 70

5 Interface engineering in $YBa_2Cu_3O_{7-\delta}$ thin films 75

5.1 Introduction ... 75
5.2 Initial growth at the substrate-film interface ... 77
5.3 Strain relaxation in ultrathin films ... 83
5.4 In-situ x-ray diffraction study during growth ... 87
5.4.1 Analysis of the layer thickness ... 88
5.4.2 Analysis of the surface morphology ... 90
5.4.3 Analysis of strain relaxation ... 92
5.5 Sub-unit cell layer epitaxy ... 94
5.5.1 Growth optimization of individual materials ... 95
5.5.2 Sequential deposition of sub-unit cell layers ... 97
5.5.3 Sub-unit cell interval deposition ... 99
5.6 Conclusions ... 103
5.7 References ... 104

6 Atomically controlled interfaces in $LaAlO_3/SrTiO_3$ multilayers 107

6.1 Introduction 107
6.2 Atomic structure at $LaAlO_3$ / $SrTiO_3$ interfaces 108
6.2.1 Layering sequence in perovskite structures 109
6.2.2 Polar-non polar interfaces 110
6.2.3 Surface termination control for thin film growth 112
6.3 Growth of atomically controlled single interfaces 114
6.3.1 Unit cell control by RHEED monitoring 114
6.3.2 Structural and electronic properties 116
6.4 Atomic interface structure at high temperatures 119
6.4.1 In-situ x-ray diffraction during growth for interface modeling 119
6.4.2 Modeling of the atomic interface stacking 122
6.5 Complementary interfaces in heteroepitaxial superlattices 125
6.5.1 Artificial growth of $LaAlO_3$-$SrTiO_3$ superlattices 126
6.5.2 Structural analysis of the superlattices 129
6.5.3 Atomic ordering analysis of the interfaces 131
6.5.4 Controlled growth of multilayers with variable thicknesses 138
6.6 Conclusions 139
6.7 References 141

7 Electronic properties of single and coupled $LaAlO_3/SrTiO_3$ interfaces 147

7.1 Introduction 147
7.2 Electronic properties of single interfaces 148
7.2.1 Transport properties 149
7.2.2 Photoelectronic properties 157
7.3 Electronically coupled complementary interfaces 161
7.4 Conclusions 166
7.5 References 168

Summary 171

Samenvatting (Summary in Dutch) 177

Dankwoord 183

Chapter 1

Introduction

Abstract

The study of atomically controlled growth in complex oxides is motivated by the nature of the electronic properties on very small length scales. This thesis describes various perovskite material compounds in which the engineering of the interfaces between the individual thin film layers, and the substrates plays a crucial role.

1.1 Motivation

Perovskite oxides and structurally related compounds have attracted great interest since they comprise of an incredibly broad range of electronic phases such as superconductors, metals, semiconductors, insulators, ferromagnets, antiferromagnets, ferroelectrics, multiferroics, dielectrics and piezoelectrics. Many of these perovskites are closely lattice-matched, which provides the possibility of fabricating heteroepitaxial structures to explore new physical phenomena and new device concepts [1-4]. The nature of these physical properties in novel oxide electronics is determined by very small characteristic length scales. Many of the interesting physical properties require high carrier densities in the order of ~10^{21} cm^{-3}, which results in screening and band-bending lengths at interfaces of 0.1 - 1 nm [5]. Because of these small characteristic length scales, growth control on an atomic level is essential in epitaxial heterostructures.

The large field of investigations on perovskite thin films and heterostructures for oxide electronics is even extended recently by the innovative growth of artificially designed structures, in which new crystal structures are formed by stacking various types of perovskite building blocks onto each other [6]. The quality of the atomic ordering at the heteroepitaxial interfaces can nowadays be analyzed with single-atom

sensitivity by scanning transmission electron microscopy [7]. By probing the individual atomic sites, it is possible to determine with a very high spatial resolution the atomic and electronic structure in many oxide materials. This is an important advantage for the investigations to tune the electronic properties in oxide structures by controlling the atomic arrangement at the interfaces. Novel heteroepitaxial devices based on this atomically controlled growth, like ferroelectric devices, Mott transition devices, superconducting devices and magnetic random-access memory devices, have great potential for future applications.

1.2 Outline of the thesis

It is the main aim of this thesis to develop a controlled growth with atomic precision for the realization of artificial perovskite structures, to exploit the exceptional physical properties of complex oxide materials such as high-temperature superconductors and conducting interfaces between band insulators.

In the following chapters the ability to tune the electronic properties of complex oxides, by controlling the growth on an atomic scale, will be demonstrated. Various perovskite material compounds will be described in which the engineering of the interfaces between the individual thin film layers, and the substrates always plays a crucial role.

In chapter 2 a brief overview is given on the origin of the field of strongly correlated electron systems. The metal-insulator transition phenomena in 3d transition-metal oxides are discussed with an extension into carrier doping in high-T_c superconductors. Modulation of the carrier concentration by applying electric fields instead of chemical substitution, to make reversible switching possible, is also described.

In chapter 3 the growth procedure by pulsed laser deposition and reflection high-energy electron diffraction is described with a discussion of their basic principles. Besides the time resolved analysis during the growth process, also ex-situ characterization techniques will be presented, which are used to define the structure, composition and electronic transport properties of the as-deposited thin films.

In chapter 4 investigations on $La_{2-x}Sr_xCuO_{4+\delta}$ thin films and multilayers, in which the carrier doping is tuned during the growth process, will be presented. The atomic interface configurations at the substrate during the initial growth as well as the epitaxial strain relaxation during subsequent growth will first be described. Subsequently the effect of variations in the stoichiometry of strontium and oxygen on electronic and magnetic properties will be determined. Finally, the sensitivity of the electronic properties on the carrier doping will be utilized to improve the fabrication process of electric field effect structures.

In chapter 5 the interface engineering in thin films of $YBa_2Cu_3O_{7-\delta}$ is described with special emphasis on the initial growth and strain relaxation mechanisms. First

the initial growth at the substrate surface is investigated to define the atomic stacking sequences at the film-substrate interface. Secondly, the strain relaxation during growth of thicker films is determined with the dependence on the initial stacking sequence at the interface. Thirdly, the growth process is analyzed by in-situ surface sensitive X-ray diffraction to define the changes in thin film properties during growth. Finally, a new deposition technique will be presented for the growth of atomically smooth films by interval deposition of sub-unit cell layers.

In chapter 6 the fabrication will be described of high-quality $LaAlO_3$-$SrTiO_3$ multilayers with atomically controlled interfaces. The growth procedure of single interfaces, superlattices and multilayers will be specified as well as the characterization of their structural properties.

In chapter 7 the analysis will be described of the electronic properties of single interfaces as well as several interfaces in $LaAlO_3/SrTiO_3$ heterostructures. A detailed analysis of the coupling between two complementary interfaces will provide new information on the transport properties, such as conductance, carrier density and mobility, as a function of the separation distance between the interfaces.

1.3 References

1. Goodenough, J.B., *MRS Bulletin* **15** (5), 23 (1990).
2. Koinuma, H., *MRS Bulletin* **19** (9), 21 (1994).
3. Koinuma, H., *Thin Solid Films* **486**, 2 (2005).
4. Rijnders, G. & Blank, D.H.A., *Nature* **433**, 369 (2005).
5. Hwang, H.Y., *MRS Bulletin* **31** (1), 28 (2006).
6. Ogale, S.B. (Ed.), *Thin Films and heterostructures for oxide electronics* (Springer, New York, 2005).
7. Pennycook, S.J., Varela, M., Hetherington, C.J.D. & Kirkland, A.I., *MRS Bulletin* **31** (1), 36 (2006).

Chapter 2

Carrier doping in strongly correlated electron systems

Abstract

Interactions between electrons play an important role in the electronic behavior of numerous materials. A brief overview is given on the origin of the field of strongly correlated electron systems. Changes in the electron interactions can lead to metal-insulator transitions by bandwidth or filling control. Both control techniques are described for several materials. The metal-insulator phenomena in $3d$ transition-metal oxides are discussed with an extension into carrier doping in high-T_c superconductors. Modulation of the carrier concentration by applying electric fields instead of chemical substitution, to make reversible switching possible, is also described.

2.1 Introduction

The discovery of new natural and artificial materials in the last decades has led to many interesting developments in condensed matter physics. A key role for the description of their physical properties is knowledge about the electronic structures. Therefore, many scientific studies are investigating the different influences on electron behavior. All material categories from insulating, semiconducting, metallic to superconducting are studied in many experimental and theoretical projects. Some of their aspects can be described accurately by relatively simple free electron models of independent electrons. For the description of materials with interacting electrons, these models are not adequate and calculations with correlation effects between electrons become necessary. These materials, where the low-energy electronic excitation is defined by electron-electron correlations, are indicated as correlated

electron systems. The strength and number of interactions can be controlled in different ways to optimize the electronic behavior for certain applications. This has led to remarkable physical properties; such as high-temperature superconductivity [1] and colossal magnetoresistance [2], and contributions to this field have resulted in a substantial number of scientists winning the Nobel Prize for Physics.

2.2 Strongly correlated electron systems

The field of strongly correlated electron systems started soon after the development of quantum mechanics in the 1920s by Heisenberg [3], Schrödinger [4], Born and Jordan [5], Dirac [6] and others, by the work of Heitler and London [7] on the ground state of the H_2 molecule, which opened the way to a theoretical understanding of chemical bonding. They treated the two electrons as being strongly correlated through the dominant coulomb and exchange energies (by the Pauli exclusion principle). A distinctly different approach to the problem of interacting electrons was taken shortly thereafter by Hartree [8], Fock [9] and Slater [10] who treated the electrons as being independent of each other and introduced the idea of the self-consistent field. This is the interaction field an electron experiences when a spatial average over the positions of all other electrons is taken. Neither one gave a perfect description of the true ground state of the H_2 molecule, which lies between the extremes of the two models.

Since then, these models have not only been applied to the H_2 molecule but more generally, to both quantum chemistry and solid state physics in common. They stand for localized versus delocalized electrons and the strength of the electron correlations in a given molecule or solid determines whether a calculation of the electronic behavior has to start from a wavefunction of the Heitler-London (strong correlation limit) or the Hartree-Fock form (independent limit).

The first microscopic theory of solids was based on non-interacting or weakly interacting ‘free’ electrons [11-13]. This theory makes a general distinction between metals and insulators at zero temperature based on the filling of the electronic bands and is indicated as the electronic band model: the band structure and the position of the Fermi level determine the behavior of the material. For insulators the highest filled band is completely filled, while for metals it is partially filled. In other words, the Fermi level lies in a band gap in insulators, while the level is inside a band for metals.

By the early 1930s, it was recognized that insulators with a small energy gap between the highest filled band and lowest empty band would be semiconductors due to thermal excitation of the electrons [14-17]. Although this band picture was successful in many respects, de Boer and Verwey [18] reported that many transition-metal oxides with a partially filled *d*-electron band were nonetheless poor conductors and indeed often insulators. Concerning their report, Peierls [19] pointed out the

importance of the electron-electron correlation: strong Coulomb repulsion between electrons could be the origin of the insulating behavior. These observations launched the long and continuing history of the field of strongly correlated electrons, particularly the effort to understand how partially filled bands could be insulators and, as the history developed, how an insulator could become a metal as controllable parameters were varied, the so-called metal-insulator transition (MIT).

These MITs can be divided in two categories [20]. In the first category, some change in the ionic lattice, such as a structural phase transition, leads to a splitting of the electronic conduction band and hence to a metal-insulator transition. In the second category the transition is purely electronic in origin and can be described by models in which the lattice is fixed. This latter category has again been divided into two classes, one in which the transition is triggered by electronic correlations (Mott transition) and one in which it is triggered by disorder (Anderson transition).

In the past seventy years, much progress has been made from both theoretical and experimental sides in understanding strongly correlated electron systems and MITs. In theoretical approaches, Mott [21-23] took the first important step towards understanding how electron-electron correlations could explain the metal-insulator transition. He imagined a crystalline array of atomic potentials with one electron per site and a Coulomb repulsion between the electrons, creating an insulator. By introducing additional electrons by chemical or other doping, new states are formed which can transfer to another site by single electron transfer. This changes the behavior of the material from insulating to metallic. A related, but continuous, metal-insulator transition was believed to occur in a tight-binding model with short-range electron-electron interactions known as the Hubbard model [24-29]. This still oversimplified model gives some insight into characteristic features of strong correlations, but has certain limitations as regards to realistic descriptions of solids.

Theoretical models that treat the kinetics and electron-electron interactions of the total system on an equal footing are very hard to handle. On an intuitive level this can be expected since in these models the collective motion of, say, 10^{23} electrons cannot be split up in small subsystems anymore without loosing the correlation effects. The lack of success in treating the full effect of correlations has lead to the development of model Hamiltonians [30,31]. These model Hamiltonians describe highly idealized systems, where most interactions between the electrons are left out. The rationale behind considering such an over simplified system is that most interesting physical phenomena occur at a low energy scale. With a model Hamiltonian one wants to describe only a part of the physical phenomena, only the essential ones, which are mostly the low energy phenomena. The trick of the trade is to find the relevant model Hamiltonian and to solve it. Both are highly non-trivial challenges.

2.3 Carrier doping in transition-metal oxides

In transition-metal ions *d* electrons experience competing forces: Coulomb repulsion tends to localize individual electrons at atomic lattice sites, while hybridization with the oxygen *p* electron states tends to delocalize the electrons. The subtle balance makes many of the transition-metal oxides excellent resources for studying and taking advantage of the metal-insulator transition that can accompany dramatic changes in these system's electronic properties.

2.3.1 Control of metal-insulator transitions

In the simple Hubbard model the metal-insulator transition will depend on the correlation strength U/t and the band filling n. The schematic metal-insulator phase diagram is given in Figure 2.1. The n=0 and n=2 fillings correspond to the band insulator state. At half filling (n=1), represented by the black line in the center of the figure, the transition from the insulating to the metallic state can be driven by changing U/t. This type of transition is called a bandwidth controlled (BC) MIT. The electron correlation strength is controlled for this transition by modifying the lattice parameters or the chemical composition while essentially maintaining the original lattice structure. The onsite (U) or intersite Coulomb interacting is kept almost unchanged during the above procedure and control of electron correlation is therefore achieved by control of the transfer interaction (t) or the one-electron bandwidth.

One of the methods to induce a bandwidth controlled MIT is the application of pressure, which decreases the interatomic distance and hence increases the transfer interaction. This is observed in V_2O_3 [32], $PrNiO_3$ and $NdNiO_3$ [33]. Another method is the modification of the chemical composition using the solid solution or the mixed-crystal effect, as for $NiS_{2-x}Se_x$ crystals [34]. The final method, which can be applied to perovskite-type compounds (ABO_3), is changing the B-O-B bond by changing the radius of the A-site ion. This will change the bond-angle buckling and reduces the bandwidth. The best example is the MIT control in $RNiO_3$, which are classified as charge transfer insulators [35], with R being trivalent rare-earth ions (La to Lu) [36].

A filling at non-integer n usually leads to the metallic phase. The most interesting phase is the one right next to the n=1 insulating line, which is derived by filling control (FC) MIT of the parent Mott insulator. The standard method for filling control is to replace in ternary or multinary compounds an atom with a high valence, with one with a lower valence, or vice versa. A good example is the band filling control (n) in the $La_{2-x}Sr_xCuO_4$ compound [37], where the trivalent La atoms are replaced with the divalent Sr atoms. Taking the insulating compound as a reference, the filling is called "hole doping" when the band filling is decreased and "electron doping" when the band filling is increased, although the carriers are not

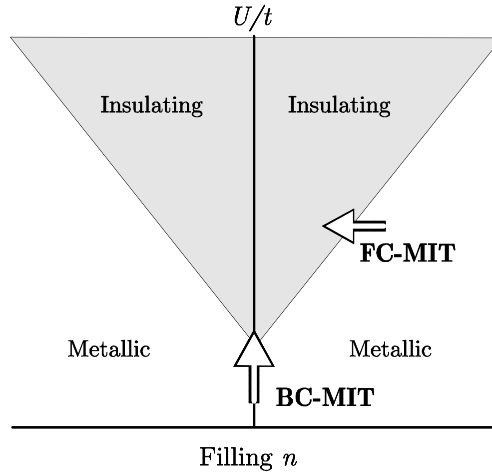

Figure 2.1 Metal-insulator phase diagram based on the Hubbard model in the plane of electron correlation strength U/t and filling *n*. The black area is in principle metallic, but can exhibit insulation behavior due to electron interactions. The black line in the middle represents the Mott insulating phase. The two routes for the metal-insulator transition are shown: filling controlled (FC-MIT) and bandwidth controlled (BC-MIT).

necessarily holes for the first case or electrons for the second. So replacing La^{3+} with Sr^{2+} in $La_{2-x}Sr_xCuO_4$ is an example of hole doping.

A large number of filling-controlled compounds can be made by forming the A-site mixed crystals of perovskites, such as $La_{1-x}Sr_xMO_3$ and $La_{2-x}Sr_xMO_4$ with M being the *3d* transition-metal element [38]. For some materials non-stoichiometry plays the role of filling control and well-known examples are $YBa_2Cu_3O_{6+y}$ [39] and $LaTiO_{3+y}$ [40]. Since the discovery of high-temperature superconductors, the concept of filling control or "carrier doping" has been widely recognized as one of the important aspects of the MIT in the *3d* electron systems.

2.3.2 Metal-insulator phenomena in 3d transition-metal oxides

Metal-insulator transitions can change the conductivity for many orders of magnitude in perovskite or layered perovskite compounds of 3*d* transition metal oxides. An intensively studied group of materials are the A-site mixed perovskites, $La_{1-x}Sr_xMO_3$ and $La_{2-x}Sr_xMO_4$ (M=Ti, V, Cr, Mn, Fe, Co, Ni and Cu), where the trivalent rare-earth ion (La) is partially replaced by a divalent alkaline-earth ion (Sr). This leads to a metal by hole-doping of the initial insulator. The filling controlled metal-insulator transitions of these materials will be described in the following section. The suitability of the materials for novel electronic devices can be determined by the magnitude of the change in conductivity as a function of the

carrier doping, the ease with which the materials can be grown in thin films and whether they posses unique properties which may increase their potential.

Titanates

The compound $LaTiO_3$ is a typical Mott-Hubbard insulator with a $3d^1$ electronic configuration for Ti^{3+}. The physical properties of $La_{1-x}Sr_xTiO_3$ evolve from antiferromagnetic insulator to semiconductor as the formal valence varies from Ti^{3+} to Ti^{4+} with substitutional doping [41]. For doping values in between, a good metal is usually formed. When $LaTiO_3$ is doped for x=0.10 with Sr, the resistivity drops four orders of magnitude [42]. This material can be grown on $SrTiO_3$, a commonly used substrate, although, the growth of thin films is not without challenges, due to the extremely reducing oxygen conditions necessary to stabilize Ti^{3+} [40,43].

Vanadates

In many ways $La_{1-x}Sr_xVO_3$ is similar to $La_{1-x}Sr_xTiO_3$. The parent compound $LaVO_3$ is a prototypical Mott-Hubbard type insulator with the electron configuration $3d^2$, and undergoes a magnetic transition from a paramagnetic to an antiferromagnetic state below the magnetic ordering temperature [44]. The material undergoes a metal-insulator transition at x=0.18, but the transition is more gradual than in the $LaTiO_3$ case [45]. The transition in total is about 4 orders of magnitude and the amount of carrier doping necessary for this transition is about twice the amount needed in the $LaTiO_3$ case. Experiments have only been done on single crystals and no results are known about thin films of $La_{1-x}Sr_xVO_3$.

Chromates

$LaCrO_3$ has a $3d^3$ electronic configuration and is a charge transfer insulator. This means that the metal-insulator transition occurs when the charge transfer gap is closed, instead of the Mott-Hubbard gap as in the $LaTiO_3$ and $LaVO_3$ compounds. The transition from insulator to metal in $La_{1-x}Sr_xCrO_3$ results in a change in resistivity of only one order of magnitude for a change in doping of x=0.20 [46]. Almost all of the research done on this material focuses on high temperature properties, because of its good mechanical properties and electrical conductivity in both oxidizing and reducing atmospheres. Thin films of $La_{1-x}Sr_xCrO_3$ have been produced [47,48], but the highly refractory nature makes sintering and densification very difficult at all temperatures, leading to off-stoichiometry, voids and non-uniform grain sizes.

Manganites

The manganites, $La_{1-x}Sr_xMnO_3$, have been extensively studied because of the observed high magnetoresistance values in the vicinity of the metal-insulator

transition temperature [49,50]. The charge transfer insulator, $LaMnO_3$, has a *3d*^{4} electronic configuration and the MIT is at x=0.18 with a resistivity drop of about 4 orders of magnitude at room temperature when x goes from 0 to 0.2 [51]. The presence of the magnetoresistance effect gives an extra possibility to lower the resistivity with a magnetic field. Another advantage of the material is that it can be grown in thin films with relative ease. It has been shown that the material can be grown atomically flat on $SrTiO_3$ [52]. A relation between the growth parameters was derived for the growth of high quality $La_{1-x}Sr_xMnO_3$ thin films [53].

Ferrites

The $LaFeO_3$ compound is a charge transfer insulator with a *3d*^{5} configuration and it is rather surprising that although $La_{1-x}Sr_xMnO_3$ and $La_{1-x}Sr_xCoO_3$ (treated in the next paragraph) become metallic for $x > 0.2$, $La_{1-x}Sr_xFeO_3$ does not exhibit a metallic phase until x is close to 1. This means that a very weak dependence of the resistivity on the doping level exists [54,55]. Still, an interesting property of the material is the charge ordering at high doping levels [56]. This phenomenon is only measurable when the material is cooled down below 200 K. Replacing La with another rare earth can change the transition temperature of the charge ordering effect, but the effect is not highly dependent on the doping level [57]. The fabrication of thin films of $La_{1-x}Sr_xFeO_3$ has only recently been achieved at very high temperatures [58].

Cobaltates

$LaCoO_3$ shows a unique electronic phase change with change of temperature. The ground state of $LaCoO_3$ is a charge transfer insulator with a *3d*^{6} electronic configuration and undergoes the spin state transition around 100 K from a nonmagnetic to a paramagnetic state. With further increase of the temperature, electrical conduction of $LaCoO_3$ shows a crossover behavior around 500 K from a thermally activated semiconductor to a conducting state with metallic conductivity. Replacing La with another rare earth (Pr, Nd, Sm, Eu and Gd) with a smaller radius increases the resistivity over the entire temperature range [59]. When doped with Sr (x=0.20), the resistivity of $La_{1-x}Sr_xCoO_3$ can be lowered at room temperature with a change in resistivity of 4 orders of magnitude [31]. This change in resistivity does not become larger when La is replaced by another rare earth, despite the higher resistivity of the compound [60]. Thin films of $La_{1-x}Sr_xCoO_3$ with x=0.5 are usually grown on $SrTiO_3$ substrates [61,62]. The growth conditions for this composition are investigated by many groups, but very little is know for lower doping levels. The compound $La_{2-x}Sr_xCoO_4$ can also be fabricated, which shows to be an antiferromagnetic insulator for x<0.5 and transforms suddenly to a ferromagnetic metal for x>0.5. The change in resistivity from x=0.5 to 1.0 is 1 order of magnitude [63].

Nickelates

The $RNiO_3$ compounds can also be classified as being charge transfer insulators [35]. The conductive properties have been studied for a number of rare earths: La, Pr,Nd, Sm and Eu [36]. $LaNiO_3$ has a *3d*^{7} electronic configuration and experiments with doping of $La_{1-x}Sr_xNiO_3$ were done, but single crystals could only be obtained for $x<0.05$, which showed no metal-insulator transition [64]. Instead, thin films of the compound $La_{2-x}Sr_xNiO_4$ can be grown in the doping-range from x=0 to 1.2 and they show a change in resistivity of 3 orders of magnitude [65].

Cuprates

Lanthanum copper oxides can crystallize to the compound $LaCuO_{3-y}$ when processed at high oxygen pressures, and changes from an insulator to a metallic conductor as y varies from 0.5 to 0. The $LaCuO_{2.5}$ compound is a charge transfer insulator with *3d*^{8} electronic configuration, but due to the difficult synthesis not suitable for practical applications. The stable $La_{1-x}Sr_xCuO_{2.5-y}$ can be formed by Sr-doping, but only in the range $0.15<x<0.25$ a single phase perovskite will be formed [66]. There is no metal-insulator transition in this range. The fabrication of thin films of $La_{1-x}Sr_xCuO_{2.5-y}$ has recently been achieved, but only for the $0.15<x<0.25$ range [67]. The $La_{2-x}Sr_xCuO_4$ compound is the simplest system among the high-T_c superconducting cuprates. The parent compound, La_2CuO_4, is an antiferromagnetic insulator and Sr-doping leads to the transition of an insulator to a superconductor [37]. Thin films of this compound can be fabricated relatively easily and many groups have investigated the physical properties for the different doping levels [68]. The insulator-superconductor transition occurs at x=0.05, but the maximum T_c is reached for compounds with x=0.15. The value for this T_c is very dependent on the epitaxial strain and oxygen configuration inside the film. The maximum T_c achieved for $La_{1.85}Sr_{0.15}CuO_4$ is 51.5 K under compressive strain and extra oxygen incorporation [69].

By summarizing the metal-insulator properties at 300 K for all A-site mixed *3d* transition metal perovskite oxides, it becomes clear that the compounds $La_{1-x}Sr_xTiO_3$, $La_{1-x}Sr_xVO_3$, $La_{1-x}Sr_xMnO_3$ and $La_{1-x}Sr_xCoO_3$ show the largest change in resistivity in orders of magnitude per carrier-doping with strontium, see Table 2.1. On the other hand $La_{1-x}Sr_xTiO_3$ and $La_{1-x}Sr_xVO_3$ produce difficulties in the thin film fabrication process, which makes $La_{1-x}Sr_xMnO_3$ and $La_{1-x}Sr_xCoO_3$ the only ideal candidates to utilize metal-insulator transitions at 300 K in novel electronic devices.

Electric field effect devices could benefit from the application of transition metal oxides because the properties don't change from the bulk values, as in semiconductors, when ultrathin layers are used. Although the difficulties in the fabrication of field effect devices were solved, see Chapter 4, no electronic devices of either $La_{1-x}Sr_xMnO_3$ or $La_{1-x}Sr_xCoO_3$ were fabricated yet. This was a direct result of

Material	ΔR/Δx (at 300K)	Composition at MIT	Ref.
$La_{1-x}Sr_xTiO_3$	4 / 0.1	$La_{0.90}Sr_{0.10}TiO_3$	[42]
$La_{1-x}Sr_xVO_3$	4 / 0.2	$La_{0.82}Sr_{0.18}VO_3$	[45]
$La_{1-x}Sr_xCrO_3$	1 / 0.2	$La_{0.80}Sr_{0.20}CrO_3$	[46]
$La_{1-x}Sr_xMnO_3$	4 / 0.2	$La_{0.82}Sr_{0.18}MnO_3$	[51]
$La_{1-x}Sr_xFeO_3$	1 / 0.9	$La_{0.1}Sr_{0.9}FeO_3$	[54]
$La_{1-x}Sr_xCoO_3$	4 / 0.2	$La_{0.82}Sr_{0.18}CoO_3$	[31]
$La_{2-x}Sr_xCoO_4$	1 / 0.5	$La_{1.50}Sr_{0.50}CoO_4$	[63]
$La_{1-x}Sr_xNiO_3$	-	-	[64]
$La_{2-x}Sr_xNiO_4$	3 / 1.0	$LaSrNiO_4$	[65]
$La_{1-x}Sr_xCuO_{2.5-y}$	-	-	[67]
$La_{2-x}Sr_xCuO_4$	1 / 0.2	$La_{1.95}Sr_{0.05}CuO_4$	[37]

Table 2.1 Metal-insulator transition properties at 300 K for the A-site mixed $3d$ transition-metal perovskite oxides with change of resistivity in orders of magnitude per change in carrier doping and the material composition at the metal-insulator transition.

continued research for new materials for field effect devices into the field of electronic reconstruction at $LaAlO_3/SrTiO_3$ interfaces, see Chapter 6 and 7. The 2-dimensional conductivity at these types of interfaces is expected to be strongly tunable by electric fields and, therefore, to be a more ideal candidate for application in field effect transistors, due to a thickness of the tunable layer close to the unit cell limit.

2.4 Carrier doping in high-T_c superconductors

Ever since the first high-temperature copper oxide superconductor was discovered in the La-Ba-Cu-O system in 1986 [1], a large variety of high-temperature superconductors (HTS) have been synthesized [70,71]. Thousands of publications have reported the syntheses, structures, properties and applications of these young materials, which share the same feature: the structures contain two-dimensional superconducting CuO_2 sheets that are separated by a non-superconducting plane or planes. However, the real mechanism of superconductivity is still under lively debate.

The improvement of sample quality in the last couple of years [72] plays an important role in the progress of clarifying the questions in HTS materials science. This may be attributed in part to the efforts to create a materials basis for the multitude of applications [73,74], which were envisioned in the unprecedented scientific euphoria after the HTS discovery. At this moment, almost two decades later, there is still no universally accepted theory for why these materials are superconductors. The complicated structure of sequences of oxide layers in these multi-element compounds is responsible for this difficult issue. In addition to the

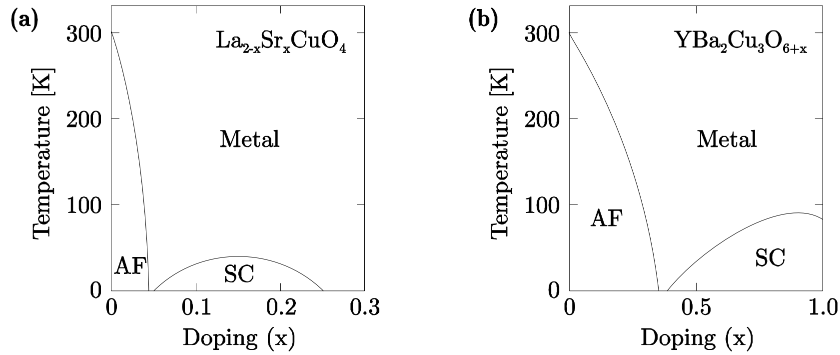

Figure 2.2 Electronic phase diagrams of the high-T_c superconductors $La_{2-x}Sr_xCuO_4$ **(a)** and $YBa_2Cu_3O_{6+x}$ **(b)** with the dependence of the transition temperatures on the doping level (x).

impurity problem due to undesired additional elements, which is a topic in all materials synthesis, intrinsic local stoichiometry defects arise in HTS from the insertion of cations in the wrong layer and defects of the oxygen sub-lattice. These microscopically details are closely connected to the macroscopically measurable superconducting properties, due to the very short superconducting coherence length of the order of the dimensions of the crystallographic unit cell. As additional requirement for the optimization of the superconducting properties, the oxygen content has to be adjusted in a compound-specific off-stochiometric ratio, but nevertheless with a spatially homogeneous microscopic distribution of the resulting oxygen vacancies or interstitials.

Another common property is the presence of antiferromagnetic (AF) order at low temperatures in the undoped regime, i.e., when no free charge carriers exist in the planes, see Figure 2.2. High temperature superconductivity (SC) is achieved at these low temperatures when a moderate density of electrons or holes is introduced. This carrier doping can be achieved by ion substitution or oxygen incorporation, for example in the insulators La_2CuO_4 and $YBa_2Cu_3O_6$. This leads to the hole-doped superconducting cuprates $La_{2-x}Sr_xCuO_4$ and $YBa_2Cu_3O_{6+x}$, commonly abbreviated as respectively LSCO and YBCO. Their electronic structures evolve from an insulator to a *d*-wave superconductor by increased doping; until the maximum transition temperature (T_c) is achieved for optimal doping.

2.5 Electric field induced carrier doping

The interactions in correlated electron systems can be changed by carrier doping, leading to novel phases through metal-insulator transitions. A disadvantage of carrier doping by chemical substitution is the lack of control on the carrier concentration in a material. The physical properties can't be adjusted without changing the chemical composition, which makes them useless for some applications

in electronic devices. Consequently, the carrier concentration needs to be controlled by a system outside the material, which would make reversible changes possible. Some methods to change the carrier density without affecting the chemical composition include the application of magnetic field [75], electric field [76], pressure [77] and photon irradiation [78]. In the following section the electrostatic field effect method will be described in more detail.

Field-effect experiments are in concept very elegant and they create many opportunities to electrostatically modulate different types of correlated electron behaviour [79]. In practice, however, there are significant challenges because the underlying physics requires structures that are difficult to achieve. The carrier concentration can be controlled by applying an external electric field to a material, which attracts or repels charge carriers, creating a thin charge accumulation or depletion layer at the surface that modifies the electrical conductivity between a source (S) and a drain (D) contact, see Figure 2.3. The field is applied across a gate insulator using a gate electrode (G). The characteristic width of the accumulation or depletion layer is given by the electrostatic screening length λ_{el}, which in the semi-classical, metallic limit is the Thomas-Fermi length. In standard metallic systems, λ_{el} is extremely short, a fraction of an atomic diameter, and thus negligible field effects are found. In low-carrier-density systems, larger screening lengths and field effects are expected, which are reasons why standard transistors are made with semiconductors rather than metals.

For the investigation of many interesting physical properties, substantial carrier modulation at carrier densities in the range of 10^{19}-10^{22} carriers cm^{-3} has to be achieved. The first method to improve the carrier modulation is to use ultrathin drain-source (DS) channels, which are only a few nanometers thick, so that the absolute number of carriers is small, ~10^{14} cm^{-2}, allowing large relative changes in their total number. Because the carrier modulation occurs in an interfacial layer, it is also advantageous to use ultrathin channels to avoid shunting effects. The second method to increase the carrier modulation is to apply extremely large electric fields across insulators that are tailored for large breakdown field strengths and dielectric constants. In addition to these requirements, leakage currents through the insulator

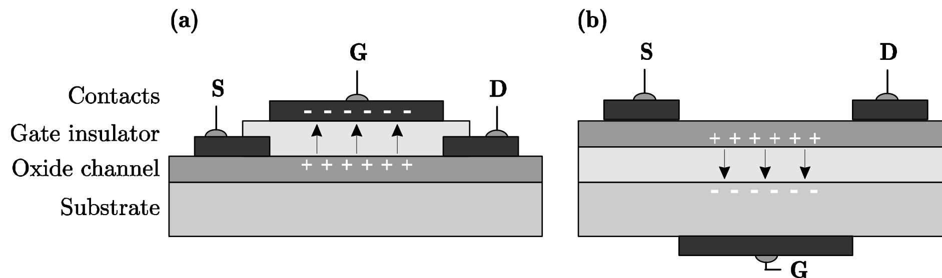

Figure 2.3 Schematic side view of typical sample geometries for field effect studies with insulating **(a)** and conducting **(b)** substrates.

must be much smaller than the DS current, and the density of localized interface states must be small compared with the modulated carrier density.

These technical challenges have been solved for complex oxides in recent years, which opened the field of carrier doping by an electric field in these oxide materials. The capability to substantially modulate the carrier density in perovskite oxides and induce a metal-insulator transition has been demonstrated in the Mott transition field effect transistor [80].

2.6 Concluding remarks

The tunability of the interactions between electrons is an intriguing subject in condensed matter physics. The number and strength of electron interactions determine the electronic properties in correlated electron systems. Control of these interactions at the boundary of the metal-insulator transition provides a tool for electronic switching.

Advances in epitaxial growth technology for thin films of transition metal oxides and high-T_c superconductors has produced well-controlled heterostructures, which makes them ideal candidates for studying their electron interactions. The large induced changes in conductivity by carrier doping, up to 4 orders in magnitude at 300 K, are also beneficial for implementation in real applications.

Electrostatic field tuning, which has been so spectacularly successful in its application to semiconductors, can be applied to correlated electron systems to enable reversible switching of the electronic properties. In particular, the polarization fields that are now routinely achievable using ferroelectric and dielectric oxides provide access to largely uncharted territory, where the interplay between charge at high carrier densities in clean systems and strong Coulomb repulsion becomes important. This continuous modulation of the electrical charge carrier density in strongly correlated electron systems will allow novel electronic devices to be realized and will also provide new input for theoretical studies.

2.7 References

1. Bednorz, J.G. & Müller, K.A., *Z. Phys. B* **64**, 189 (1986).
2. Von Helmolt, R., Wecker, J., Holzapfel, B., Schultz, L. & Samwer, K. *Phys. Rev. Lett.* **71**, 2331 (1993).
3. Heisenberg, W., *Z. Phys.* **33**, 879 (1925).
4. Schrödinger, E., *Ann. Physik* **79**, 361 (1926).
5. Born, M., Heisenberg, W. & Jordan, P., *Z. Phys.* **35**, 557 (1926).
6. Dirac, P.A.M., *Proc. R. Soc. London A* **113**, 621 (1926).
7. Heitler, W. & London, F., *Z. Phys.* **44**, 455 (1927).
8. Hartree, D.R., *Proc. Cambridge Philos. Soc.* **24**, 89 (1928).
9. Fock, V., *Z. Phys.* **61**, 126 (1930).
10. Slater, J.C., *Phys. Rev.* **35**, 210 (1930).
11. Bethe, H., *Ann. Phys. (Leipzig)* **87**, 55 (1928).
12. Sommerfeld, A., *Z. Phys.* **47**, 1 (1928).
13. Bloch, F., *Z. Phys.* **57**, 545 (1929).
14. Wilson, A.H., *Proc. R. Soc. London A* **133**, 458 (1931).
15. Wilson, A.H., *Proc. R. Soc. London A* **134**, 277 (1931).
16. Fowler, R.H., *Proc. R. Soc. London A* **140**, 505 (1933).
17. Fowler, R.H., *Proc. R. Soc. London A* **141**, 56 (1933).
18. De Boer, J.H. & Verwey, E.J.W., *Proc. Phys. Soc. London A* **49**, 59 (1937).
19. Peierls, R., *Proc. Phys. Soc. London A* **49**, 72 (1937).
20. Mott, N.F., *Metal-Insulator Transitions* (Taylor and Francis, London, 1990).
21. Mott, N.F., *Proc. Phys. Soc. London A* **62**, 416 (1949).
22. Mott, N.F., *Can. J. Phys.* **34**, 1356 (1956).
23. Mott, N.F., *Philos. Mag.* **6**, 287 (1961).
24. Anderson, P.W., *Phys. Rev.* **115**, 2 (1959).
25. Hubbard, J., *Proc. R. Soc. London A* **276**, 238 (1963).
26. Kanamori, J., *Prog. Theor. Phys.* **30**, 275 (1963).
27. Gutzwiller, M., *Phys. Rev. Lett.* 10, 159 (1963).
28. Hubbard, J., *Proc. R. Soc. London A* **277**, 237 (1964).
29. Hubbard, J., *Proc. R. Soc. London A* **281**, 401 (1964).
30. Belitz, D. & Kirkpatrick, T.R., *Rev. Mod. Phys.* 66, 261 (1994).
31. Imada, M., Fujimori, A. & Tokura, Y., *Rev. Mod. Phys.* 70, 1039 (1998).
32. McWhan, D.B., Remeika, J.P., Rice, T.M., Brinkman, W.F., Maita, J.P. & Menth, A., *Phys. Rev. Lett.* **27**, 941 (1971).
33. Canfield, P.C., Thompson, J.D., Cheong, S-W. & Rupp, L.W., *Phys. Rev. B* **47**, 12357 (1993).
34. Miyasaka, S., Takagi, H., Sekine, Y., Takahashi, H., Mori, N. & Cava, R.J., *J. Phys. Soc. Jpn.* **69**, 3166 (2000).
35. Zaanen, J., Sawatzky, G.A. & Allen, J.W., *Phys. Rev Lett.* **55,** 418 (1985).

36. Torrance, J.B., Lacorre, P., Nazzal, A.I., Ansaldo, E.J. & Niedermayer, C., *Phys. Rev. B* **45**, 8209 (1992).
37. Takagi, H., Ido, T., Ishibashi, S., Uota, M., Uchida, S. & Tokura, Y., *Phys. Rev. B* **40**, 2254 (1989).
38. Tokura, Y., *Physica C* **235-240**, 138 (1994).
39. Jorgensen, J.D., Veal, B.W., Paulikas, A.P., Nowicki, L.J., Crabtree, G.W., Claus, H. & Kwok, W.K., *Phys. Rev. B* **41**, 1863 (1990).
40. Lichtenberg, F., Widmer, D., Bednorz, J.G., Williams, T., Reller, A., *Z. Phys. B* **82**, 211 (1991).
41. Tokura, Y., Taguchi, Y., Okada, Y., Fujishima, Y., Arima, T., Kumagai, K. & Iye, Y., *Phys. Rev. Lett.* **70**, 2126 (1993).
42. Katsufuji, T. & Tokura, Y., *Phys. Rev. B* **50**, 2704 (1994).
43. Ohtomo, A., Muller, D.A., Grazul, J.L. & Hwang, H.Y., *Appl. Phys. Lett.* **80**, 3922 (2002).
44. Miyasaka, S., Okuda, T. & Tokura, Y., *Phys. Rev. Lett.* **85**, 5388 (2000).
45. Inaba, F., Arima, T., Ishikawa, T., Katsufuji, T. & Tokura, Y., *Phys. Rev. B* **52**, R2221 (1995).
46. Y.J. Yang, Y.J., Wen, T.L., Tu, H., Wang, D.Q. & Yang, J., *Solid State Ionics* **135**, 475 (2000).
47. Kajimura, A., Sasaki, H., Otoshi, S., Suzuki, M., Ippommatsu, M., Kawai, T. & Kawai, S., *Solid State Ionics* **76**, 41 (1995).
48. Brosha, E.L., Mukundan, R., Brown, D.R., Jia, Q.X., Lujan, R. & Garzon, F.H., *Solid State Ionics* **166**, 425 (2004).
49. Tokura, Y., Tomioka, Y., Kuwahara, H., Asamitsu, A., Moritomo, Y. & Kasai, M., *J. Appl. Phys.* **79**, 5288 (1996).
50. Coey, J.M.D., Viret, M. & Von Molnar, S., *Adv. Phys.* **48**, 167 (1999).
51. Urushibara, A., Moritomo, Y., Arima, T., Asamitsu, A., Kido, G. & Tokura, Y., *Phys. Rev. B* **51**, 14103 (1995).
52. Izumi, M. & Konishi, Y., *Appl. Phys. Lett.* **73**, 2497 (1998).
53. Haghiri-Gosnet, A.M. & Renard, J.P., *J. Phys. D: Appl. Phys.* **36**, R127 (2003).
54. Chern, G., Hsieh, W.K., Tai, M.K. & Hsung, K.S., *Phys. Rev. B* **58**, 1252 (1998).
55. Matsuno, J., Mizokawa, T., Fujimori, A., Mamiya, K., Takeda, Y., Kawasaki, S. & Takano, M., Phys. Rev. B **60**, 4605 (1999).
56. Li, J.Q., Matsui, Y., Park, S.K. & Tokura, Y., *Phys. Rev. Lett.* **79**, 297 (1997).
57. Park, S.K., Ishikawa, T., Tokura, Y., Li, J.Q. & Matsui, Y., *Phys. Rev. B* **60**, 10788 (1999).
58. Wadati, H., Kobayashi, D., Kumigashira, H., Okazaki, K., Mizokawa, T., Fujimori, A., Horiba, K., Oshima, M., Hamada, N., Lippmaa, M., Kawasaki, M. & Koinuma, H., *Phys. Rev. B* **71**, 035108 (2005).
59. Yamaguchi, S., Okimoto, Y. & Tokura, Y., *Phys. Rev. B* **54**, R11022 (1996).
60. Señarís-Rodríguez, M.A., Breijo, M.P., Castro, S., Rey, C., Sanchez, M., Sanchez, R.D., Mira, J., Fondado, A. & Rivas, J., *Int. J. Inorg. Mater.* **1**, 281 (1999).

61. E.A.F. Span, E.A.F., Roesthuis, F.J.G., Blank, D.H.A. & Rogalla, H., *Appl. Phys. A* **69**, S783 (1999).
62. Chen, X., Wu, N.J. & Ignatiev, A., *J. Eur. Ceram. Soc.* **19**, 819 (1999).
63. Iguchi, E., Nakatsugawa, H. & Futakuchi, K., *J. Solid State Chem.* **139**, 176 (1998).
64. García de la Cruz, R.M., Falcón, H., Peña, M.A. & Fierro, J.L.G., *Appl. Catal. B-Environ.* **33**, 45 (2001).
65. Kanai, M., Matsuura, D., Kawai, T. & Miki, H., *Physica C* **289**, 223 (1997).
66. Yu, H-C. & Fung, K-Z., *J. Mater. Res.* **19**, 943 (2004).
67. Yu, H-C., Chen, Y-H., Liao, C-L. & Fung, K-Z., *J. Alloy. Compd.* **395**, 286 (2005).
68. Zeng, X.H., Si, W., Stum, M. & Xi, X.X., *IEEE T. Appl. Supercon.* **11**, 3213 (2001).
69. Bozovic, I., Logvenov, G., Belca, I., Narimbetov, B. & Sveklo, I., *Phys. Rev. Lett.* **89**, 107001 (2002).
70. Park, C. & Snyder, R.L., *J. Am. Ceram. Soc.* **78**, 3171 (1995).
71. Cava, R.J., *J. Am. Ceram. Soc.* **83**, 5 (2000).
72. Narlikar, A.V. (Ed.), *High Temperature Superconductivity 1: Materials* (Springer-Verlag, Berlin, 2004).
73. Khare, N., *Handbook of High-Temperature Superconductor Electronics* (Marcel Dekker, New York, 2003).
74. Narlikar, A.V. (Ed.), *High Temperature Superconductivity 2: Engineering Applications* (Springer-Verlag, Berlin, 2004).
75. Asamitsu, A., Moritomo, Y., Tomioka, Y., Arima, T. & Tokura, Y., *Nature* **373**, 407 (1995).
76. Ohno, H., Chiba, D., Matsukura, F., Omiya, T., Abe, E., Dietl, T., Ohno, Y. & Ohtani, K., *Nature* **408**, 944 (2000).
77. Chu, C.W., Gao, L., Chen, F., Huang, Z.J., Meng, R.L. & Xue, Y.Y., *Nature* **365**, 323 (1993).
78. Miyano, K., Tanaka, T., Tomioka, Y. & Tokura, Y., *Phys. Rev. Lett.* **78**, 4257 (1997).
79. Ahn, C.H., Triscone, J.-M. & Mannhart, J., *Nature* **424**, 1015 (2003).
80. Newns, D.M., Misewich, J.A., Tsuei, C.C., Gupta, A., Scott, B.A. & Schrott, A., *Appl. Phys. Lett.* **73**, 780 (1998).

Chapter 3

Fabrication and characterization of oxide thin films

Abstract

Important factors for the performance and lifetime of oxide electronic devices are the purity, structural perfection and homogeneity of the epitaxial layers, and the flatness and abruptness of the layer surfaces and interfaces. Control of the growth mode during the thin film fabrication process determines the layer and surface perfection. An atomically controlled fabrication process is essential for high level performance in new applications and can be achieved by pulsed laser deposition with monitoring by reflection high-energy electron diffraction. Characterization of the structure and composition of the oxide thin films is furthermore essential to determine the origin of the final electronic properties.

3.1 Introduction

New applications of thin film devices are putting higher demands on their performance every year. This development forces the characterization of the thin films, during and after the fabrication process, to be performed with the highest precision. Time resolved analysis during the growth process, such as pulsed laser deposition (PLD), by reflection high-electron energy diffraction (RHEED) enables direct exploration of the growth dynamics and surface morphology. Thin film characterization after the fabrication process can be divided in two categories. The first group of analysis techniques defines the structure and composition of the thin film and includes scanning probe microscopy (SPM), scanning electron microscopy (SEM), x-ray diffraction (XRD), transmission electron microscopy (TEM) and

rutherford backscattering spectrometry (RBS). The second group describes the electronic transport properties by for instance temperature dependent conductivity measurements, Hall effect measurements and UV-Vis spectrophotometry measurements.

In this chapter all fabrication and characterization techniques mentioned above will be presented and shortly discussed.

3.2 Thin film growth by pulsed laser deposition

Although the theoretical ideas were developed in the fifties with the emergence of the maser, the "laser era" is generally considered to have begun in 1960 with a publication on the demonstration of the first optical maser [1]. Among the first experiments using the new, intense light sources were those involving the interactions of laser radiation with solid surfaces, where the emission spectrum of material vaporized by a focused ruby laser was analyzed [2]. The first demonstration of pulsed laser deposition (PLD), in 1965 [3], by ablation of a variety of materials with a ruby laser, did not produce significant interest, as the films deposited were inferior to those obtained via other deposition techniques, such as chemical vapor deposition or molecular beam epitaxy. For approximately twenty years, the technique was only used for analysis of various materials [4] and remained unexploited for thin film growth. Until 1987, then PLD was used to grow a film of the high temperature superconducting material $YBa_2Cu_3O_{7-\delta}$ [5], which was discovered in the same year [6]. The films obtained were found to be superior in quality to those previously grown using other deposition methods and triggered worldwide interest in the technique. Since then, pulsed laser deposition has emerged as a relatively simple and flexible technique for the deposition of high-quality (epitaxial) films from a wide variety of materials, including superconductors, metals, ferroelectrics, ferromagnetics, dielectrics and their multilayers.

3.2.1 Principles of the deposition process

Pulsed laser deposition is a physical vapor deposition technique based on the evaporation of material by means of an intense laser beam. The lasers most commonly employed in PLD are pulsed excimer (ArF, KrF, XeCl) or solid-state Nd:YAG lasers operating at repetition frequencies of 1-100 Hz. Typical wavelengths are 248 nm and 355 nm for, respectively KrF excimer and Nd:YAG lasers. The pulsed, highly energetic laser beam is focussed by a lens in order to get a sufficiently large energy density needed for ablation of the source material. The vaporized material forms a plume and when a substrate is placed inside or near the plume, a part of the evaporated material will form a thin film on this substrate, see Figure 3.1.

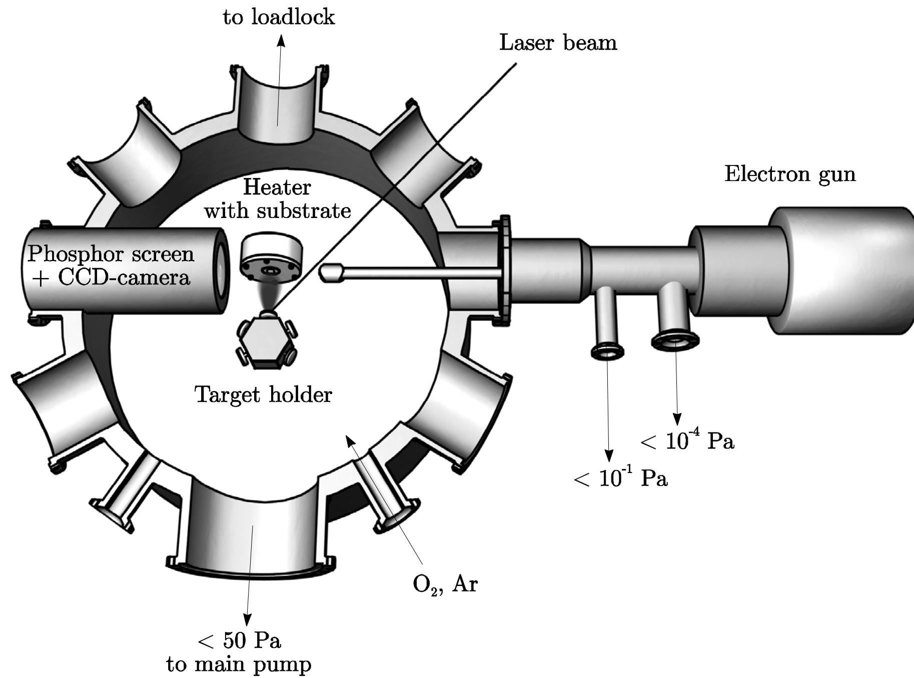

Figure 3.1 Schematic view of the pulsed laser deposition process.

A number of parameters like the absorption coefficient and reflectivity of the target material, and the pulse duration, wavelength and energy of the laser beam affect the interaction of the laser beam with the target. In general the interaction between the laser radiation and the solid material takes place through the absorption of photons by electrons of the atomic system. The absorbed energy causes electrons to be in excited states with high energy and as a result heat the material up to very high temperatures in a very short time. Due to the high temperature some material will be evaporated and it will scatter the laser beam, resulting in even more absorption of laser energy. The temperature of the evaporated material increases therefore rapidly to extremely high values and will further accelerate the electrons. This effect leads to a very high pressure near the target and due to the pressure gradient the evaporated material will expand. Most of the particles will move in the direction perpendicular to the target surface. These excited particles will emit photons, leading to a highlighted plasma plume, which is characteristic for the laser ablation process.

During the expansion of the plasma plume, there is a strong interaction between the vaporized particles due to the high instantaneous ablation rates. Although the vapour does not gain energy after the laser pulse has ended, these collisions cause an important redistribution of energy amongst the various degrees of freedom of the thermodynamical system of the laser generated plasma plume [7]. The processes in

the plume during transport are influenced by the background gas parameters, i.e., mass and pressure, and, as a result, characterize the kinetic energy of the particles arriving at the substrate. This kinetic energy can be varied from high energy (~100 eV) in vacuum to low energy (~1 eV) at large ambient pressures and can be used to modify thin film growth. Several models can be utilized to predict the velocity of the expanding high-pressure vapour as a function of the distance and pressure [8-10].

To grow a thin film of the initial material, a substrate has to be placed inside or near the plasma plume to collect a part of the evaporated material. The quality of the final thin film depends mainly on the absorption/desorption [11] and diffusivity [12,13] of the particles on the surface. The impact energy on the substrate (1-100 eV) [14] does not damage the surface, but induces an enhanced mobility of species on the substrate. This increased surface mobility is generally translated into a well-controlled growth mode, which leads to high-density films. This important aspect gives rise to a better crystallinity in comparison with conventional deposition techniques by using similar or lower substrate temperatures [15,16].

One of the significant advantages of PLD over other deposition methods [17] is the capability for stoichiometric transfer of material from target to substrate. That is, the exact chemical composition of a complex material can be reproduced in the film, when the focused laser energy density is chosen properly [18]. Another advantage is the exceptionally high temporary deposition rate, due to the pulsed nature of laser deposition. Although the mean deposition rate is equal to values of other techniques, each instantaneous deposition is followed by a relatively long time interval where no deposition takes place. This leads to a actual deposition rate, orders of magnitude higher than other physical vapour deposition techniques [19]. The separation in time of the random deposition and the growth is a unique feature of PLD and is very useful in growth kinetics studies [20]. The fact that a laser is used as an external energy source also provides the opportunity to use inert and reactive background gasses as O_2, O_3, NO_2 and N_2O.

In spite of these advantages, industrial uptake of PLD has been slow and to date most applications have been confined to the research environment. An important reason is the lack of thickness uniformity over a large area. A focussed laser beam produces a distribution of ablated material that is strongly peaked in the forward direction. Therefore, uniform thickness films are produced only in a relatively narrow angular range [21]. A practical solution is to move the ablation plume relative to the substrate [22], which would make commercial large-area and high-throughput PLD-systems feasible. In spite of this, PLD-systems used these days are still relatively small-scale and research-based, because no major application has forced industry to upgrade PLD to a real production process [23].

3.2.2 Pulsed laser deposition setup

All thin films, used for experiments described in this thesis, were fabricated by PLD at the Thin Film Laboratory (Twente University, The Netherlands), see Figure 3.2, using a KrF excimer laser (Lambda Physik LPX 210, Göttingen, Germany) with a wavelength of 248 nm [20,24,25]. The maximum pulse energy is 1000 mJ and the repetition rate can be varied from 1 to 100 Hz. The width of the laser pulse is 25 ns. The pressure in the vacuum system during deposition ($1x10^{-5}$ – $3x10^{-1}$ mbar) is controlled by the effective pump speed and the total gas mass flow (0 – 40 ml/min). The effective pump speed is adjusted through a variable restriction between the deposition chamber and the turbo-molecular drag pump. For the background gas, inert gas (Ar) as well as reactive gasses (O_2 and O_3) was used. The amount of material ablated from the target surface is determined by the spot energy density and the spot size. To keep the spatial energy variation within this laser spot below 5%, a very small, homogenous part of the laser beam is selected by using a mask, which is projected onto the target under an incidence angle of 45° by means of a focusing lens with a focal length of ~453 mm. By varying, both, the laser energy and the spot size on the target, the energy density at the target is varied from 1.0 to 7.0 J/cm^2. As a result of using a mask rotation system, which is connected to the target rotation system, different masks can be chosen for different targets. This provides

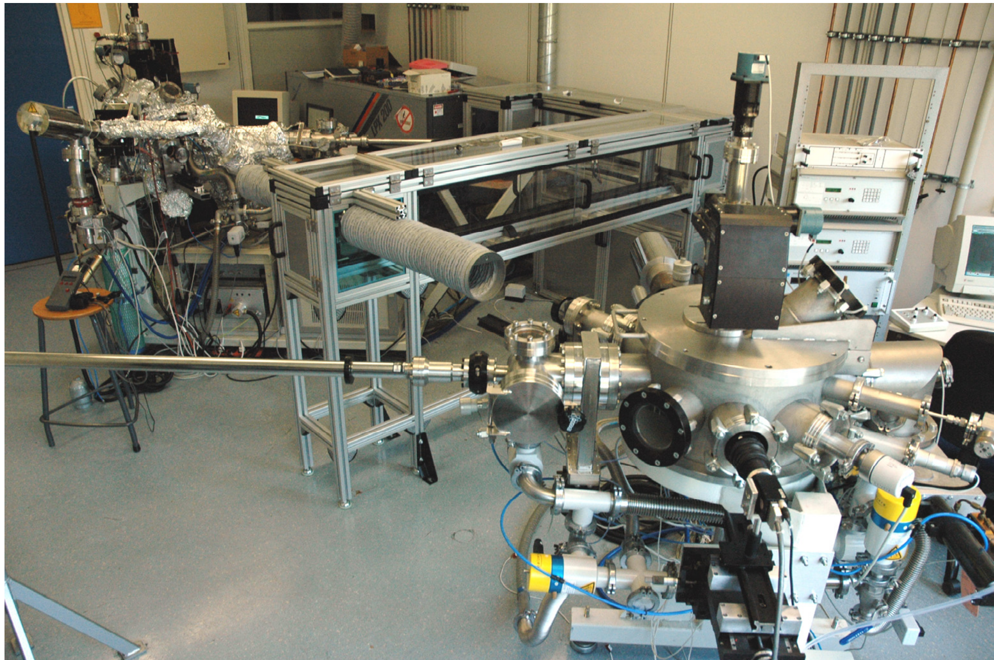

Figure 3.2 Picture of the Pulsed Laser Deposition systems with RHEED monitoring at the Thin Film Laboratory (Twente University, The Netherlands).

Material	pO_2 (mbar)	T (°C)	E_d (J/cm^2)	Deposition rate (Å/pulse)	Target type
SrO	0.13	600 - 850	1.3	0.1	single crystal
$SrTiO_3$	$3x10^{-5}$ - 0.13	600 - 850	1.3	0.1 - 0.3	"
$LaAlO_3$	$3x10^{-5}$ - 0.13	850	1.3	0.05 - 0.1	"
TiO_2	$3x10^{-5}$	850	1.3	0.2	sintered pellet
Al_2O_3	0.05	100 - 300	3.5	0.3	"
Au	0.22 (Ar!)	100	4.0	0.1	"
$La_{2-x}Sr_xCuO_{4+\delta}$	0.08 - 0.18	700 - 740	1.2	0.1	"
$YBa_2Cu_3O_{7-\delta}$	0.13	780	1.3	1.0	"
$YBa_2Cu_2O_x$	0.13	780	7.0	1.0	"
$BaCuO_2$	0.10 - 0.30	600 - 650	1.3	0.15	"
$Y_2Cu_2O_5$	0.10 - 0.30	600 - 650	1.3	0.05	"
$SrRuO_3$	0.13	600	2.5	0.2	"

Table 3.1 Optimized pulsed laser deposition settings for different target materials.

the capability of changing the energy densities on different targets independently. During deposition the targets are scanned horizontally in the laser beam to optimize the usage of the entire target surface. Selection of the masks, targets, laser repetition rate and the number of pulses for each target is computer controlled, allowing automated multilayer depositions with optimized settings for each individual layer. On the multi-target holder a maximum of five targets can be placed and it is mounted, as well as the substrate holder with heater, on a computer controlled xyz-rotation stage. Both of them can be inserted via a loadlock into the system without breaking the vacuum, which makes the thin film fabrication much faster. The substrate holder with heater can be heated up to 950 °C and the temperature is measured using a K-type thermocouple. The optimized deposition settings are given in Table 3.1, for the target materials used in the experiments, which will be described in this thesis.

3.2.3 Growth monitoring by reflection high-energy electron diffraction

The study of film growth has been increasingly characterized by the application of surface-science methods to understand growth at the atomic level. A model study of film growth typically involves deposition of a controlled amount of atoms onto a well-characterized crystalline substrate at a prescribed set of growth conditions. The mode of nucleation and initial growth depends on the bonding between the substrate and the deposited film [26,27].

Initial nucleation and growth

The chain of processes following the impact of a molecule (or atom/ion) on the substrate surface is schematized in Figure 3.3. First, the molecule may be elastically reflected (without energy exchange) and turn back to the gas, or be captured at the surface after transferring its kinetic energy to the surface molecules. If this transfer is total, one says that the molecule is “thermalized”. The probability for a molecule being captured is expressed by the ratio of the number of captured molecules to the total number of molecules that have hit the surface, and it is commonly designated as the sticking coefficient. The energy transfer concerns the molecules incorporated in the surface as well as those present in the adsorption layer. In the case of thin layer formation, when those molecules are of different species, the contribution of each of them results in a peculiar dependence of the probability of a molecule to be captured on surface coverage. For this reason an unambiguous definition of the sticking coefficient is that of capture probability at zero degree of coverage.

Once adsorbed on the surface, a molecule may desorb into the vapour or change adsorption site. The molecule-surface interaction is described by a potential that is a periodic function of two coordinates parallel to the surface and a decreasing function of a third coordinate normal to it. In other words, the energy profile of the surface has a hill-and-valley morphology, the valleys corresponding to the adsorption sites, the hills to the less visited spots, and the saddle points to the natural routes of passage of adsorbed molecules when changing sites. The adsorbed molecule may thus visit few or many adsorption sites before being detached. During this surface migration (or surface diffusion), it can meet sites favourable to its incorporation into the crystal or in a surface layer, in the case of a thin film on foreign substrate. Incorporation and detachment can proceed also via the step through step diffusion. The further behaviour of an already adsorbed molecule (or atom/ion) depends on the nature of the substrate. On a foreign substrate, a two-dimensional or three-dimensional nucleation takes place, depending on the wetting of the substrate by the layer.

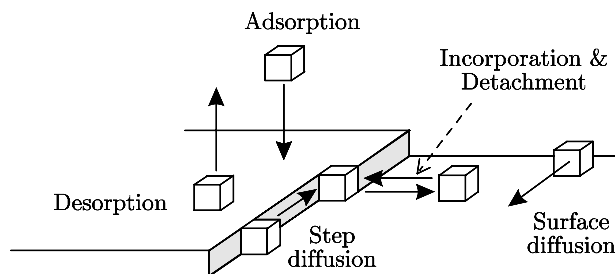

Figure 3.3 Schematic view of the elementary processes during nucleation.

Growth modes

Different growth modes can be determined for the nucleation process on a foreign substrate. In addition to the three classical growth modes [28,29] four other distinct growth modes can be identified [30], see Figure 3.4. The bonding between the substrate and the deposited film, hence the surface and interfacial free energies, can be used to distinguish the growth modes at the initial phase of film formation. When the total free energy of the film surface and the interface equals the free energy of the substrate surface, significant wetting is expected. This leads to layer-by-layer growth as described by Frank and Van der Merwe [31]. For the case of an increased total free energy, little wetting will happen and the deposit will form discrete nuclei that successively grow three-dimensionally and coalesce to a compact continuous film; this is the Volmer-Weber growth mechanism [32]. An intermediate case, when the substrate-film interactions are stronger than the binding within the film, results first in a continuous film of one or two monolayers onto which in the second phase discrete islands are formed that eventually coalesce. This so-called Stranski-Krastanov growth [33] can occur in heteroepitaxy.

These classical modes can qualitatively describe certain epitaxial phenomena. However, different growth modes have been observed for the same substrate-film system, thus indicating that growth techniques and growth parameters influence the growth modes. These aspects are important for the structural perfection of the layers and therefore the device performance. A complete description of all growth modes is based on the most important growth parameters: thermodynamic driving force (supersaturation), crystallographic misfit between film and substrate, and the misorientation of the substrate (the angular deviation of the substrate surface from the ideal crystallographic plane). In homoepitaxial growth the deposited material is identical to the substrate material and the crystalline structure of the substrate is extended into the growing film. Complicating effects, like misfit, do not play a role

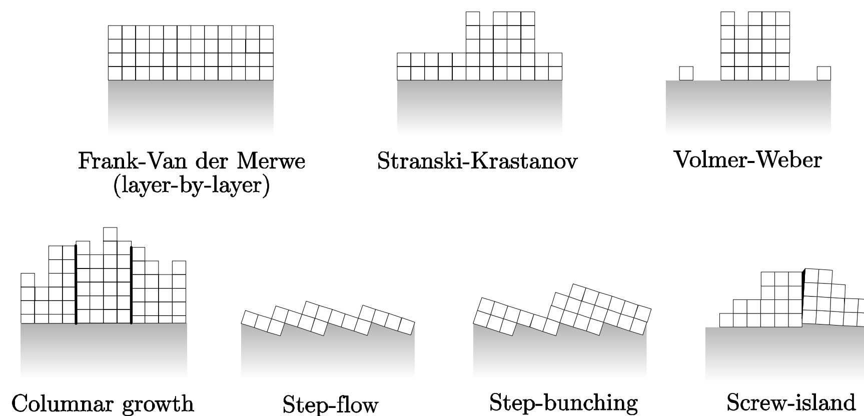

Figure 3.4 Schematic cross sections of substrate-film for the different growth modes.

and only 2D-growth modes are expected, depending on the behaviour of the deposited species [20,34].

On the other hand, in heteroepitaxy the lattice mismatch between substrate and film, the so-called misfit, has to be close to zero at growth temperatures for 2D layer-by-layer (Frank-Van der Merwe) growth. Misfit normally induces Volmer-Weber growth except for large interface energies between substrate and deposited films, which will cause the Stranski-Krastanov growth. If structurally perfect layers or quasi-atomically flat surfaces are required, either homoepitaxy or substrates with zero misfit have to be applied. It is experimentally found that the supersaturations in epitaxy from the vapour phase are so high that epitaxial deposition can be achieved even at very high misfit. Continued growth of the layer, after the initial Volmer-Weber growth, occurs by columnar growth, unless there is a healing procedure involving surface diffusion, for instance by growth interruption or temperature increase.

The misorientation of the substrate is providing steps depending on the angle and the direction of the misorientation. For a given supersaturation, even for the large supersaturation in vapour phase epitaxy, the density of the misorientation steps can be made so high and the interstep distance so small, that 2D-nucleation and the Volmer-Weber and Stranski-Krastanov modes can be suppressed. The layers grow then in the step-flow mode and have a relatively high structural perfection because defects due to coalescence are prevented. Step bunching is observed when a high density of steps moves with large velocities over the growth surfaces. By fluctuations, higher steps catch up with lower steps and then move together as double, triple, etc. steps. This can be suppressed by lowering the supersaturation. The final growth mode, the screw-island mode or spiral-island mode, was discovered during surface investigations of epitaxial layers of the high-temperature superconductor $YBa_2Cu_3O_{7-\delta}$ [35,36]. Coalescence of the large number of initial growth islands led to screw-islands due to the internal layer structure of the material. Similar formation of screw dislocations has been described for organic [37] and inorganic layer structures [38]. Less misorientation steps, lower supersaturation or higher temperatures can reduce the number of screw-islands.

Growth monitoring

Reflection high-energy electron diffraction (RHEED) has proven to be a very versatile technique for growth and surface studies of thin films [39,40,41]. The combination of the forward scattering geometry of RHEED with the arrangement of pulsed laser deposition, in which the plasma plume is incident normally on the substrate, enables diffraction features to be monitored during growth, see Figure 3.5. In RHEED, high-energy electrons with energies of 10-35 keV are incident on the surface of a crystal at a grazing angle of a few degrees (1-5°). The high-energy electrons only interact strongly with the first few layers of material, because of the

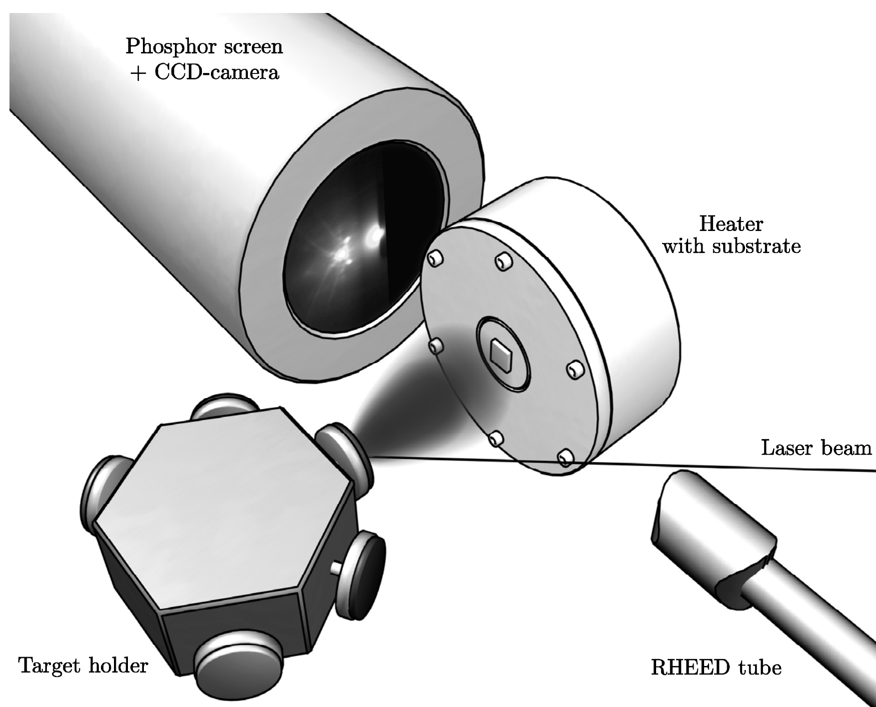

Figure 3.5 Schematic view of RHEED monitoring during growth.

grazing angle. This makes RHEED extremely sensitive to surface morphology. In the deposition setup the electron source and phosphor screen (as detector) are located far from the sample to avoid interference with the deposition process. The electrons are scattered from the crystal surface resulting in a characteristic diffraction pattern on the phosphor screen. The features in this diffraction pattern can be used to analyze the surface structure. The diffraction pattern is a combination of true reflection diffraction on smooth surfaces and transmission-reflection diffraction through particles on the surface. When the first case dominates the pattern exhibits spots lying on concentric circles, called Laue circles, while in the second case a rectangular pattern of spots is present. Much more difficult is to understand the variations in the absolute intensities of the features.

One of the most interesting applications of RHEED to structural analysis of crystal surfaces is the possibility to explore the growth dynamics of thin films by monitoring the variations in the intensity of various features in the RHEED pattern. Since 1981 it has become apparent that when growth is initiated, the intensity of RHEED features shows an oscillatory behaviour, which is directly related to the growth rate [42,43]. The oscillations are associated with periodic changes in the roughness of the growing surface, as atoms forming a new monolayer gradually fill vacant surface lattice sites [44]. In the case of a vicinal surface there are two

competing modes of growth, the mode associated with the advancement of steps due to the attachment of atoms to step edges, and the mode associated with the nucleation of new atoms on flat terraces [45]. The first case represents step-flow growth and because the morphology does not change, the RHEED oscillations do not occur and the intensity stays constant. The second case is similar to a singular surface and exhibits oscillatory behaviour, see Figure 3.6a. In case of island-formation on the surface, the oscillations will be damped and the intensity will decrease, due to the increased surface roughness, see Figure 3.6b. The structure and morphology of these growing surfaces can be derived from the observed intensity variations by applying the step density model [46,47]. This model can be adjusted and applied for the case of pulsed laser deposition [20].

The combination of RHEED monitoring and pulsed laser deposition induces some complications, because the techniques require background pressures, which differ many orders of magnitude. RHEED is often used for the analysis and monitoring of thin film growth in ultra-high vacuum deposition systems, because the pressure has to be sufficiently low to avoid electron scattering by the ambient gas. On the other hand, a high pressure is an important parameter during PLD, because it influences the shape and size of the plasma. Moreover, the oxidation power is much higher at higher pressures, which enables growth at higher temperatures, leading to better crystallinity of the deposited films. Therefore, relative high pressures are favourable in PLD.

Attenuation of the e-beam intensity is expected at high ambient pressure due to elastic and inelastic electron scattering [48,49]. Furthermore, a low pressure is required near the filament of the electron source, to avoid decreasing the lifetime of the filament. The two most important requirements to combine RHEED and PLD

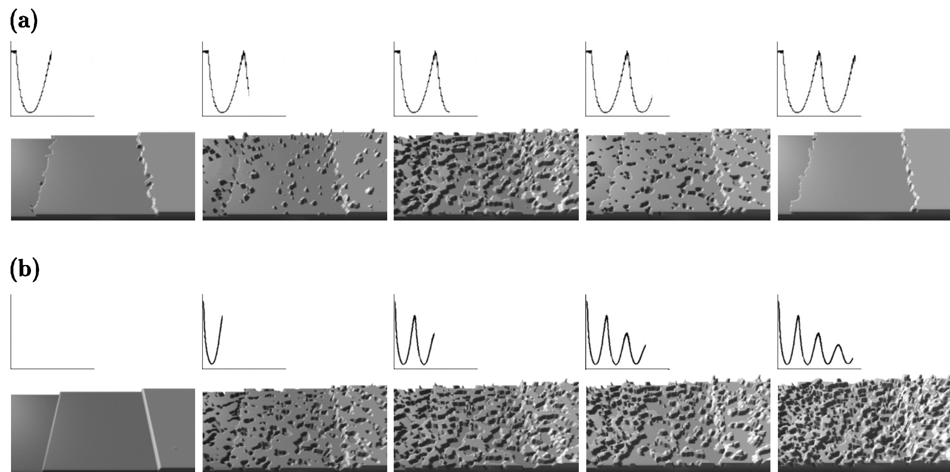

Figure 3.6 Simulation of homoepitaxial $SrTiO_3$ growth from experimental RHEED intensity analysis, shown in the insets, for ideal 2-dimensional growth **(a)** and 3-dimensional island formation **(b)**.

are: a low pressure inside the electron source and a short travelling distance of the electrons through the high background gas. In 1992, these requirements were satisfied for the first time by the development of a differentially pumped RHEED system, which raised the maximum deposition pressure to 0.01 mbar, while the pressure at the filament of the electron source was 10^4 times lower [50]. Several groups showed intensity oscillations while monitoring the growth of complex oxides with RHEED, but needed molecular oxygen, NO_2, O_3 and alternatively pulsed oxygen sources to incorporate oxygen at these low pressures compatible with their RHEED setup. Higher deposition pressures would be beneficial for the reduction of stress and decomposition and increase of oxygen incorporation in the films. This led to the development of the two-stage differentially pumped RHEED system in 1997 [51], which increased the maximum deposition pressure to 0.5 mbar, while keeping the pressure at the filament at the preferred low pressure.

A schematic view of the high-pressure RHEED setup, used for the experiments described in this thesis, is depicted in figures 3.1 and 3.5. The electron source (EK-2035-R, STAIB Instruments) can obtain a minimum beam size of 100 μm even at large working distances. A differential pumping unit is used to maintain a vacuum of better than 5 x 10^{-6} mbar in the electron source. An extension tube, separating the electron source from the deposition chamber, is kept below 10^{-3} mbar and reduces the travelling distance in the high-pressure environment to 50 mm. The diffraction pattern of the scattered electrons is visualized on a phosphor screen and monitored using a digital CCD camera (Uniq Up-610) and acquisition software (K-Space Associates). The software allows time-resolved spot intensity measurements with a minimum acquisition time for every data point of 9 ms. This inventive deposition system has enabled numerous growth experiments of complex oxides and their multilayers over the last years [20,24,25].

3.3 Thin film structure analysis

In order to determine the relation between the initial fabrication process and the final electronic properties of the thin films, characterization of the structural properties is essential. Thorough analysis of the surface morphology, crystalline structure and chemical composition is therefore necessary. The morphology of the surface can be monitored during and after growth by RHEED, as mentioned in the previous section, but the results provide information over a rather large area. By scanning probe microscopy (SPM) and scanning electron microscopy (SEM) the quality of the surface can be analyzed in more detail at the angstrom and nanometer scale, respectively. The crystalline structure is characterized by x-ray diffraction (XRD) and transmission electron microscopy (TEM), where the latter gives the added capability of performing analysis over very small selected areas. The chemical composition can be derived indirectly from the results of the surface morphology and

crystalline structure, but energy dispersive x-ray (EDX) analysis and rutherford backscattering (RBS) were applied for a couple of samples to provide control methods. All thin film analysis measurements are performed at the Low Temperatures group and the Thin Film Laboratory (Twente University, The Netherlands), unless mentioned otherwise.

3.3.1 Scanning probe microscopy

Atomic force microscopy (AFM) experiments were performed on a Multimode scanning probe microscope (Veeco, Cambridge, UK) with a Nanoscope IV controller, which is capable of measuring a broad range of surface characteristics, such as topography, friction, conductivity, piëzo-response and tunneling currents. The surface properties can be imaged in contact or tapping mode and exchangeable scanners for the large (150 x 150 μm^2) and small scale (16 x 16 μm^2) make the system suitable for different research topics. For contact mode, silicon probes were used with nominal force constants of k = 0.20 Nm^{-1} (Innovative Solutions Bulgaria, Sofia, Bulgaria) and k = 0.58 Nm^{-1} (DI, Santa Barbara, USA), whereas for tapping mode silicon probes with resonance frequencies from 260 to 410 kHz (Nanoworld, Neuchatel, Switzerland) were utilized. For some thin films the conducting properties were determined by conducting atomic force microscopy (c-AFM) with platinum-coated probes with k = 2.0 Nm^{-1} (Veeco, Cambridge, UK). All AFM-measurements were performed *ex-situ* directly after thin film growth or sample structuring to minimize surface contamination. Scanning tunnelling microscopy (STM) in variable magnetic fields at 4.2 K is used to study the vortex structures in superconducting thin films[I]. This is possible, due to the capability of STM to measure the electronic density of states and therefore, being sensitive on the scale of the superconducting coherence length.

3.3.2 Scanning electron microscopy

Scanning electron microscopy investigations were carried out on a JSM-5610 (Jeol, Tokyo, Japan) operating between 0.5 and 30 kV. The maximum resolution at 30 kV and a working distance of 6 mm is 3.0 nm. The system is capable of surface analysis by secondary electron imaging as well as backscattered electron imaging, which adds information of the chemical composition to the topography.

[I] Scanning tunneling microscopy measurements in variable magnetic fields at 4.2K were performed at the Kamerlingh Onnes Laboratory (Leiden University, The Netherlands).

Chemical compositions were precisely investigated on a LEO 1550 high-resolution field emission scanning electron microscope (LEO, Cambridge, UK)[II]. The system is equipped with a cryo-cooled x-ray detector and a MAXray parallel beam spectrometer (Thermo Electron Corporation, Waltham, USA) to perform energy-dispersive x-ray (EDX) analysis for a quantitative chemical analysis of a point or region and map of the elemental distribution within a region or along a line.

3.3.3 X-ray diffraction

The structural ordering of the thin films is determined by X-ray diffraction on a four-circle single-crystal diffractometer (CAD4, Enraf Nonius, Delft, The Netherlands) as well as on a thin film diffractometer[III] (X'pert, Philips, Eindhoven, The Netherlands) using a Cu-Kα radiation source. The crystalline structure was analyzed by performing several scans, such as θ-2θ, ω-2θ, Matthieson, hkl and ϕ−scans, to determine thickness, roughness, orientation, phase composition and crystal structure. The instrumental broadening is estimated to be 0.20^o for the CAD4 system and 0.03^o for the X'pert system. The scans on the CAD4 system show additional peaks corresponding to spectral $\lambda/2$ and $\lambda/3$ lines transmitted by the strong reflections of the substrates. The X'pert system did not contain these spectral contributions, due to the presence of a monochromator and a parallel plate collimator.

In-situ X-ray diffraction measurements were also performed during the growth of thin films by pulsed laser deposition on a 2+3 type surface diffractometer with vertical scattering geometry[IV]. By the use of high intensity x-rays, available at third generation synchrotron sources, it is possible to study simultaneously the surface morphology, composition and strain state during growth.

[II] Scanning electron microscopy measurements on the LEO 1550 were performed at the Central Materials Analysis Laboratory (Mesa+, Twente University, The Netherlands).

[III] X-ray diffraction measurements on the X'pert thin film diffractometer were performed at Dannalab (Mesa+, Twente University, The Netherlands).

[IV] In-situ x-ray diffraction measurements during pulsed laser deposition were performed at BM26 (DUBBLE) at the European Synchotron Radiation Facility (ESRF, Grenoble, France).

3.3.4 Transmission electron microscopy

Transmission electron microscopy images were taken on a Philips CM30 Twin/STEM[V], operating at 300 kV, to investigate the crystal structure and epitaxial quality of thin films. The resolution (~2.3 Å) is limited by the image transfer function; determined by the instrumental parameters such as spherical aberration, defocus spread, beam divergence, focus of the objective lens and the acceleration voltage.

Therefore, high-resolution transmission electron microscopy (HRTEM) was performed on a JEOL 4000EX[VI] (Jeol, Tokyo, Japan) operating at 400 kV to provide more detailed information of the crystalline structure. The point-resolution is 1.7 Å. This technique is only applicable for a small area and to increase the investigated area, a scanning technique was chosen.

Scanning transmission electron microscopy (STEM) on a JEOL 3000F[VI] (Jeol, Tokyo, Japan) and a Titan 80-300[VII] (FEI, Eindhoven, The Netherlands), operating at respectively 300 kV and 80 - 300 kV, was used to investigate the crystalline structure at an atomic level. Atomic-resolution high-angle annular dark-field scanning-transmission electron microscopy (HAADF-STEM), also known as Z-contrast imaging, is a promising technique to assess chemical information on the atomic scale. The resolution of the JEOL 3000F and the Titan 80-300 are 2.0 Å and 0.7 Å, respectively. The HAADF-STEM images are recorded with an annular detector at large inner angles, see Figure 3.7. In this way the contribution of the Bragg reflections is minimized and incoherent thermal diffuse scattering becomes the prevailing contribution to the image intensity. Such incoherent STEM images are almost insensitive to defocus and/or thickness changes, and in contrast to HRTEM images, the atomic columns always appear as white dots. Since the intensities are related to the average atomic number, Z, of the atomic columns, a qualitative interpretation of HAADF-STEM images is relatively straightforward. A quantitative interpretation of such images, however, requires image simulations and image matching.

[V] Transmission electron microscopy measurements on the Philips CM30 Twin/STEM were performed at the Central Materials Analysis Laboratory (Mesa$^+$, Twente University, The Netherlands).

[VI] High-resolution electron microscopy measurements on the JEOL 4000EX and scanning transmission electron microscopy measurements on the JEOL 3000F were performed at the EMAT research centre (University of Antwerp, Belgium).

[VII] Scanning transmission electron microscopy measurements on the Titan 80-300 were performed at FEI company (Eindhoven, The Netherlands).

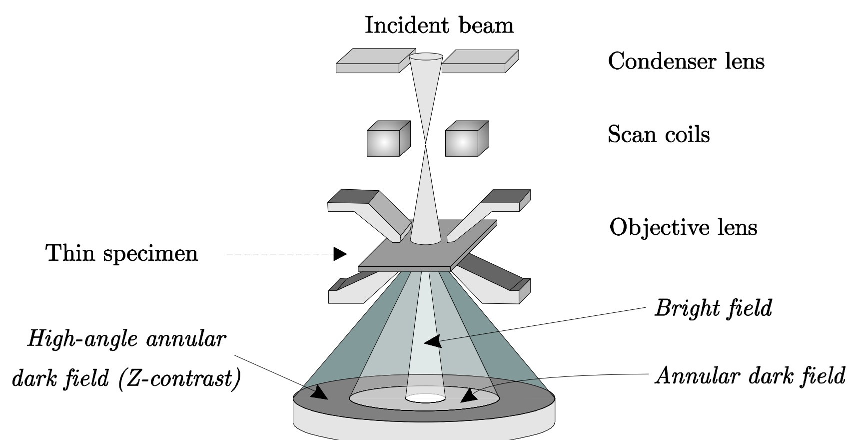

Figure 3.7 Schematic view of HAADF-STEM.

3.3.5 Rutherford backscattering spectrometry

Rutherford backscattering spectrometry (RBS) is performed on several samples to compare the measured stoichiometry of the thin films with the expected values[VIII]. RBS is a very sensitive tool for detecting high atomic number elements. The mass resolution, or ability to distinguish between elements, is very low for low atomic number elements. However, for heavy elements the resolution is very good. Therefore, RBS is often used to measure the stoichiometry of thin films.

3.4 Electronic transport analysis

In addition to the structural properties, the electronic transport properties provide information about the quality of thin film conductors and it's applicability in devices. Measurement of the conductivity, electron density, mobility and type of charge carriers is therefore very important. In the first place, the conductivity is measured for all thin films at variable temperatures between 4.2 and 300 K. Secondly, a variable magnetic field between −1.0 and 1.0 Tesla is applied in a Hall setup to analyze the charge carriers for some samples. As a next step the reflectance and transmittance of different thin films and multilayers are measured by an UV-Vis spectrophotometer.

[VIII] Rutherford backscattering spectrometry measurements were performed at Philips company (Eindhoven, The Netherlands).

3.4.1 Temperature dependent conductivity measurements

All temperature dependent investigations are current-sourced measurements in a four-point method. The current is applied by a diode sensor current source, which can be switched between 10 and 100 μA, or a Keithley 220 programmable current source. During all measurements, the applied current is monitored, to ensure accurate conductivity measurements. All voltages are monitored by HP 34401A multimeters. The contacts are wire-bonded to the sample with aluminum wire. In this way, the surface of the sample is damaged and the wire is connected into the sample to a depth of tenths of nanometers. A rhodium-iron sensor is placed close to the sample inside the holder to determine the temperature value accurately down to 1.4 K. The shielded holder is mounted on a stick and lowered in a dewar with liquid helium or nitrogen to cool the sample down. The position of the sample holder in the dewar determines the temperature and the lowering or pull-up speed fixes the cool down or warm up rate. Measurements were done during cool down as well as during warm up to identify possible hysteresis.

3.4.2 Hall effect measurements

The forces acting on moving charges in a conductor can be analyzed by measuring the Hall effect. To determine the charge characteristics, contacts are wire-bonded to the sample in a Van der Pauw geometry. This enables measurement of the sheet resistance as well as the electron density, mobility and type of charge carrier when an external magnetic field is applied perpendicular to the sample. All Hall effect measurements are performed at room temperature in a variable magnetic field between −1.0 and 1.0 Tesla[IX]. The current and voltage are respectively sourced and measured by a Keithley 2400 source-measure unit.

3.4.3 UV-Vis spectrophotometry measurements

The Cary 50 UV-Vis spectrophotometer (Varian Instruments, Palo Alto, USA) is used for measuring reflectance and transmittance as a function of wavelength (190 – 1100 nm) for the different thin films and multilayers. In this spectrophotometer, a double-beam design is used to permit measurement with continuous change in wavelength. Both sample beam and reference beam are monitored continuously, so that reflectance (or transmittance) can be calculated at each wavelength. In this way, source fluctuations and drift are also minimized.

[IX] Hall effect measurements were performed at the SMI group (Twente University, The Netherlands).

3.4.4 Probing station

Contacts to the samples for transport measurements were fabricated by wire bonding. This leads to considerable damage of the thin film layer, which is an immense problem for the characterization of dielectric materials. To avoid this problem, dielectric materials were analyzed in a probing station. Instead of wire-bonded contacts, probes are placed gently on the surface and the underlying layer is kept intact. Measurements were done on a Karl Suss PM 8 analytical probing station[X] to determine the capacitance and leakage characteristics of dielectric layers.

To enable temperature dependent probe measurements, a cryogenic probing station was installed. The micro-manipulated cryogenic probe system (model ST-4LF-0-TX, Janis, Wilmington, USA) consists of a sample chamber with four ports for independent micro-manipulated probe stations and a continuous flow cryostat system. A quartz window ensures clear viewing of the sample area and the four probes by a Leica GZ6 microscope. A control heater and a silicon diode thermometer (DT-670B-CU, Lakeshore, Westerville, USA) are mounted on the cold-finger for active temperature control by a PID controller (Scientific Instruments, West Palm Beach, USA) with a stability of 0.05 K in the entire temperature range between 4.2

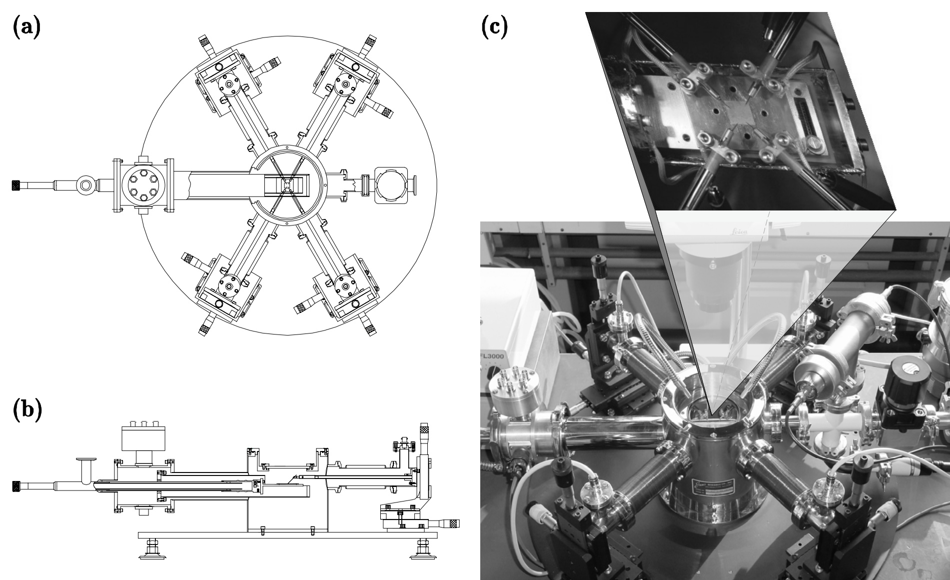

Figure 3.8 Schematic top view **(a)**, side view **(b)** and picture **(c)** of cryogenic probing station.

[X] Dielectric characterizations on the Karl Suss PM 8 probing station were performed at the MESA$^+$ Test Centre (Twente University, The Netherlands).

and 300 K. Four independent probe stations are mounted on x, y, z translation stages, providing 25 mm along the probe x-axis, 14 mm in the y-direction and 10 mm along the vertical z-direction perpendicular to the plane of the sample. Each stage is capable of an incremental translation of 10 μm with typical 2.5 μm sensitivity. On each probe, a single-tip triaxial probe holder with a replaceable tungsten tip is wired with flexible triaxial cables to triaxial hermetic feedthroughs. A second silicon diode thermometer (DT-670B-CU, Lakeshore, Westerville, USA) is mounted close to the sample for accurate temperature measurements.

Good thermal contact between the sample and the sampleholder as well as the sampleholder and the cold-finger is essential to reach temperatures below 10 K. A very small amount of vacuum grease (Apiezon N, Manchester, UK) will give the best thermal contact between the sampleholder and the coldfinger. To provide the best thermal contact between the sample and the sampleholder, silver paste has to be placed between them and the sample has to be clamped down by tantalum clamps. Placing the probes on the surface of the sample will induce heat transfer to the sample and increase the temperature. Therefore, the probeholders are connected by copper wires to the cryostat shielding, which is at 50 K, to pre-cool the probeholders and lower the heat transfer to the sample.

3.5 Concluding remarks

An important condition for modern materials physics and nanoscience is control of materials to atomic dimensions. For complex oxides, pulsed laser deposition (PLD) has proven to be a growth technique in which the deposited material can be controlled at the atomic scale. Stoichiometric transfer, high deposition rate and tunable energy of the arriving particles are properties, which make 2-dimensional layer by layer growth feasible for various complex oxides with a surface roughness of only one unit cell. This makes fabrication of thin films, heterostructures and superlattices possible with high quality surfaces and interfaces, which can be applied in novel electronic devices. However, the combination of pulsed laser deposition with reflection high-energy electron diffraction (RHEED), to monitor in-situ the thin film growth, is essential to obtain this high quality. Monitoring of the RHEED intensity provides information about the surface morphology as well as the diffusion and nucleation processes. Several analysis techniques can be used to determine the structural quality of the grown thin films and provide some insight in the effect of the various processes during growth on the eventual electronic properties.

3.6 References

1. Maimon, T.H., *Nature* **187**, 493 (1960).
2. Breech, F. & Cross, L., *Appl. Spectrosc.* **16**, 59 (1962).
3. Smith, H.M. & Turner, A.F., *Appl. Opt.* **4**, 147 (1965).
4. Cremers, D.A., Radziemski, L.J., Laser Plasmas for Chemical Analysis, in *Laser Spectroscopy and Its Applications,*ed, by Radziemski, L.J., Solarz, R.W. & Paisner, J.A. (Marcel Decker, New York, 1987).
5. Dijkkamp, D., Venkatesan, T., Wu, X.D., Shaheen, S.A., Jisrawi, N., Min-Lee, Y.H., McLean, W.L. & Croft, M., *Appl. Phys. Lett.* **51,** 619 (1987).
6. Wu, M.K., Ashburn, J.R., Torng, C.J., Hor, P.H., Meng, R.L., Gao, L., Huang, Z.J., Wang, Y.Q. & Chu, C.W., *Phys. Rev. Lett.* **58**, 908 (1987).
7. Kools, J.C.S., *Laser Ablation and Deposition of Metals*, PhD thesis, Technical University Eindhoven, The Netherlands (1992).
8. Geohegan, D.B., *Thin Solid Films* **220**, 138 (1992).
9. Kools, J.C.S., Baller, T.S., De Zwart, S.T. & Dieleman, J., *J. Appl. Phys.* **71**, 4547 (1992).
10. Strikovski, M. & Miller, J.H., *Appl. Phys. Lett.* **73**, 1733 (1998).
11. Tyunina, M., Levoska, J. & Leppävuori, S., *J. Appl. Phys.* **83**, 5489 (1998).
12. Dam, B. & Stäuble-Pümpin, *J. Mater. Sci.-Mater. El.* **9**, 217 (1998).
13. Blank, D.H.A., Rijnders, G.J.H.M., Koster, G. & Rogalla, H., *Appl. Surf. Sci.* **138**, 17 (1999).
14. Kools, J.C.S., *J. Appl. Phys.* **74**, 6401 (1993).
15. Dieleman, J., Van de Riet, E. & Kools, J.C.S., *Jpn. J. Appl. Phys.* **31**, 1964 (1992).
16. Kwok, H.S., *Thin Solid Films* **218**, 277 (1992).
17. Chrisey, D.B. & Hubler, G.K. (Eds.), *Pulsed Laser Deposition of Thin Films* (John Wiley & Sons, New York, 1994).
18. Lowndes, D.H., Geohegan, D.B., Puretzky, A.A., Norton D.P. & Rouleau, C.M., *Science* **273**, 898 (1996).
19. Geohegan, D.B. & Puretzky, A.A., *Appl. Phys. Lett.* **67**, 197 (1995).
20. Rijnders, A.J.H.M., *The initial growth of complex oxides: study and manipulation*, PhD thesis, University of Twente, The Netherlands (2001).
21. Venkatesan, T., Wu, X.D., Inam, A. & Wachtman, J.B., *Appl. Phys. Lett.* **52**, 1193 (1988).
22. Greer, J.A. & Tabat, M.D.*, J. Vac. Sci. Technol. A* **13**, 1175 (1995).
23. Greer, J.A. in *Pulsed Laser Deposition of Thin Films,* ed, by Chrisey, D.B. & Hubler, G.K. (John Wiley & Sons, New York, 1994), pp. 293-311
24. Koster, G., *Artificially layered oxides by pulsed laser deposition*, PhD thesis, University of Twente, The Netherlands (1999).
25. Leca, V., *Heteroepitaxial growth of copper oxide superconductors by pulsed laser deposition*, PhD thesis, University of Twente, The Netherlands (2003).
26. Zhang, Z. & Lagally, M.G., *Science* **276**, 377 (1997).

27. Mutaftschiev, B. (Ed.), *The Atomistic Nature of Crystal Growth* (Springer, Berlin, 2001), pp. 279-289
28. Bauer, E., *Z. Kristallogr.* **110**, 395 (1958).
29. Le Lay, G. & Kern, R., *J. Cryst. Growth* **44**, 197 (1978).
30. Scheel, H.J. & Fukuda, T. (Ed.), *Crystal Growth Technology* (John Wiley & Sons, Chichester, 2003).
31. Frank, F.C. & Van der Merwe, J.H., *Proc. Roy. Soc. London A* **198**, 216 (1949).
32. Volmer, M. & Weber, A., *Z. Phys. Chem.* **119**, 277 (1926).
33. Stranski, I.N. & Krastanov, *Acad. Wiss. Math.-Naturw. Klasse IIb* **146**, 797 (1938).
34. Rosenfeld, G., Poelsema, B. & Comsa, G., in *Growth and Properties of Ultrathin Epitaxial Layers,* ed, by King D.A. & Woodruff, D.P. (Elsevier, Amsterdam, 1997), pp. 66-101
35. Hawley, M., Raistrick, I.D., Beery, J.G. & Houlton, R.J., *Science* **251**, 1587 (1991).
36. Gerber, C., Anselmetti, D., Bednorz, J.G., Mannhart, J. & Schlom, D.G., *Nature* **350**, 279 (1991).
37. Kozlovskii, M.I., *Sov. Phys. – Crystallogr.* **3**, 236 (1958).
38. Baronnet, A., *J. Cryst. Growth* **19**, 193 (1973).
39. Larsen, P.K. & Dobson, P.J. (Eds.), *Reflection High-Energy Electron Diffraction and Reflection Electron Imaging of Surfaces* (Plenum Press, New York, 1988).
40. Braun, W., *Applied RHEED: reflection high-energy electron diffraction during crystal growth* (Springer, Berlin, 1999).
41. Peng, L.M., Dudarev, S.L. & Whelan, M.J., *High-Energy Electron Diffraction and Microscopy* (Oxford University Press, Oxford, 2004).
42. Harris, J.J., Joyce, B.A. & Dobson, P.J., *Surf. Sci.* **103**, L90 (1981).
43. Wood, C.E.C., *Surf. Sci.* **108**, L441 (1981).
44. Neave, J.H., Joyce, B.A., Dobson, P.J. & Norton, N., *Appl. Phys. A* **31**, 1 (1983).
45. Van Hove, J. M., Lent, C.S., Pukite, P.R. & Cohen, P.I., *J. Vac. Sci. Technol. B* **1**, 741 (1983).
46. Stoyanov, S., *Surf. Sci.* **199**, 226 (1988).
47. Stoyanov, S. & Michailov, M., *Surf. Sci.* **202**, 109 (1988).
48. Garcia, G., Roteta, M. & Manero, F., *Chem. Phys. Lett.* **264**, 589 (1997).
49. Garcia, G., Blanco, F. & Williart, A., *Chem. Phys. Lett.* **335**, 227 (2001).
50. Karl, H. & Stritzker, B. *Phys. Rev. Lett.* **69**, 2939 (1992).
51. Rijnders, A.J.H.M., Koster, G., Blank, D.H.A. & Rogalla, H., *Appl. Phys. Lett.* **70**, 1888 (1997).

Chapter 4

Carrier doping control in $La_{2-x}Sr_xCuO_{4+\delta}$ ultrathin films

Abstract

The electronic properties of $La_{2-x}Sr_xCuO_{4+\delta}$ thin films can be tuned from insulating to superconducting by altering the strontium and oxygen stoichiometry. The perovskite crystal structure enables the growth of highly ordered superconducting thin films and multilayers with thicknesses down to a few unit cells. The fabrication process of electric field effect structures was improved by using the sensitivity of the superconducting properties on variations in the carrier doping.

4.1 Introduction

In November 1986 the results of Bednorz and Müller [1] became known to a small group of scientists interested in superconductivity. Within one month measurements were performed, which showed that the superconducting transition temperature in the original Ba-La-Cu-O system increased significantly under the application of pressure; i.e., T_c increased as the crystal lattice got smaller [2,3]. At the same moment it was determined that the compound, which was actually superconducting, was the layered K_2NiF_4-type oxide solid-solution $La_{2-x}Ba_xCuO_4$ [4]. These observations led, before Christmas 1986, to the discovery of the superconducting strontium analog of the K_2NiF_4-type compound, $La_{1.8}Sr_{0.2}CuO_4$, which was found to be superconducting at the then astonishingly high temperature of 38 K [5]. This was consistent with the notions obtained from the high-pressure

results that smaller lattices (strontium is smaller than barium) might lead to higher transition temperatures.

Investigations on the structural, magnetic and electronic properties of compounds in the $La_{2-x}Sr_xCuO_4$ series for $0.05 \leq x \leq 1.1$ revealed superconductivity among several compounds [6]. In the following years extensive studies were carried out on this system, because of the attractiveness of this system as a prototype material system for the study of high-T_c superconductivity. This is due to the simple crystal structure and the fact that it maintains the same over the entire composition range, allowing studies of wide variations in hole concentration and their effects on superconductivity. References 7 and 8, and the references therein, are a good overview of the $La_{2-x}Sr_xCuO_4$ studies in the first two years.

The $La_{2-x}Sr_xCuO_4$ compound crystallizes in a body-centered tetragonal structure of the K_2NiF_4-type, see Figure 4.1a (taken from ref. 9). The CuO_2 planes are ~6.6 Å apart, separated by two LaO planes. In the crystal, oxygen is in an O^{2-} valence state that completes the *p* shell. Lanthanum loses three electrons and becomes La^{3+}, which is in a stable closed-shell configuration. To conserve charge neutrality, the copper atoms must be in a Cu^{2+} state, which is obtained by losing the (*4s*) electron, which is weakly bounded to the atom, and also one *d* electron. This creates a hole in the *d* shell. Each copper atom in the conducting planes has an oxygen above and below in the z-direction, the so-called apical O atoms. Then, the copper atoms are surrounded by an octahedral of oxygen atoms as in a perovskite structure. However, the distance between the copper atom and the apical O atom is ~2.4 Å, which is considerably larger than the Cu-O distance in the planes, ~1.9 Å.

Upon doping, Sr^{2+} atoms randomly replace La^{3+} atoms and thus fewer electrons are donated, which results to the transfer of one electron to the site of the Sr atom and thus creating one hole in the CuO_2 plane. A combined phase diagram for single crystals [8,10-12] is shown in Figure 4.1b. More details about the electronic phases inside the pseudogap can be found in reference 13. Superconductivity appears for doping levels (x) beyond a critical concentration of x=0.05 and the transition temperature reaches its maximum value of 38 K for the optimal doping of x=0.15. The anomalous suppression of superconductivity in $La_{2-x}Sr_xCuO_4$ (and related compounds), when the hole concentration (x) is near 1/8, can be related to stripe correlations of spins and holes [14].

Since the first fabrication of $La_{2-x}Sr_xCuO_4$ thin films in 1989 [15], many groups have grown them for applied and fundamental studies. It has been found that in the well-crystallized films unrelieved epitaxial strain exists, induced by the substrate, which has a very significant impact on the superconducting properties [16]. For compressively strained films on $LaSrAlO_4$ substrates, introduced by Trofimov et al. [17,18], the transition temperature can be enhanced over the bulk values [19-21] with the present record of 51.5 K [22] on the condition that the films are fully oxygenated.

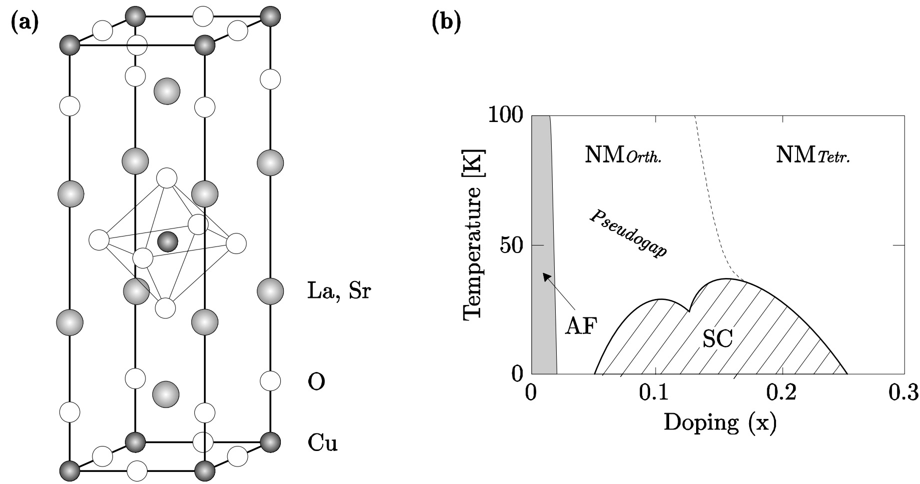

Figure 4.1 Body-centered tetragonal crystal structure **(a)** and phase diagram **(b)** of $La_{2-x}Sr_xCuO_4$ summarizing structural, magnetic and transport properties with the dependence on the doping level (x). Antiferromagnetic (AF), superconducting (SC) and normal metal (NM) regions are indicated, with the transition between the high-temperature tetragonal and the low-temperature orthorhombic phases.

Investigations on pulsed laser deposited $La_{2-x}Sr_xCuO_{4+\delta}$ thin films and multilayers, in which the carrier doping is tuned during the growth process, will be presented in this chapter. The atomic interface configurations at the substrate during the initial growth as well as the epitaxial strain relaxation during subsequent growth will initially be described. Subsequently the effect of variations in the stoichiometry of strontium and oxygen on electronic and magnetic properties will be determined. Finally, the sensitivity of the electronic properties on the carrier doping will be utilized to improve the fabrication process of electric field effect structures. Targets with different doping levels (x=0, 0.05, 0.125, 0.15 and 0.25) are used to investigate a wide range in the phase diagram.

4.2 Initial growth at the substrate surface

Perovskite oxides are commonly described in terms of their cubic unit cells, with the generic formula ABO_3. It is instructive to describe the perovskites in terms of their constituting AO and BO_2 layering sequence. The unit cell of the $SrTiO_3$ substrate consists of Ti atoms occupying the corner positions and a Sr atom occupying the body center position. The Ti atom is 6-fold coordinated by oxygen, forming the corner-sharing oxygen octahedral. The structure can be viewed as a stack of alternating SrO (AO) and TiO_2 (BO_2) planes along one of the principal axes. The surface of the $SrTiO_3$ single-crystal can therefore be terminated by SrO or

TiO_2, when cut perpendicular to one of the principal axes, or by a mixture of both. Control of this surface termination can create single-terminated surfaces, which is crucial for accurate growth studies. Single-terminated TiO_2 surfaces are achieved by removing the remaining SrO by a chemical treatment, followed by an annealing procedure [23]. The opposite single-terminated SrO surfaces are fabricated by depositing a SrO monolayer on a single-terminated TiO_2 surface by pulsed laser interval deposition [24] from a SrO single-crystal target.

In heteroepitaxy of perovskite structures the AO-BO_2 stacking sequence is maintained and, therefore, the surface termination of the substrate determines the initial growth of the thin film. However, in the case of $La_{2-x}Sr_xCuO_4$ two AO layers are stacked on top of each other with an in-plane shift and form the rock-salt structure. This could theoretically lead to four possible stacking sequences at the interface for growth on $SrTiO_3$, see Figure 4.2. For two cases the interface stacking sequence can be observed as a perovskite structure (A and C), while for the other two cases it forms a rock-salt structure (B and D). For depositions on a TiO_2-terminated surface, the film growth would always start with a (La,Sr)O layer and result in two possible interface configurations (A and B). For the case of a SrO-terminated surface the first layer can be either CuO_2 (C) or (La,Sr)O (D), but would also result in two possible interface configurations.

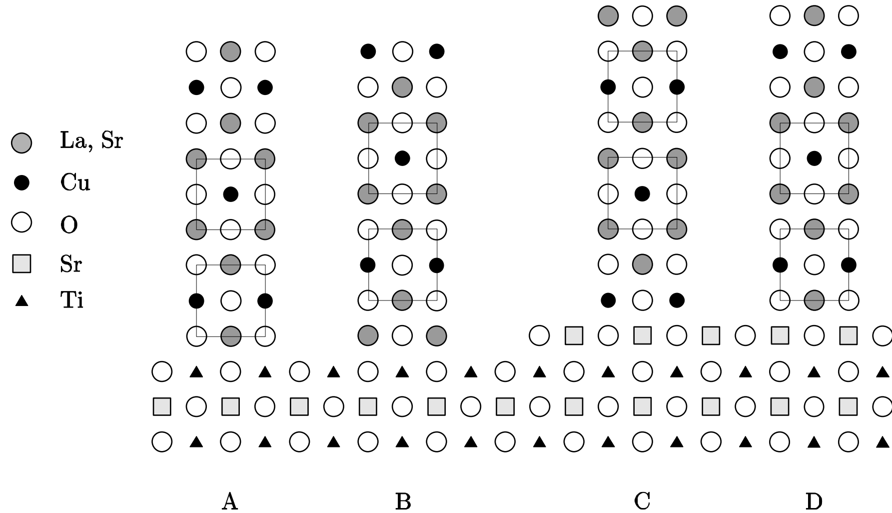

Figure 4.2 Different types of possible interface configurations for $La_{2-x}Sr_xCuO_4$ growth on $SrTiO_3$: (A) bulk-SrO-TiO_2-(La,Sr)O-CuO_2-(La,Sr)O-(La,Sr)O-CuO_2-(La,Sr)O-bulk, (B) bulk-SrO-TiO_2-(La,Sr)O-(La,Sr)O-CuO_2-(La,Sr)O-(La,Sr)O-CuO_2-(La,Sr)O-bulk, (C) bulk-SrO-TiO_2-SrO-CuO_2-(La,Sr)O-(La,Sr)O-CuO_2-(La,Sr)O-(La,Sr)O-CuO_2-(La,Sr)O-bulk and (D) bulk-SrO-TiO_2-SrO-(La,Sr)O-CuO_2-(La,Sr)O-(La,Sr)O-CuO_2-(La,Sr)O-bulk .

Using pulsed laser deposition, thin films of $La_{2-x}Sr_xCuO_4$ (LSCO) were grown on single-terminated (001) $SrTiO_3$ substrates. Sintered ceramic targets with different Sr-doping levels (x=0, 0.05, 0.125, 0.15 and 0.25) were used to investigate a wide range in the phase diagram. During growth, the substrates were heated to a temperature of 700 °C and an oxygen background pressure of 0.13 mbar was applied. During deposition at a repetition rate of 4 Hz with an energy density of 1.2 J/cm^2, the film growth was monitored in-situ by RHEED. The RHEED intensity fluctuations for $La_{1.875}Sr_{0.125}CuO_4$ growth on SrO- and TiO_2-terminated $SrTiO_3$ are shown in respectively Figure 4.3a and b. During the initial growth RHEED oscillations were observed, indicating layer-by-layer growth. The growth unit, deposited during every oscillation, was determined ex-situ by an x-ray small angle θ-2θ scan with respect to the substrate normal. Pronounced intensity fringes, caused by the interference between the two x-ray beams specularly reflected at the air/film and film/substrate interfaces, were used to resolve the film thickness. This value was consistent with

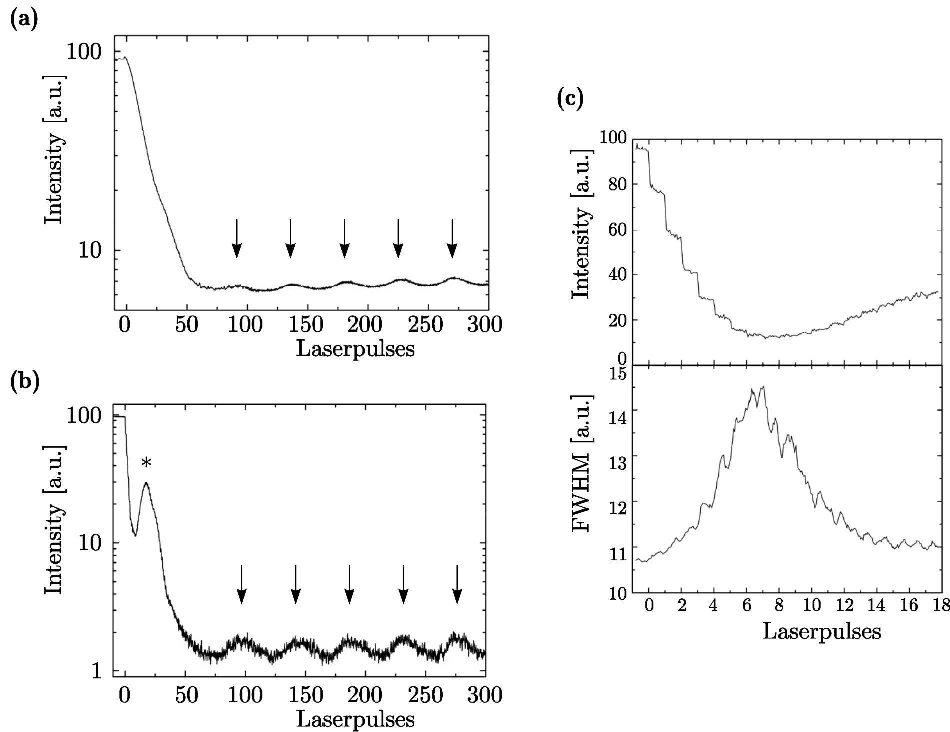

Figure 4.3 RHEED intensity fluctuations during initial growth of $La_{1.875}Sr_{0.125}CuO_4$ on SrO-terminated $SrTiO_3$ **(a)** and on TiO_2-terminated $SrTiO_3$ **(b).** Solid arrows indicate monolayer growth of half unit cell layers. **(c)** RHEED intensity and FWHM results for the deposition of the first monolayer of $La_{1.875}Sr_{0.125}CuO_4$ on TiO_2-terminated $SrTiO_3$, which is indicated by an asterisk in Figure 4.3b.

the thickness determined from the RHEED oscillations, assuming the growth unit was half of the unit cell (6.6 Å) and thus consisted of three atomic layers: (La,Sr)O, CuO_2 and (La,Sr)O. This growth unit is correct with charge neutrality and has been observed by other groups using PLD [25] and reactive co-evaporation [26] techniques.

The first unit cell of $La_{1.875}Sr_{0.125}CuO_4$ on a SrO-terminated surface is stabilized after 92 laserpulses, which is consistent with two RHEED oscillation periods. Further growth occurs in a layer-by-layer fashion of half unit cell monolayers, see Figure 4.3a. This confirms the expected initial growth as shown in interface configuration D in Figure 4.2, indicating layer-by-layer growth of half unit cell monolayers directly from the interface. In case of growth on a TiO_2-terminated surface a different growth mode is clearly visible during the first couple of laserpulses, see Figure 4.3b. A sharp maximum in the RHEED intensity, after depositing 20% of a unit cell, indicates stabilization of a layer with low roughness. Further growth leads to stabilization of the first unit cell after depositing 110% of the amount of material, which is needed during the rest of the deposition to form a unit cell, determined from the RHEED oscillation periods. The RHEED intensity and FWHM during growth of the first atomic layers on a TiO_2-terminated surface are shown in Figure 4.3c. The low FWHM value after 17 laserpulses, same as initial value, supports the conclusion from the RHEED maximum that a smooth layer is stabilized. These observations of a smooth layer after 20% of a unit cell suggest interface configuration B in Figure 4.2 for growth on a TiO_2-terminated $SrTiO_3$ surface, where first a monolayer of (La,Sr)O is formed at the interface before correct layer-by-layer growth of half unit cell monolayers is started. The RHEED analysis of $La_{1.875}Sr_{0.125}CuO_4$ growth on TiO_2-terminated as well as on SrO-terminated $SrTiO_3$ suggest the formation of a rock-salt atomic structure at the interface.

Thin films of LSCO deposited on a SrO-terminated surface appear to exhibit a higher surface roughness. This is caused by the formation of precipitates on the surface, probably due to the fact that the double (La,Sr)O layer on the surface is not very stable and reacts with water vapour in ambient atmosphere. The phenomena of a better surface morphology in case of growth on a TiO_2-terminated surface and the stabilization of a smooth layer after depositing 20% of a unit cell are observed for all depositions of LSCO with different doping levels.

4.3 Epitaxial strain

Epitaxial growth of LSCO thin films on single-crystal substrates will induce strain, which can be compressive or tensile when grown on respectively $LaSrAlO_4$ or $SrTiO_3$. The in-plane misfit between the $La_{2-x}Sr_xCuO_4$ (3.76-3.82 Å) and $SrTiO_3$ (3.905 Å) crystals is about 2–4%. Due to this small misfit, LSCO layers of considerable thickness can be grown in a layer-by-layer mode, while the surface roughness remains comparable to the initial substrate surface. Figure 4.4a shows the RHEED fluctuations during growth of a 50 nm $La_{1.875}Sr_{0.125}CuO_4$ layer on a TiO_2-terminated $SrTiO_3$ substrate. The RHEED oscillations indicate 2-dimensional layer-by-layer growth of half unit cell monolayers for the total duration. Atomic force microscopy shows smooth terraces separated by half unit cell steps, similar to the original substrate surface, confirming the layer-by-layer growth, see Figure 4.4b. The high-quality crystalline surface produces clear 2-dimensional spots in the RHEED pattern, see Figure 4.4c and d. The occurrence of Kikuchi lines is an extra indication of a flat and crystalline surface and is visible for the initial TiO_2-terminated $SrTiO_3$ substrate surface.

The quality of the thin film crystal and the epitaxial relation to the substrate are investigated by x-ray diffraction. The θ-2θ and φ scans for the LSCO thin films

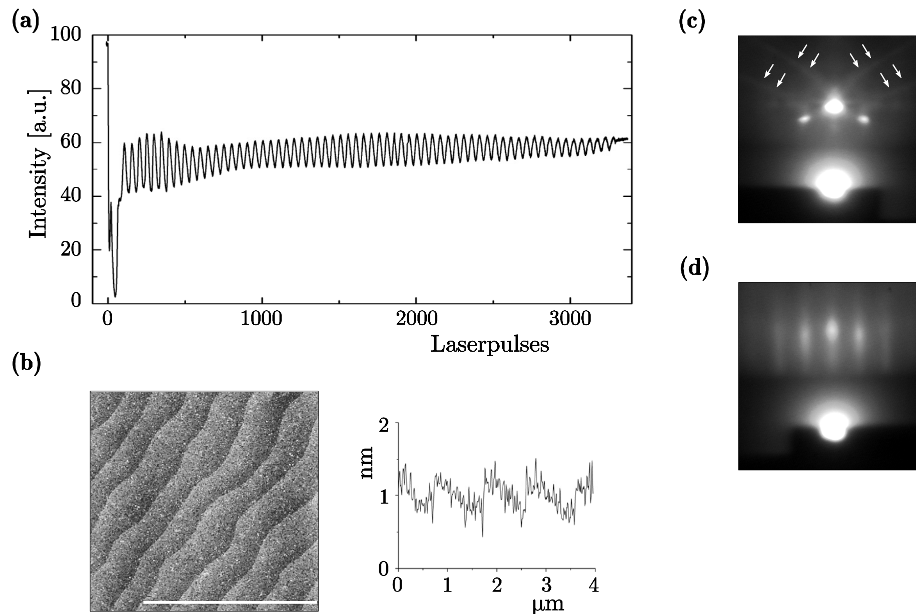

Figure 4.4 **(a)** Specular RHEED intensity oscillations during growth of 50 nm $La_{1.875}Sr_{0.125}CuO_4$ on TiO_2-terminated $SrTiO_3$. The intensity is manually increased after 50 laserpulses. **(b)** AFM micrograph and surface roughness analysis of the deposited layer. **(c,d)** RHEED patterns of respectively the initial TiO_2-terminated $SrTiO_3$ surface and the final $La_{1.875}Sr_{0.125}CuO_4$ surface. The arrows emphasize the positions of the Kikuchi lines.

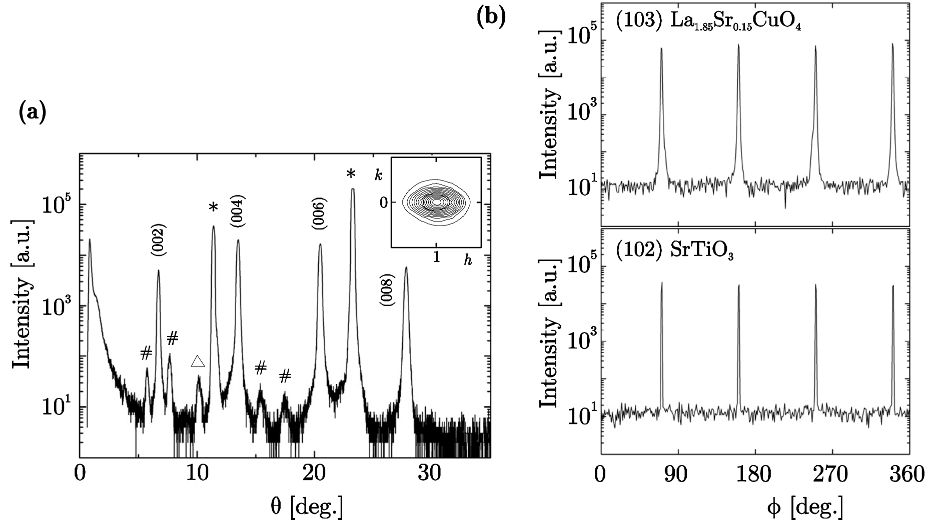

Figure 4.5 X-ray diffraction spectra for a 100 nm $La_{1.85}Sr_{0.15}CuO_4$ layer on a $SrTiO_3$ substrate: **(a)** θ-2θ scan, and **(b)** ϕ scans. The $SrTiO_3$ substrate reflections are indicated with an asterisk and their spectral contributions (λ/2 and λ/3) with a cross. The triangle (Δ) indicates the λ/2 spectral contribution of the (006) peak of the LSCO layer. The inset in (a) shows a reciprocal space map of the (103) LSCO reflection.

show excellent in-plane and out-of-plane alignments between the $SrTiO_3$ substrates and the thin films for all Sr-doping levels. A typical θ-2θ scan for a 100 nm $La_{1.85}Sr_{0.15}CuO_4$ thin film grown on a TiO_2-terminated $SrTiO_3$ (001) substrate is shown in Figure 4.5a. Only the (00*l*) peaks from the LSCO are present along with the peaks from the STO substrate, indicating c-axis growth. Figure 4.5b shows the φ scan of the (103) LSCO peak for the same sample. Sharp peaks appear at φ angles with 90° intervals, suggesting the layer to be single crystalline. Peaks appear at the same φ angles for the thin film and the substrate, indicating that the a-axes are well aligned. The width of the diffraction peaks in the omega-direction is a direct measure of the range of orientation on mosaic spread present in the irradiated area of the crystal. High resolution is necessary for an accurate analysis and is determined by the width of the x-ray beam. The rocking curves of the LSCO thin films give a full width at half maximum (FWHM) of 0.32°, a little bit wider than that of the STO substrate (0.20°). All thin films have c-axis lattice constants of about ~13.20 Å and are crystallized in a tetragonal structure with an a-axis of ~3.81 Å. The tetragonality is confirmed by reciprocal space mapping the single (103) peak of the $La_{1.85}Sr_{0.15}CuO_4$ layer in an *hk*-scan, see inset in Figure 4.5a, which would be split in a number of peaks for the orthorhombic case [27]. In contrast to bulk samples, thin films of $La_{2-x}Sr_xCuO_4$ remain tetragonal even in the undoped case, due to the present in-plane strain.

4.4 Carrier doping dependence of the superconducting properties

The excellent epitaxy between the LSCO thin films and the STO substrates for all Sr-doping levels enables study of the superconducting properties over the total carrier doping range. Beside strain, the Sr concentration and the oxygen stoichiometry are parameters, which influence the superconductivity. They control the doping level and therefore the superconducting properties. To systematically study the carrier doping dependence on the superconducting properties, both parameters were investigated independently.

$La_{2-x}Sr_xCuO_{4+\delta}$ films were grown on TiO_2-terminated $SrTiO_3$ substrates by pulsed laser deposition with an energy density of 1.2 J/cm^2 and a repetition rate of 4 Hz. The substrate was heated to 700 ºC and kept in an oxygen pressure of 0.13 mbar during the deposition. After the deposition, the films were annealed at 700 ºC for 15 min. in deposition pressure and subsequently cooled down to room temperature at 4 ºC/minute. Two cooling procedures, with different atmospheres, were investigated: first, 1 bar of pure O_2 and secondly, 0.23 mbar of a flowing O_2/O_3 mixture with 8wt.% ozone concentration at a flow rate of 100 sccm, which was directed over the film surface. During the first cooling procedure in a high O_2 pressure, the temperature was stabilized at 600 ºC and 450 ºC for respectively, 15 and 30 minutes to improve the oxygen indiffusion. The O_2/O_3 mixture in the second cooling procedure had a much stronger oxidation power and causes better oxygenation of the thin films, leading even to oxygen incorporating interstitially ($\delta>0$). The temperature dependence of the resistivity $\rho(T)$, without oxygen doping ($\delta=0$), is shown in Figure 4.6a for various strontium concentrations. A transition from an insulator (x=0.05) to a superconductor (x=0.125) is clearly visible. The maximum transition temperature of 26 K is measured for x=0.15 and reduces for a further increase in Sr-doping (x=0.25). The T_c at optimum doping is smaller than the bulk

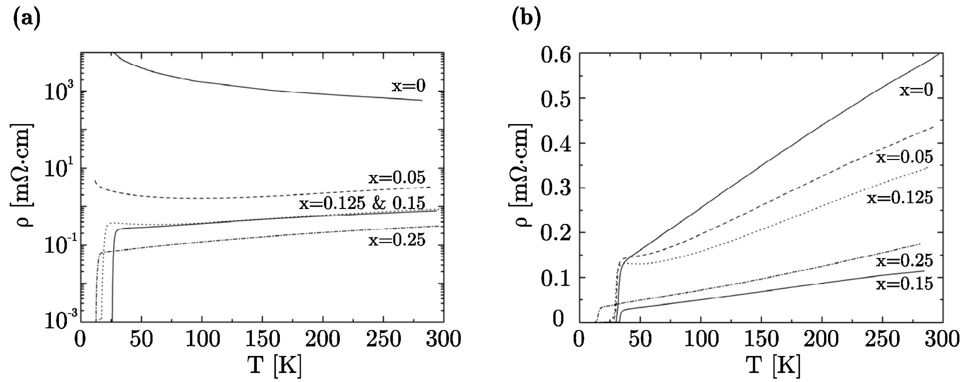

Figure 4.6 Temperature dependence of the resistivity $\rho(T)$ for $La_{2-x}Sr_xCuO_{4+\delta}$ with various Sr concentration. The films are cooled after deposition in different atmospheres: O_2 ($\delta=0$) **(a)** and O_2/O_3 mixture ($\delta>0$) **(b)**.

value of 38 K, due to tensile strain in the thin film. However, when an O_2/O_3 mixture is used during cooling, T_c is as high as the bulk value at optimum doping and superconductivity is present in the underdoped region even down to the undoped case, see Figure 4.6b. These observations are in good agreement with reported results for oxygen doping in $La_2CuO_{4+\delta}$ [28].

To summarize the behavior of T_c for the films cooled in different oxygen environments, the maximum obtained T_c values are plotted in Figure 4.7a. The results agree with data from ref. 28 and show a profound effect of oxygen stochiometry on the superconductivity in LSCO thin films. It is, however, similar to the results in bulk LSCO prepared by room temperature chemical oxidation, where excess oxygen is inserted to the interstitial sites [29]. The observed changes in superconducting properties suggest that the dependence of carrier doping on Sr concentration, which is clearly present in bulk and thin films, is dominated by the insertion of interstitial oxygen when cooled in an O_2/O_3 mixture.

The influence of carrier doping on the crystal structure was investigated by x-ray diffraction at room temperature. The lattice constants are plotted in Figure 4.7b against the Sr-concentration. Values for thin films without (δ=0) and with (δ>0) excess oxygen are given and clear differences are visible with values for bulk LSCO, indicated by the dashed lines. The doping induced orthorhombic to tetragonal transition, which is located in bulk LSCO at x=0.05, is not observed in these thin films. This is due to the large epitaxial strain still present in LSCO films with 100 nm thicknesses. The tensile strain, induced by the $SrTiO_3$ (3.905 Å) substrate,

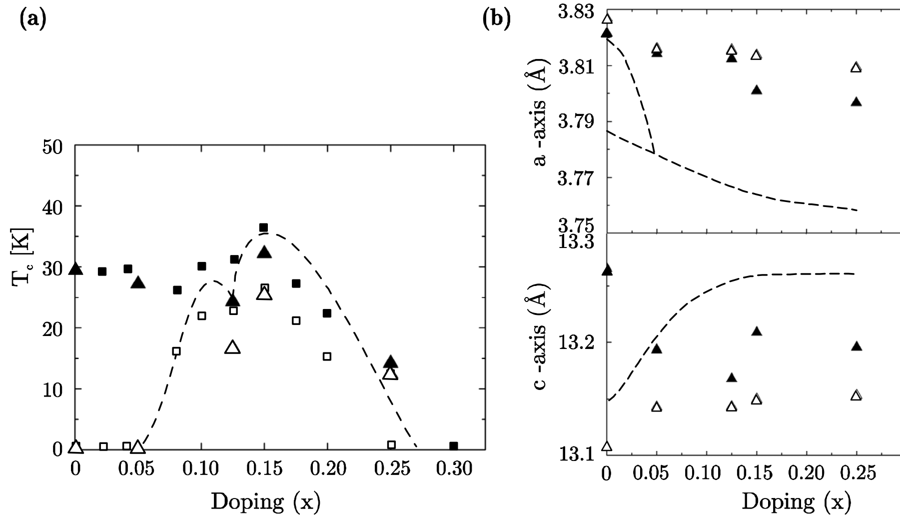

Figure 4.7 Composition dependences of T_c **(a)** and crystal structure **(b)** for 100 nm $La_{2-x}Sr_xCuO_{4+\delta}$ thin films on $SrTiO_3$ substrates. Open and closed triangles are respectively for films without (δ=0) and with (δ>0) excess oxygen. The open and closed squares are data from ref. 28. The dashed lines are the results of bulk LSCO [8].

elongates the in-plane axes above bulk values. A direct effect caused by this in-plane elongation is the shortening of the crystal in the c-axis direction when there is no excess of oxygen ($\delta=0$) in the crystal structure. The influence of the Sr-concentration on these changes in the a- and c-directions is only very small. In case of interstitial oxygen incorporation ($\delta>0$) in the thin films, the crystal structure will contain the same in-plane strain, but the c-axes will be longer due to filling of interstitial positions by oxygen. In the undoped $La_2CuO_{4+\delta}$ compound, excess of oxygen even enhanced the c-axis length over the bulk value. The thin film stoichiometry was confirmed by Rutherford back-scattering spectrometry (RBS) experiments[I] of LSCO thin films deposited on silicon.

4.5 Ultrathin superconducting films

One of the most interesting issues in the study of thin film growth of high temperature superconductors is the minimum number of CuO_2 planes required for superconductivity. This is significant not only for clarification of the mechanism of high-T_c superconductivity but also for applications such as the fabrication of superconducting field effect transistors [30,31]. Towards a solution to this problem, many studies on the growth of ultrathin films and superlattices have been conducted for $YBa_2Cu_3O_7$ and $Bi_2Sr_2CaCu_2O_8$. Although it has been suggested that superconductivity can occur in one-unit-cell-thick films [32,33], these films still contained two CuO_2 planes in their unit cells. Moreover, the superconducting layers were adjacent to a buffer and/or cap layer, which also contained CuO_2 planes and possibly influenced the interpretation of the results.

Growth of $La_{2-x}Sr_xCuO_4$ ultrathin films offers the possibility to stack single CuO_2 planes one by one with a spacing of 6.6 Å along the c-axis. Thin films of $La_{1.85}Sr_{0.15}CuO_4$ on (001) $SrLaAlO_4$ substrates, without any buffer or cap layers, have been reported to exhibit a decrease in T_c for thicknesses below four unit cells, where T_c even disappeared in films less then two unit cells thick [34]. When a metallic buffer layer of $La_{1.6}Sr_{0.4}CuO_4$ is used to decouple the film-substrate interface, the superconducting thickness was even reduced to a single unit cell [35]. However, the Sr interlayer diffusion from the buffer and cap layer (x=0.4) to the single unit cell layer (x=0.1) raise the doping level of the superconducting layer(s) and increase the effective thickness. To exclude the increase of the effective thickness and the Sr indiffusion, the buffer and cap layer should be insulating with x=0.05 or lower, although still extra CuO_2 planes will be present.

To investigate the effect of strain relaxation on the superconducting properties, thin films of $La_{1.875}Sr_{0.125}CuO_4$ were grown on (001) $SrTiO_3$ substrates with a buffer

[I] RBS measurements were performed at Philips company (Eindhoven, the Netherlands).

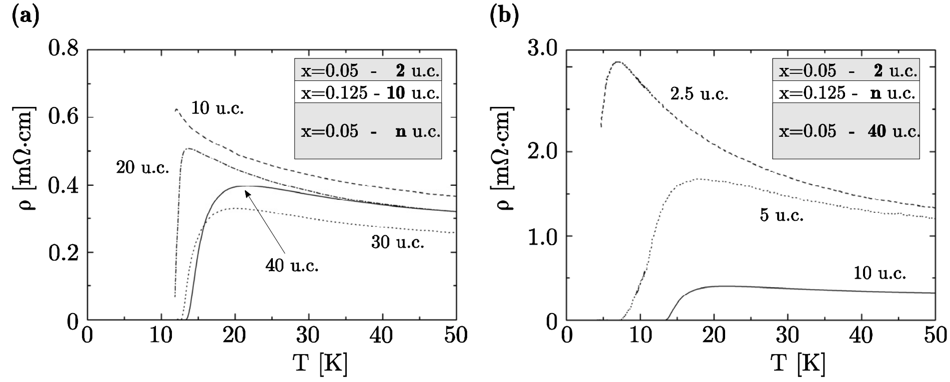

Figure 4.8 Temperature dependence of the resistivity ρ(*T*) for $La_{2-x}Sr_xCuO_4$ multilayers for various thicknesses *n* of the bufferlayer **(a)** and the superconducting layer **(b)**.

and cap layer of insulating $La_{1.95}Sr_{0.05}CuO_4$. The thickness of the insulating buffer layer was varied to determine the change in the properties of the superconducting layer by induced strain from the substrate-film interface. The layer thicknesses were controlled very accurately by monitoring the RHEED oscillations during growth. The coupling between the LSCO film and the STO substrate is very strong and therefore extensive tensile strain will be present over a large thickness, as described in section 4.4, leading to a reduced transition temperature. The results of the resistivity measurements are given in Figure 4.8a for different thicknesses of the insulating buffer layer (x=0.05). The thickness of the superconducting layer (x=0.125) is constant at 10 unit cells, while the cap layer (x=0.05) has a constant thickness of 2 unit cells. The resistances could be measured in a helium vessel down to 12 K, because of the inaccuracy of the Pt-100 thermocouple below this value. In the sample with a 10 unit cell bufferlayer a lot of strain is present and only a small onset is visible just above 12 K. When the thickness of the bufferlayer is increased some strain relaxation occurs, which is reflected by the increase of the onset temperature to 13.7, 20.0 and 21.6 K, for respectively 20, 30 and 40 unit cells. The T_c (R=0) for a 10 unit cell $La_{1.875}Sr_{0.125}CuO_4$ layer on a bufferlayer of 30 or 40 unit cells (12.8 and 13.4 K) is still lower than the value for a 100 nm thick film (16.8 K), which is shown in figure 4.6a. This is an indication of the large distances over which the strain relaxation takes place.

The thickness of the intermediate superconducting layer was varied to study the superconducting properties of ultrathin layers. The thickness of the insulating buffer and cap layers were kept constant at respectively, 40 and 2 unit cells. Figure 4.8b shows the results of the thin film multilayers with different thicknesses of the superconducting layer, which were measured in a flow cryostat with accurate temperature analysis down to 4.2 K. The reduction of the layer thickness induces an increase in the normal state resistance and a decrease in the transition temperature.

The onset temperature decreases from 21.6 K to 17.9 K and 7.0 K for 10, 5 and 2.5 unit cells. The $La_{1.875}Sr_{0.125}CuO_4$ layer with a thickness of 2.5 unit cells shows a clear onset, but does not become superconducting above 4.2 K. For a 5 unit cell $La_{1.875}Sr_{0.125}CuO_4$ layer the superconducting transition is clearly visible and T_c (R=0) is 7.5 K.

Superconducting LSCO (x=0.125) layers, sandwiched between insulating LSCO (x=0.05) layers, on $SrTiO_3$ substrates show reduced transition temperatures when compared to the case of metallic (x=0.4) buffer and cap layers [35]. This can be explained by the absence of Sr-diffusion and, therefore, the thinner effective thickness of the superconducting layer. Superconductivity is present in 5 unit cell thick layers, which is not possible when grown directly on a $SrTiO_3$ substrate [34, 36], because of the large tensile strain.

4.6 Vortex lattice imaging

When a magnetic field is applied to LSCO magnetic flux is able to penetrate the material due to the formation of vortices. At high temperatures the vortices are mobile while at low temperatures they form a lattice. The vortex freezing temperature is also the temperature below which phase coherent superconductivity, characterized by zero resistance, occurs. For the imaging of vortex structures in superconductors, a useful technique is scanning tunneling microscopy (STM) in combination with scanning tunneling spectroscopy (STS). One of the principal advantages in comparison with other imaging tools, such as magnetic force microscopy, magneto-optics, Bitter decoration, scanning SQUID microscopy and terahertz radiation imaging [37], is that STM measures the electronic density of states instead of the magnetic flux density, thus being sensitive on the scale of the superconducting coherence length ξ, rather than the magnetic penetration depth λ. For optimally doped single-crystal LSCO ξ and λ are respectively, 32 Å [38] and 2300 Å [39]. This sensitivity opens a much larger magnetic field region for investigations, in particular the field region where the vortex–vortex spacing is smaller than λ. However, due to the requirements of having a clean, almost atomically flat surface, vortices in high-T_c compounds have been observed by STM/STS mainly in single crystals of YBCO [40] and BSCCO [41].

Major obstacles in vortex imaging of thin films are surface roughness and oxidation, which make tunneling and scanning impossible. Therefore, only few STM/STS experiments were performed on the LSCO compound with true vacuum tunneling [42-44]. Only recently the topography of a cracked LSCO crystal was imaged with nearly atomic resolution [45,46]. However, the surface appeared to be not very stable in time and vortices couldn't be imaged. To overcome these problems a passivation technique can be used [47,48]. To achieve this, a 48 nm thick amorphous α-$Mo_{2.7}Ge$ layer can be rf-sputtered at room temperature in an Ar

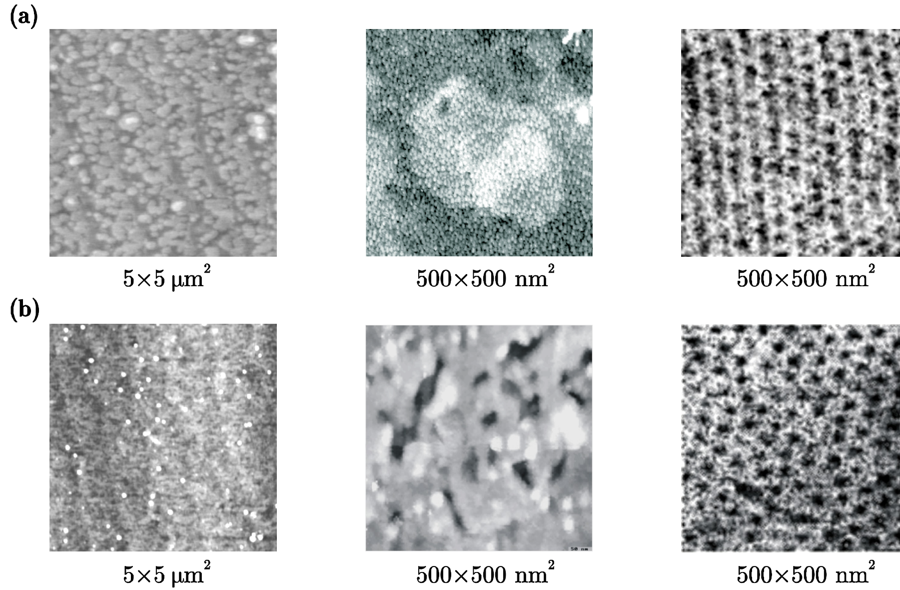

Figure 4.9 Overview of results from experiments performed on samples with LSCO layers, which were cooled down after deposition in oxygen **(a)** and ozone **(b)**. (left) Room temperature AFM images. (middle) Topography as measured by STM at 4.2 K. (right) Formation of vortices as measured by STS at 4.2 K and 0.6 T and 0.7 T for respectively oxygen and ozone.

atmosphere on the LSCO thin films to reduce the surface roughness. Next, an Au capping layer has to be deposited immediately by first sputtering 3 nm Au in an Ar (100%) atmosphere to obtain a closed layer, followed by another 3 nm Au in an Ar/O_2 (95%/5%) atmosphere to obtain a flat surface consisting of small grains. The superconducting α-$Mo_{2.7}Ge$ layer has a T_c of 6.5 K and an upper critical field of 6 T at 4.2 K. It shows moderate intrinsic pinning strength, basically due to the absence of grain boundaries. The capping of the superconducting layers with Au still allows gap spectroscopy due to the proximity effect. The important point is that the vortex positions as measured on the Au surface are still dictated by the pinning of the vortices in the LSCO layer, since the pinning by the α-$Mo_{2.7}Ge$ layer is much too weak to influence the vortex configuration.

Thin films of $La_{1.85}Sr_{0.15}CuO_4$ were deposited on TiO_2-terminated $SrTiO_3$ substrates by pulsed laser deposition and subsequently cooled down in either pure O_2 or an O_2/O_3 mixture, as described in section 4.4. The thin films had a thickness of 100 nm and a T_c of 23.5 K and 32.3 K when cooled down in respectively, oxygen or ozone. Atomic force microscopy (AFM) images show smooth surfaces with the imprint of the substrate terraces still visible, see Figure 4.9. For the thin films cooled in ozone, precipitates are formed on the surface with a height of ~4 nm. The rms-values are 0.27 nm and 0.54 nm for the LSCO layers with respectively oxygen and

ozone. The α-$Mo_{2.7}Ge$ and Au layers were deposited ex-situ on the LSCO layers for passivation[II].

The surface topography of the heterostructure was measured at 4.2 K by scanning tunneling microscopy (STM) and showed similar roughness levels as was observed on the surface of the initial LSCO layer by AFM. The small grains of the top Au layer can easily be distinguished in the STM-image of the heterostructure with the oxygenized LSCO layer, while the surface of the other sample with the ozonized LSCO layer still shows precipitates. The terraces, which are observed in the STM-investigations, have step heights with typical values of 0.6±0.1 nm, 1.1±0.1 nm and 1.6±0.2 nm. These values correspond to about half unit cell height differences (6.6 Å), which were observed before on LSCO layers, see section 4.3. The surfaces were also analyzed by scanning tunneling spectroscopy (STS) to measure locally the variation in tunneling current, which can be related to the electronic density of states. For all STS experiments the full I-V spectroscopy method was employed. Instead of acquiring single current values, a full I(V) curve was measured while ramping the bias voltage. The STM and STS measurement techniques and data analysis are described in detail in reference 48. The STS-images show an ordering of the vortices in case of an oxygenized LSCO layer, but much more disorder for the ozonized LSCO layer. This disorder is most likely caused by the presence of precipitates on the LSCO surface, which will disturb locally the superconducting properties. The ordering of the vortices in the oxygenized LSCO layer was observed up to the maximum applied magnetic field of 1.2 T.

The most striking feature occurring in the vortex state of the high-T_c materials is the vortex lattice transition as a function of applied magnetic field. A transition from a triangular lattice to a square lattice has been observed by small angle neutron scattering in $YBa_2Cu_3O_{7-\delta}$ [49] and $La_{1.83}Sr_{0.17}CuO_{4+\delta}$ [50] at a certain magnetic field, but was absent for $Nd_{1.85}Ce_{0.15}CuO_4$ [51]. For the LSCO compound, the transition sets in at ~0.05 T, where the lattice was found to deviate from the triangular lattice, and was almost completely changed into a square lattice at ~0.4 T. Investigations on the nature of the vortex lattice by STM/STS measurements could possibly provide extra information to explain the origin of this exotic behavior.

Proper analysis of the vortex lattices, as shown in Figure 4.9, was not possible, due to the low contrast of the data. To improve the quality of the vortex images, the heterostructures had to be optimized with a higher stability of the individual layers. To prevent oxygen diffusion from the LSCO layer to the α-$Mo_{2.7}Ge$ layer, a four-layer structure was fabricated with an in-situ deposited 3 nm thick Au layer on

---

[II] Sputter deposition of α-$Mo_{2.7}Ge$ and Au layers and vortex lattice analysis by STM/STS measurements were performed at the Kamerlingh Onnes Laboratory, Leiden University, the Netherlands.

the LSCO surface, see Figure 4.10a. From independent experiments it is expected that the intermediate thin Au layer will not influence the coupling of the vortex lattice in the LSCO layer to the α-$Mo_{2.7}Ge$ layer [48].

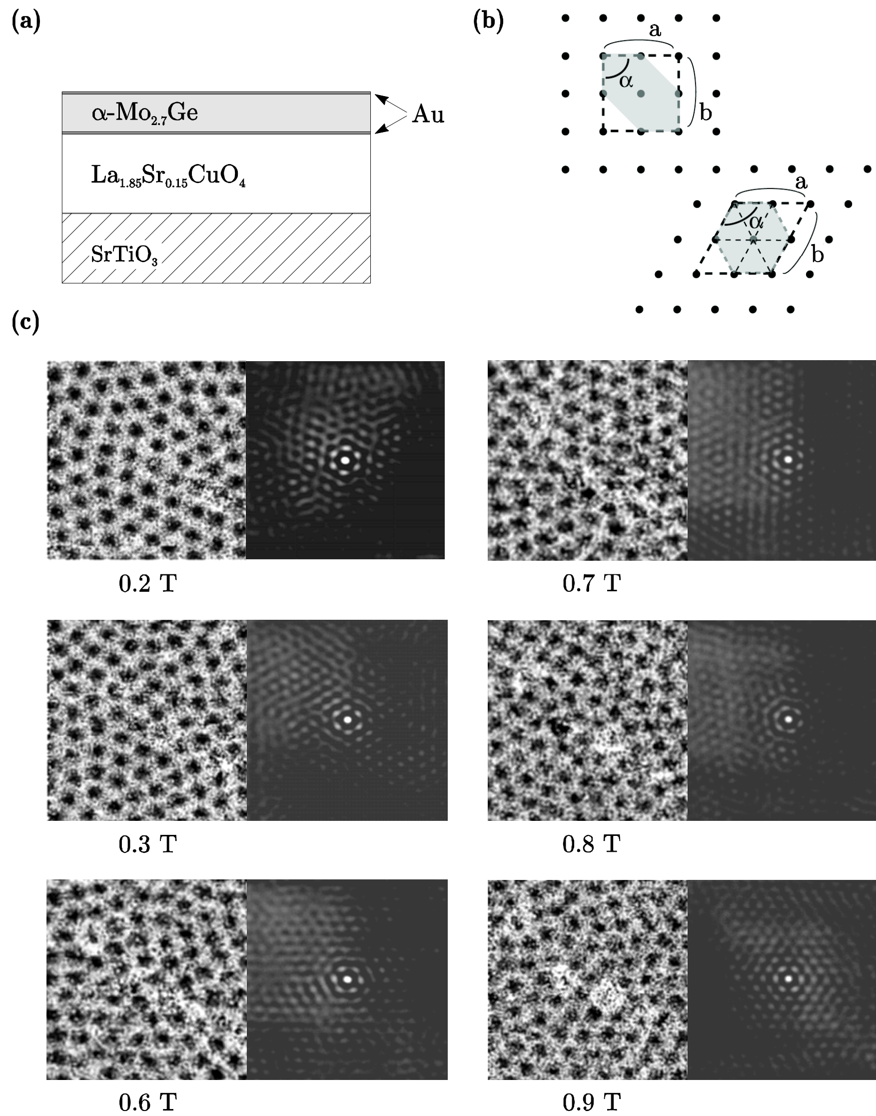

Figure 4.10 Vortex imaging results of the STM/STS experiments performed at different magnetic fields. **(a)** Schematic view of the characterized heterostructure. **(b)** Sketch of the vortex configurations for a square and triangular lattice. The parameters α, a and b are indicated. **(c)** Imaging results together with autocorrelation analysis for various magnetic fields. The scan range is constant at 360×360 nm^2. The fast scan direction is horizontal, while the slow scan direction is from top to bottom.

This four-layer structure yielded better results and clear vortex images were obtained up to a magnetic field of 1.0 T, see Figure 4.10c. The average diameter of the vortices is ~25 nm, while the average distance between the vortex centers is ~40 nm. All vortex images show a more or less regular pattern. This regularity comes out more clearly in the autocorrelation images, which accompany the real space images. The autocorrelation analysis shows regular hexagonal patterns, which originates from a triangular vortex lattice, see Figure 4.10b. For all values of the applied magnetic field angles α are 120° and almost no deformation of the triangular vortex lattice was observed. This indicates the absence of a transition in the lattice structure and shows clearly the stability of a triangular lattice up to a magnetic field of 1.0 T. The range of the lattice ordering is about $3a_0$, with a_0 the vortex lattice parameter.

A possible transition in the vortex lattice would be driven by interactions with the underlying electronic and crystal structures, against vortex-vortex interactions and pinning. Since disorder usually directly enhances pinning, knowledge about the pinning properties of the heterostructures will be very useful. This can be achieved by measuring the values of the critical currents in the heterostructures. A method to determine the critical currents is based on magnetic relaxation measurements. Quenched disorder in the sample will hamper homogeneous (re)distribution of the vortices over the sample when the applied magnetic field is changed. The decay of the magnetization in time was measured very sensitively by a SQUID (Scanning QUantum Interference Device) magnetometer and related to the critical current [48,52]. The measured value for the heterostructures was 1×10^6 A/cm^2 at 0.25 T and was similar for the case of an oxygenized or an ozonized LSCO layer. In order to relate the results to properties for single crystals, a comparison was made with a LSCO crystal of Gilardi *et al.* [51], which showed a critical current of 0.2×10^6 A/cm^2 at 0.25 T. Measurements of the temperature dependent magnetization yielded a T_c of 37.5 K for the single crystal. The values for the critical currents in the LSCO thin films are 5 times larger than in the single crystal. This indicates an enhanced pinning of the vortices in thin films, which can possibly prevent the transition of the vortex lattice structure. The origin of the pinning is still unclear, due to the fact that it seems to be independent of the surface morphology.

The possible influence of the difference in order-parameter between 'd-wave' LSCO and 's-wave' α-$Mo_{2.7}Ge$ requires further investigation. In this view a decrease in the interface roughness would result in a reduced coupling of the vortex formation in the LSCO layer to the measured α-$Mo_{2.7}Ge$ layer.

4.7 Towards electric field modulated carrier doping

The possibility of altering the carrier concentration and thereby changing the superconducting properties of a thin superconducting film, by applying a strong perpendicular electric field, was already discussed and shown in 1960 [53]. In thin Sn and In films the carrier density was changed by ~0.01%, which changed the critical temperature of the samples by ~10^{-4} K. The concept was explained by Landauer and Hall by a simple hydraulic system [54] in which the flow of an incompressible fluid through a pipe is controlled by the motion a fluid-activated piston. By applying pressure the piston will block the channel and hence reduce the flow. Because of the three terminals, source, drain and gate, such a device is also referred to as a three terminal device. Low-T_c field effect transistors have been fabricated in the following years, but due to the high carrier concentration and the large coherence lengths, the electric field effects remained marginal and far too small to be seriously considered for application in devices. However, high-T_c cuprates turned out to have a carrier concentration approximately two orders of magnitude lower than low-T_c metallic superconductors. Consequently, their discovery stimulated renewed efforts to obtain electric field effects on superconducting thin films [55].

4.7.1 Theoretical aspects of superconducting field effect devices

Although the concept behind field effect experiments is very elegant, putting it into practice can pose problems. A current flows from source to drain and by applying an electric field to the channel material charge carriers are attracted or repelled in a thin layer at the interface between the active superconducting layer and the gate insulator. Electrostatic screening counteracts the penetration of the electric field and thus limits the electric field effects. The Thomas-Fermi model describes this type of screening and the screening length is given by:

$$\lambda_{TF} = \sqrt{\frac{\varepsilon_0 \varepsilon_S}{e n_0}}, \tag{4.1}$$

where ε_S is the dielectric constant of the superconductor, ε_0 the permittivity of free space, e is the electron charge and n_0 is the density of charge carriers. For $La_{1.85}Sr_{0.15}CuO_4$, n_0 is ~1.6×10^{21} cm^{-3} and ε_S is about 30 [56], which gives a screening length of ~10.6 Å. Compared to the unit cell of $La_{2-x}Sr_xCuO_4$, with a c-axis length of ~13.2 Å, the field thus only penetrates less than a unit cell. Although the field is screened within an extremely small distance from the interface, the superconducting state is affected by the electric field at larger distances (of the order of the coherence length ξ) because of the proximity effect. For all the superconducting properties in the field-penetrated layer to be dependent on the applied electric field, $\lambda_{TF}(T)$ has to be at least comparable to the coherence length $\xi(T)$ or larger. The $La_{1.85}Sr_{0.15}CuO_4$

compound exhibits coherence lengths of 32 Å in the a/b-direction and 2.2 Å in the c-direction [38] and satisfies therefore the condition $\lambda_{TF}(T) \geq \xi(T)$.

It can be assumed that the total charge induced by the electric field participates in the conductivity and that the surface and bulk carrier mobilities are equal. Then, the field-induced change of the charge carrier concentration over an active layer thickness d is given by [57]:

$$\Delta n = \frac{1}{d}\int_0^d \frac{\varepsilon_0 \varepsilon_I E}{e\lambda_{TF}} e^{-z/\lambda_{TF}} dz = \frac{\varepsilon_0 \varepsilon_I E}{ed}(1 - e^{-d/\lambda_{TF}}), \quad (4.2)$$

where ε_I is the dielectric constant of the gate insulator and E is the applied electric field. The dielectric constant of the insulator has been assumed to be independent of the electric field. When $d >> \lambda_{TF}$, which is almost always the case, the term between brackets goes to 1 and the equation simplifies to:

$$\Delta n = \frac{\varepsilon_0 \varepsilon_I E}{ed} \quad (4.3)$$

This equation gives the number of charge carriers added to a volume of the active layer material and it becomes clear that a thin superconducting layer, a large electric field and a high dielectric constant of the gate insulator provide the largest increase in carrier concentration.

Superconducting parameters that are expected to change under influence of an electric field are the normal state resistivity (R), the critical temperature (T_c) and the critical current density (J_c). A linear relation between the change in the normal state resistivity, critical temperature and the variation of the carrier density has been observed over a wide doping range [58]:

$$\frac{\Delta N}{N} = -\frac{\Delta R}{R} = \frac{\Delta T_c}{T_c} \quad (4.4)$$

where $N=nd$ with n the number of charge carriers per unit volume. When $\Delta N/N$ becomes large and approaches the depletion of the layer, the change in normal state resistivity no longer follows this rule. In the case of critical temperature this relationship seems valid even up to higher values of ΔN. It has been shown experimentally [59] and theoretically [60] that the relative change in critical current is larger than the relative change in charge carriers.

4.7.2 High quality Al_2O_3 gate dielectric by interval annealing

The number of charge carriers that can be added to, or removed from the superconducting layer depends on the quality of the gate dielectric. The most used parameter to indicate the strength of the effective electric field is the polarization, or areal charge density, and is defined as:

$$\sigma = \int_0^{V_G} \frac{\varepsilon_0 \varepsilon_I(V)}{t} dV, \tag{4.5}$$

where the gate voltage V_G has to be below the breakdown voltage and t is the thickness of the insulating dielectric layer. Apart from the high polarization demand on the gate insulator, the leakage current has to be small compared to the source-drain current and the number of localized states near the interface has to be small compared to the modulated carrier density. Although the gate insulator most used in standard field effect transistors (FET), SiO_2, has excellent leakage current characteristics and a very low number of localized states, it cannot provide the polarizations that are required for superconducting FETs. With a breakdown field of 10 MV/cm and a dielectric constant of 3.9 the maximum polarization is 3.5 μC/cm^2, while for a 10% change in carrier concentration in 2 unit cells of $La_{1.85}Sr_{0.15}CuO_4$ a polarization of 6.6 μC/cm^2 is required.

To reach high polarizations a different gate dielectric is necessary and many groups have therefore performed investigations on devices with various gate dielectrics. For bulk $SrTiO_3$ and $Ba_xSr_{1-x}TiO_3$ dielectric constants up to 2.4×10^4 have been reported [61,62]. However, the dielectric properties are significantly reduced in thin films [63] and a further decrease is even observed as a function of the applied field down to a value of a few hundred at breakdown [64]. Another disadvantage is the low bandgap, which is present for all materials with a high dielectric constant.

A promising dielectric material to replace SiO_2 is Al_2O_3 [65,66]. This material has a high bandgap (8.8 eV), similar to SiO_2, but in combination with a medium dielectric constant of about ~9. Thin films of Al_2O_3 were grown by various deposition techniques on silicon for standard MOSFET technology [67-70], but an ultrahigh vacuum fabrication process was necessary to prevent the formation of a SiO_2 interfacial layer [71,72]. This problem is absent in multilayers with perovskite oxides and therefore the layers can be grown in an oxygen environment.

Thin films of Al_2O_3 were grown by pulsed laser deposition on TiO_2-terminated conducting Nb-doped (1 w.t.%) $SrTiO_3$ substrates at different deposition conditions. By photolithography and Au sputtering, a metal Au gate was created ex-situ on the Al_2O_3 surface, which made characterization of the dielectric properties possible in a probe station. The Au gate electrode had an area of ~1.8×10^{-4} cm^2 and a thickness of 200 nm. Atomically flat amorphous thin Al_2O_3 films with low leakage currents could be fabricated, when grown at 300 ºC in an oxygen environment at 5.8×10^{-2} mbar with a laser repetition rate of 5 Hz and an energy density of 3.0 J/cm^2. A slow cooling procedure at 5 deg./min. in 1 bar of oxygen reduced the number of oxygen vacancies and improved the dielectric properties.

The dielectric properties could even be enhanced further by an interval annealing process. In this process the Al_2O_3 layer was deposited in multiple steps with each time an annealing period in between. In oxidation experiments of Al it has

already been observed that only a limited thickness of Al_2O_3 can be fully oxidized [73]. The deposition was therefore divided in several deposition sequences with intermediate interval annealing cycles for 15 min in an O_2/O_3-mixture with 1% ozone at 0.25 mbar. Atomic force microscopy measurements showed atomically flat surfaces, while the layer thickness could be accurately determined by x-ray diffraction from the fringes in small angle θ-2θ scans.

The electric field dependence of the leakage current density is shown in Figure 4.11 for a 9 nm thick Al_2O_3 film, which was fabricated with various number of interval annealing steps. A reduction in the leakage current can be observed, while increasing the number of annealing periods from 1 to 3 and 6. This is probably caused by better oxidation of the total film and as a result a reduction in the number of oxygen vacancies. However, in case of 12 annealing periods the leakage current is increased, which is probably caused by the fact that the deposited material during each sequence doesn't form a fully closed layer and consequently induces extra defects in the final layer. The breakdown fields, which were observed for a thin Al_2O_3 layer with six interval annealing steps, are relatively high compared to results of other groups [71] and seem to be enough to induce a considerable electric field effect in an adjacent superconducting LSCO layer [74-78]. Measured breakdown fields of +7 MV/cm and −12 MV/cm will induce charge densities at the interface with a superconducting layer of +5.6 μC/cm^2 and −9.6 μC/cm^2.

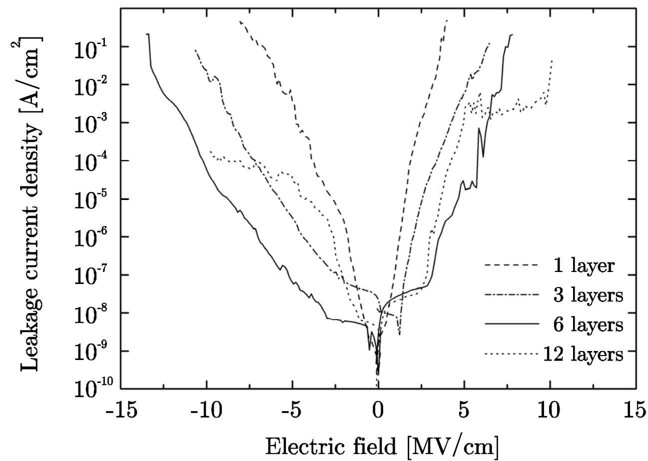

Figure 4.11 Leakage current density as a function of applied electric field for 9 nm thick Al_2O_3 films, which are deposited with various number of intermediate layers accompanied by interval annealing periods.

4.7.3 Field effect device fabrication

Pulsed laser deposition was used to grow a heterostructure of LSCO, Al_2O_3 and Au, which would serve as a template for the fabrication of a field effect device. From the fact that the layers were deposited in-situ, interfaces were expected with the highest possible quality and the lowest amount of impurities. The heterostructure was grown on an insulating TiO_2-terminated $SrTiO_3$ substrate. The LSCO layer had a thickness of 66 nm and consisted of an insulating bufferlayer of $La_{1.95}Sr_{0.05}CuO_4$ (40 unit cells) and a superconducting layer of $La_{1.875}Sr_{0.125}CuO_4$ (10 unit cells), as described in section 4.5. This was followed by a 9 nm thick Al_2O_3 layer, which was deposited in six intermediate steps with interval annealing, as described in section 4.6. Finally, a 20 nm thick Au gate electrode layer was grown in-situ by continuous deposition at 100 ºC in an argon environment at 0.22 mbar with a laser repetition rate of 4 Hz and an energy density of 4.0 J/cm^2. This heterostructure was structured into a field effect device by several etching, sputtering and lift-off steps, see Figure 4.12. These steps in the structuring process will be described briefly.

All the structuring was done with the aid of photolithography in which Shipley 1813 photoresist was used to create structures of photoresist with a uniform thickness of 1.2 μm. The first step in the structuring process was etching of the main structure in the total heterostructure for four-point measurements, see Figure 4.12a. This was done by reactive argon ion etching under an angle of 45º while rotating the sample. This produced shallow slopes and a better separation between the Au gate electrode and the LSCO superconducting layer. The etching speed was 7.5, 2.0, 2.1 and 2.2 nm/pulse for respectively Au, Al_2O_3, LSCO and STO.

The second structuring step was the sputter deposition of the gate contact paths, which were made from 5 nm Ti and 150 nm Au. This thin Ti layer was necessary to improve the connection between the Au and the oxide material. To prevent direct contact between this Au layer and the LSCO superconducting layer a 150 nm thick insulating SiO_2 layer had to be deposited in between. Holes were created in the SiO_2 layer by lift-off to make contact possible between the Au paths and the top Au layer of the heterostructure, see Figure 4.12b. In this way connections can be made to the gate electrode at the exterior of the sample without damaging the sensitive field effect heterostructure, see Figure 4.12c.

The next step involved the deposition of Au contacts to make low ohmic connections to the superconducting LSCO layer. To do this the Au and Al_2O_3 layers in the heterostructure were locally etched away by reactive argon ion etching till halfway into the superconducting LSCO layer. Then Au was sputter deposited as described in the previous step. To finish the field effect device the thin Au layer, which was still present at the top of the heterostructure in the long four-point-measurement leads, was etched away with a few etch pulses. In this step the whole sample was etched, but only the Au layer was removed because of the higher etching

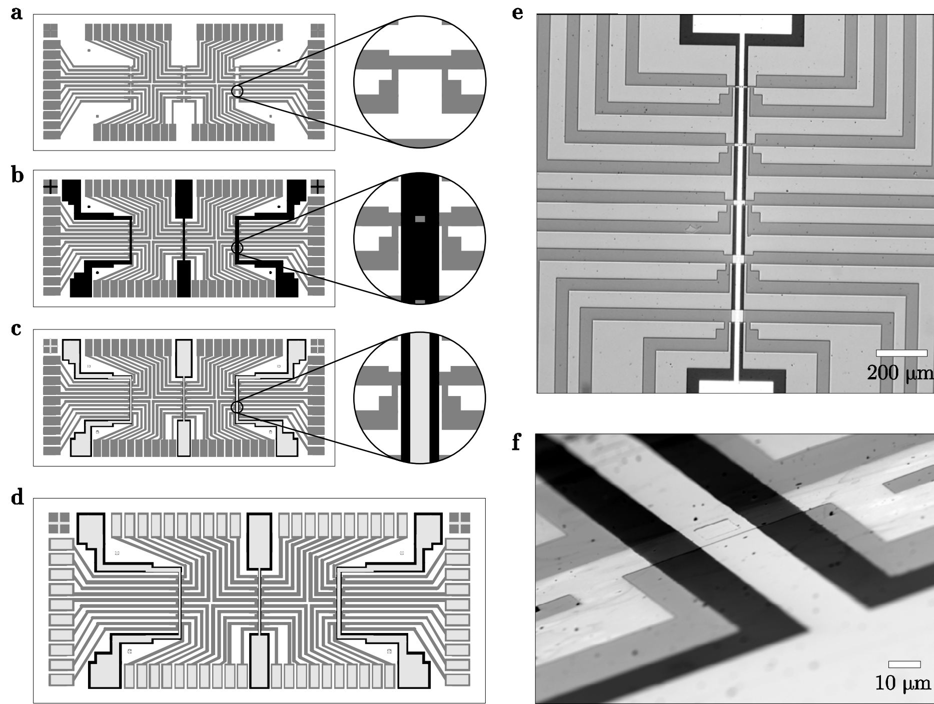

Figure 4.12 Structuring process to fabricate a field effect device. **(a)** Etching of the main structure in the LSCO/Al_2O_3/Au heterostructure for four-point measurements. **(b)** Sputter deposition of the insulating SiO_2 layer. **(c)** Sputter deposition of the Au contact paths. **(d)** Ion etching into the LSCO layer, followed by sputter deposition of Au contacts. To finish, the total sample was ion etched to remove the top Au layer of the heterostructure. **(e)** Photograph of the structured field effect devices with a constant length of 50 μm and various widths from top to bottom of 5, 10, 20, 35 and 50 μm. **(f)** Scanning electron micrograph of a field effect device with an area of 50×50 μm^2.

speed and the low thickness (~20 nm) compared to the other layers (~150 nm or more), see Figure 4.12d.

The final sample consisted of 15 individual field effect devices with various geometries, which were placed in three columns with gate lengths of 20, 50 and 100 μm (from left to right in Figure 4.12d). The widths of the gates were 5, 10, 20, 35 and 50 μm, respectively from top to bottom. A column of field effect devices with a gate length of 50 μm can be seen in a photograph in Figure 4.12e. A 50×50 μm^2 field effect device is shown in more detail in a scanning electron microscopy image in Figure 4.12f.

During analysis of the field effect devices several problems were encountered, which had to be solved to make proper measurement of the field effects possible. The fabrication and structuring process was therefore improved a number of times by some changes, which will be briefly described. In the first place the quality of the

superconducting LSCO layer was easily reduced, due to a loss of oxygen. The sensitivity of the transition temperature T_c on oxygen was already shown in section 4.4. In a LSCO/Al_2O_3/Au multilayer the T_c of LSCO was reduced, because of oxygen gettering by Al_2O_3 from this layer. This was tested by introducing an intermediate $SrTiO_3$ layer with a thickness of 2 nm, which prevented the oxygen diffusion but can never be applied in such field effect devices because of the large band-offset differences. Secondly, the Shipley 1813 photoresist, which was used during all photolithography steps, turned out to be reacting with the LSCO layer, which decreased the transition temperature. This was solved by replacement by the Olin 907-12 photoresist in combination with the ODP-4262 developer. And thirdly, the SiO_2 barrier layer drew oxygen from the LSCO layer over a period of weeks and deteriorated the superconducting layer. Replacement by a pulsed laser deposited 150 nm thick Al_2O_3 layer took away this problem. The first 18 nm were deposited with the same procedure as the thin Al_2O_3 gate oxide layer, followed by a continuous deposition at 1 Hz to optimize the oxidation of the layer.

Still, the field effect devices appeared to contain high contact resistances and high leakage currents. To lower the contact resistance between the Au paths and the underlying superconducting LSCO layer, the contact area was increased, see Figure

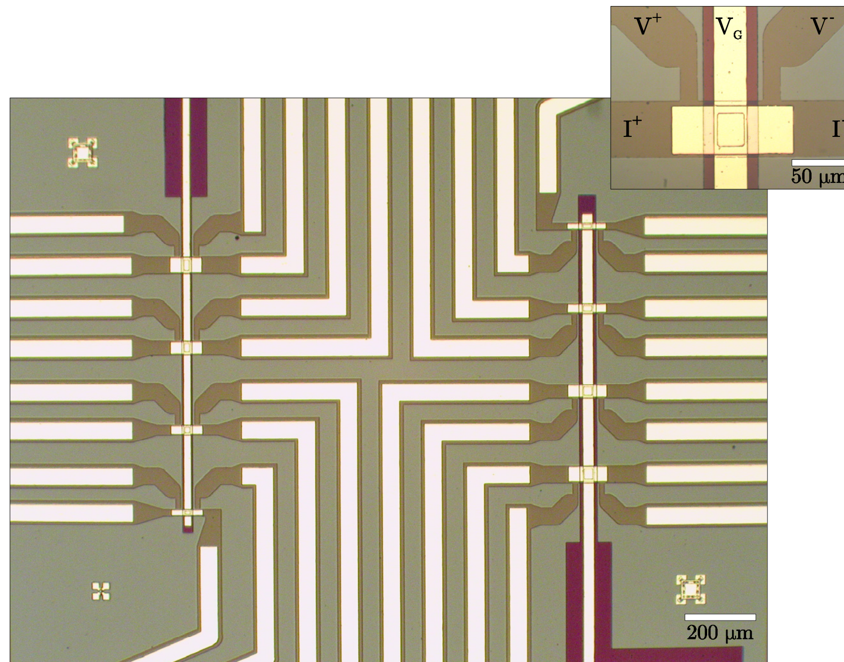

Figure 4.13 Photograph of the final field effect devices placed in two columns with gate lengths of 90 and 110 μm for respectively left and right. The gate widths are 16, 24, 34 and 44 μm, which are placed in different order in both columns. The inset shows a 44×110 μm^2 field effect device in more detail with the arrangement of the measurement contacts.

4.13. To reduce the leakage current between the Au gate electrode and the superconducting LSCO layer, the width of the Au gate area was decreased, which increased the lateral distance between the Au gate layer and the LSCO layer, see Figure 4.13. A separation of 5 μm between the Au gate area and the slope in the heterostructure increased the possible path of the leakage current considerably. Also the lengths of all Au gate areas were increased to cover the heterostructure over the total distance between the voltage contacts of the four-point measurements, see Figure 4.13. These improvements would facilitate measurement of the electric field effects.

First investigations on the optimized field effects devices showed superconductivity in the $La_{1.875}Sr_{0.125}CuO_4$ layer with a transition temperature T_c(R=0) of 9.0 K, see inset Figure 4.14. This value is reduced when compared to the Tc's of ultrathin LSCO films, consisting of 40 unit cells of insulating $La_{1.95}Sr_{0.05}CuO_4$ and 10 unit cells of superconducting $La_{1.875}Sr_{0.125}CuO_4$ together with a 2 unit cell thick cap layer of insulating $La_{1.95}Sr_{0.05}CuO_4$, which is 13.4 K, see section 4.5. Probably, the thickness of the superconducting layer was decreased due to oxygen out-diffusion. This thickness dependence of the transition temperature was shown in Figure 4.8b and exhibited a decrease in T_c from 13.4 K to 7.5 K for a reduction in thickness from 10 to 5 unit cells. The measured T_c of 9.0 K in the field effect device suggests therefore a thickness of the superconducting layer of only 7 unit cells.

The critical current density was determined at different temperatures below the transition temperature, see Figure 4.14. Measured values for the critical current density at 6.4 K, 3.5 K and 2.8 K were 0.05, 0.38 and 0.43×10^6 A/cm^2 with a 2 μV

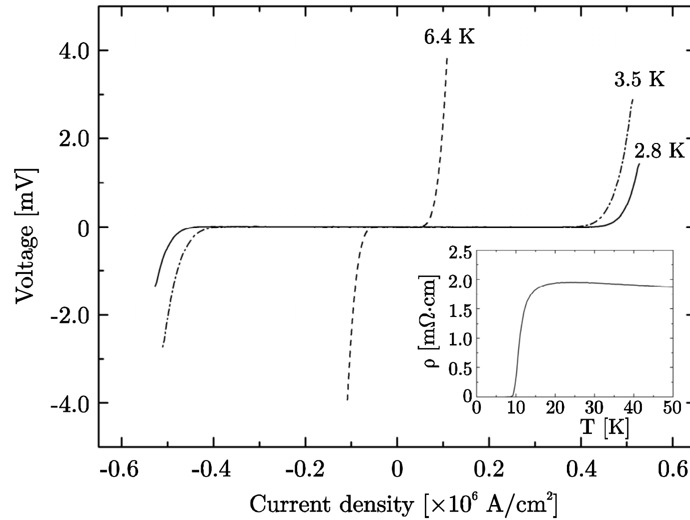

Figure 4.14 IV-characteristics of the superconducting $La_{1.875}Sr_{0.125}CuO_4$ layer in a field effect device at different temperatures with a gate voltage of 0 V. The inset shows the temperature dependence of the resistivity at 0 V gate voltage.

criterion. These values are in the same order of magnitude as the critical current density in thick LSCO/α-$Mo_{2.7}Ge$/Au multilayers, which were measured by a SQUID magnetometer in 0.25 T, see section 4.6.

Nevertheless, modulations in the critical current density couldn't be induced by variations in the applied electric field. No changes were measured, which were larger than the thermal noise caused by temperature fluctuations. The determined decrease in layer thickness of the superconducting LSCO can provide a possible explanation for this problem. If a part of the superconducting LSCO layer is transformed into an insulating or semiconducting layer, by oxygen out-diffusion, it's very likely that this new insulating layer will be situated at the interface with the Al_2O_3 layer. The charge carriers, which are added or removed by the electric field, will therefore not be present at the predicted interface between the superconducting LSCO layer and the dielectric Al_2O_3 layer, but between an insulating LSCO layer and the dielectric. If that's the case, no variations will ever be measured in the critical current density of the superconducting layer by applied electric fields. An accurate control on the oxygen distribution in the LSCO layer is therefore essential to perform electric field investigations with large effects. However, the aim of the utilization of the LSCO compound was to improve the fabrication process of electric field effect structures, while other materials are better candidates to actually observe electric field effects, see Chapter 2.

4.8 Conclusions

The $La_{2-x}Sr_xCuO_{4+\delta}$ compound is an ideal material to study the influence of small variations in the stoichiometry on the electronic properties, because small alterations of the strontium and oxygen doping result in dramatic changes in the conductivity behavior. In the described growth experiments several strontium doping levels were used (x=0, 0.05, 0.125, 0.15 and 0.25), while additionally the background gas was chosen to either oxygen ($\delta=0$) or ozone ($\delta>0$). These growth parameters provide the possibility to tune the electronic properties from insulating until superconducting, while maintaining the same tetragonal perovskite crystal structure.

The initial growth of $La_{2-x}Sr_xCuO_{4+\delta}$ thin films was found to be dependent on the termination of the $SrTiO_3$ substrate surface. In heteroepitaxy of perovskite structures the AO-BO_2 stacking sequence is maintained. However, in a $La_{2-x}Sr_xCuO_4$ crystal two AO layers are stacked on top of each other with an in-plane shift and form the rock-salt structure. This could theoretically lead to four possible stacking sequences at the interface with $SrTiO_3$. Experiments indicate that during the initial growth on the substrate surface the first atomic layers will form a rock-salt structure. In case of growth on a TiO_2-terminated surface, the film will start with two (La,Sr)O layers while for a SrO-terminated surface a single (La,Sr)O layer will be formed first. However, a thin film on a SrO-terminated surface exhibited a higher

surface roughness, due to the formation of very small precipitates on the thin film surface.

The small misfit (2-4%) between the $La_{2-x}Sr_xCuO_{4+\delta}$ thin films and the $SrTiO_3$ substrate leads to a layer-by-layer growth mode of half unit cell monolayers up to large thicknesses (~100 nm). The surface roughness remains comparable to the initial substrate surface with smooth terraces separated by half unit cell steps.

The maximum superconducting transition temperature for optimum strontium doping, without extra oxygen doping, was found to be 26 K. This is lower than the bulk value of 38 K, due to the large tensile strain present in the thin films. However, when additional oxygen doping is used, the superconducting transition temperature is as high as the bulk value at optimum strontium doping and superconductivity is present in the underdoped region even down to the undoped case.

The ability to maintain the same crystal structure in the investigated doping region provided the possibility to fabricate multilayer structures of thin layers with variable doping levels. In this way a suppression of the superconducting transition temperature, due to the large epitaxial strain between the $La_{2-x}Sr_xCuO_{4+\delta}$ thin films and the $SrTiO_3$ substrate, was found to exist over thicknesses up to 30 unit cells. On the other hand, the multilayer structures were used to investigate ultrathin superconducting films, where a superconducting transition temperature of 7.5 K was observed for only 5 unit cells.

The formation of the vortex lattice was investigated in $La_{2-x}Sr_xCuO_{4+\delta}/\alpha\text{-}Mo_{2.7}Ge/Au$ heterostructures and was found to be triangular without any induced transition by an applied magnetic field.

Various difficulties, connected with the sensitivity of $La_{2-x}Sr_xCuO_{4+\delta}$ to oxidation, complicated measurements of electric field effects. However, this sensitivity of the electronic properties on the carrier doping was used very successfully in the improvement of the fabrication process of electric field effect structures.

4.9 References

1. Bednorz, J.G. & Müller, K.A., *Z. Phys. B* **64**, 189 (1986).
2. Chu, C.W., Hor., P.H., Meng, R.L., Gao, L., Huang, Z.J. & Wang, Y.Q., *Phys. Rev. Lett.* **58**, 405 (1987).
3. Chu, C.W., Hor., P.H., Meng, R.L., Gao, L., Huang, Z.J. & Wang, Y.Q., *Science* **235**, *567* (1987).
4. Takagi, H., Uchida, S., Kitazawa, K. & Tanaka, S., *Jpn. J. Appl. Phys.* **26**, L123 (1987).
5. Cava, R.J., Van Dover, R.B., Batlogg, B. & Rietman, E.A., *Phys. Rev. Lett.* **58**, 408 (1987).
6. Tarascon, J.M., Greene, L.H., McKinnon, W.R., Hull, G.W. & Geballe, T.H., *Science* **235**, 1373 (1987).
7. Torrance, J.B., Tokura, Y., Nazzal, A.I., Bezinge, A., Huang, T.C. & Parkin, S.S.P., *Phys. Rev. Lett.* **61**, 1127 (1988).
8. Takagi, H., Ido, T., Ishibashi, S., Uota, M., Uchida, S. & Tokura, Y., *Phys. Rev. B* **40**, 2254 (1989).
9. Dagotto, E., *Rev. Mod. Phys.* **66**, 763 (1994).
10. Radaelli, P.G., Hinks, D.G., Mitchell, A.W., Hunter, B.A., Wagner, J.L., Dabrowski, B., Vandervoort, K.G., Viswanathan, H.K. & Jorgensen, J.D., *Phys. Rev. B* **49**, 4163 (1994).
11. Hwang, H.Y., Batlogg, B., Takagi, H., Kao, H.L., Kwo, J., Cava, R.J., Krajewski, J.J. & Peck Jr., W.F., *Phys. Rev. Lett.* **72**, 2636 (1994).
12. Yamada, K., Lee, C.H., Kurashashi, K., Wada, J., Wakimoto, S., Ueki, S., Kimura, H., Endoh, Y., Hosoya, S., Shirane, G., Birgeneau, R.J., Greven, M., Kastner, M.A. & Kim, Y.J., *Phys. Rev. B* **57**, 6165 (1998).
13. Oda, M., Momono, N. & Ido, M., *J. Phys. Chem. Solids* **65**, 1381 (2004).
14. Tranquada, J.M., Sternlieb, B.J., Axe, J.D., Nakamura, Y. & Uchida, S., *Nature* **375**, 561 (1995).
15. Suzuki, M., *Phys. Rev. B* **39**, 2312 (1989).
16. Kao, H.L., Kwo, J., Fleming, R.M., Hong, M. & Mannaerts, J.P., *Appl. Phys. Lett.* **59**, 2748 (1991).
17. Trofimov, I.E., Johnson, L.A., Ramanujachary, K.V., Guha, S., Harrison, M.G., Greenblatt, M., Cieplak, M.Z. & Lindenfeld, P., *Appl. Phys. Lett.* **65**, 2481 (1994).
18. Cieplak, M.Z., Berkowski, M., Guha, S., Cheng, E., Vagelos, A.S., Rabonowitz, D.J., Wu, B., Trofimov, I.E. & Lindenfeld, P., *Appl. Phys. Lett.* **65**, 3383 (1994).
19. Sato, H. & Naito, M., *Physica C* **274**, 221 (1997).
20. Locquet, J.-P., Perret, J., Fompeyrine, J., Mächler, E., Seo, J.W. & Van Tendeloo, G., *Nature* **394**, 453 (1998).
21. Si, W., Li, H.-C. & Xi, X.X., *Appl. Phys. Lett.* **74**, 2839 (1999).
22. Bozovic, I., Logvenov, G., Belca, I., Narimbetov, B. & Sveklo, I., *Phys. Rev. Lett.* **89**, 107001 (2002).

23. Koster, G., Kropman, B.L., Rijnders, G.J.H.M., Blank, D.H.A. & Rogalla, H., *Appl. Phys. Lett.* **73**, 2920 (1998).
24. Koster, G., Rijnders, G.J.H.M., Blank, D.H.A. & Rogalla, H., *Appl. Phys. Lett.* **74**, 3729 (1999).
25. Chern, M.Y., Gupta, A. & Hussey, B.W., *Appl. Phys. Lett.* **60**, 3045 (1992).
26. Terashima, T., Bando, Y., Iijima, K., Yamamoto, K., Hirata, K., Hayashi, K., Kamigaki, K. & Terauchi, H., *Phys. Rev. Lett.* **65**, 2684 (1990).
27. Dekkers, J.M., Rijnders, G., Harkema, S., Smilde, H.J.H., Hilgenkamp, H., Rogalla, H. & Blank, D.H.A., *Appl. Phys. Lett.* **83**, 5199 (2003).
28. Zeng, X.H., Si, W., Stum, Z.M. & Xi, X.X., *IEEE T. Appl. Supercon.* **11**, 3213 (2001).
29. Rial, C., Moran, E., Alario-Franco, M.A., Amador, U. & Andersen, N.H., *Physica C* **254**, 233 (1995).
30. Xi, X.X., Li, Q., Doughty, C., Kwon, C., Bhattacharya, S., Findikoglu, A.T. & Venkatesan, T., *Appl. Phys. Lett.* **59**, 3470 (1991).
31. Mannhart, J., Bednorz, J.G., Muller, K.A. & Schlom, D.G., *Z. Phys. B* **83**, 307 (1991).
32. Triscone, J.-M., Fischer, Ø., Brunner, O., Antognazza, L., Kent, A.D. & Karkut, M.G., *Phys. Rev. Lett.* **64**, 804 (1990).
33. Bozovic, I., Eckstein, J.N., Klausmeier-Brown, M.E. & Virshup, G., *J. Supercond.* **5**, 19 (1992).
34. Sato, H., Yamamoto, H. & Naito, M., *Physica C* **274**, 227 (1997).
35. Rüfenacht, A., Chappatte, P., Gariglio, S., Leemann, Fompeyrine, J., Locquet, J.-P. & Martinoli, P., *Solid-State Electron.* **47**, 2167 (2003).
36. Jaccard, Y., Cretton, A., Williams, E.J., Locquet, J.-P., Mächler, E., Gerber, C., Schneider, T., Fischer, Ø & Martinoli, P., *Proc. SPIE* **2158**, 200 (1994).
37. Ohshima, S., Tanabe, K., Morishita, T. & Tonouchi, M., *Top. Appl. Phys.* **91**, 53 (2003).
38. Suzuki, M. & Hikita, M., *Phys. Rev. B* **44**, 249 (1991).
39. Paget, K.H., Guha, S., Cieplak, M.Z., Trofimov, I.E., Turneaure, S.J. & Lemberger, T. R., *Phys. Rev. B* **59**, 641 (1999).
40. Maggio-Aprile, I., Renner, Ch., Erb, A., Walker, E. & Fischer, Ø., *Phys. Rev. Lett.* **75**, 2754 (1995).
41. Renner, Ch., Revaz, B., Kadowaki, K., Maggio-Aprile, I. & Fischer, Ø., *Phys. Rev. Lett.* **80**, 3606 (1998).
42. Tanaka, S., Ueda, E., Sato, M., Tamasaku, K. & Uchida, S.-i., *J. Phys. Soc. Jpn* **64**, 1476 (1995).
43. Tanaka, S., Ueda, E., Sato, M., Tamasaku, K. & Uchida, S.i., *J. Phys. Soc. Jpn* **65**, 2212 (1996).
44. Oda, M., Matsuzaki, T., Momono, N. & Ido, M., *Physica C* **341-348**, 847 (2000).
45. Kato, T., Morimoto, H., Katagiri, A., Okitsu, S. & Sakata, H., *Physica C* **392-396**, 221 (2003).
46. Kato, T., Okitsu, S., Murakoso, M., Yokoi, M., Saitou, R., Maruyama, T. & Sakata, H., *Physica C* **412-414**, 250 (2004).

47. Van Baarle, G.J.C., Troianovski, A.M., Nishizaki, T., Kes, P.H. & Aarts, J., *Appl. Phys. Lett.* **82**, 1081 (2003).
48. Van Baarle, G.J.C., *Vortices in superconductors imaged by Scanning Tunnelling Microscopy: Vortex structures in superconducting thin films of a-$Mo_{2.7}Ge$ and $(La,Sr)_2CuO_4$*, PhD thesis, Leiden University, The Netherlands (2005).
49. Brown, S.P., Charalambous, D., Jones, E.C., Forgan, E.M., Kealey, P.G., Erb, A. & Kohlbrecher, J., *Phys. Rev. Lett.* **92**, 067004 (2004).
50. Gilardi, R., Mesot, J., Brown, S.P., Forgan, E.M., Drew, A., Lee, S.L., Cubitt, R., Dewhurst, C.D., Uefuji, T. & Yamada, K., *Phys. Rev. Lett.* **93**, 217001 (2004).
51. Gilardi, R., Mesot, J., Drew, A., Divakar, U., Lee, S.L., Forgan, E.M., Zaharko, O., Conder, K., Aswal, V.K., Dewhurst, C.D., Cubitt, R., Momono, N. & Oda, M., *Phys. Rev. Lett.* **88**, 217003 (2002).
52. Maley, M.P., Willis, J.O., Lessure, H. & McHenry, M.E., *Phys. Rev. B* **42**, 2639 (1990).
53. Glover, R.E. III & Sherrill, M.D., *Phys. Rev. Lett.* **5**, 248 (1960).
54. Landauer, R. & Hall, J.J., *Science* **160**, 736 (1968).
55. Mannhart, J., *Mod. Phys. Lett.* **6**, 555 (1992).
56. Chen, C.Y., Birgeneau, R.J., Kastner, M.A., Preyer, N.W. & Thio, T., *Phys. Rev. B* **43**, 392 (1991).
57. Konsin, P. & Sorkin, B., *Phys. Rev. B* **58**, 5795 (1998).
58. Xi, X.X., Doughty, C., Walkenhorst, A., Kwon, C., Li, Q. & Venkatesan, T., *Phys. Rev. Lett.* **68**, 1240 (1992).
59. Walkenhorst, A., Doughty, C., Xi, X.X., Li, Q., Lobb, C.J., Mao, S.N. & Venkatesan, T., *Phys. Rev. Lett.* **69** (1992).
60. Burlachkov, L., Khalfin, I.B. & Shapiro, B. Ya., *Phys. Rev. B* **48**, 1156 (1993).
61. Davis, L. Jr. & Rubin, L.G., *J. Appl. Phys.* **24**, 1194 (1953).
62. Müller, K.A. & Burkard, H., *Phys. Rev. B* **19**, 3593 (1979).
63. Christen, H.-M., Mannhart, J., Williams, E.J. & Gerber, Ch., *Phys. Rev. B* **49**, 12095 (1994).
64. Abe, K. & Komatsu, S., *J. Appl. Phys.* **77**, 6461 (1995).
65. Kingon, A.I., Maria, J.-P. & Streiffer, S.K., *Nature* **406**, 1032 (2000).
66. Wilk, G.D., Wallace, R.M. & Anthony, J.M., *J. Appl. Phys.* **89**, 5243 (2001).
67. Higashi, G.S. & Fleming, C.G., *Appl. Phys. Lett.* **55**, 1963 (1989).
68. Klein, T.M., Niu, D., Epling, W.S., Li, W., Maher, D.M., Hobbs, C.C., Hegde, R.I., Baumvol, I.J.R. & Parsons, G.N., *Appl. Phys. Lett.* **75**, 4001 (1999).
69. Copel, M., Cartier, E., Gusev, E.P., Guha, S., Bojarczuk, N. & Poppeller, M., *Appl. Phys. Lett.* **78**, 2670 (2001).
70. Groner, M.D., Elam, J.W., Fabreguette, F.H. & George, S.M., *Thin Solid Films* **413**, 186 (2002).
71. Gusev, E.P., Copel, M., Cartier, E., Baumvol, I.J.R., Krug, C. & Gribelyuk, M.A., *Appl. Phys. Lett.* **76**, 176 (2000).

72. Guha, S., Cartier, E., Bojarczuk, N.A., Bruley, J., Gignac, L. & Karasinski, J., *J. Appl. Phys.* **90**, 512 (2001).
73. Jeurgens, L.P.H., Sloof, W.G., Tichelaar, F.D. & Mittemeijer, E.J., *Thin Solid Films* **418**, 89 (2002).
74. Watanabe, Y., *Appl. Phys. Lett.* **66**, 1770 (1995).
75. Newns, D.M., Misewich, J.A., Tsuei, C.C., Gupta, A., Scott, B.A. & Schrott, A., *Appl. Phys. Lett.* **73**, 780 (1998).
76. Misewich, J.A. & Schrott, A.G., *Appl. Phys. Lett.* **76**, 3632 (2000).
77. Nagaraj, B., Wu, T., Ogale, S.B., Venkatesan, T. & Ramesh, R., *J. Electroc.* **8**, 233 (2002).
78. Grekhov, I., Delimova, L., Liniichuk, I., Mashovets, D. & Veselovsky, I., *Physica E* **17**, 640 (2003).

Chapter 5

Interface engineering in $YBa_2Cu_3O_{7-\delta}$ thin films

Abstract

The electronic properties of $YBa_2Cu_3O_{7-\delta}$ thin films depend on the crystallinity and the defect density, which are determined by the initial growth at the substrate-film interface. Control of the number of stacking sequences at the interface between $YBa_2Cu_3O_{7-\delta}$ and $SrTiO_3$ enables tuning of the density of antiphase boundaries. Strain relaxation depends on the initial defect density and produces different critical thicknesses during subsequent growth. Analysis of this interface engineering can be performed during growth by reflection high-energy electron diffraction and surface X-ray diffraction. Sub-unit cell layer epitaxy, in which crystal structures are formed by sequential deposition of sub-unit cell layers, is investigated as a promising growth technique for future applications.

5.1 Introduction

After the discovery of the increased transition temperature in the new high-T_c $La_{2-x}Sr_xCuO_4$ compound [1], which confirmed the results of the high-pressure experiments on the original $La_{2-x}Ba_xCuO_4$ compound [2,3], attempts were taken in 1987 to shrink the crystal lattice even more. The smaller yttrium was substituted for the lanthanum in the original formula, leading to the new Y-Ba-Cu-O compound with an increased T_c of 93 K [4]. This was the first time the superconducting state could be obtained beyond the liquid-nitrogen boiling point at 77 K, which increased the number of applications drastically due to the economic advantages relative to liquid helium cooling.

The new superconductor was soon identified as $YBa_2Cu_3O_7$ [5], with a crystal structure very unlike the structure of any oxide perovskite that previously had been observed, see Figure 5.1a. There are two significant differences between this material and the K_2NiF_4 forerunners. The first is that there are two layers of CuO_2 planes in close proximity (~3.4 Å apart) instead of one. The second is that there are remarkable one-dimensional chains of corner-shared CuO_4 squares running along one crystallographic direction. The crystal structure is orthorhombic at room temperature with an extended c-axis of ~11.7 Å and a- and b-axes of ~3.82 Å and ~3.88 Å. Changes in the oxygen stoichiometry lead to the oxygen deficient $YBa_2Cu_3O_6$, which is non-superconducting and tetragonal [6], see Figure 5.1b. The dramatic effect of this phase transition on the superconducting properties is shown in Figure 5.1c.

Thin film growth of $YBa_2Cu_3O_{7-\delta}$ is since the discovery a subject of extensive research and can be achieved by various physical vapor deposition techniques [10]. Independent of the deposition technique, oscillations of the reflection high-energy electron diffraction (RHEED) intensity were observed, caused by two-dimensional layer-by-layer growth [11,12]. It was found that the oscillation period corresponds to the time necessary for the deposition of one unit cell layer in the c-axis direction, which is the minimum growth unit that satisfies charge neutrality. Another important subject for the epitaxial growth of $YBa_2Cu_3O_{7-\delta}$ is the choice of substrate [13], which determines the structural and electrical properties of the fabricated thin films.

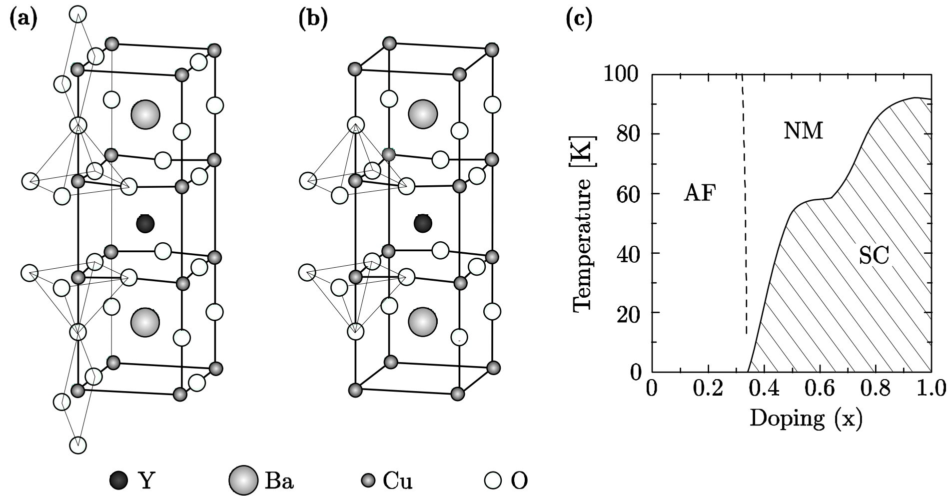

Figure 5.1 Crystal structures of $YBa_2Cu_3O_7$ **(a)** and $YBa_2Cu_3O_6$ **(b)** together with the phase diagram of $YBa_2Cu_3O_{6+x}$ **(c)** showing magnetic and electronic properties with the dependence on the doping level (x) [7-9]. Antiferromagnetic (AF), superconducting (SC) and normal metal (NM) regions are indicated.

In this chapter the interface engineering in thin films of $YBa_2Cu_3O_{7-\delta}$ is described with special emphasis on the initial growth and strain relaxation mechanisms. First the initial growth at the substrate surface is investigated to define the atomic stacking sequences at the film-substrate interface. Secondly, the strain relaxation during growth of thicker films is determined with the dependence on the initial stacking sequence at the interface. Thirdly, the growth process is analyzed by in-situ surface sensitive X-ray diffraction to define the changes in thin film properties during growth. Finally, a new deposition technique will be presented for the growth of atomically smooth films by interval deposition of sub-unit cell layers.

5.2 Initial growth at the substrate-film interface

The structural properties, i.e., defect and crystalline structure and surface morphology, of $YBa_2Cu_3O_{7-\delta}$ (Y123) thin films influence their electrical properties, and therefore, the applicability of these superconducting cuprates in heteroepitaxial structures. For instance, structural defects, grain boundaries, and antiphase boundaries (APBs) play an important role in flux pinning mechanisms [14-17], whereas the surface morphology of Y123 thin films is important for multilayer structures, which require smooth surfaces. The structural properties and surface morphology are a direct result of thin film growth, influenced by deposition conditions and substrate properties.

When all constituents are provided simultaneously, for instance in the case of pulsed laser deposition, the growth unit is the Y123 unit cell. One direct implication of this fact is the requirement of a specific stacking sequence of the individual atomic layers constituting this unit-cell. During the initial stage of growth, the stacking sequence will be influenced by the substrate surface properties, i.e., the terminating atomic layer and its crystalline structure. The first atomic layer and, consequently, the sequence of the initial Y123 unit cell layer will depend on these properties. High-resolution electron microscopy measurements of the stacking sequence at the interface (SSI) of Y123 on single TiO_2-terminated $SrTiO_3$ (STO) substrates [18] have shown, that a perovskite-like interface is present with two SSIs: *bulk–SrO–*TiO_2*–BaO–CuO–BaO–*CuO_2*–Y–*CuO_2*–BaO–bulk* (referred as Y133) and *bulk–SrO–*TiO_2*–BaO–*CuO_2*–Y–*CuO_2*–BaO–bulk* (referred as Y122). The coexistence of different SSIs leads to surface roughening and plays an essential role in the formation of APBs oriented perpendicularly to the substrate–film interface. These APBs, which are the most prominent type of defects occurring in ultrathin Y123 films, start at the interface and persist over the total film thickness. Some authors have related such planar defects to unit-cell steps on the substrate [19,20], but the density of APBs in Y123 ultrathin films grown on TiO_2-terminated STO is large compared to the density of substrate unit cell steps [18], indicating that APBs are formed on the

atomically smooth terraces due to the coalescence of neighboring islands with different SSIs.

To study the influence of the stacking sequence at the substrate–film interface and the related network of APBs on the electrical properties of *c*-axis oriented Y123 ultrathin films, three different interface configurations are used, see Figure 5.2.

I. Y123 on as-received vicinal STO substrates. The surface of these substrates consists of terraces with disordered step ledges and islands on the terraces with height differences of integer numbers of half a unit cell (~2 Å). This indicates the coexistence of the two possible surface arrangements [21]: SrO- and TiO_2-terminated domains (double-termination (DT)). This will lead to four possible SSIs [22].

II. Y123 on TiO_2-terminated STO substrates. Using the procedure described in ref. 22, STO substrates are treated in order to get atomically smooth single terminated TiO_2 surfaces. This will lead to two different SSIs [18].

III. Y123/Y122 on TiO_2-terminated STO substrates. Stoichiometric deposition with a cation ratio Y:Ba:Cu=1:2:2 during growth of the first unit-cell layer leads to the precise control of the interface configuration by suppression of the Y133 configuration. This procedure gives rise to only one SSI.

These films, presenting different interface configurations, were deposited by PLD on (100) STO and their growth was in-situ monitored by RHEED, allowing control of the thickness. The initial pseudomorphic growth mode changed to island growth

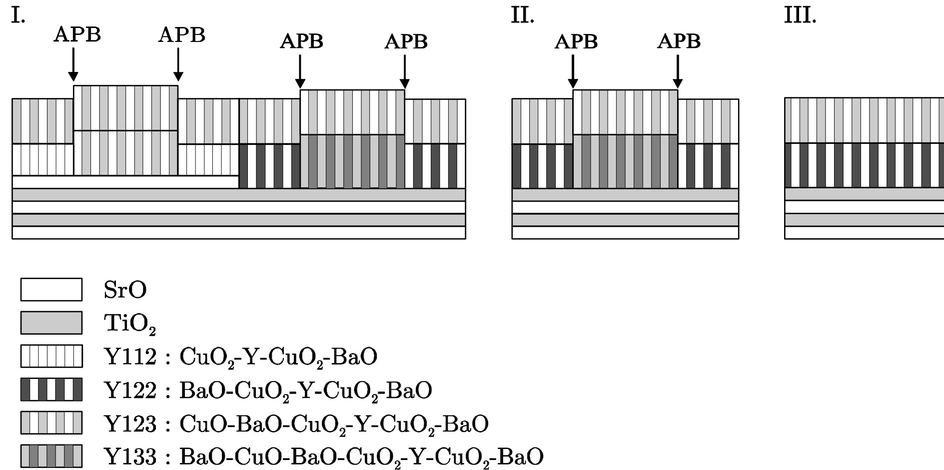

Figure 5.2 Schematic representation of the three interface configurations used on growing Y123: (I.) on as-received double-terminated STO, where four stacking sequences at the interface are possible, (II.) on single TiO_2-terminated STO, allowing two different SSIs, and (III.) on TiO_2-terminated STO using Y122 for the first unit cell layer, giving rise to a single stacking sequence at the interface. In these cases, the coalescence of islands with different stacking sequences causes the formation of antiphase boundaries (APBs), which are indicated by arrows.

to release the epitaxial strain over a critical thickness, which scaled with the inverse of the lattice mismatch. For Y123 on STO, the critical thickness was found to be dependent on the $SrTiO_3$ termination [23] and estimated to be in the range of 20 nm, about 17 unit cells, for TiO_2 terminated substrates [24]. All films studied here present thicknesses ranging from 5 to 10 unit cells, which allows study of the influence of the SSI on the superconducting properties without interference from strain relaxation mechanisms.

Concerning the PLD deposition conditions, a sintered ceramic target with the nominal stoichiometry Y:Ba:Cu =1:2:3 was ablated with an energy density of 1.3 J/cm^2 at 1 Hz. During growth, the substrate was held at 780 °C in an oxygen environment at 0.13 mbar. Similar temperature and oxygen background pressure conditions were used when depositing the Y122 layer, but the energy density at the target (nominal stoichiometry Y:Ba:Cu=1:2:2) was 7 J/cm^2. In this case, pulsed laser interval deposition [25] was used at 50 Hz to obtain an atomically smooth single unit-cell layer, followed by in-situ annealing for one hour at 830°C before depositing the Y123 layer. On top of the samples a protective $SrRuO_3$ layer was grown at 600 °C in an oxygen pressure of 0.13 mbar, to facilitate electrical characterization. Finally, all samples were annealed in an oxygen atmosphere at 0.7 bar for 30 min. at respectively, 600 °C and 450 °C.

In Figure 5.3, the RHEED specular intensities, recorded during the growth of the Y123 layers with the different interface configurations, are shown. A large recovery of the RHEED intensity was observed during growth of the initial Y122

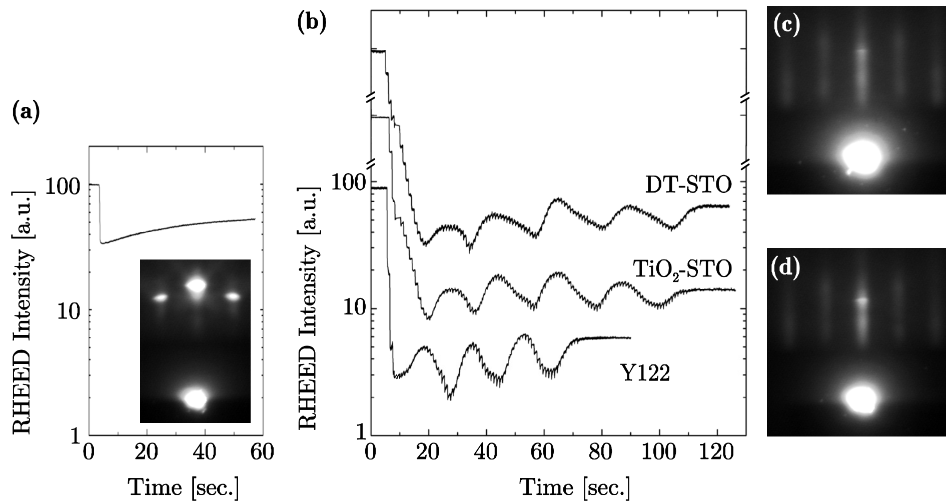

Figure 5.3 RHEED intensity recorded during growth of Y123 ultrathin films with different control on the interface stacking. **(a)** Deposition of the initial Y122 layer on TiO_2-terminated STO. **(b)** Deposition of Y123 on double (DT) and single (TiO_2) terminated STO and on the Y122 layer. The RHEED patterns are shown after: **(inset in a)** the initial Y122 layer, **(c)** and **(d)** the deposition of Y123 on DT-STO and Y122, respectively.

layer, see Figure 5.3a. This and the corresponding RHEED pattern, exhibiting clear two-dimensional spots, see inset Figure 5.3a, indicated a perfect and atomically flat crystalline surface. During subsequent deposition of Y123, clear intensity oscillations are observed, which indicated 2D growth, see Figure 5.3b. Oscillations of the specular RHEED intensity were also observed during deposition of Y123 on double (DT) and TiO_2-terminated STO substrates, but the recovery was smaller than in the case of an initial Y122 layer. Moreover, on a DT-STO substrate only streaks could be seen (Figure 5.3c), while clear 2D spots were observed in the RHEED pattern of Y123 on Y122 (Figure 5.3d). Both facts reflected that the surface step density and, therefore, the surface roughness increased when increasing the number of possible interface stacking sequences.

In order to analyze the in-plane ordering and, subsequently, the network of antiphase boundaries, the (00*l*)-rocking curves (ω-scans) were measured by X-ray diffraction (XRD). In Figure 5.4a (005)-rocking curves are shown for 10 unit cells of Y123 grown on an initial Y122 layer and on DT-STO. In both cases, the observed shape exhibits two parts: a satellite (broad) component and a main peak (narrow component), which is characteristic for weakly disordered systems [26]. The δ-shaped coherent peak, related to perfectly aligned regions, cannot be resolved due to the resolution limitation of the apparatus. The line shapes of the broad components are

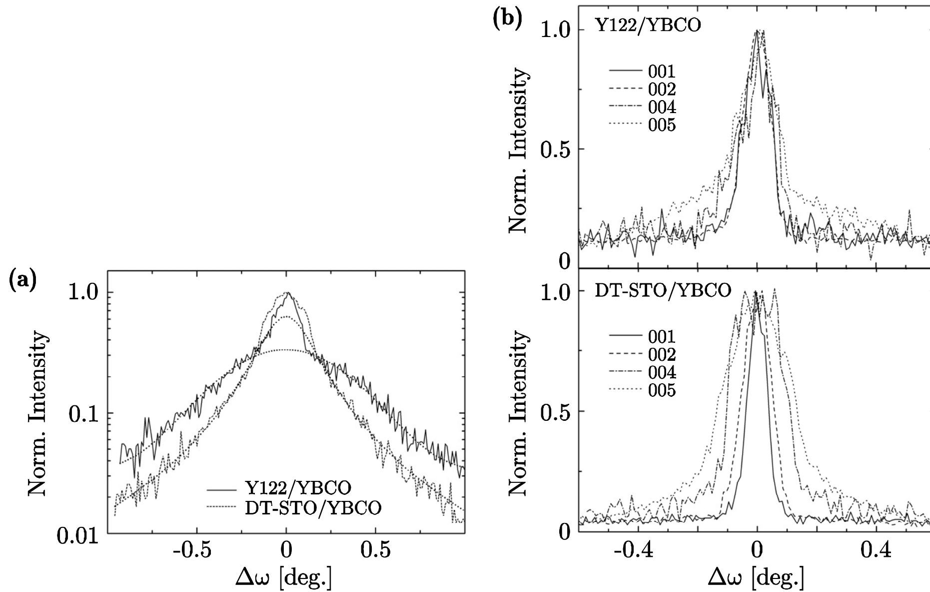

Figure 5.4 Normalized (00*l*)-rocking curves of Y123 films (10 unit cells) with different stacking sequences at the interface with the substrate. **(a)** The (005)-rocking curves of Y123 films grown on Y122 and double terminated STO, presenting the two component characteristics of weakly disordered systems. **(b)** The (00*l*)-rocking curves (*l*=1,2,4,5) of Y123 grown on Y122 and double-terminated STO, showing respectively a constant and an increasing angular width.

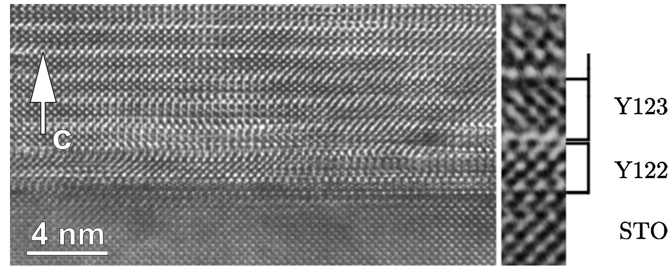

Figure 5.5 High-resolution electron microscopy image of an YBCO film with a single unit cell of Y122 as buffer layer on a TiO_2-terminated STO substrate. An enlargement of the film-substrate interface is also shown.

different in both cases (Gaussian on an initial Y122 layer and Lorentzian on DT-STO), which has been previously attributed to different densities of APBs [27]. Moreover, on increasing the number of possible interfacial configurations the ratio between the intensity of the narrow and broad components (R) decreases from R=3 for Y123 grown on an initial Y122 layer to R=2 for Y123 grown on DT-STO. This is caused by the extension of the diffuse spots perpendicularly to the diffraction vector when increasing the defect density [26].

Further information on the disorder as a function of interface engineering can be obtained by comparing the ω−scans of different (00l)-reflections. Lattice mismatched epitaxial layers such as the Y123 films can be considered as separated mosaic blocks on a substrate. In this picture, the diffuse component of the rocking curve is influenced by two main factors: slightly in-plane misorientation and small coherence length parallel to the substrate [28]. In Figure 5.4b it is shown that the main peak of Y123 with an initial Y122 layer presents a constant lateral width in angle space, $\Delta\omega=\omega-\theta_1$, with θ_1 being the position of the corresponding Bragg reflection, which is a clear indication of disorder of rotational nature [27,28]. Meanwhile, the film on DT-STO exhibits a width increase with l, which means that the broadening of the rocking curve is related also to a shortening of the coherence length caused by a higher density of in-plane defects.

All these observations are supported by high-resolution electron microscopy (HREM) analysis[I] of a pulsed laser deposited YBCO film grown on TiO_2-terminated STO with a Y122 single unit cell buffer layer, see Figure 5.5. It proves that using an initial Y122 layer results in a high quality film with good epitaxial properties: $(001)_{YBCO}$ parallel to $(001)_{STO}$ and $(100)_{YBCO}$ parallel to $(100)_{STO}$ [29,30]. The misfit between film and substrate (~2%) causes local bending of the lattice planes. Antiphase boundaries in the film occur only occasionally and their spacing is

[I] High-resolution electron microscopy analysis was performed at EMAT, University of Antwerp, Belgium.

comparable with the terrace width. Therefore, it can be concluded that antiphase boundaries are only formed at unit cell steps at the substrate surface and not as a result of a variable interface configuration. Consequently, the interface stacking sequence of this film is the single type as shown in Figure 5.2 (III).

In Figure 5.6 the normalized electrical resistance against temperature curves are given for 7-unit-cell-thick films with the three available interface configurations. It can be seen that there is a close relationship between the electrical properties and the density of APBs, controlled by the number of SSIs. It is shown that a higher density of APBs leads to a higher superconducting transition temperature, T_c, and a steeper slope of the temperature dependence of the normal state resistance. This behavior is attributed to the degree of oxidation of the YBCO ultrathin films, since these planar defects are supposed to favor oxygen in-diffusion in Y123 thin films, in a similar way as other defects, like dislocations, do [31]. Oxygen diffusion in the c-direction in a single crystal, without any defects, is 10^4-10^6 times slower than diffusion in the (a,b)-direction [32,33]. An observation giving support to this idea is that after a post-growth oxidation treatment of these films in 1 bar oxygen at 600 °C for 6 hours and 450 °C for 18 hours, T_c tends to approach the same value for all ultrathin films, as shown in the inset in Figure 5.6. This indicates that the low concentration of defects in the film with the Y122 interface is the main cause for the oxygen deficiency and, therefore, the reduced superconducting properties observed in these as-made films. The diffusion of oxygen in the film is comparatively slower and requires longer oxidation times. In other words, the presence of APBs in the thin films favors the oxygen in-diffusion, but is unfortunately accompanied by an increase in the disorder [34].

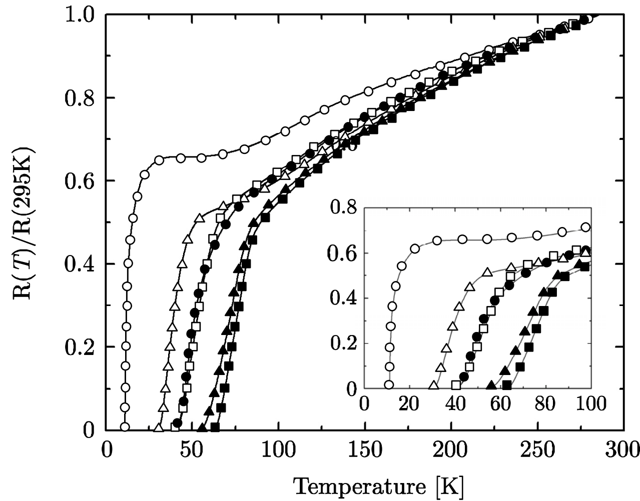

Figure 5.6 Temperature dependence of the normalized resistance curves for 7 unit cell thick films with different degrees of control at the interface, i.e., Y122 (○), TiO_2-STO (△) and DT-STO (□). The closed symbols mark the normalized resistance after a post-growth oxidation treatment.

5.3 Strain relaxation in ultrathin films

Heteroepitaxial growth of thin films can produce strained heterostructures in the case of low misfit substrates. If the lattice mismatch between substrate and growing epitaxial layer is sufficiently small, the first deposited atomic layers will be strained to match the substrate, until a critical thickness is reached, above which relaxation takes place by introduction of twins and/or dislocations. $YBa_2Cu_3O_{7-\delta}$ thin films are grown at high temperatures where the equilibrium phase is tetragonal, but they undergo a phase transition to orthorhombic upon cooling. The relaxation of these films has to accommodate not only a lattice mismatch, but also this tetragonal to orthorhombic transition. Several strain relieving mechanisms have been proposed for $YBa_2Cu_3O_{7-\delta}$ deposited on $SrTiO_3$ by PLD with critical thicknesses ranging between 5 and 20 nm, ~4 and 17 unit cells [24,35-38]. The large difference in the experimentally determined critical thickness values was supposed to be a result of the different growth conditions [10]. These growth conditions determine the surface morphology and therefore the nucleation of dislocations.

Strain relaxation in a structurally perfect film with a smooth surface is very difficult. In case of $YBa_2Cu_3O_{7-\delta}$ growth dislocations are formed, to reduce the epitaxial strain, only after a critical thickness for an initial pseudomorphic layer. The critical thickness was indeed found to be dependent on the surface termination of the $SrTiO_3$ substrate [23] with the highest critical thickness for TiO_2 terminations. It has also been observed that the epitaxial relationship between the film and the substrate is influenced by the magnitude of the miscut angle of the vicinal (001) STO substrates. Up to a miscut angle of 1.2°, YBCO films grow on the optical surface, whereas above this angle films are grown on the crystallographic surface [39-41]. The reported critical thickness for YBCO grown on TiO_2-terminated STO

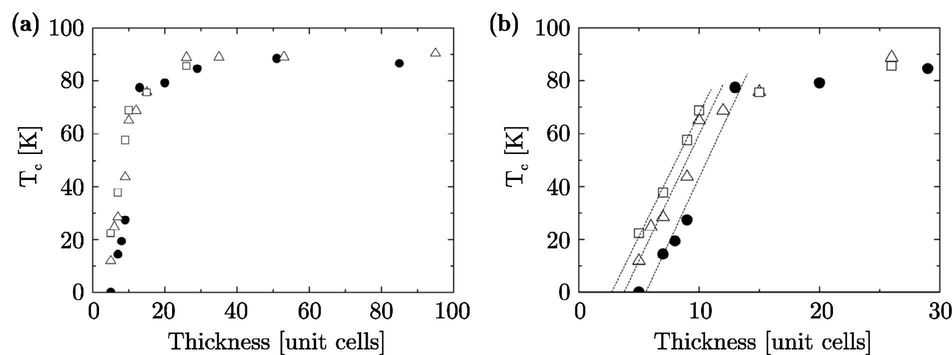

Figure 5.7 The transition temperature T_c (R=0) as a function of the thickness of the YBCO layer for different degrees of control at the substrate interface, i.e., Y122 (●), TiO_2-STO (△) and DT-STO (□). **(a)** All films have comparable T_c values (~90 K) for large thicknesses, **(b)** but show different behavior for ultrathin films (below ~15 unit cells). The dashed lines indicate the increase in T_c with thickness for ultrathin films.

substrates by PLD, corresponding to the point of tetragonal to orthorhombic transition, is ~11.5 nm for low miscut angles [42].

To investigate the influence of the density of APB's on the strain relaxation, YBCO (Y123) layers with different thicknesses were grown on Y122, TiO_2-STO and DT-STO. The deposition conditions are described in section 5.2. During deposition of Y123, clear intensity oscillations were observed up to a thickness of ~20 unit cells, which was used to determine the exact layer thickness. For thicker films the total thickness was estimated from the growth rate at the initial stage. Figure 5.7a shows the variation in transition temperature T_c (R=0) with the number of YBCO unit cells for different densities of APB's at the STO substrate. The control of the APB density, enabled by growth on Y122, TiO_2-STO and DT-STO, will influence the formation of dislocations and therefore the strain relaxation. For thicker films, the

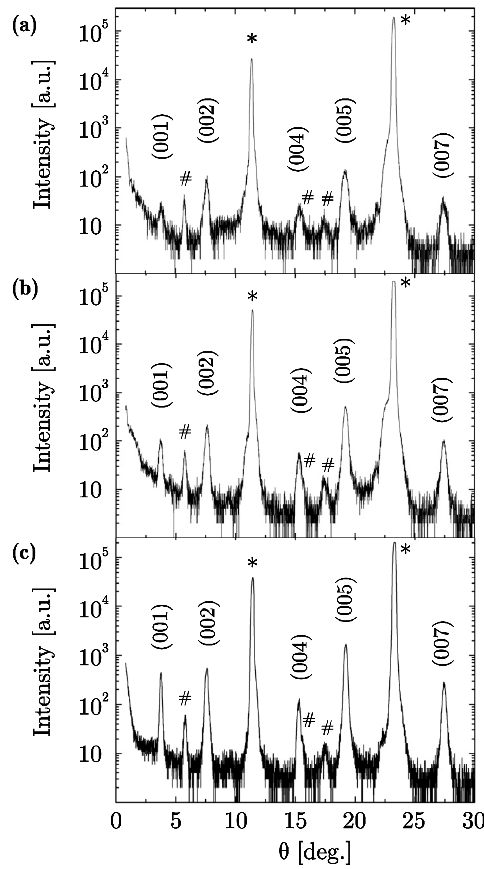

Figure 5.8 X-ray diffraction θ-2θ scans of Y123 layers on TiO_2-terminated $SrTiO_3$ with an Y122 initial layer. The thickness of the total YBCO layer is **(a)** 9, **(b)** 15 and **(c)** 40 unit cells. The $SrTiO_3$ substrate reflections are indicated with an asterisk and their spectral contributions (λ/2 and λ/3) with a cross.

effect of the initial APB density on the transition temperature is negligible and the T_c is ~90 K. However, the APB density does play an important role for ultrathin films below ~15 unit cells, see Figure 5.7b. YBCO layers with a thickness of 5 unit cells do not become superconducting when grown on an Y122 layer, due to the low number of APB's and the corresponding low level of oxygen in-diffusion. On the other hand, when 5 unit cell thick YBCO is grown on TiO_2-terminated STO and double terminated (DT) STO, the density of APB's increases and causes better oxidation of the film. This leads to superconductivity with T_c values of 11.9 K and 22.4 K for YBCO films on respectively, TiO_2-STO and DT-STO.

By increasing the thickness of the YBCO layer, the number of dislocations to release the strain increases, which improves the oxygen indiffusion. This will induce an increase in the transition temperature, which is visible in Figure 5.7b for all three cases. For all three, the increase in T_c with every extra YBCO layer is comparable and is about 9.6 K per unit cell (u.c.). This means that although the density of APB's at the beginning of the growth is different, the formation of dislocations to release the strain is similar during subsequent growth. This results in different thickness values for the transition from non-superconductivity to superconductivity. Critical thicknesses were estimated from linear fits to be: 5.2 u.c. (6.1 nm), 3.4 u.c. (4.0 nm) and 2.4 u.c. (2.8 nm) for YBCO layers on respectively Y122, TiO_2-STO and DT-STO. The thickness where the strain appears to be relaxed for the major part of the film, and only a small increase in T_c is visible for higher values, is different for the three cases. The YBCO layer on double-terminated STO seems to be relaxed after ~10 unit cells, while this thickness value is slightly higher in case of growth on single-terminated TiO_2-STO, namely ~11 unit cells. The major part of the YBCO layer grown on the Y122 layer appears to be relaxed after ~13 unit cells.

These values agree very well with results from other groups for pulsed laser deposited YBCO on STO, but show clearly the dependence of the critical thickness on the initial defect (APB) density at the film-substrate interface.

Due to the substrate-induced strain, ultrathin films will have in-plane lattice parameters comparable to those of the substrate. This leads to the pseudomorphic YBCO phase with in-plane tensile strain and, therefore, out-of-plane shortening of the c-axis. To study the relationship between the thickness of the YBCO layer and the substrate-induced strain, the films were examined by X-ray diffraction. The θ-2θ scans along the direction normal to the surface exhibit only (00l) reflections, which implies that the films are c-axis oriented, see Figure 5.8. No other peaks are observed indicating the absence of unwanted phases. YBCO films grown on STO with an initial Y122 layer are shown for total thicknesses of 9, 15 and 40 unit cells. The observation of the (00l) reflections allows calculation of the c-axis lattice parameter by using Bragg's law. This is an advantage, because determination of the unit cell structure by fitting of numerous peaks is not possible for ultrathin films, as only the (00l) reflections are sufficiently strong to be observed. The value for the c-

axis can be calculated by comparing the Bragg angles of the (005) YBCO peak and the (200) STO peak:

$$c_{YBCO} = a_{STO} \frac{N_{YBCO}}{N_{STO}} \frac{\sin\theta_{STO}}{\sin\theta_{YBCO}}, \tag{5.1}$$

where a_{STO}=3.905 Å is the lattice constant of the cubic STO substrate and θ_{STO} and θ_{YBCO} are the Bragg angles of the STO and YBCO peaks. N_{STO} and N_{YBCO} indicate the reflection orders of the STO and YBCO reflection peaks. The calculated c-axis lattice parameters are given in Figure 5.9 for YBCO layers with different thicknesses on STO with an initial Y122 layer as well as on double-terminated STO and TiO_2-terminated STO. The YBCO films show a decrease in c-axis length for all three cases when the thickness is decreased. Below a critical thickness, a reduced c-axis is expected due to a contraction of the c-axis caused by the in-plane tensile strain from the larger substrate lattice. The YBCO films on DT and TiO_2-STO show this decrease in c-axis below 10-12 unit cells. Surprisingly, the YBCO films on the initial Y122 layer show a small increase in c-axis when the thickness is decreased to ~12 unit cells, followed by a sharp drop in c-axis when the thickness is further reduced. This is caused by the interplay of two mechanisms, strain relaxation and oxygenation, which have opposite effects on the c-axis parameter. While for ultrathin films with a low defect density the c-axis is reduced due to large in-plane tensile strain, at the same time this highly ordered structure leads to a low level of oxygen incorporation, which results in an enlargement of the c-axis. The observation of a reduced c-axis for ultrathin films is in good agreement with results for sputter deposition [43,44], but contradict earlier results by pulsed laser deposition [27]. An important point is the $SrRuO_3$ cap layer in these experiments, which was not present in the other PLD experiments. This cap layer will protect the delicate ultrathin films and prevent the exposure to ambient atmosphere, which can affect the surface and degrade the superconducting layer.

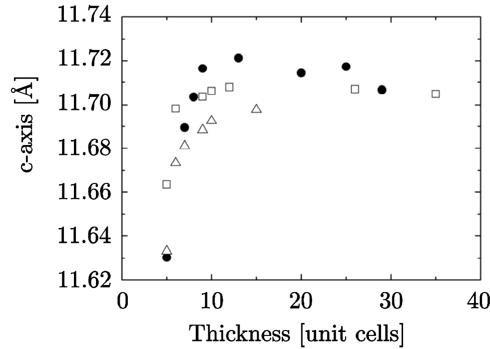

Figure 5.9 The c-axis length of the YBCO crystal structure as a function of the layer thickness for different degrees of control at the substrate interface, i.e., Y122 (●), TiO_2-STO (△) and DT-STO (□).

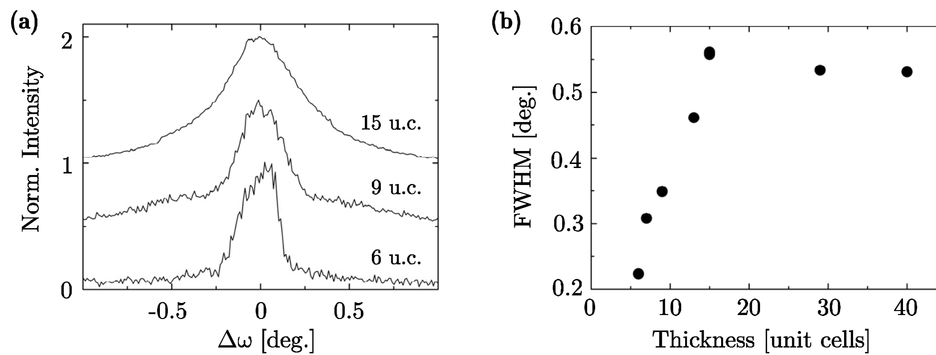

Figure 5.10 Thickness dependence of the (005)-rocking curve of YBCO grown on TiO_2-terminated $SrTiO_3$ with an initial Y122 layer. **(a)** Normalized X-ray (005)-rocking curves of 6, 9 and 15 unit cells thick YBCO films. For clarity are the curves of the 9 and 15 unit cells thick YBCO films displaced by respectively 0.5 and 1.0. **(b)** Thickness dependence of the full width at half maximum of the (005) YBCO rocking curves.

The relaxation of the in-plane lattice parameters could not be verified, as only the (00l) reflections in the ultrathin films are sufficiently strong to be observed. However, (00l) rocking curves provide important information on the lattice perfection of the thin films. Rocking curves (ω-scans) were taken around the (005) reflection of the YBCO layer on the initial Y122 layer. The rocking curves exhibit initially a broad and a narrow component, see Figure 5.10a. The narrow peak indicates that the lattice is highly ordered and in a strained pseudomorphic status. The peak broadening, which can be observed for an increase in thickness, can be attributed to the increase of the number of defects by the strain relaxation. The values for the full width at half maximum (FWHM) are given in Figure 5.10b. They show an increase up to a thickness of ~15 unit cells, after which the FWHM value becomes constant at ~0.55°. This value is in good agreement with results for thick pulsed laser deposited YBCO films from other groups [27,45]. These findings imply strongly that the defect density depends on the thickness. When the layer thickness reaches the critical value at ~15 unit cells, the major part of the strain is relieved and the defect density stays constant for thicker films.

5.4 In-situ X-ray diffraction study during growth

The dynamics of the growth during pulsed laser deposition have been extensively studied by using RHEED, which provides information about surface diffusion, particle nucleation and surface morphology. However, with RHEED hardly any information is obtained about strain evolution and relaxation of the crystal structure. By the use of high intensity X-rays, available now at third generation synchrotron sources, it is possible to study simultaneously the surface morphology,

composition and strain state of the deposited thin film *during* growth. The first in-situ surface sensitive X-ray diffraction measurements were only recently reported for pulsed laser deposited homoepitaxial growth of $SrTiO_3$ [46,47] and heteroepitaxial growth of $EuTiO_3$ on $SrTiO_3$ [48].

Heteroepitaxial growth of YBCO on STO was investigated by in-situ X-ray diffraction to obtain more knowledge about the formation of the crystal structure and the strain relaxation during the growth process. The tetragonal to orthorhombic transition could also be investigated during the cool down procedure. In all experiments, at a grazing angle of 1.0 degree for the X-ray beam, the intensity of the reciprocal point (0,0,0.151), in STO lattice units, was monitored during deposition. For this point, the measurement had the highest surface sensitivity. Short interruptions of the deposition allowed quick measurements of the reflectivity ridge (θ-2θ) scan, which provides information about the c-axis, total film thickness and, to a certain extent, the film roughness.

The experiments were carried out in a PLD chamber [49] mounted on a 2+3 type surface diffractometer with vertical scattering geometry[II]. The X-ray beam was monochromatized to a wavelength of 0.775 Å. A KrF excimer laser (Lambda Physik EMG101) was used to ablate a sintered YBCO target with an energy density of ~1.5 J/cm^2. In order to obtain sufficient statistics of the diffracted signals, the laser repetition rate was kept at 0.5 Hz. During deposition the substrate temperature was kept at 780 °C, while the oxygen pressure in the chamber was 0.1 mbar.

Three topics were investigated during the heteroepitaxial growth experiments of $YBa_2Cu_3O_{7-\delta}$ on TiO_2-terminated $SrTiO_3$ and will be shortly described.

5.4.1 Analysis of the layer thickness

During growth, oscillations were observed in the measured X-ray intensity. These oscillations are shown in Figure 5.11 together with the reflectivity ridge scans, which were measured during the growth interruptions. Consecutive intensity maxima during growth have clearly distinct maximum intensity values, which can be attributed to the analysis of successively even and uneven numbers of YBCO unit cell layers. The overall intensity is slowly decreasing due to surface roughening, but the values of the successive intensity maxima during growth also exhibit variations. This is caused by the fact that the (0,0,0.55) reciprocal space point, in YBCO lattice units, is monitored and not precisely half way to the (001) YBCO reflection. From the diffraction measurements the c-axis and total film thickness could be determined and they are listed in Table 5.1 together with the number of observed intensity maxima during growth and the calculated number of unit cell layers. In the

[II] The in-situ x-ray diffraction studies during pulsed laser deposition were performed at BM26 (DUBBLE) [50] at the European Synchrotron Radiation Facility (ESRF), Grenoble, France.

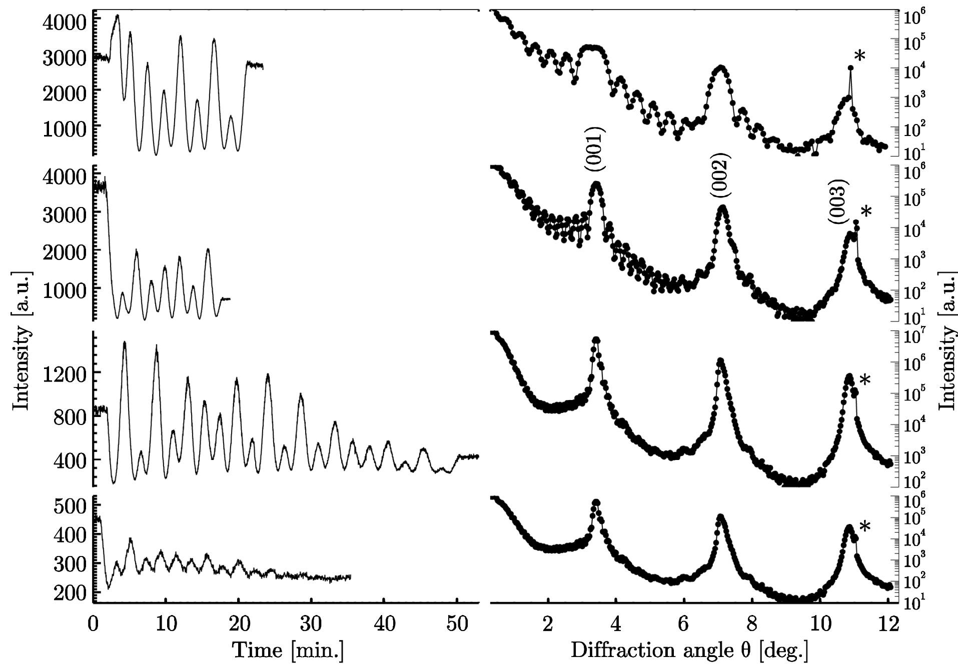

Figure 5.11 In-situ YBCO growth monitoring with X-ray diffraction. **(left)** Intensity oscillations during growth of YBCO on TiO_2-terminated STO. The amount of deposited material increases from top to bottom. **(right)** θ-2θ scans along the (00l) direction taken during a deposition interruption. Due to non-ideal sampling of the very sharp (001) substrate reflection at 11.2 degrees, indicated by asterisks, it appears with different intensities in the different scans.

reflectivity ridge θ-2θ scans Kiessig fringes are visible, which arise from interference effects from the top and bottom part of the film and are therefore related to the total thickness. Unlike the Bragg points, which are originating from a periodicity at an atomic scale, the fringes are sensitive to much longer length scales and therefore probe the average electron density.

Using the last consideration to explain the discrepancy between the observed number of intensity maxima during growth and the calculated number of unit cell layers, shown in Table 5.1, leads to the hypothesis that the first smooth layer deposited on the STO substrate does not consist of a normal YBCO unit cell. The number of observed intensity maxima is systematically one larger than the number of YBCO unit cell layers deduced from thickness and c-axis length measurements. This can also be concluded by comparing the time needed to deposit the first smooth layer and subsequent unit cell layers. Assuming that the deposition rate stays relatively constant during growth, the first smooth layer was deposited in about 2/3 of the time of the subsequent layers. This observation is in good agreement with earlier results, which stated that two stacking sequences [18] are

Intensity maxima	Thickness (Å)	c-axis (Å)	N_{layers}
9	96(1)	11.91(5)	8.06(8)
17	192(1)	11.95(4)	16.1(1)
38	448(1)	12.0(1)	37.3(4)
52	610(4)	12.0(1)	50.8(5)
-	605(11) *	11.716(2) *	52(1) *

Table 5.1 Structural parameters of an YBCO film during growth, determined from the data shown in Figure 5.11. The data indicated by the asterisks are measured after cooling down to room temperature.

possible at the TiO_2-terminated STO substrate surface (Y122 and Y133, as described in section 5.2) and that only after this initial growth the first correct YBCO unit cell is formed. Observation of the first smooth layer after 2/3 of the material of a unit cell is suggestive of stabilization of the Y122 phase at the substrate surface. The elongation of the c-axis, as shown in Table 5.1, can simply be attributed to thermal expansion in the direction perpendicular to the substrate surface. When taking the bulk lattice parameter in the c-direction of oxygen deficient tetragonal $YBa_2Cu_3O_6$ of ~11.82 Å [7] and the bulk value of the thermal expansion in the c-direction of 21×10^{-6} K^{-1} [51], an elongated c-axis of ~12.01 Å is expected at 780 °C.

The YBCO layer was eventually cooled down to room temperature in an oxygen pressure of 1 bar. This procedure provided the necessary oxygen in-diffusion and lowered the c-axis significantly, as shown in Table 5.1. In the end the sample had a superconducting transition temperature T_c of ~85 K. This is lower than the bulk value, which suggests that the oxygenation of the layer is not optimal. A slower cooling procedure will probably improve the oxygen indiffusion.

5.4.2 Analysis of the surface morphology

The surface morphology of the deposited thin films was investigated by successive deposition of 1 and 0.5 unit cell layers. In RHEED analysis experiments maximum intensity corresponds to 100% coverage of the surface and low surface roughness, while minimum intensity indicates 50% coverage and high surface roughness. To investigate this roughness evolution in in-situ X-ray diffraction, the reflectivity scans were measured for three different layer thicknesses, see Figure 5.12. The first scan is for an YBCO layer with a thickness of approximately 5 unit cells. Upon subsequent deposition of more material, the intensity of the (0,0,0.55) reciprocal space point, in YBCO lattice units, is carefully monitored. The deposition was stopped in the next maximum, indicating 1 unit cell layer growth, and the reflectivity scan was measured. Next a similar procedure was followed, but now the deposition was stopped at the minimum intensity, indicating 0.5 unit cell layer growth, and again the reflectivity scan was measured.

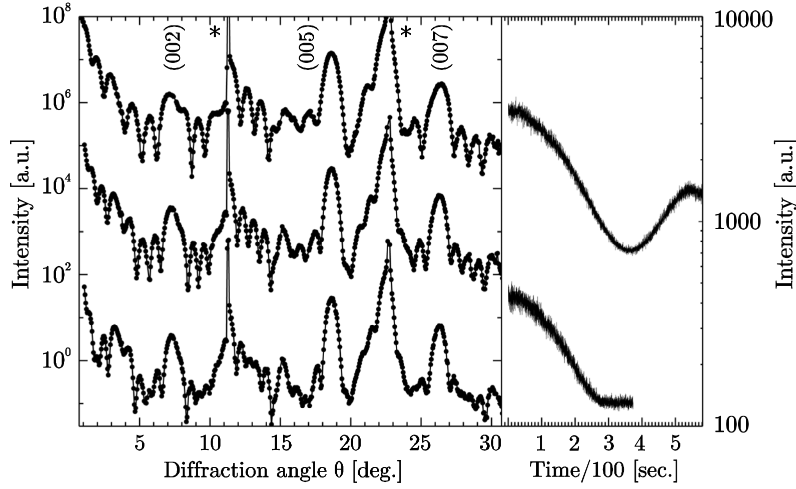

Figure 5.12 In-situ roughnesses monitoring with X-ray diffraction. **(left)** Diffraction patterns along (00l) direction of an YBCO film. Shown are the initial scan (top) of ~5 unit cell thick YBCO, after adding one extra unit cell layer (middle) and a half unit cell layer (bottom). For clarity the top and bottom curves are multiplied by a factor of 10^3 and 10^{-3} respectively. The sharp peaks at 11.2 and 22.3 degrees, indicated by asterisks, are the STO substrate (001) and (002) reflections respectively. **(right)** The intensity of the (0,0,0.55) reciprocal point, in YBCO lattice units, during deposition of ~1 unit cell layer (top) and 0.5 unit cell layer (bottom) of YBCO.

The shape of the resulting diffraction patterns can be explained qualitatively by the following equation, which describes the specularly diffracted intensity of the thin film when disregarding substrate and defect scattering.

$$I \propto \frac{\sin^2(Nq_z c/2)}{\sin^2(q_z c/2)}, \tag{5.2}$$

where q_z is the projected scattering vector in the z-direction (perpendicular to the surface) and c is the c-axis lattice parameter of the YBCO thin film. In the case of N completely smooth unit cell layers, there will be N-2 Kiessig fringes in between two neighboring Bragg peaks. By growing one extra unit cell layer, one extra Kiessig fringe appears between the Bragg peaks, as can be seen when going from the top to the middle diffraction profile in Figure 5.12. When depositing another half a unit cell layer, the diffraction profile is built up of two contributions [52] and the slight difference in periodicity results in the washing out of the fringes, which is most pronounced half way the Bragg peaks. This can be seen in the bottom diffraction pattern of Figure 5.12.

5.4.3 Analysis of strain relaxation

During the interruption periods of the thin film growth process, the crystal structure was characterized. The out-of-plane direction of the Bragg reflections was scanned for different thicknesses, as described in section 5.5.1, and the pronounced Kiessig fringes were used to accurately determine the layer thickness, see Figure 5.13. The c-axis lattice parameter of the YBCO film was obtained from the angular positions of several Bragg peaks. The constant c-axis lattice parameter of ~12.0 Å, as can be observed in Tables 5.1 and 5.2, suggests that the epitaxial relationship between film and substrate is unchanged during deposition up to a thickness of 52 unit cells. The effect of strain relaxation can clearly be seen in the room temperature data, which were measured after the oxygen in-diffusion during the cooling procedure. The room temperature (001) Bragg reflection of the YBCO film, shown at the bottom in Figure 5.13, shows some distinct differences compared with the high temperature diffraction peaks. First of all, the position is shifted due to the changes in thermal expansion and oxygen content, resulting in a decrease of the c-axis. Secondly, the fringe contrast decreased, which is an indication of surface roughening. Thirdly, the integrated intensity diminished, which can be ascribed to a decrease in crystal quality or to a change in crystal structure. All the aforementioned differences can arise from additional strain relaxation during the cooling procedure by the formation of defects.

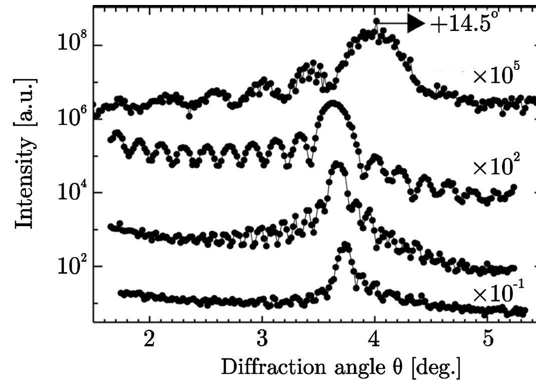

Figure 5.13 Kiessig fringes around Bragg reflections at different interruptions of the YBCO deposition. Shown are the (005) reflection for a 11 nm film (top), (001) reflection for a 21 nm film (second from top) and (001) reflection for a 42 nm film (second from bottom) at deposition conditions. The (001) reflection after cool down to room temperature is also shown (bottom). For clarity are the reflections displaced by multiplication of the intensities. In addition, the (005) reflection (top) is shifted by 14.5 degrees to make it appear in the same range.

Intensity maxima	Thickness (Å)	c-axis (Å)	N_{layers}
10	108(1)	12.05(4)	9.0(1)
19	210(1)	12.04(1)	17.4(1)
35	419(2)	12.055(4)	34.8(2)
-	382(8) *	11.710(3) *	33(1)*

Table 5.2 Structural parameters of an YBCO film during growth, determined from the data shown in Figure 5.13. The data indicated by the asterisks are measured after cool down to room temperature.

The evolution of the YBCO lattice parameters from deposition conditions to room temperature were investigated by measuring two types of reflections, of type *hhl* (115 and 225) and *00l* (005), during the cooling procedure. The resulting c-axis and average in-plane $\overline{a} = \frac{1}{2}(a + b)$ as a function of temperature are shown in Figure 5.14. The thermal expansion coefficients are determined by linear fits to the data-points as function of temperature. The obtained values are $\alpha_c = 30(3)\times10^{-6}$ K^{-1} and $\alpha_{\overline{a}}=6(3)\times10^{-6}$ K^{-1}, which agree well with values for bulk YBCO single crystals, $\alpha_c=21(1)\times10^{-6}$ K^{-1} and $\alpha_{\overline{a}}=10(1)\times10^{-6}$ K^{-1} [51]. No significant change in peak shape was observed that would indicate the tetragonal to orthorhombic phase transition and subsequent twin-formation [39]. The superconducting transition temperature T_c was measured to be ~76 K, indicating a reduction from optimal conditions. A slower cooling procedure has to be used to improve the oxygen indiffusion.

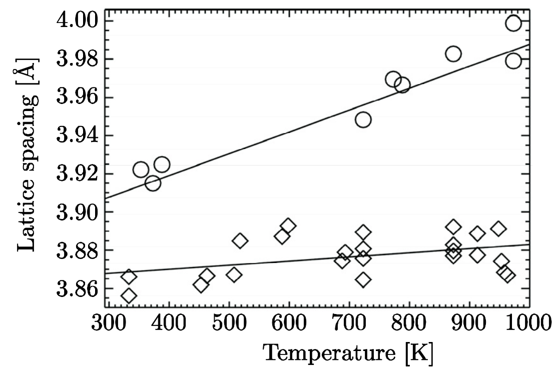

Figure 5.14 Evolution of the lattice parameters during cooling down from deposition temperature (780 °C) to room temperature of a 42 nm YBCO film. Shown are values of the c-axis (circles), given by c/3, and the average in-plane $\overline{a}$ (diamonds) as a function of temperature. The lines are fits as function of temperature to the data-points and render the thermal expansion coefficients $\alpha_c = 30(3) \times 10^{-6}$ K^{-1} and $\alpha_{\overline{a}}=6(3) \times 10^{-6}$ K^{-1}.

5.5 Sub-unit cell layer epitaxy

Control of the stacking sequence at the film-substrate interface can be used to prevent the formation of antiphase boundaries and surface roughening during the initial stage of $YBa_2Cu_3O_{7-\delta}$ growth on $SrTiO_3$, as discussed in section 5.2. During subsequent deposition, however, 3D island growth is observed due to strain relaxation mechanisms, as described in section 5.3. The increased defect density improves the oxygen in-diffusion and therefore leads to good superconducting properties. Still, this surface morphology prevents the growth of epitaxial heterostructures with high quality interfaces and hampers, therefore, the application in planar multilayer devices. Necessary control of the growth process, to obtain atomically smooth surfaces and interfaces, can possibly be achieved by deposition of sub-unit cell blocks of the $YBa_2Cu_3O_{7-\delta}$ compound.

In case of complex oxides usually charge neutral blocks of various atomic layers are deposited. An example is 'standard' PLD where the components are supplied simultaneously through stoichiometric transfer from target to substrate. The target consists of the correct phase and therefore the ratio of the different deposited constituents is ideal to grow the desired phase. Another method is block-by-block epitaxy, where the blocks are deposited sequentially and they will react afterwards to the desired compound. The sequence can be chosen such that the reaction between the blocks only leads to the desired phase and not to any stable intermediate phases. The deposition temperature has to be sufficiently high, since inter-diffusion is necessary to form the desired phase.

This method was used in molecular beam epitaxy (MBE) to grow $DyBa_2Cu_3O_{7-\delta}$ thin films on $SrTiO_3$ at 700 ºC in a mixture of atomic and molecular oxygen [53]. It was also applied in sequential PLD to grow $YBa_2Cu_3O_{7-\delta}$ thin films from separate oxide targets [54]. Two oxide pairs, YBa_2O_x/CuO and $Y_2Cu_2O_5$/$BaCuO_2$, were investigated at a growth temperature of 750 ºC. Formation of the desired phase was observed due to intermixing and reaction of the constituents of the two targets. The epitaxial nucleation of the $YBa_2Cu_3O_{7-\delta}$ phase was observed at the substrate interface due to grain-boundary diffusion of the second precursor component through the first precursor oxide layer. The initial nuclei acted as a template for subsequent epitaxial growth of the $YBa_2Cu_3O_{7-\delta}$ phase during deposition of the second precursor until the entire first oxide layer was consumed. Above the critical thickness, approximately 100 nm for the individual oxide layers, the intermixing was found to be insufficient for $YBa_2Cu_3O_{7-\delta}$ formation [55]. Both methods were used to grow good quality films, but still considerable surface roughening was observed.

To prevent or minimize this roughening an alternative deposition method has to be used, where $YBa_2Cu_3O_{7-\delta}$ is grown by sequential deposition of sub-unit cell layers, i.e., $BaCuO_x$ and $YCuO_x$. This method has been successfully applied for the

preparation of the $CuBa_2(Sr_xCa_{1-x})_nCu_{n-1}O_y$ compound, by fabrication of layered structures by sequential deposition of $BaCuO_x$ and $(Sr_xCa_{1-x})CuO_y$ [56,57].

5.5.1 Growth optimization of individual materials

The $YBa_2Cu_3O_{7-\delta}$ unit cell can be described as one $YCuO_x$ monolayer between two $BaCuO_x$ monolayers, see Figure 5.1a, which can be deposited by sequential ablation from a $BaCuO_2$ and an $Y_2Cu_2O_5$ target. Since no inter-diffusion is necessary between the sub-unit cell layers the growth temperature can be lower than for stoichiometric growth of YBCO, see section 5.1. The $BaCuO_x$ phase could only be stabilized when grown in at least a double unit cell layer [56] at temperatures up to 650 ºC [58], which also limits the growth temperature of the $YCuO_x$ layer.

The growth rate of the individual materials, i.e., $BaCuO_2$ and $Y_2Cu_2O_5$, was determined to ensure correct stoichiometry in the eventually deposited layer to stabilize the correct $YBa_2Cu_3O_{7-\delta}$ phase. The growth mode of the $BaCuO_2$ compound is layer-by-layer at 500 ºC, which makes it feasible to determine the growth rate by real-time monitoring of the RHEED intensity oscillations. In Figure 5.15a the RHEED intensity fluctuations are shown during $BaCuO_2$ growth at 500ºC in an oxygen pressure of 0.11 mbar with a laser energy density of 1.3 J/cm^2 at 5 Hz. Figure 5.15a shows the growth on a TiO_2-terminated $SrTiO_3$ substrate. The RHEED pattern, after growth of a 19 unit cells thick layer, shows still a clear 2-dimensional spot, see inset in Figure 5.15a, indicating formation of a smooth surface without island growth. This is confirmed by X-ray diffraction analysis, as shown in Figure 5.15b. The small angle θ-2θ scan exhibits clear Kiessig fringes [59], see inset in Figure 5.15b, which can only be observed for smooth surfaces. The calculated thickness

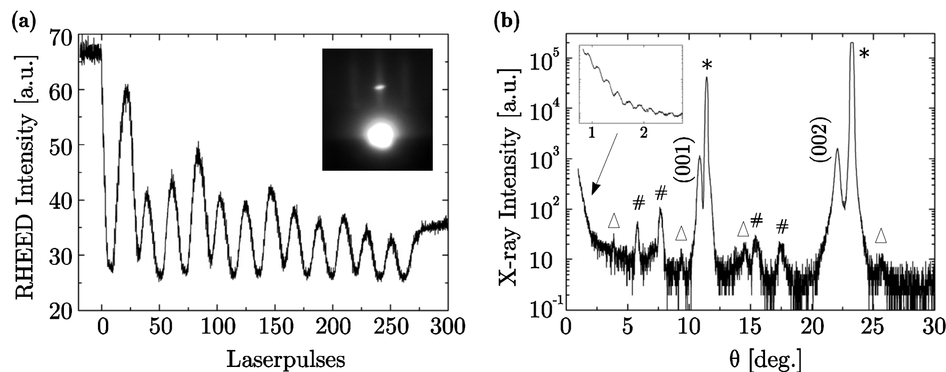

Figure 5.15 Epitaxial growth of $BaCuO_2$ on $SrTiO_3$. **(a)** RHEED intensity oscillations during growth with RHEED pattern after 19 unit cells in inset. **(b)** X-ray diffraction θ-2θ scan for a 37 unit cells thick $BaCuO_2$ layer. The $SrTiO_3$ substrate reflections are indicated with an asterisk and their spectral contributions (λ/2 and λ/3) with a cross. The triangles indicate the peak positions of an unidentified phase. The inset shows an enlarged small angle θ-2θ scan with clear Kiessig fringes.

from these fringes corresponds to the number of RHEED oscillations, when the growth unit is one unit cell. In the θ-2θ scan of a 37 unit cells thick $BaCuO_2$ layer the (001) and (002) peaks of the $BaCuO_2$ phase can clearly be distinguished, which indicates c-axis growth with a lattice parameter of ~4.10 Å. From numerous peak fitting it can be concluded that the $BaCuO_2$ layer is epitaxially grown cube-on-cube on the $SrTiO_3$ substrate with in-plane strained lattice parameters equal to the $SrTiO_3$ substrate.

A different procedure is used to determine the growth rate of the $YCuO_x$ phase, because it can only be stabilized between two $BaCuO_x$ sub-unit cell layers at the used deposition temperatures. To impose layer-by-layer growth, pulsed laser interval deposition [25] has to be applied, because this cannot be achieved by 'standard' PLD due to the formation of multilevel islands [58]. For this method the number of pulses, needed to complete one monolayer of the $YCuO_x$ phase, must be known. This can be obtained by real-time monitoring of the RHEED intensity during sequential deposition of $YCuO_x$ and $BaCuO_x$. Initially 4 unit cells of $BaCuO_2$ were grown on a TiO_2-terminated $SrTiO_3$ substrate before starting the sequential deposition. The same deposition conditions were used as for $BaCuO_2$. The RHEED intensity exhibits a sharp decrease when some amount of $YCuO_x$ is deposited at 50 Hz, see Figure 5.16a. When subsequently $BaCuO_x$ is deposited at 5 Hz, the RHEED intensity displays oscillations, which indicates the growth of individual unit cell layers. From this measurement the amount of $BaCuO_x$ can be determined, which is needed to stabilize one or two unit cell layers, indicated in Figure 5.16a by respectively a circle and a triangle. When next the $BaCuO_x$ growth is stopped in the fourth RHEED intensity maximum by deposition of some extra material, a smooth surface is again formed. This procedure can be repeated for different amounts of $YCuO_x$ material and will give the dependence of the $BaCuO_x$ maxima on the $YCuO_x$ growth, see

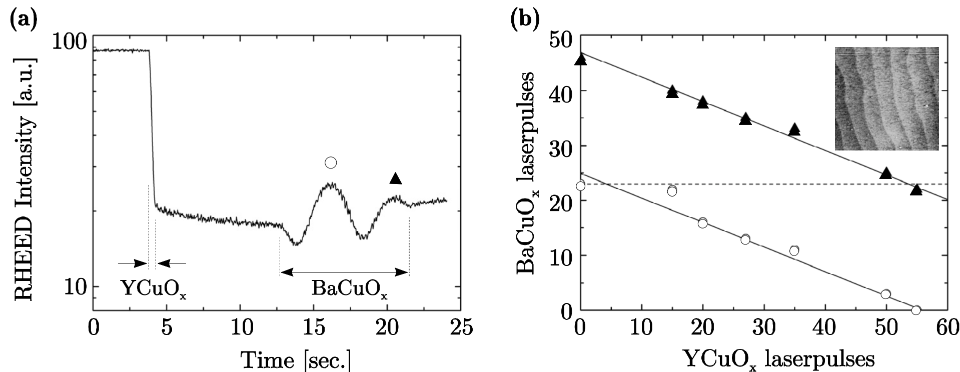

Figure 5.16 Sequential growth of $YCuO_x$ and $BaCuO_x$ on $SrTiO_3$. **(a)** RHEED intensity variations during $YCuO_x$ growth at 50 Hz and $BaCuO_x$ growth at 5 Hz. The stabilization of smooth unit cell layers is indicated by respectively a circle and a triangle. **(b)** Dependence of the $BaCuO_x$ maxima on the $YCuO_x$ growth. The inset shows an atomic force microscopy image (1.2×1.2 μm^2) of the final multilayer surface.

Figure 5.16b. From Figure 5.15a can be determined that 23 laserpulses are necessary to grow a single monolayer of $BaCuO_x$. When in the sequential deposition the amount of deposited $YCuO_x$ increases, the number of laserpulses to stabilize the first full monolayer by subsequential deposition of $BaCuO_x$ will decrease. For 55 laserpulses at 50 Hz a full monolayer of $YCuO_x$ is deposited and deposition of $BaCuO_x$ will only form the next unit cell layer without intermixing. In this way the $YCuO_x$ layer can be stabilized between several $BaCuO_x$ layers without the formation of islands. This is confirmed by atomic force microscopy of the final multilayer surface, which displays atomically smooth terraces with single unit cell steps, see inset in Figure 4.16b. During the determination of the growth rate of the $YCuO_x$ layer, a surplus of $BaCuO_x$ (4 unit cells) was deposited every time to facilitate the measurement procedure and the $YCuO_x$ stabilization.

5.5.2 Sequential deposition of sub-unit cell layers

To form the wanted $YBa_2Cu_3O_{7-\delta}$ phase, the correct amount of both sub-unit cell materials has to be deposited sequentially to grow fully closed individual monolayers. This was done at the same deposition conditions with 23 and 55 laserpulses for every monolayer of respectively $BaCuO_x$ and $YCuO_x$. The $BaCuO_2$ target was ablated at 5 Hz, while the laser frequency was increased to 50 Hz for ablation of the $Y_2Cu_2O_5$ target. The multilayer was grown on a TiO_2-terminated $SrTiO_3$ substrate and started with a $BaCuO_x$ doublelayer. Next a sequence of 55 pulses of $YCuO_x$ at 50 Hz and 46 pulses of $BaCuO_x$ at 5 Hz was repeated 17 times to form a 20 nm thick multilayer. After the deposition the multilayer was cooled to room temperature in the deposition pressure of 0.11 mbar of oxygen.

X-ray diffraction analysis of the multilayer displays features of the YBCO phase, as can be seen in the top θ-2θ scan in Figure 5.17a. However, the intensities of the (00l) peaks are very low and a strong (002) $BaCuO_2$ peak is also clearly visible. This indicates the presence of a large amount of $BaCuO_x$, which has not formed the YBCO phase. To improve the YBCO formation, the multilayer was post-annealed for 1 hour at 720 ºC and 1 hour at 450 ºC in 1 bar of oxygen pressure. This reduced the (002) $BaCuO_2$ peak significantly and increased the (00l) YBCO peaks, see middle θ-2θ scan in Figure 5.17a. The c-axis lattice parameter of the YBCO phase also decreased from ~11.91 Å to ~11.76 Å. A second post-anneal treatment for 2 hours at 600 ºC and 12 hours at 450 ºC in 1 bar of oxygen pressure even fully removed the (002) $BaCuO_2$ peak, while the intensity and position of the (005) YBCO peak were unchanged, see bottom θ-2θ scan in Figure 5.17a. An increase in the amount of $YCuO_x$ to 65 pulses for every layer showed similar behavior, see θ-2θ scans in Figure 5.17b.

These observations lead to the conclusion that a deposition temperature of 500 ºC is too low to form the YBCO phase during deposition of the individual sub-unit cell layers. Extra anneal treatments are an improvement, however, the YBCO layers

are still oxygen deficient and semiconducting, which could already be concluded from their enlarged c-axis of ~11.76 Å. An additional effect of these ex-situ anneal treatments is an increased surface roughening.

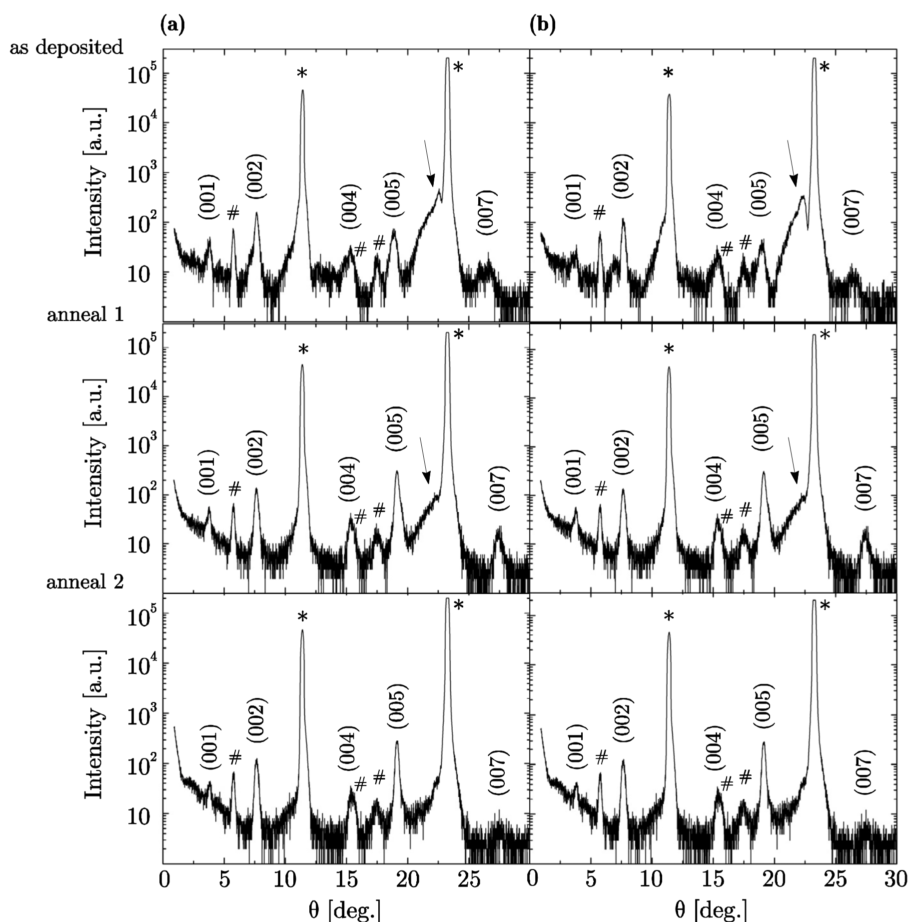

Figure 5.17 X-ray diffraction θ-2θ scans of $BaCuO_x/YCuO_x$ multilayers on $SrTiO_3$ substrates with 46 laserpulses for every $BaCuO_x$ layer and 55 **(a)** or 65 **(b)** laserpulses for every $YCuO_x$ layer. From top to bottom are θ-2θ scans of the multilayers after respectively the deposition (top), the first anneal treatment for 1 hour at 720 °C and 1 hour at 450 °C in 1 bar of oxygen pressure (middle) and the second anneal treatment for 2 hours at 600 °C and 12 hours at 450 °C in 1 bar of oxygen pressure (bottom). The arrows indicate the positions of the (002) $BaCuO_2$ peaks. The $SrTiO_3$ substrate reflections are indicated with an asterisk and their spectral contributions (λ/2 and λ/3) with a cross.

5.5.3 Sub-unit cell interval deposition

When the deposition temperature is increased to 600 °C, the growth mode of $BaCuO_2$ is no longer layer-by-layer and 'standard' PLD has to be replaced by pulsed laser interval deposition. The growth of a $BaCuO_x$ stack, consisting of two unit cell layers, by interval deposition at 50 Hz was optimized by observation of the RHEED intensity and the full width at half maximum of the RHEED peak while making small variations in the number of laserpulses. The RHEED intensity exhibits a sharp drop at the start of the deposition and recovers to a constant level after a couple of seconds, due to surface diffusion of the deposited material. The intensity after recovery will be maximal when the number of laserpulses is precisely chosen for the deposition of one $BaCuO_x$ doublelayer. The surface will then contain the lowest possible roughness.

Multilayer fabrication by pulsed laser interval deposition was applied by sequential ablation at 50 Hz to grow either a doublelayer of $BaCuO_x$ or a monolayer of $YCuO_x$, see Figure 5.18a. After every deposition an annealing period was added to improve the surface morphology by surface diffusion. The recovered RHEED

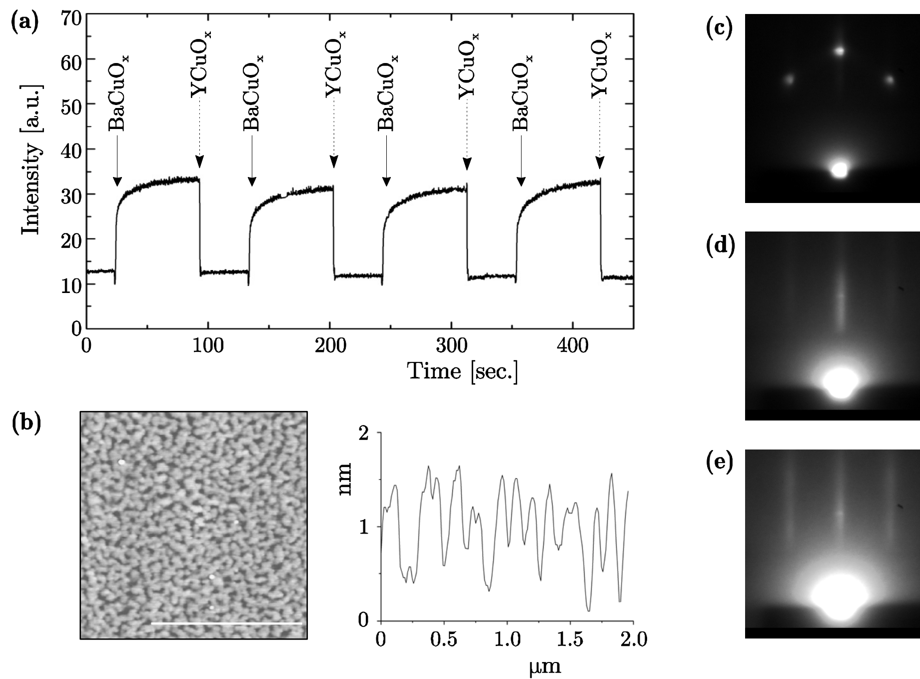

Figure 5.18 Multilayer growth of $BaCuO_x$ doublelayers and $YCuO_x$ monolayers on a TiO_2-terminated $SrTiO_3$ substrate. **(a)** RHEED intensity variations during pulsed laser interval depositions. **(b)** Atomic force microscopy image with roughness analysis of a 50 nm thick $BaCuO_x/YCuO_x$ multilayer. **(c)** RHEED pattern of the TiO_2-terminated $SrTiO_3$ substrate. **(d,e)** RHEED patterns of the multilayer after respectively 15 and 40 $BaCuO_x/YCuO_x$ sequences.

intensity after every $BaCuO_x$ doublelayer stayed constant, which was suggestive of a constant surface roughness. RHEED patterns confirmed the low surface roughness, see Figures 5.18c, d and e, and show respectively the transition of the 2-dimensional spot of the TiO_2-terminated $SrTiO_3$ substrate into streaks after 15 $BaCuO_x/YCuO_x$ sequences and finally 40 sequences. The total deposition was started and finished by a $BaCuO_x$ doublelayer. After the deposition the temperature was increased to 800 ºC, to approach the decomposition line [60], which would enhance the YBCO formation. Next the oxygen pressure was increased to 1 bar and the multilayer was cooled down to 450 ºC, where it stabilized in the correct $YBa_2Cu_3O_{7-\delta}$ phase in an hour. Subsequently the multilayer was cooled down to room temperature in the same oxygen pressure. Figure 5.18b shows an atomic force microscopy image of the multilayer with 40 $BaCuO_x/YCuO_x$ sequences featuring a total thickness of ~ 50 nm. The surface exhibits multilevel step heights with a maximum peak-to-peak surface roughness of about ~1 nm.

The multilayer was analyzed by high-resolution X-ray diffraction[III] to investigate the YBCO formation by pulsed laser interval deposition. The θ-2θ scan shows high intensity (00l) YBCO peaks indicating c-axis growth with a lattice parameter of ~11.78 Å, see Figure 5.19a. This enlarged c-axis indicates the presence of the oxygen deficient, semiconducting $YBa_2Cu_3O_{6.3}$ phase [7]. The sharpness of the reflection peaks, however, indicates a good quality internal structure. The reflectivity measurement in the small angle θ-2θ scan displays numerous Kiessig fringes, see Figure 5.19b. A fit could be applied to the fringes when the 40 unit cells with a

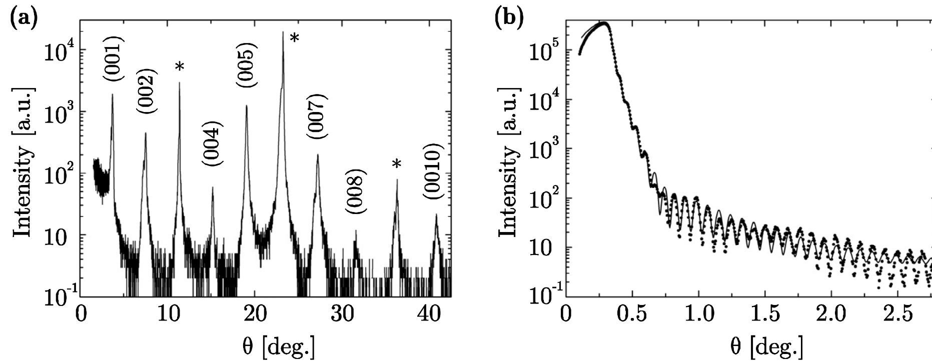

Figure 5.19 High-resolution X-ray diffraction analysis of a 50 nm thick $BaCuO_x/YCuO_x$ multilayer displaying (00l) YBCO reflections in the θ-2θ scan **(a)** and Kiessig fringes in the small angle θ-2θ scan **(b)**. The $SrTiO_3$ substrate reflections are indicated with an asterisk.

III High-resolution x-ray diffraction analysis was performed at Dannalab, MESA+ Institute, Twente University, the Netherlands.

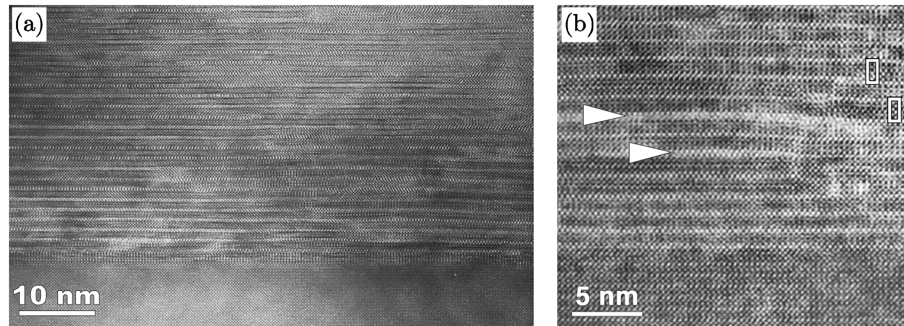

Figure 5.20 High-resolution electron microscopy images of an YBCO layer grown on TiO_2-terminated $SrTiO_3$ **(a)** and GaO_2-terminated $NdGaO_3$ **(b)** by sub-unit cell interval deposition. Extra $BaCuO_x$ and $YCuO_x$ blocks are marked by arrowheads, whereas white rectangles indicate $YBa_2Cu_4O_x$ defects.

measured c-axis length of ~11.78 Å was taken into account as well as an extra toplayer of 2 unit cells of $BaCuO_2$.

The good quality internal structure of the YBCO film was confirmed by high-resolution electron microscopy (HREM) analysis[IV]. The 40 unit cells thick YBCO layer grown on TiO_2-terminated $SrTiO_3$ exhibits good epitaxial properties between film and substrate: $(001)_{YBCO}$ is parallel to $(001)_{STO}$ and $(100)_{YBCO}$ is parallel to $(100)_{STO}$, see Figure 5.20a. In case of YBCO growth by sub-unit cell interval deposition on GaO_2-terminated $NdGaO_3$, which single terminated surface was prepared as described in ref. 61[V], the a- and b-directions of the film are rotated in-plane over 45° with respect to those of the substrate: $(001)_{YBCO}$ is parallel to $(001)_{NGO}$ and $(100)_{YBCO}$ is parallel to $(110)_{NGO}$, see Figure 5.20b. Structural defects are sometimes observed. In Figure 5.20b extra $BaCuO_x$ and $YCuO_x$ blocks inserted in the matrix are marked by arrowheads, whereas white rectangles indicate local $YBa_2Cu_4O_x$ defects, which have an extra CuO plane inserted [62,63]. The fact that antiphase boundaries are only occasionally observed, suggests a single type of interface configuration. The first deposited material on the substrate surface is a $BaCuO_x$ doublelayer, which implies an interface stacking sequence of Y133, see section 5.2. From Figures 5.20a and b can also be concluded that YBCO films grown by sub-unit cell interval deposition are oriented on the crystallographic surface of

[IV] HREM analysis was performed at EMAT, University of Antwerp, Belgium.

[V] The surface of a (001) $NdGaO_3$ substrate was GaO_2-terminated by combining a 10 min. water and 2 min. HF-acid (20 ml buffered HF (12.5 vol% HF + 87.5 vol% NH_4F), 3 ml NH_4OH and 110 ml demineralized water: final pH-level is 4.0) treatment in an ultrasonic bath with a 2 hour annealing procedure at 1000 °C in a flow of normal air.

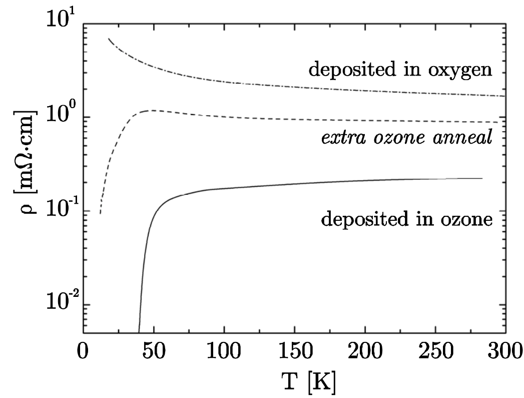

Figure 5.21 Temperature dependence of the resistivity of a 50 nm thick YBCO layer grown on TiO_2-terminated $SrTiO_3$ after sub-unit cell interval deposition (dash-dotted line) and after an extra ex-situ anneal treatment at 550 °C in an O_2/O_3 mixture with 10% ozone for 10 min. followed by 30 min. at 450 °C (dashed line). A 50 nm thick YBCO layer grown by sub-unit cell interval deposition in an O_2/O_3 environment with 10% ozone in combination with an in-situ anneal treatment at 450 °C for 30 min. (solid line).

the substrates and not at the optical surface as reported for YBCO films by 'standard' PLD [39-41].

The obtained YBCO films are oxygen deficient, which is already clear from the enlarged c-axis of ~11.78 Å in the X-ray diffraction analysis. The temperature dependence of the resistivity of this semiconducting YBCO film is given by the dash-dotted line in Figure 5.21. This fits with all analyis data of the sub-unit cell interval deposited YBCO layer and leads to the conclusion that for these deposition conditions a high quality YBCO film can be grown with low surface roughness, but still, due to poor oxygen indiffusion, the superconducting properties are absent or very low. The poor oxygen incorporation can be attributed to the low amount of defects in the YBCO layer, as described in section 5.2.

Improvement of the oxidation of YBCO films can be achieved by ozone, as was already shown previously [64-66]. An extra anneal treatment at 550 °C in an O_2/O_3 mixture with 10% ozone for 10 min. followed by 30 min. at 450 °C increased the oxygen indiffusion and lowered the normal state resistance, see dashed line in Figure 5.21. An onset to superconductivity can be observed at a transition temperature of 50 K, but no T_c(R=0). Using ozone during deposition can even further enhance the oxygen indiffusion. Therefore, an YBCO layer was fabricated by sub-unit cell interval deposition in an O_2/O_3 environment with 10% ozone in combination with an anneal treatment at 450 °C for 30 min. after deposition. This YBCO film shows a significant improvement in the oxygen level and exhibits a further decrease in the normal state resistance together with a clear superconducting transition temperature T_c(R=0) of 40 K, see solid line in Figure 5.21. However, the utilization of ozone also

increases the surface roughness considerably and is therefore no option for the fabrication of atomically smooth superconducting YBCO films.

These results on the growth of YBCO by a new deposition technique, in which the crystal structure is formed by sequential deposition of sub-unit cell layers, show to contain some possibilities for correct crystal formation. Still, further investigations are necessary to improve this technique for applications in the future.

5.6 Conclusions

In thin films of $YBa_2Cu_3O_{7-\delta}$ the structural properties, i.e., defect and crystalline structure and surface morphology, influence their electrical properties. The applicability of these superconducting cuprates in heteroepitaxial structures is, therefore, hampered. The structural properties and surface morphology are a direct result of thin film growth, influenced by deposition conditions and substrate properties. The atomic stacking sequence at the substrate–film interface plays an essential role in the heteroepitaxial growth of $YBa_2Cu_3O_{7-\delta}$. During initial growth, the interface configuration influences the surface morphology and structural properties of the film, due to the formation of anti-phase boundaries by coalescence of islands with different stacking sequences. The interface configuration can be accurately controlled by both the terminating atomic layer of the $SrTiO_3$ substrate and the stoichiometry of the first unit cell layer. Using this capability the network of anti-phase boundaries and, therefore, the in-plane ordering is tuned, allowing the study of its influence on the structural and electrical properties of the $YBa_2Cu_3O_{7-\delta}$ film. The superconducting transition temperature was found to be depressed by improvement of the in-plane ordering, which strongly indicates that the absence of anti-phase boundaries hampers the oxygen in-diffusion.

In the heteroepitaxial growth of $YBa_2Cu_3O_{7-\delta}$ on $SrTiO_3$ the first deposited atomic layers are strained to match the substrate, due to the small lattice mismatch. However, above a critical thickness for this strained pseudomorphic layer the strain will relax by the introduction of defects. The initial defect density, which is already present at the substrate-film interface, will determine the value for this critical thickness during subsequent growth, because the process of strain relaxation is improved by the number of antiphase boundaries.

The engineering of the interface between $YBa_2Cu_3O_{7-\delta}$ and $SrTiO_3$ can be analyzed in-situ during growth by reflection high-energy electron diffraction and surface X-ray diffraction.

Sub-unit cell layer epitaxy is investigated as a novel growth technique for the artificial growth of perovskite structures. By this technique new crystals can be formed by sequentially depositing its sub-unit cell layers. Initial results demonstrate the fabrication of crystalline films with low roughness surfaces, while further investigations are necessary to improve the superconducting transition temperature.

5.7 References

1. Cava, R.J., Van Dover, R.B., Batlogg, B. & Rietman, E.A., *Phys. Rev. Lett.* **58**, 408 (1987).
2. Chu, C.W., Hor., P.H., Meng, R.L., Gao, L., Huang, Z.J. & Wang, Y.Q., *Phys. Rev. Lett.* **58**, 405 (1987).
3. Chu, C.W., Hor., P.H., Meng, R.L., Gao, L., Huang, Z.J. & Wang, Y.Q., *Science* **235***, 567* (1987).
4. Wu, M.K., Ashburn, J.R., Torng, C.J., Hor, P.H., Meng, R.L., Gao, L., Huang, Z.J., Wang, Y.Q. & Chu, C.W., *Phys. Rev. Lett.* **58**, 908 (1987).
5. Cava, R.J., Batlogg, B., Van Dover, R.B., Murphy, D.W., Sunshine, S., Siegrist, T., Remeika, J.P., Rietman, E.A., Zahurak, S. & Espinosa, G.P., *Phys. Rev. Lett.* **58**, 1676 (1987).
6. Jorgensen, J.D., Beno, M.A., Hinks, D.G., Soderholm, L., Volin, K.J., Hitterman, R.L., Grace, J.D., Schuller, I.K., Segre, C.U., Zhang, K. & Kleefisch, M.S., *Phys. Rev. B* **36**, 3608 (1987).
7. Jorgensen, J.D., Veal, B.W., Paulikas, A.P., Nowicki, L.J., Crabtree, G.W., Claus, H. & Kwok, W.K., *Phys. Rev. B* **41**, 1863 (1990).
8. Poulsen, H.F., Andersen, N.H., Andersen, J.V., Bohr, H. & Mouritsen, O.G., *Nature* **349**, 594 (1991).
9. Rossat-Mignod, J., Regnault, L.P., Vettier, C., Burlet, P., Henry, J.Y. & Lapertot, G., *Physica B* **58-65**, 169 (1991).
10. Rijnders, A.J.H.M., *The initial growth of complex oxides: study and manipulation*, Chapter 5, PhD thesis, University of Twente, The Netherlands (2001).
11. Terashima, T., Bando, Y., Iijima, K., Yamamoto, K., Hirata, K., Hayashi, K., Kamigaki, K. & Terauchi, H., *Phys. Rev. Lett.* **65**, 2684 (1990).
12. Karl, H. & Stritzker, B., *Phys. Rev. Lett.* **69**, 2939 (1992).
13. Phillips, J.M., *J. Appl. Phys.* **79**, 1829 (1996).
14. Hylton, T.L. & Beasley, M.R., *Phys. Rev. B* **41**, 11669 (1990).
15. McElfresh, M., Miller, T.G., Schaefer, D.M., Reifenberger, R., Muenchausen, R.E., Hawley, M., Foltyn, S.R. & Wu, X.D., *J. Appl. Phys.* **71**, 5099 (1992).
16. Haage, T., Zegenhagen, J., Li, J.Q., Habermeier, H.-U., Cardona, M., Jooss, Ch., Warthman, R., Forkl, A. & Kronmüller, H., *Phys. Rev. B* **56**, 8404 (1997).
17. Dam, B., Huijbrechtse, J.M., Klaassen, F.C, Van der Geest, R.C.F., Doornbos, G., Rector, J.H., Testa, A.M., Freisem, S., Martinez, J.C., Stäuble-Pümpin, B. & Griessen, R., *Nature* **399**, 439 (1999).
18. Bals, S., Rijnders, G., Blank, D.H.A. & Van Tendeloo, G., *Physica C* **355**, 225 (2001).
19. Wen, J.G., Træholt, C. & Zandbergen, H.W., *Physica C* **205**, 354 (1993).
20. Dam, B., Træholt, C., Stäuble-Pümpin, B., Rector, J. & De Groot, D.G., *J. Alloys Compd.* **251**, 27 (1997).

21. Koster, G., Kropman, B.L., Rijnders, G.J.H.M., Blank, D.H.A. & Rogalla, H., *Appl. Phys. Lett.* **73**, 2920 (1998).
22. Zegenhagen, J., Siegrist, T., Fontes, E., Berman, L.E. & Patel, J.R., *Solid State Comm.* **93**, 763 (1995).
23. Huijbregtse, J.M., Rector, J.H. & Dam, B., *Physica C* **351**, 183 (2001).
24. Zheng, X.-Y., Lowndes, D.H., Zhu, S., Budai, J.D. & Warmack, R.J., *Phys. Rev. B* **45**, 7584 (1992).
25. Koster, G., Rijnders, G.J.H.M., Blank, D.H.A. & Rogalla, H., *Appl. Phys. Lett.* **74**, 3729 (1999).
26. Kaganer, V.M., Köhler, R., Schmidbauer, M., Opitz, R. & Jenichen, B., *Phys. Rev. B* **55**, 1793 (1997).
27. Dam, B., Huijbregtse, J.M. & Rector, J.H., *Phys. Rev. B* **65**, 064528 (2002).
28. Miceli, P.F. & Palstrøm, C.J., *Phys. Rev. B* **51**, 5506 (1995).
29. Bals, S., *Optimisation of superconducting thin films and tapes by transmission electron microscopy*, Chapter 4, PhD thesis, University of Antwerp, Belgium (2003).
30. Bals, S., Van Tendeloo, G., Rijnders, G., Huijben, M., Leca, V. & Blank, D.H.A., *IEEE Trans. Appl. Supercond.* **13**, 2834 (2003).
31. Kursumovic, A., Berghuis, P., Dediu, V., Evetts, J.E., Matacotta, F.C. & Wagner, G.A., *Physica C* **331**, 185 (2000).
32. Tu, K.N., Yeh, N.C., Park, S.I. & Tsuei, C.C., *Phys. Rev. B* **39**, 304 (1989).
33. Rothman, S.J., Routbort, J.L., Welp, U. & Baker, J.E., *Phys. Rev. B* **44**, 2326 (1991).
34. Rijnders, G., Curras, S., Huijben, M., Blank, D.H.A. & Rogalla, H., *Appl. Phys. Lett.* **84**, 1150 (2004).
35. Gau, T.-S., Chang, S.-L., Hung, H.-H., Lee, C.-H., Huang, T.-W., Lu, H.-B., Yang, S.-J. & Hsu, S.-E., *Appl. Phys. Lett.* **65**, 1720 (1994).
36. Frey, T., Chi, C.C., Tsuei, C.C., Shaw, T. & Bozso, F., *Phys. Rev. B* **49**, 3483 (1994).
37. Abert, A., Contour, J.P., Défossez, A., Ravelosona, D., Schwegle, W. & Ziemann, P., *Appl. Surf. Science* **96**, 703 (1996).
38. Cao, L.X., Zegenhagen, J., Sozontov, E. & Cardona, M., *Physica C* **337**, 24 (2000).
39. Dekkers, J.M., Rijnders, G., Harkema, S., Smilde, H.J.H., Hilgenkamp, H., Rogalla, H. & Blank, D.H.A., *Appl. Phys. Lett.* **83**, 5199 (2003).
40. Maurice, J.-L., Durand, O., Drouet, M. & Contour, J.-P., *Thin Solid Films* **319**, 211 (1998).
41. Méchin, L., Berghuis, P. & Evetts, J.E., *Physica C* **302**, 102 (1998).
42. Vonk, V., Van Reeuwijk, S.J., Dekkers, J.M., Harkema, S., Rijnders, A.J.H.M. & Graafsma, H., *Thin Solid Films* **449**, 133 (2004).
43. Zhai, H.Y. & Chu, W.K., *Appl. Phys. Lett.* **76**, 3469 (2000).
44. Varela, M., Grogger, W., Arias, D., Sefrioui, Z., Léon, C., Vazquez, L., Ballesteros, C., Krishnan, K.M. & Santamaria, J., *Phys. Rev. B* **66**, 174514 (2002).
45. Pedarnig, J.D., Rössler, R., Delamare, M.P., Lang, W., Bäuerle, D., Köhler, A. & Zandbergen, H.W., *Appl. Phys. Lett.* **81**, 2587 (2002).

46. Eres, G., Tischler, J., Yoon, M., Larson, B., Rouleau, C., Lowndes, D. & Zschack, P., *Appl. Phys. Lett.* **80**, 3379 (2002).
47. Fleet, A., Dale, D., Suzuki, Y. & Brock, J.D., *Phys. Rev. Lett.* **94**, 036102 (2002).
48. Wang, H.-H., Fleet, A., Brock, J.D., Dale, D. & Suzuki, Y., *J. Appl. Phys.* **96**, 5324 (2004).
49. Vonk, V., Konings, S., Barthe, L., Gorges, B. & Graafsma, H., *J. Synchr. Rad.* **12**, 833 (2005).
50. Borsboom, M., Bras, W., Cerjak, I., Detollenaere, D., Van Loon, D.G., Goedtkindt, P., Konijnenberg, M., Lassing, P., Levine, Y.K., Munneke, B., Oversluizen, M., Van Tol, R. & Vlieg, E., *J. Synchr. Rad.* **5**, 518 (1998).
51. Specht, E.D., Sparks, C.J., Dhere, A.G., Brynestad, J., Cavin, O.B., Kroeger, D.M. & Oye, H.A., *Phys. Rev. B* **37**, 7426 (1988).
52. Vonk, V., *Growth and structure of complex oxide thin films*, PhD thesis, University of Twente, The Netherlands (2006).
53. Locquet, J.-P., Catana, A., Mächler, E., Gerber, Ch. & Bednorz, J.G., *Appl. Phys. Lett.* **64**, 372 (1994).
54. Hussey, B.W. & Gupta, A., *J. Appl. Phys.* **72**, 287 (1992).
55. Hussey, B.W., Gupta, A. & Olsson, E., *J. Appl. Phys.* **76**, 2807 (1994).
56. Aruta, C., Balestrino, G., Martellucci, S., Paletti, A. & Petrocelli, G., *J. Appl. Phys.* **81**, 220 (1997).
57. Koster, G., Verbist, K., Rijnders, G., Rogalla, H., Van Tendeloo, G. & Blank, D.H.A., *Physica C* **353**, 167 (2001).
58. Rijnders, A.J.H.M., *The initial growth of complex oxides: study and manipulation*, Chapter 6, PhD thesis, University of Twente, The Netherlands (2001).
59. Kiessig, H., *Ann. Phys.* **10**, 769 (1931).
60. Hammond, R.H. & Bormann, R., *Physica C* **162-164**, 703 (1989).
61. Leca, V., *Heteroepitaxial growth of copper oxide superconductors by pulsed laser deposition*, Chapter 4, PhD thesis, University of Twente, The Netherlands (2003).
62. Hewat, A.W., Fischer, P., Kaldis, E., Hewat, E.A., Jilek, E., Karpinski, J. & Rusiecki, S., *J. Less-Common Metals* **164-165**, 39 (1990).
63. Xin, Y., Zhou, W. & Humphreys, C.J., *Physica C* **249**, 319 (1995).
64. Berkley, D.D., Johnson, B.R., Anand, N., Beauchamp, K.M., Conroy, L.E., Goldman, A.M., Maps, J., Mauersberger, K., Mecartney, M.L., Morton, J., Tuominen, M. & Zhang, Y.-J., *Appl. Phys. Lett.* **53**, 1973 (1988).
65. Zhu, Y., Sabatini, R.L., Wang, Y.L. & Suenaga, M., *J. Appl. Phys.* **73**, 3407 (1993).
66. Gibbons, B.J., Eom, C.B., Rao, R.A., Trolier-McKinstry, S. & Schlom, D.G., *J. Mater. Res.* **17**, 884 (2002).

Chapter 6

Atomically controlled interfaces in $LaAlO_3/SrTiO_3$ multilayers

Abstract

Perovskite oxides exhibit a range of exceptional electronic properties, providing the basis for novel concepts of oxide-electronic devices. The interest in these materials is even extended by the remarkable characteristics of their interfaces. For the two wide-bandgap insulators $LaAlO_3$ and $SrTiO_3$, the interfaces have been found to be either high-mobility conducting or insulating, depending on the atomic stacking sequences. Single interfaces, superlattices and multilayers were grown with a control on the atomic scale, which was proven by various analysis techniques.

6.1 Introduction

Interface and surface physics have become an ever more important sub-discipline within the physics of condensed matter in recent decades. This is mainly caused by the advanced miniaturization in nanotechnology, which increased the interest for interface and surface phenomena and required a better understanding on the atomic scale.

In bulk solid-state physics the macroscopic properties, of the large number of atoms involved, are described on the assumption of an infinitely extended solid. This neglects the properties of the relatively small number of atoms forming the surface of the macroscopic solid. A solid interface can be defined as the few atomic layers that separate two solids in contact with one another, where the properties differ significantly from those of the bulk material it separates. The approach of the

classical solid-state physics becomes incorrect for thin film technology, where a thin solid film is bounded by a solid-solid interface and by its film-vacuum interface (surface). The properties of such a thin film are very dependent on the properties of its two interfaces.

At the interface the bulk electronic system is altered, due to many reasons, and sometimes with dramatic consequences. Interfaces break the translational symmetry of the bulk, but also induce strain, which changes the distances between the ions. This can lead to structural or electronic reconstruction of the lattice. At the interface point defects, dislocations and stacking faults tend to be incorporated into the lattice, which have their own electronic or magnetic properties and may act as scattering centers. The eventual effect of these interface phenomena depend in magnitude on the microscopic properties [1].

There is not only a change of the correlations at the interfaces, but due to charge transfer, the state occupancy also varies. Due to ionic imbalances, most interfaces modify the electronic potential and thereby produce space charge layers, altering locally the density of mobile charge carriers. This effect is well known from semiconductor heterostructures, which are called two dimensional electron/hole systems dependent on the type of charge carriers [2-6]. Well-known examples are two-dimensional electron- [7,8] and hole [9-11] gasses with very high carrier mobilities in GaAs/AlGaAs heterostructures.

Recently interface conductivity was observed in $LaAlO_3$-$SrTiO_3$ multilayers, where mobile electrons were present at the interface [12], similar to two-dimensional electron gasses in semiconductors. This phenomenon at the interface between two band insulators provides an extension of the exceptional electronic properties in complex oxides and can possibly be integrated with different functional oxides for novel concepts of oxide-electronic devices [13,14].

In this chapter the fabrication will be described of high-quality $LaAlO_3$-$SrTiO_3$ multilayers with atomically controlled interfaces. The growth procedure of single interfaces, superlattices and heterostructures will be specified as well as the characterization of their structural properties.

6.2 Atomic structure at $LaAlO_3$ / $SrTiO_3$ interfaces

The investigated materials, $LaAlO_3$ and $SrTiO_3$, belong to the perovskite structural family. This originates from the mineral Perovskite ($CaTiO_3$), which is named for a Russian mineralogist, Count Lev Aleksevich von Perovski. The mineral was discovered and named by Gustav Rose in 1839 from samples found in the Ural Mountains. Historically however, Perovskite would have remained a mineralogical curiosity were it not for Goldschmidt and his school of geochemists in Oslo, who made and studied a large number of the first synthetic perovskites with different compositions in 1924-26. The interest in perovskite materials increased drastically

during and after the Second World War, when the newly obtained dielectric and ferroelectric properties opened up an enormous amount of useful applications. This was even extended by the observation of superconductivity in reduced strontium titanate in 1964-65 [15,16] and in niobium-doped strontium titanate in 1980 [17]. Still, the big breakthrough for perovskites occurred in 1986-87, when high-temperature superconductivity was discovered in this type of crystal structures [18-20]. Since then, many groups have expanded investigations on all types of perovskites with varying compositions and as a result they are now applied extensively in electronic devices in common daily life.

The interest in the specific perovskite compounds, $LaAlO_3$ and $SrTiO_3$, was also increased after the discovery of high-T_c superconductivity, because they were soon identified as ideal single crystalline substrates for epitaxial growth of superconducting thin films [21,22]. Although very high critical currents could be obtained in superconducting films on $SrTiO_3$ substrates, its large dielectric constant [23] hampered high frequency applications. For this, $LaAlO_3$ substrates were used with a much lower dielectric constant [24]. Extensive research has also been performed on $LaAlO_3$ and $SrTiO_3$ as alternative dielectrics to silicon dioxide for memory and logic devices [25].

6.2.1 Layering sequence in perovskite structures

The $SrTiO_3$ compound consists at room temperature of a simple cubic structure, which is used to typify perovskite crystal structures. The lattice parameters are 3.905 Å with the Ti atoms located at the corners and the Sr atoms at the center of the cube [26,27], see Figure 6.1a. The oxygen atoms are placed at the centers of the twelve cube edges, giving corner-shared strings of TiO_6 octahedra, which extend infinitely in three dimensions. The TiO_6 octahedra are perfect with 90° angles and six equal Ti-O bonds at 1.952 Å. Each Sr atom is surrounded by twelve equidistant oxygen atoms at 2.760 Å. The $SrTiO_3$ compound undergoes a second-order phase transition from cubic (spacegroup $Pm\overline{3}\,m$) to tetragonal (spacegroup $I4/mcm$) at a temperature of ~110 K, due to rotation of neighbouring TiO_6 octahedra in opposite directions [28-31]. In the ionic limit this material can be described as $Sr^{2+}Ti^{4+}O^{2-}{}_3$.

On the other hand, the $LaAlO_3$ compound consists at room temperature of a rhombohedrally distorted perovskite structure (spacegroup $R\overline{3}\,c$), which undergoes a transition to the ideal cubic perovskite structure (spacegroup $Pm\overline{3}\,m$) at ~813 K [32,33]. The rhombohedral low temperature structure can be described as a perovskite structure with an antiphase rotation of the AlO_6 octahedra. This can be observed in diffraction analysis from a subtle splitting of the main peaks, attributed to a distortion from the cubic structure. However, this splitting is very small and can only be observed in high-resolution experiments. There have been many investigations of this phase transition [30,34-38] including recent ones using neutron powder methods to examine the thermal evolution of the structure [39-41] The

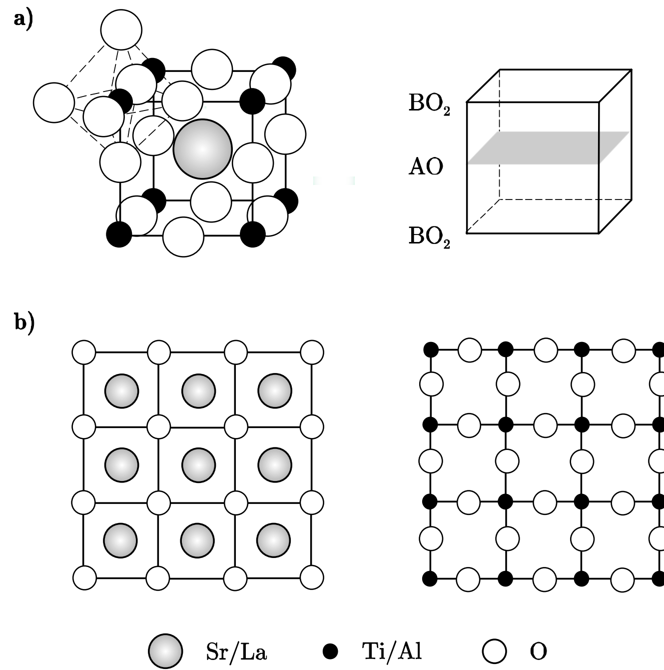

Figure 6.1 Schematic view of the $SrTiO_3$ (and $LaAlO_3$) unit cell. **(a)** The ABO_3 perovskite structure and it's layering sequence in the (001)-direction. **(b)** Individual sub-unit layers of SrO & LaO (AO: left) and TiO_2 & AlO_2 (BO_2: right). The schematic images are taken from ref. 42.

rhombohedral structure at room temperature can be described as a psuedocubic with lattice parameters of 3.791 Å with Al atoms located at the corners and the La atoms at the center of the cube [41], see Figure 6.1a. This compound can be described in the ionic limit as $La^{3+}Al^{3+}O^{2-}{}_3$.

Perovskite oxides are commonly described in terms of their cubic unit cells, with the generic formula ABO_3. It is also very instructive to describe the perovskites in terms of their constituting AO and BO_2 layering sequence in the three principal directions, see Figure 6.1b. For example, whereas $SrTiO_3$ and $LaAlO_3$ are seemingly similar, the $Sr^{2+}O^{2-}$ and $Ti^{4+}O^{2-}{}_2$ layers are charge-neutral, while in the ionic limit the charge states in the $LaAlO_3$ are positive for $La^{3+}O^{2-}$ and negative for $Al^{3+}O^{2-}{}_2$.

6.2.2 Polar-non polar interfaces

Polarity discontinuities at the interfaces between different crystalline materials can lead to nontrivial local atomic and electronic structures, owing to the presence of dangling bonds and incomplete atomic coordinations [43]. In semiconductors the growth of polar materials on non-polar substrates (like GaAs on Si or Ge) results in a roughening, unless the composition is graded at the interface to ensure there is no

net interface charge [44-46]. This grading results in a microscopically rough interface and in many cases also in a measurable electrical band offset.

In perovskite heterostructures the AO-BO_2 stacking sequence is maintained, and consequently a polarity discontinuity arises at the $LaAlO_3$-$SrTiO_3$ interface. Unlike conventional semiconductors where each ion has a fixed valence, in complex oxides compositional roughening is not the only option for charge rearrangement, but mixed valence charge compensation can also occur if electrons can be redistributed al lower energy cost than redistributing ions. This results in the net transfer of electrons per two-dimensional unit cell from $LaAlO_3$ to $SrTiO_3$ across the interface, see Figure 6.2a. The extra electrons at the LaO:TiO_2 interface were confirmed by metallic conductivity and Hall measurements by Ohtomo and Hwang [12]. The induced interface charges at this 'n-type' interface are compensated by electronic reconstruction through mixed-valence Ti states (Ti^{4+} to Ti^{3+}) that place extra electrons in the $SrTiO_3$ conduction band. The analogous construction of the AlO_2:SrO interface is shown in Figure 6.2b where the SrO layer must now acquire extra holes per two-dimensional unit cell to maintain charge neutrality. This interface is formally called 'p-type'. Electrically, however, this interface was insulating [12]. As this p-charging is still conceivable and there are no available mixed valence states to compensate the holes, an atomic reconstruction is required and will most likely be formed by the introduction of oxygen vacancies.

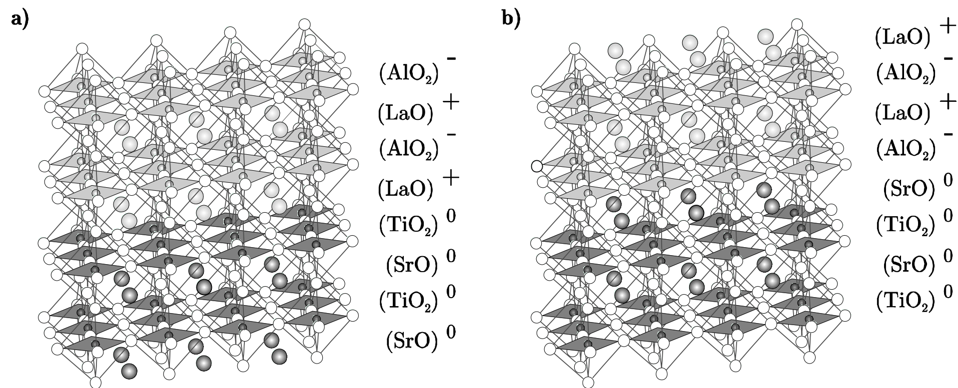

Figure 6.2 Schematic models of the two possible interfaces between $SrTiO_3$ and $LaAlO_3$ in the (001)-direction. The resulting $(LaO)^+/(TiO2)^0$ **(a)** and $(AlO2)^-/(SrO)^0$ interfaces **(b)**, showing the composition and the ionic charge state of each layer. The schematic models are taken from ref. 12.

6.2.3 Surface termination control for thin film growth

Interfaces between $SrTiO_3$ and $LaAlO_3$ can only be fabricated with a control on the atomic scale, when the surface of the initial substrate is already atomically smooth. However, a perovskite substrate surface, obtained by cleaving or cutting, consists of an equal amount of AO- and BO_2-terminated domains separated by half unit-cell steps, see Figure 6.3a. Thin film growth on these as-received substrates will result in an interface with a mixture of both types. To fabricate a single type interface, the initial substrate has to be single terminated by either AO or BO_2.

A chemical route was suggested to achieve this single termination for $SrTiO_3$ substrates by combining a chemical treatment and a thermal treatment to form perfectly crystalline TiO_2-terminated $SrTiO_3$ surfaces [47]. This treatment was later investigated in more detail and optimized [48,49]. For this procedure, the $SrTiO_3$ substrates are first soaked in demineralized water for 30 min. using ultrasonic agitation. Because of this, SrO in the outermost substrate layer will react with water and form $Sr(OH)_2$. This Sr-hydroxide can then easily be removed by a short dip (30 sec.) in a commercially available buffered HF-solution (NH_4F:HF=87.5:12.5, pH=5.5) using ultrasonic agitation. The short time in combination with the high pH-value of the HF-solution prevents the formation of etch pits. Thermal treatment for typically 1 hour at 950 ºC and an oxygen pressure of 1 bar with an oxygen flow rate of ~150 l/h is used to obtain reproducibly the perfect crystalline TiO_2-terminated $SrTiO_3$ surfaces, see Figure 6.3b. However, the heating time depends on the vicinal angle of the substrates. To obtain straight step ledges at the substrate

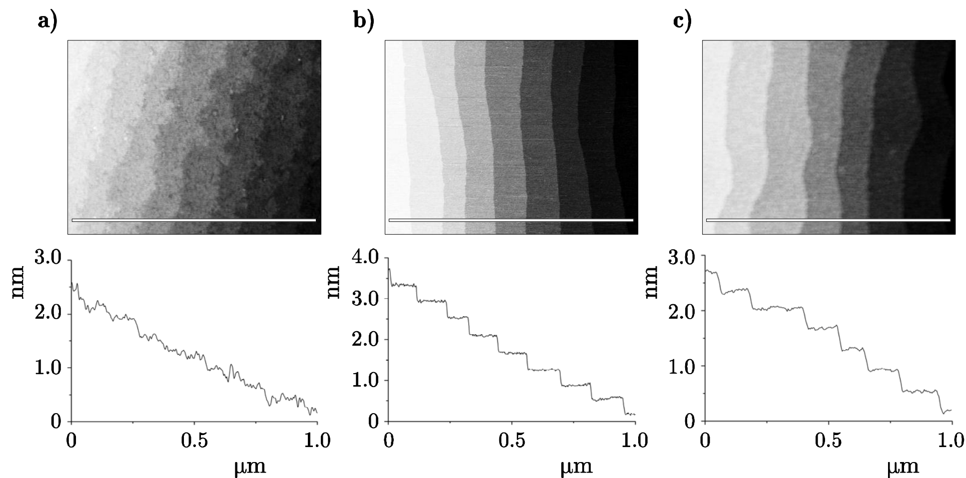

Figure 6.3 Surface analysis of $SrTiO_3$ substrates by atomic force microscopy. AFM micrograph and surface roughness analysis result of an as-received (ethanol cleaned) double-terminated surface **(a)**, a chemically and thermally treated single TiO_2-terminated surface **(b)** and a pulsed laser deposited single SrO-terminated surface **(c)**.

surface, 1 hour is used for substrates with vicinal angles between 0.2° and 0.5°. Longer time, typically 2-3 hours, is necessary for substrates with lower vicinal angles. Very low vicinal angles ($<0.05°$) will almost never result in perfect straight step ledges, due to the very large diffusion lengths. Only recently a new surface treatment was reported with an additional etch procedure [50], which was investigated by high-resolution synchrotron-radiation photoemission spectroscopy to result in very stable TiO_2-terminated surfaces [51].

Until now, no chemical treatments have been reported to produce the opposite single-terminated SrO surfaces, while heat treatment of the as-received $SrTiO_3$ substrates usually results in a mixed termination. Therefore, the single-terminated SrO surfaces can only be obtained by deposition of a SrO monolayer on a single-terminated TiO_2 surface. Epitaxial growth of SrO has been reported to occur in a layer-by-layer mode for molecular beam epitaxy [52] as well as for pulsed laser deposition [53]. However, this could only be obtained for relatively low temperatures (400-500°C), while for SrO monolayer growth, at normal $SrTiO_3$ deposition temperatures (850°C), pulsed laser interval deposition has to be applied [54,55]. In this deposition technique the total number of laser pulses for one monolayer has to be ablated simultaneously (50 Hz) to stabilize the correct SrO layer without multi-level islands. Concerning the deposition conditions, a single-crystal SrO target was ablated with an energy density of 1.3 J/cm^2. During growth, the substrate was held at 850 °C in an oxygen environment at 0.13 mbar. This results in crystalline SrO-terminated $SrTiO_3$ surfaces with perfect straight step ledges, see Figure 6.3c.

Surfaces of single crystalline $LaAlO_3$ substrates can be formed with a single termination by a thermal treatment. Surface studies have shown that the surface stoichiometry is a strong function of the sample temperature [56-58]. From room temperature up to ~150 °C the surface was terminated by an AlO layer and above ~250 °C the surface consisted of a LaO layer. Only in the intermediate region of 150-250 °C mixed terminations, containing La, Al and O atoms, were observed. The low- and high-temperature surfaces were terminated exclusively in either AlO or LaO layers, respectively. It was suggested that this low-temperature surface stoichiometry change was linked to a creation of surface oxygen deficiencies upon heating. However, growth studies of LaO and AlO films on $LaAlO_3$ substrates have also suggested the opposite AlO surface termination of the substrate at high temperatures [59].

As a result, only $SrTiO_3$ single crystalline substrates with single surface terminations of either TiO_2 or SrO were used to fabricate atomically controlled interfaces in $LaAlO_3$ – $SrTiO_3$ multilayers.

6.3 Growth of atomically controlled single interfaces

In the last couple of years, the growth of epitaxial thin films of $SrTiO_3$ [60,61] and $LaAlO_3$ [62,63] on silicon has been investigated for applications in silicon-based technology. Their high dielectric constants and their potential use as buffer layers for the epitaxial growth of various perovskite-type films, such as high-temperature superconductors, ferroelectrics and colossal magnetoresistance oxides, have resulted in numerous growth studies. These investigations benefited considerably from the already present knowledge, which was obtained in the last decades during the extensive experiments on homo- and hetero-epitaxial growth of $SrTiO_3$ and $LaAlO_3$ thin films on various perovskite substrates and thin films.

One of the successful deposition techniques for perovskite thin film growth is pulsed laser deposition, which has been used for the homoepitaxial growth of $SrTiO_3$ [47-49,64-68] as well as $LaAlO_3$ [69,70]. High-quality heteroepitaxial growth of $SrTiO_3$ and $LaAlO_3$ has also been obtained by pulsed laser deposition, but very rarely by combining both materials. Growth of $SrTiO_3$ thin films on $LaAlO_3$ substrates was only applied to produce electronically tunable microwave devices, such as resonators, filters and phase shifters [71-76]. On the other hand, heteroepitaxial growth of $LaAlO_3$ films on $SrTiO_3$ substrates has only recently gained interest after the discovery of conductivity at their interfaces [12]. This has resulted in a number of growth studies in the past two years [77-84].

6.3.1 Unit cell control by RHEED monitoring

Thin films of $LaAlO_3$ have been grown by pulsed laser deposition on single-terminated $SrTiO_3$ substrates to investigate the properties of the two possible heteroepitaxial interfaces. To obtain well controllable layer-by-layer growth, a single-crystal $LaAlO_3$ target was ablated by applying a KrF excimer laser at a repetition rate of 1 Hz and a laser fluency of ~1.3 J/cm^2. The deposition temperature was 850 ^oC and the oxygen pressure 3×10^{-5} mbar. The surface of the thin film was monitored during growth by Reflection High-Energy Electron Diffraction (RHEED).

$LaAlO_3$ thin films were grown on single TiO_2-terminated $SrTiO_3$ substrates as well as on single SrO-terminated $SrTiO_3$ substrates. The fluctuations in the RHEED intensity during the initial growth of the first unit cells are shown in Figure 6.4 for both types of surface terminations. Oscillations in the RHEED intensity can be observed in both cases, which indicate 2-dimensional layer-by-layer growth of $LaAlO_3$ for both types of $SrTiO_3$ surface terminations. The clear 2-dimensional spots in the RHEED pattern, shown in the insets, confirmed this growth behavior. The sharp decrease in RHEED intensity in both cases for the first $LaAlO_3$ unit cells can be explained by the difference in position for optimal diffraction conditions for both materials. The RHEED monitoring was aligned with the $SrTiO_3$ unit cell of the substrate. The difference in c-axis length between the initial $SrTiO_3$ unit cell (~3.905

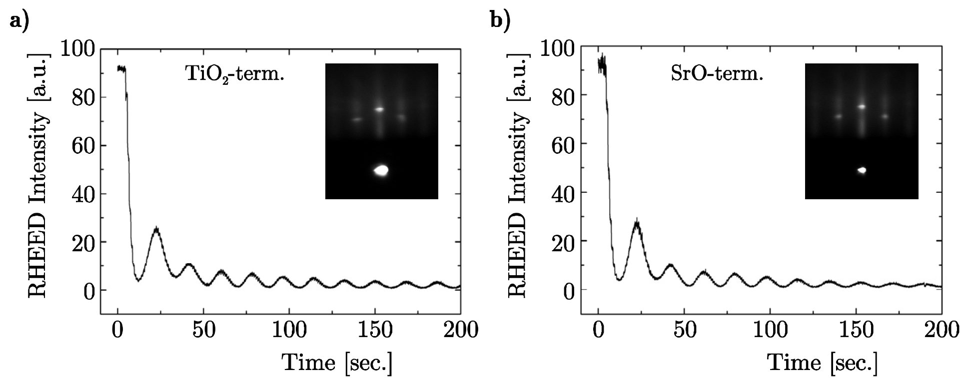

Figure 6.4 Monitoring of the RHEED intensity during initial growth of $LaAlO_3$ unit cells on single-terminated $SrTiO_3$ substrates with a TiO_2-terminated surface **(a)** and a SrO-terminated surface **(b)**. In the insets are the RHEED patterns shown with the clear 2-dimenisonal RHEED spots after growth of 26 unit cells of $LaAlO_3$.

Å) and the deposited $LaAlO_3$ unit cell (~3.791 Å) requires a new alignment of the RHEED monitoring for optimal surface analysis.

For well-aligned RHEED analysis, the 2-dimensional layer-by-layer growth of individual $LaAlO_3$ unit cells can be observed up to thicknesses of ~50 nm. The oscillations in the RHEED intensity were investigated to indicate growth of individual unit cells. The constant number of laser pulses, which is required to form one unit cell, and the constant RHEED intensity at the maximum of the oscillation suggest the growth of individual unit cells of $LaAlO_3$ with a constant surface roughness, see Figure 6.5. This was confirmed by the fluctuations in the full width at half maximum (FWHM) of the specular RHEED spot, which exhibit identical

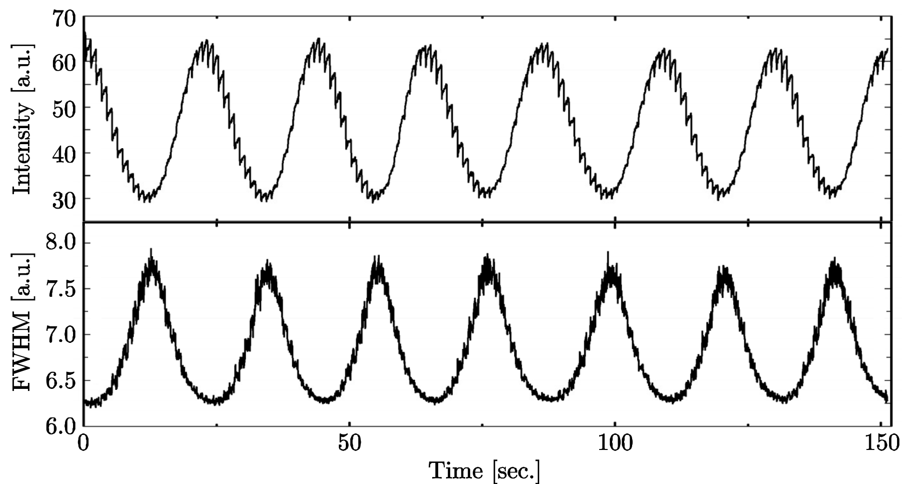

Figure 6.5 RHEED intensity and FWHM monitoring under optimal conditions during growth of $LaAlO_3$ unit cells on a $SrTiO_3$ substrate, exhibiting clear oscillations.

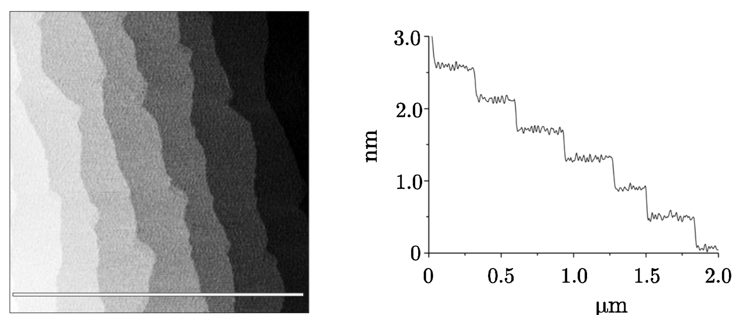

Figure 6.6 Surface analysis by atomic force microscopy of a 26 unit cells thick $LaAlO_3$ thin film on a TiO_2-terminated $SrTiO_3$ substrate. The roughness analysis shows smooth terraces with unit cell steps.

oscillations, but inverted compared to the RHEED intensity. The constant FWHM value, after growth of each $LaAlO_3$ unit cell, indicates constant surface roughness without the formation of islands.

The low level of surface roughness was confirmed by atomic force microscopy of a 26 unit cells (~10 nm) thick $LaAlO_3$ film on a TiO_2-terminated $SrTiO_3$ substrate, see Figure 6.6. The micrograph and the roughness analysis show smooth terraces with clear unit cell steps. This suggests strongly the presence of a single-terminated $LaAlO_3$ surface.

6.3.2 Structural and electronic properties

The quality of the $LaAlO_3$ thin films and the epitaxial relation to the $SrTiO_3$ substrates are investigated by x-ray diffraction for both types for heteroepitaxial interfaces. In Figure 6.7a are θ-2θ scans shown for 26 unit cells thick $LaAlO_3$ thin films grown on $SrTiO_3$ substrates with a TiO_2-terminated surface as well as a SrO-terminated surface. In both cases are only the (00*l*) reflections of the $LaAlO_3$ unit cell present along with the reflections from the $SrTiO_3$ substrate, indicating c-axis growth. The lattice parameters of the $LaAlO_3$ unit cell are determined by fitting of numerous peaks. The $LaAlO_3$ unit cell is grown cube-on-cube on the $SrTiO_3$ unit cell with their a- and b-axes perfectly aligned. This results in an in-plane tensile strain in the thin film with in-plane lattice parameters similar to the substrate. Consequently the c-axis lattice parameter of the $LaAlO_3$ thin film is shortened as compared to the bulk value (3.791 Å). However, analysis of the precise value for the c-axis suggests even a very small difference for both types of heteroepitaxial interfaces, although this measured difference is close to the resolution of the apparatus. In case of growth on a TiO_2-terminated surface the c-axis of the $LaAlO_3$ unit cell is ~3.739 Å, while for growth on a SrO-terminated surface the c-axis length is ~3.728 Å.

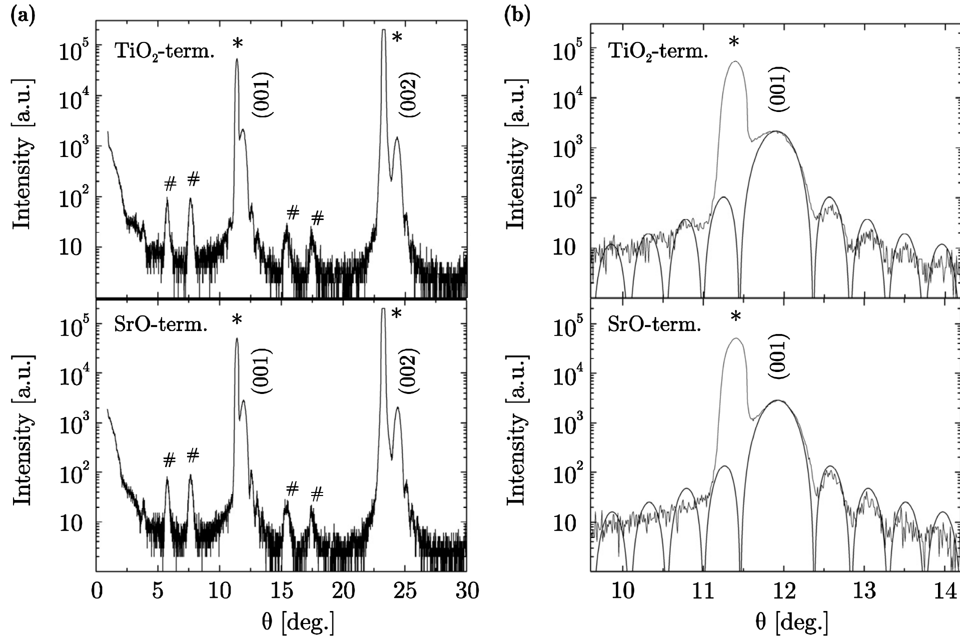

Figure 6.7 X-ray diffraction analysis of a 26 unit cells thick $LaAlO_3$ thin film on $SrTiO_3$ substrates with a TiO_2-terminated surface (top) and a SrO-terminated surface (bottom). Shown are large angle θ-2θ scans **(a)** as well as more detailed θ-2θ scans around the (001) reflections of the $LaAlO_3$ thin films **(b)**. A fit to the Kiessig fringes in the detailed θ-2θ scans is also shown. The $SrTiO_3$ substrate reflections are indicated with an asterisk and their spectral contributions (λ/2 and λ/3) with a cross.

A more detailed analysis of the (001) reflections of the $LaAlO_3$ unit cell shows clear Kiessig fringes next to the main peak, see Figure 6.7b. The presence of these fringes indicates a high quality thin film with a constant thickness between two well-defined interfaces. The shape of the resulting diffraction patterns can be explained qualitatively by the following equation, which describes the specularly diffracted intensity of the thin film when disregarding substrate and defect scattering.

$$I = I_0 \frac{\sin^2(Nq_z c/2)}{\sin^2(q_z c/2)}, \tag{6.1}$$

where q_z ($q_z = 4\pi \times \sin(\theta)/\lambda$) is the projected scattering vector in the z-direction (perpendicular to the surface) and c is the c-axis lattice parameter of the $LaAlO_3$ thin film. The $LaAlO_3$ thin films consist of 26 unit cells (N=26) and their lattice parameters in the c-axis direction are described above. By choosing correctly the values for I_0, the result of equation 6.1 will lead to a very close fit to the measured diffraction data. However, the asymmetry between the fringes on both sides of the

main peak could not be fitted with this simple equation. To describe this asymmetry accurately, the change in the structure factor with the change in angle θ has to be taken into account.

The structural properties of the $LaAlO_3$ thin films grown on both types of single-terminated $SrTiO_3$ substrates are very similar, as was observed by RHEED and XRD. However, very large differences are present in their electronic properties. Thin films with different heteroepitaxial interfaces were measured in a 4-wire configuration. Contacts were wire-bonded to unstructured $LaAlO_3$ thin films with the voltage contacts only 200 μm apart. This contacting method induces locally some damage to the thin film and is therefore very useful for contacting the buried conducting layer at the interface. The measured temperature dependence of the resistance is shown in Figure 6.8 for both types of heteroepitaxial interfaces. The thickness of the conducting layer at the interface is unknown and therefore the measured resistance can't be converted in the resistivity. The difference in resistance at room temperature between both interfaces is a factor of ~10^3 and while the $LaAlO_3$ film on a TiO_2-terminated surface shows metallic behavior down to low temperatures, the $LaAlO_3$ film on a SrO-terminated surface shows insulating behavior and can't be accurately measured at low temperatures. This very large difference in resistance was already mentioned by Ohtomo and Hwang [12].

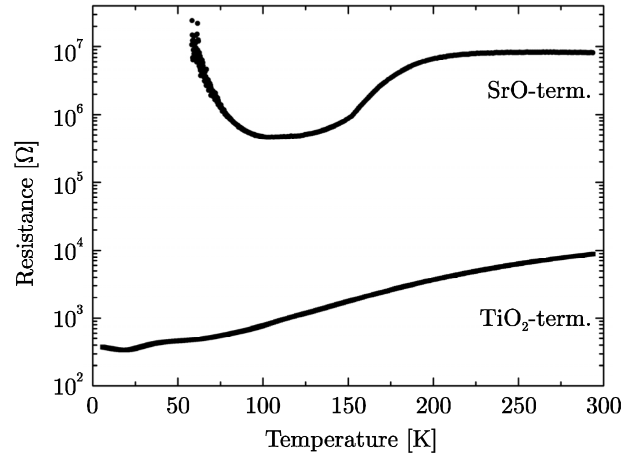

Figure 6.8 Temperature dependence of the resistance for 26 unit cells thick $LaAlO_3$ films on $SrTiO_3$ substrates with a TiO_2-terminated surface and a SrO-terminated surface.

6.4 Atomic interface structure at high temperatures

In order to better understand and model the properties of the aforementioned heteroepitaxial interfaces, it is important to determine the atomic structure very accurately. Surface X-ray Diffraction (SXRD) is a well-established technique for the structure determination of surfaces and interfaces [85]. In contrast to techniques like Transmission Electron Microscopy (TEM), SXRD provides the atomic structure averaged over typically several mm^2, which in general is the surface area illuminated by the x-ray beam. Obtaining structural information that includes microscopic length scales will provide useful extra information for understanding the phenomenon of interface conductivity. The heteroepitaxial interfaces were grown by pulsed laser deposition and studied by SXRD in the same vacuum chamber. This assured that the potentially delicate surface was not exposed to impurity-containing environments.

6.4.1 In-situ x-ray diffraction during growth for interface modeling

The experiments were carried out in a PLD chamber [86] mounted on a 2+3 type surface diffractometer with vertical scattering geometry[I]. The x-ray beam was monochromatized to a wavelength of 0.775 Å. A KrF excimer laser (Lambda Physik EMG101) was used to ablate a single-crystal $LaAlO_3$ target with an energy density of ~1.3 J/cm^2. During deposition the substrate temperature was kept at 850 °C (1123 K), while the oxygen pressure in the chamber was 1×10^{-4} mbar. The $LaAlO_3$ thin films were grown on TiO_2-terminated $SrTiO_3$ substrates.

At a grazing angle for the incoming x-ray beam, the intensity of a surface-sensitive reciprocal space point $(00l)$, in $SrTiO_3$ lattice units, was monitored while depositing. During the first intensity oscillation, i.e. about a coverage less than one unit cell layer, the deposition was stopped. Two samples were fabricated during different deposition runs and individually analyzed. For one sample the temperature was lowered to 473 K after the deposition, while for another sample the temperature was kept constant at the deposition temperature of 1123 K. For both samples several crystal truncation rods (CTRs) were measured. In order to monitor the stability of the structure at 1123 K, the reciprocal point (2,0,1.9) was recorded several times during data collection. Over six hours the integrated intensity of this particular point fluctuated 4% around its average value, which is an indication that the crystal structure of the $LaAlO_3$ monolayer maintained stable. For the sample, which was cooled down to 473 K directly after deposition, the reflectivity ridge scan

[I] The in-situ x-ray diffraction studies during pulsed laser deposition were performed at BM26 (DUBBLE) [87] at the European Synchrotron Radiation Facility (ESRF), Grenoble, France.

	1123 K	473 K
no. points	60	45
CTRs	10,11,20,21	10,11,20
θ_1	0.38(2)	0.48(1)
θ_2	0.57(1)	0.50(1)
$\theta_1+\theta_2$	0.95(2)	0.97(2)
χ^2	2.1	2.6

Table 6.1 Details of the CTR measurements at both temperatures together with the final results of the refinement of the model, where fraction θ_1 is the part of the undistorted substrate surface, θ_2 is the fraction of the distorted substrate surface, which is covered by $LaAlO_3$, and χ^2 is the minimization factor.

(θ-2θ) before and after the data collection showed no significant differences, indicating that also this sample was stable.

Several CTRs were measured for both samples and the results are listed in Table 6.1. For each CTR fifteen diffraction profiles were measured, integrated and corrected to obtain structure factors [88]. Due to limited access to reciprocal space, caused by the configuration of the vacuum chamber and the supporting equipment, it was not possible to measure symmetry related reflections. In the absence of redundancy of the measured data, the systematic errors were estimated at 15%, which seems realistic in view of previous data collections on bare $SrTiO_3$ substrates [89].

Subsequently the measured data can be described by a structural model, in which a TiO_2-terminated $SrTiO_3$ substrate is partly covered by a unit cell layer of $LaAlO_3$. The area of the substrate that is covered by $LaAlO_3$ is not known in advance. Since it is possible that the surface atoms in the $SrTiO_3$ lattice in the part of the substrate that is covered with $LaAlO_3$ will distort, a model is needed in which the total interference sum of both distorted and undistorted areas are taken into account:

$$F_{SUM} = \frac{F_{STO}}{1 - e^{-i2\pi l}} + \theta_1 F_{STO} + \theta_2 (F'_{STO} + F_{LAO}), \tag{6.2}$$

where F_{STO} is the structure factor of bulk $SrTiO_3$ and the first term on the right-hand side renders the well-known CTR of the bulk $SrTiO_3$ substrate. The fraction θ_1 is the part of the undistorted substrate surface and θ_2 is the fraction of the distorted substrate surface (F'_{STO}), which is covered by $LaAlO_3$ (F_{LAO}). The program ROD [90] was used to refine the atomic positions against the experimental data. Since the fractional occupancies were not defined as θ_1=1-θ_2, the two parameters (θ_1 and θ_2) were refined independently and their values are listed in Table 6.1. The sum of their independently refined values is close to 1, which implies that the model describes indeed the total surface area. The ROD-program uses a χ^2-minimization method to

determine the best-fit parameters. As an indication of how well the model describes the measured data, the following parameter is calculated:

$$\chi^2 = \frac{1}{N-p-1}\sum_{\mathrm{hkl}} \frac{\left(\left|F_{\mathrm{obs}}(\mathrm{hkl})\right| - s\left|F_{\mathrm{calc}}(\mathrm{hkl})\right|\right)^2}{\sigma^2(F_{\mathrm{obs}}(\mathrm{hkl}))}, \tag{6.3}$$

with N the number of observed structure factors, p the number of refined parameters, s the overall scalefactor and σ the errors, mainly determined by the systematic errors. The results of the refined atomic positions are listed in Table 6.2 and a schematic view of the refined model at 473 K is shown along one principal crystallographic direction in Figure 6.9. Attempting to refine the thermal parameters resulted in very large estimated standard deviations. In the final best-fits, the thermal parameters were kept at bulk-like values, see Table 6.2, inferred from references 26 and 39.

At both temperatures (1123 K and 473 K), the uncovered area of the $SrTiO_3$ surface remains bulk TiO_2-terminated. However, the area of the $SrTiO_3$ surface, which is covered by the $LaAlO_3$ layer, is slightly distorted. This distortion is very small at 1123 K, where $SrTiO_3$ as well as $LaAlO_3$ consist of cubic unit cells, but increases significantly at 473 K. The transition in $LaAlO_3$ from the perfect cubic structure to the rhombohedral structure for temperatures below ~813 K [32,33] might be the driving force for the increased atomic distortion.

In the distorted model only the first $SrTiO_3$ unit cell layer was allowed to distort. Allowing more $SrTiO_3$ unit cell layers in the bulk to distort as well resulted in negligible atomic displacements for these layers and in order to reduce the number of fit parameters these distortions were neglected.

Layer	Atom	x	y	z_{1123K}	z_{473K}	B_{1123K} (Å^2)	B_{473K} (Å^2)
AlO_2	Al	$\frac{1}{2}$	$\frac{1}{2}$	1.99(1)	2.031(8)	2.0	1.0
	O1	$\frac{1}{2}$	0	1.99(2)	1.88(2)	3.0	2.0
LaO	La	0	0	1.536(4)	1.565(2)	2.0	1.0
	O2	$\frac{1}{2}$	$\frac{1}{2}$	1.58(5)	1.40(2)	3.0	2.0
TiO_2	Ti	$\frac{1}{2}$	$\frac{1}{2}$	1.01(1)	0.997(6)	1.56	0.7
	O3	$\frac{1}{2}$	0	1.04(2)	0.92(2)	2.56	1.5
SrO	Sr	0	0	0.513(5)	0.536(3)	2.2	1.2
	O4	$\frac{1}{2}$	$\frac{1}{2}$	0.57(3)	0.51(2)	2.56	1.5

Table 6.2 Refined fractional coordinates of the atomic positions of the best-fit model at both temperatures. Listed are also the isotropic thermal parameters (B), which were used in the refinement procedures.

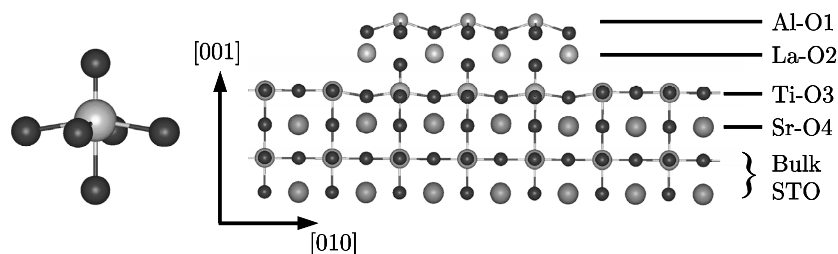

Figure 6.9 Schematic view of the best-fit model with the interface stacking sequence of bulk-SrO-TiO_2-LaO-AlO_2 after refinement against the CTR measurements obtained at 473 K. The area of the $SrTiO_3$ which is covered by the $LaAlO_3$ layer is slightly distorted, whereas the uncovered area of the $SrTiO_3$ remains bulk terminated. An enlargement of the distorted surface TiO_6 octahedron is shown on the left.

6.4.2 Modeling of the atomic interface stacking

In addition to the 'bulk-SrO-TiO_2-LaO-AlO_2' model various other models with different atomic interface stackings were also tested: 'bulk-SrO-AlO_2-LaO', 'bulk-SrO-LaO-AlO_2' (Ruddlesden-Popper phase [91]), 'bulk-TiO_2-AlO-LaO_2' and 'bulk-TiO_2-AlO_2-LaO' (where the AlO_2-LaO layer was displaced by the in-plane vector $(\frac{1}{2},\frac{1}{2},0)$. All these alternative models did not describe the measured data very accurately. The calculated χ^2 values for these models were respectively 10, 20, 30 and >1000 at 1123 K and 8.2, 22, 19 and >1000 at 473 K, which are significantly larger than the χ^2 values for the best-fit 'bulk-SrO-TiO_2-LaO-AlO_2' model of 2.1 and 2.6 for respectively 1123 K and 473 K, see Table 6.1. As a comparison with the best-fit model, Figure 6.10 shows CTRs, which are calculated by using two bulk-like models with both types of $SrTiO_3$ surface terminations. In those two cases, the inter-atomic distances across the heteroepitaxial interfaces are kept at the pseudo-cubic bulk $LaAlO_3$ lattice parameter. The results in Figure 6.10 show clearly that the distorted best-fit model, with the atomic positions as listed in Table 6.2, produces a much better fit to the measured data than the two bulk-like models.

In order to better understand the refined, distorted model, some of the inter-atomic distances are listed in Table 6.3. The variations from the bulk $SrTiO_3$ lattice distances are also shown. Clearly, almost all atoms in the high-temperature interface structure at 1123 K are within two times the estimated standard deviation from a bulk $SrTiO_3$ lattice site. In contrast to the low-temperature interface structure (473 K), where the displacements from the bulk $SrTiO_3$ lattice sites are statistically relevant. Starting from the bulk $SrTiO_3$ lattice underneath, the Ti atoms are both at high and low temperatures in a bulk position. The Al atoms, which follow on top of the Ti atoms in a crystallographic similar position, are at low temperature displaced away from the bulk $SrTiO_3$ lattice site, as can be seen in the schematic view in

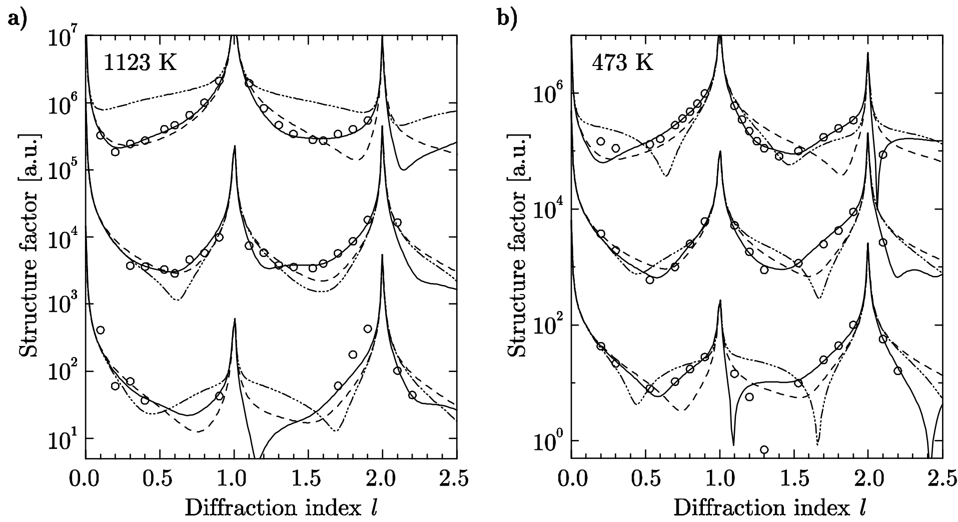

Figure 6.10 Measured data points and calculated CTRs using three different models. Both data and modeled CTRs are shown for measurements at 1123 K **(a)** and 473 K **(b)**. For both temperatures the 10 (top), 11 (middle) and 20 (bottom) crystal truncation rods are shown. The solid lines indicate the CTRs calculated with the atomic positions as listed in Table 6.2. As a comparison, the CTRs calculated by using two bulk-like models are shown as well, for 'bulk-TiO_2-LaO-AlO_2' (dashed lines) and 'bulk-SrO-AlO_2-LaO' (dash-dotted lines).

Figure 6.9. The Sr and La atoms are also on bulk lattice sites at high temperature, whereas at low temperature the atoms also displace away from the surface. The oxygen atoms show similar behavior, but displace in the opposite direction from the cations. All these displacements result in very large inter-atomic distances, when compared to the bulk lattice parameters of $LaAlO_3$ and $SrTiO_3$. The interatomic distances between the cations across the interface become as large as ~4.03 Å, which is not expected since the $LaAlO_3$ unit cell is tensile strained in-plane. This strain implies normally that the out-of-plane interatomic distance shortens, which was indeed observed for ~10 nm thick $LaAlO_3$ films in section 6.3.2. However, bulk material properties can't be used to describe interface structures.

The results of the low temperature interface structure agree very well with results obtained by Maurice *et al.* [80]. They studied thin $LaAlO_3$ films with a thickness of several nanometers on $SrTiO_3$ substrates by high-resolution transmission electron microscopy (HRTEM). The measurements obtained in those studies revealed that on either side of the interface the atomic layers were expanded. Their results indicate that at room temperature the last three $SrTiO_3$ unit cell layers at the interface expand up to 4.05 Å and that the first three $LaAlO_3$ unit cell layers distort in a similar way. Here, the inter-atomic distances $d_{\text{Al-Ti}}$ and $d_{\text{La-Sr}}$ across the low temperature interface are also elongated with equal lengths.

The atomic displacements found here and by HRTEM result in a distortion of the topmost TiO_6 octahedra, see Figure 6.9. In bulk $SrTiO_3$, these octahedra are completely symmetric, whereas for the low temperature $SrTiO_3$-$LaAlO_3$ interface they are distorted to become asymmetric. Maurice *et al.* ascribed the distorted oxygen octahedra to a Jahn-Teller effect, where the introduction of an extra electron in the *3d* band, by changing from Ti^{4+} to Ti^{3+}, will lead to a distortion of the octahedra in order to minimize the energy. However, distorted TiO_6 octahedra with similar atom displacements are observed in various perovskite compounds, i.e. $BaTiO_3$ and $PbTiO_3$, and result in ferroelectricity by a switchable macroscopic polarization [92]. The term ferroelectricity shouldn't be used for the octahedra distortions at this heteroepitaxial interface, because no switching behavior was demonstrated. Still, the calculated displacements of the atoms would suggest a polarization of ~100 μC/cm^2 for the distorted unit cell layers at the interface at 473 K, while no significant polarization can be determined for the heteroepitaxial interface at 1123 K, due to the negligible distortions. This calculated polarization value is larger than commonly observed in perovskite compounds. However, the large influence of epitaxial strain on the polarization in perovskites has been demonstrated before [93, 94] and is therefore not unrealistic for such highly strained heteroepitaxial interfaces.

	1123K(Å)	473K(Å)	1123K ($\frac{d}{a_{STO}}$)	473K ($\frac{d}{a_{STO}}$)
a_{STO}	3.935(5)	3.915(5)	-	-
a_{LAO}	3.824	3.797	-	-
$d_{Al\text{-}Ti}$	3.86(4)	4.03(4)	0.98(1)	1.03(1)
$d_{La\text{-}Sr}$	4.03(2)	4.03(2)	1.023(6)	1.029(6)
$d_{O1\text{-}O3}$	3.7(1)	3.8(8)	0.95(3)	0.96(2)
$d_{O2\text{-}O4}$	4.0(2)	3.5(2)	1.01(6)	0.90(3)
$d_{bulk\text{-}Ti}$	3.97(4)	3.90(2)	1.01(1)	0.997(6)
$d_{bulk\text{-}Sr}$	3.99(2)	4.06(1)	1.013(5)	1.036(3)
$d_{bulk\text{-}O3}$	4.09(8)	3.60(8)	1.04(2)	0.92(2)
$d_{bulk\text{-}O4}$	4.2(1)	3.95(8)	1.07(3)	1.01(2)

Table 6.3 Inter-atomic distances calculated from the atomic positions listed in Table 6.2. Both the absolute as well as the fractional distances, related through the bulk lattice parameter of $SrTiO_3$, are shown. The values $d_{bulk\text{-}atom}$ indicate the distance from a particular atom to the nearest identical atom-type in the bulk. The lattice parameters for the bulk pseudo-cubic $LaAlO_3$ are estimated from values in ref. 39.

6.5 Complementary interfaces in heteroepitaxial superlattices

Research on artificially structured materials was initiated in 1969, when an engineered semiconductor superlattice with a one-dimensional periodic potential was proposed [95]. The idea of the superlattice occurred as a natural extension of double-, triple- and multiple-barrier structures. This artificial periodic structure consisted of alternate layers of two dissimilar semiconductors with layer thicknesses of the order of nanometers. An important parameter for the expected observation of quantum effects in these structures was the bulk quality as well as the interface quality of the crystals. The introduction of the one-dimensional superlattice potential perturbed the band structure of the host materials and yielded a series of narrow subbands and forbidden gaps. Therefore, the superlattice was expected to exhibit unprecedented electronic properties.

The first strained GaAs-$GaAs_{0.5}P_{0.5}$ superlattice, with a relatively large lattice mismatch, was fabricated in 1970 [96] and this achievement initiated also research into compositional GaAs-$Ga_{1-x}Al_xAs$ superlattices [97]. Since in this way a one-dimensional potential could be introduced along with the growth direction, well-known examples in the history of one-dimensional mathematical physics could be practiced in a laboratory for the first time. These results triggered a wide spectrum of experimental and theoretical investigations on superlattices and quantum wells in the next decades. This new degree of freedom through advanced materials engineering resulted in observations of not only predicted effects but also totally unknown phenomena [98].

The engineering of superlattices didn't remain confined to semiconductor research, but was also applied in new experimental investigations in complex oxide materials, such as perovskites. Due to their similar crystal structures, sequential epitaxial growth of different perovskite compounds could result in new artificially structured materials with properties that could open the door to substantial improvements in device performance or even radically new types of devices [99]. Therefore, numerous experiments have been performed to fabricate perovskite superlattices, in which material properties were tuned or newly induced. Examples of such systems are artificial superconductors ($BaCuO_2$-(Ca,Sr)CuO_2 [100,101]), ferroelectrics ($BaTiO_3$-$SrTiO_3$ [102-105], $PbZrO_3$-$PbTiO_3$ [106,107], $PbTiO_3$-$SrTiO_3$ [108,109], $KNbO_3$-$KTaO_3$ [110,111]), ferromagnets ($La_{0.67}Ca_{0.33}MnO_3$-$SrRuO_3$ [112], $LaFeO_3$-$LaCrO_3$ [113], $SrRuO_3$-$SrTiO_3$ [114], $La_{0.6}Sr_{0.4}MnO_3$-$La_{0.6}Sr_{0.4}FeO_3$ [115], $CaMnO_3$-$CaRuO_3$ [116]) and multiferroics ($SrRuO_3$-$BaTiO_3$ [117], $Pr_{0.85}Ca_{0.15}MnO_3$-$Ba_{0.6}Sr_{0.4}TiO_3$ [118,119], $Pr_{0.85}Ca_{0.15}MnO_3$-$BaTiO_3$ [120], $La_{0.7}Ca_{0.3}MnO_3$-$BaTiO_3$ [121]). Recently, this type of artificial fabrication was even extended into three-component superlattices [122,123].

The charge ordering, which results in perovskites in modulations of the electron density in the form of planes, has been investigated in $SrTiO_3$-$LaTiO_3$ superlattices,

where the titanium valence was varied from 4+ to 3+ [124]. An interesting related subject is charge modulation in $LaAlO_3$-$SrTiO_3$ superlattices, consisting of complementary 'n-type' and 'p-type' interfaces. However, this effect is still uninvestigated.

6.5.1 Artificial growth of $LaAlO_3$-$SrTiO_3$ superlattices

In order to grow epitaxial superlattices, composed of alternate layers of $LaAlO_3$ and $SrTiO_3$, with a control on the atomic scale, the materials were deposited by pulsed laser deposition on single TiO_2-terminated $SrTiO_3$ substrates. The individual $LaAlO_3$ and $SrTiO_3$ layers were grown with the same deposition conditions as used for the growth of single heteroepitaxial $LaAlO_3/SrTiO_3$ interfaces, which are described in section 6.3.1. However, the in-situ target change, required for multilayer fabrication, could be carried out within seconds. During growth of both type of compounds RHEED oscillations were observed, which were used to accurately control the thickness of the individual layers. Figure 6.11 shows the fluctuations in RHEED intensity during growth of a 60 nm thick $[(LaAlO_3)_8/(SrTiO_3)_8]_{10}$ superlattice, which consists of a superlattice with 10 periods of 8 unit cells of $LaAlO_3$ and 8 unit cells of $SrTiO_3$.

The first two sequences of $(LaAlO_3)_8/(SrTiO_3)_8$ growth are visible at the top and middle position in Figure 6.11. The similarity of the RHEED fluctuations in both sequences indicates identical growth for every individual layer, independent of moment of deposition during the total deposition. The epitaxial stabilization is maintained during the entire superlattice growth and leads to a constant growth mode even for the last deposition sequence, which is shown at the bottom in Figure 6.11. Due to an alignment of the RHEED analysis with the initial TiO_2-terminated $SrTiO_3$ substrate, the RHEED monitoring displays a decrease in intensity during $LaAlO_3$ growth and an increase in intensity during $SrTiO_3$ growth. The actual values for the RHEED intensity can only be compared within a sequence, because the intensity is manually changed, and set close to 100, every time at the beginning of a sequential deposition. The RHEED monitoring displays, therefore, the relative changes during growth of a single $(LaAlO_3)_8/(SrTiO_3)_8$ sequence on a TiO_2-terminated $SrTiO_3$ layer.

An atomically controlled layer-by-layer growth mode will produce 'n-type' TiO_2-LaO interfaces at the beginning of the $LaAlO_3$ layer growth, while 'p-type' AlO_2-SrO interfaces are formed at the beginning of the $SrTiO_3$ layer growth. The final quality of the superlattices will depend on the sharpness of the individual interfaces. Interface roughness by atomic disordering can be reduced by accurately interrupting the deposition procedure, when the RHEED intensity displays a maximum intensity during an oscillation. This suggests a closed surface with a low level of extra material on top. Clearly visible during the total deposition are the intensity recoveries after every laser pulse. This process is caused by the surface diffusion of

the adatoms, which results finally in coalescence at growing islands or at the terrace steps. The step density, and therefore the probability of a diffusing atom to coalesce, changes during 2-dimensional layer-by-layer growth. This can be observed in the various relaxation times for every intensity recovery. When the RHEED intensity is at it's maximum value during an oscillation, the probability of a diffusing atom to coalesce is low and long relaxation times are observed (τ~ 2 sec.).

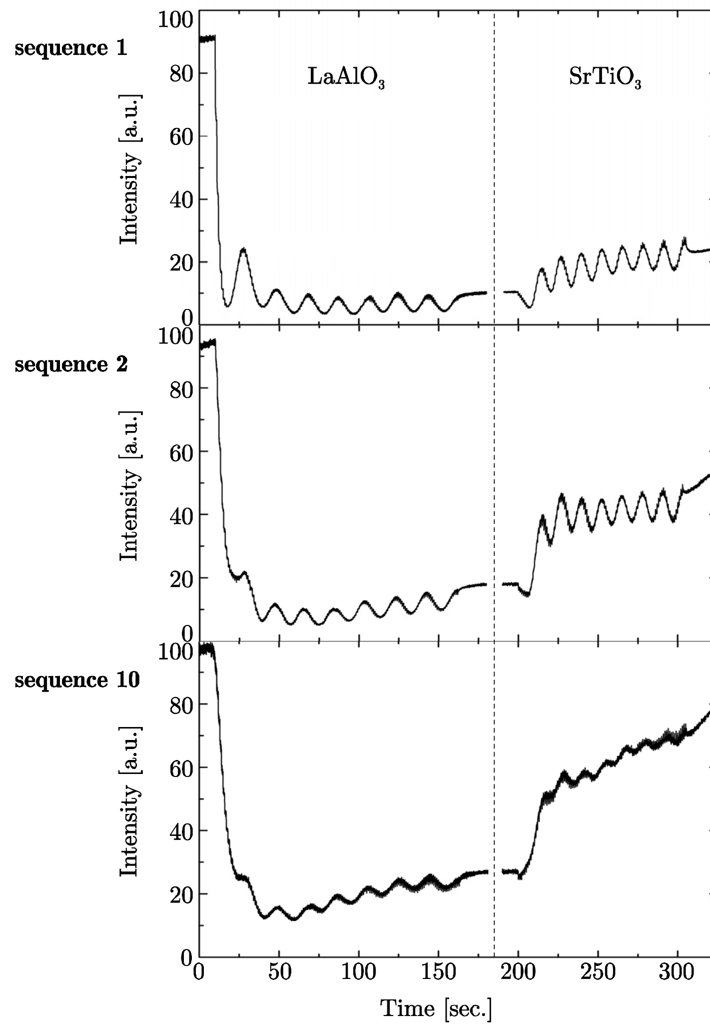

Figure 6.11 RHEED intensity variations during growth of a $[(LaAlO_3)_8/(SrTiO_3)_8]_{10}$ superlattice by pulsed laser deposition on a TiO_2-terminated $SrTiO_3$ substrate. Clearly visible are the oscillations in the RHEED intensity during the first two sequences (respectively at the top and middle position) and also during the final sequence (at the bottom).

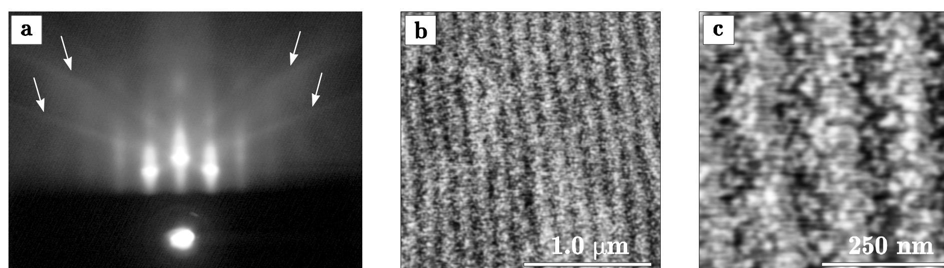

Figure 6.12 Surface analysis of a $[(LaAlO_3)_{10}/(SrTiO_3)_{10}]_{10}$ superlattice. **(a)** RHEED pattern exhibiting 2-dimensional spots as well as Kikuchi lines, which are indicated by the arrows. **(b)** Atomic force micrograph displaying clearly the terrace step orientation of the initial $SrTiO_3$ substrate. **(c)** Atomic force micrograph showing a surface roughness of single unit cell steps from the terrace steps and the 2-dimensional islands.

The atoms will diffuse over the terrace to coalesce eventually at the terrace steps or at the sides of the 2-dimensional islands. This will result in atomically smooth surfaces with only unit cell height steps for each individual $LaAlO_3$ or $SrTiO_3$ layer during the superlattice deposition. As a result, the final interface roughness will be as low as possible and lead to the highest superlattice quality for this growth technique. This is confirmed by the RHEED pattern of a finished $[(LaAlO_3)_{10}/(SrTiO_3)_{10}]_{10}$ superlattice in which clear 2-dimensional spots are visible as well as Kikuchi lines, see Figure 6.12a. Superlattices of $LaAlO_3$ and $SrTiO_3$ were fabricated with various settings for the individual thicknesses and number of sequences. All superlattices were eventually investigated by atomic force microscopy and they displayed clearly the imprint of the terrace step orientation of the initial $SrTiO_3$ substrate, see Figure 6.12b. Detailed surface analysis showed a surface roughness of single unit cell steps, which are originating from the terrace steps as well as the 2-dimensional islands. As an example, the surface analysis of a $[(LaAlO_3)_{10}/(SrTiO_3)_{10}]_{10}$ superlattice is given in Figure 6.12c.

Coherently strained $LaAlO_3/SrTiO_3$ superlattices were reported to exhibit critical thicknesses of the strained individual layers [125]. However, RHEED monitoring during superlattice growth showed no abrupt intensity variations for the $LaAlO_3$ layer up to 26 unit cells, although a decrease in intensity was visible for $SrTiO_3$ layers of more than 11 unit cells, see Figure 6.13. Above this thickness the energy for the formation of misfit dislocations was apparently smaller than the energy of the in-plane deformation of the $SrTiO_3$ layer. As a result, some 3-dimensional islands are formed, which can be observed in the final RHEED pattern, see inset in Figure 6.13.

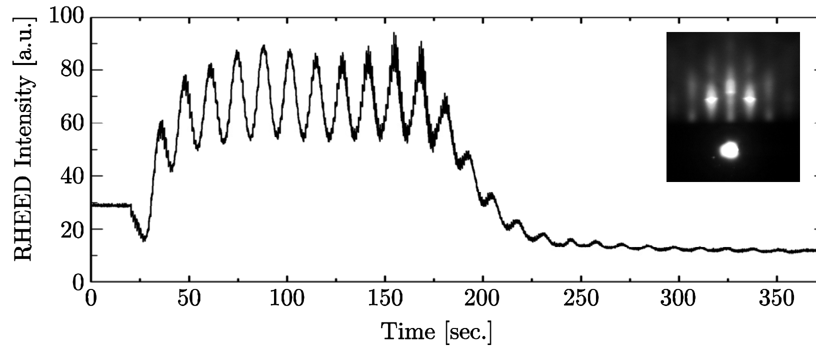

Figure 6.13 Monitoring of the RHEED intensity during growth of $SrTiO_3$ unit cells on a 13 unit cells thick $LaAlO_3$ layer on a $SrTiO_3$ substrate. In the inset is the RHEED pattern shown after growth of 26 unit cells of $SrTiO_3$. Besides the 2-dimensional RHEED spots are some extra spots vaguely visible arising from the 3-dimensional islands on the surface.

6.5.2 Structural analysis of the superlattices

In order to investigate the strain status, epitaxial orientation and atomic ordering of the structure, the superlattices were measured by x-ray diffraction. In Figure 6.14 are the θ-2θ diffraction profiles shown for a $[(LaAlO_3)_5/(SrTiO_3)_6]_{10}$ and a $[(LaAlO_3)_{10}/(SrTiO_3)_{11}]_{10}$ superlattice. The characteristic lengths in superlattices are the lattice spacings of the constituent materials (t_{LAO} and t_{STO}) and the modulation length ($\Lambda = t_{LAO} + t_{STO}$). This modulation length, or superlattice period, gives rise to the occurrence of equidistant satellite peaks, besides the $(00l)$ $SrTiO_3$ substrate reflections. The small width and high intensity of the satellite peaks indicate the high quality of the superlattices, obtained by pulsed laser deposition. The modulation lengths can be determined by the following equation:

$$\Lambda = \frac{\lambda}{2\left|\sin\theta_{n\pm1} - \sin\theta_n\right|}, \tag{6.4}$$

with λ the wavelength of the radiation and θ_n the angle of the nth order satellite peak. The resulting modulation lengths for the $[(LaAlO_3)_5/(SrTiO_3)_6]_{10}$ and $[(LaAlO_3)_{10}/(SrTiO_3)_{11}]_{10}$ superlattices are respectively, ~42.08 Å and ~80.85 Å. These values agree very well with the expected modulation lengths by using the bulk values for $LaAlO_3$ (3.791 Å) and $SrTiO_3$ (3.905 Å). In addition, a full dataset was collected by measuring numerous superlattice reflections in reciprocal space to determine the superlattice unit cell with the c-axis value as given above. The determined in-plane lattice parameters were very close to the ones of the $SrTiO_3$ substrate, as expected. Due to the cube-on-cube epitaxial growth, the a- and b-axes of the superlattice structure were aligned with the in-plane axes of the substrate.

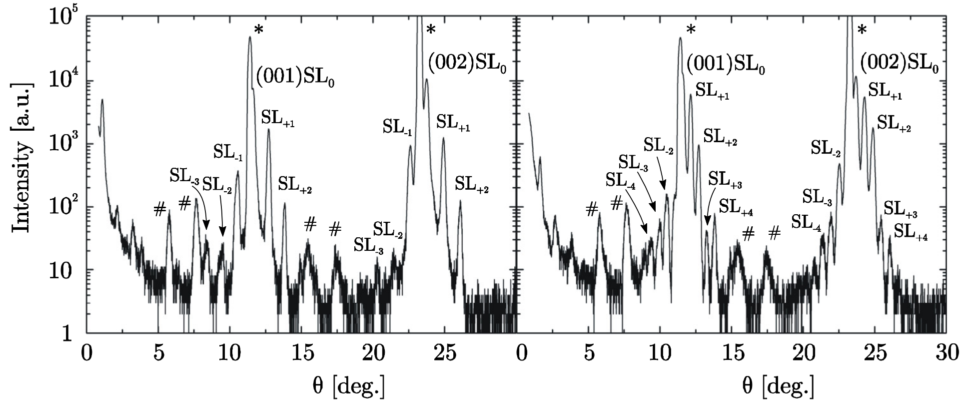

Figure 6.14 X-ray diffraction θ-2θ scans of the $[(LaAlO_3)_5/(SrTiO_3)_6]_{10}$ superlattice (Λ~42.08 Å) **(left)** and the $[(LaAlO_3)_{10}/(SrTiO_3)_{11}]_{10}$ superlattice (Λ~80.85 Å) **(right)**. The superlattice (SL) satellite peaks are numbered by their order on both sides of the $(00l)SL_0$ main peaks. The $SrTiO_3$ substrate reflections are indicated with an asterisk and their spectral contributions (λ/2 and λ/3) with across.

The ordering of the atoms inside the superlattice unit cell was examined by measuring an extensive dataset of ~300 superlattice reflections, which was subsequently fitted to a perovskite superstructure model. All computations involving data reduction and the solution and refinement of the structure were carried out using the Enraf-Nonius crystallographic software system MolEN. The final result is shown in Figure 6.15, where only one period of a $[(LaAlO_3)_6/(SrTiO_3)_6]_{10}$ superlattice is displayed. The direction of growth is indicated in the figure and through this the position of each interface can be defined. The refinement procedure determined that the interface at the bottom of every $SrTiO_3$ layer (nr. 1) was AlO_2-SrO, while the interface on top of every $SrTiO_3$ layer (nr. 2) was LaO-TiO_2. It also gave an average distance between the Sr-atoms in the $SrTiO_3$ layer of 3.92±0.04 Å, which was more or less the bulk lattice parameter (3.905 Å). However, the average distance between the La-atoms in the $LaAlO_3$ was 3.73±0.04 Å, which was somewhat smaller than the bulk value (3.791 Å). This possible shortening of the c-axis could be a result of the in-plane tensile strain in the $LaAlO_3$ layer. The distances between the La-Sr atoms at both interfaces were equal and corresponded to the lattice parameter of $SrTiO_3$.

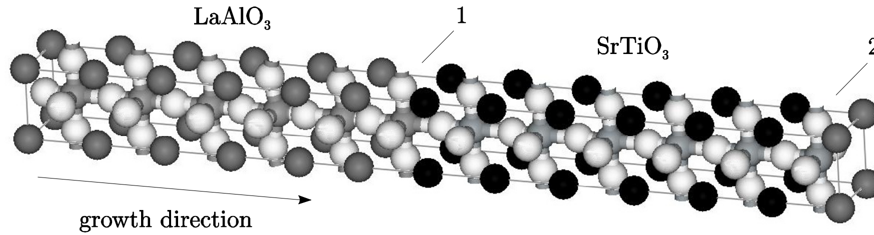

Figure 6.15 Schematic model of one modulation length in a $[(LaAlO_3)_6/(SrTiO_3)_6]_{10}$ superlattice with the two types of interfaces indicated by numbers 1 and 2.

6.5.3 Atomic ordering analysis of the interfaces

The interface phenomena between $LaAlO_3$ and $SrTiO_3$ layers require high-quality interfaces on the atomic scale. To investigate the atomic ordering by transmission electron microscopy (TEM)[II], cross-sectional slices were obtained from a $[(LaAlO_3)_{10}/(SrTiO_3)_{11}]_{10}$ superlattice by cutting along the (010)-direction of the $SrTiO_3$ substrate and then gluing the superlattice surfaces face to face. Cross-sectional specimens were subsequently prepared by mechanical grinding, polishing, and dimpling, followed by Ar-ion milling at 2.5 kV under an angle of 3-4° [126]. The principles and fundamentals of the preparation methods and measurement techniques are explained in ref. 127 to 130. A cross-sectional view of the total superlattice, from the $SrTiO_3$ substrate at the bottom until the glue at the top, is shown in Figure 6.16a. The individual $LaAlO_3$ and $SrTiO_3$ layers show highly perfect single crystalline structures and the epitaxial relation is maintained over the total superlattice. A constant thickness can be seen for each of the individual layers.

A selected area electron diffraction (SAED) pattern, taken from the area including the superlattice as well as the $SrTiO_3$ substrate is shown in Figure 6.16b, which was recorded with the electron beam direction parallel to the (100) zone axis of the $SrTiO_3$ substrate. It is identified to be a superposition of a (100) zone SAED pattern of the cubic $SrTiO_3$ substrate and a (100) zone SAED pattern of the $[(LaAlO_3)_{10}/(SrTiO_3)_{11}]_{10}$ superlattice. Satellite reflections of the superlattice, corresponding to a periodicity of ~81 Å along the growth direction, can be seen close to the $SrTiO_3$ substrate reflections.

TEM-analysis, at a higher magnification, of the first couple of superlattice layers on the $SrTiO_3$ substrate is shown in Figure 6.16c. Although, the crystalline quality of the individual $LaAlO_3$ and $SrTiO_3$ layers and the epitaxial relation between them can clearly be extracted from this image, it's not possible to extract any detailed information about the atomic arrangement at the interfaces. The limited resolution, determined by the instrument, prevents the analysis of the interfaces on the atomic scale.

Therefore, high-resolution transmission electron microscopy (HRTEM)[III] was used to provide more detailed information, which can be achieved due to a point-resolution of 1.7 Å. While analyzing the superlattice on the atomic scale, some structural imperfections become visible. Interface dislocations are occasionally found, see Figure 6.17a. The appearance of dislocations at these interfaces can be expected

[II] Specimen preparation and transmission electron microscopy measurements were performed at the Central Materials Analysis Laboratory ($MESA^+$, Twente University).

[III] High-resolution transmission electron microscopy measurements and scanning transmission electron microscopy measurements were performed at the EMAT research centre (University of Antwerp, Belgium).

because of the in-plane misfit (~3%) between both materials, $LaAlO_3$ and $SrTiO_3$. Besides this, also abrupt variations in the image structure are visible, see Figure 6.17b. These vague spots with different structure can also be distinguished in the total superlattice TEM-image in Figure 6.16a. Although, these variations suggest intermixing of both superlattice layers, it's very unlikely that outgrowth of one layer has occurred this far into the other layer. Presumably, the specimen preparation procedure has caused these defects at the cross-sectional surface.

Although HRTEM is an excellent technique to study the atomic structure of thin films and multilayers, it's always difficult to determine the stacking sequence of the atomic layers at the interface between two materials. In this case the difficulty is due to the strong similarities between $SrTiO_3$ and $LaAlO_3$ (both materials are perovskites and they have almost the same lattice parameters), but also because of

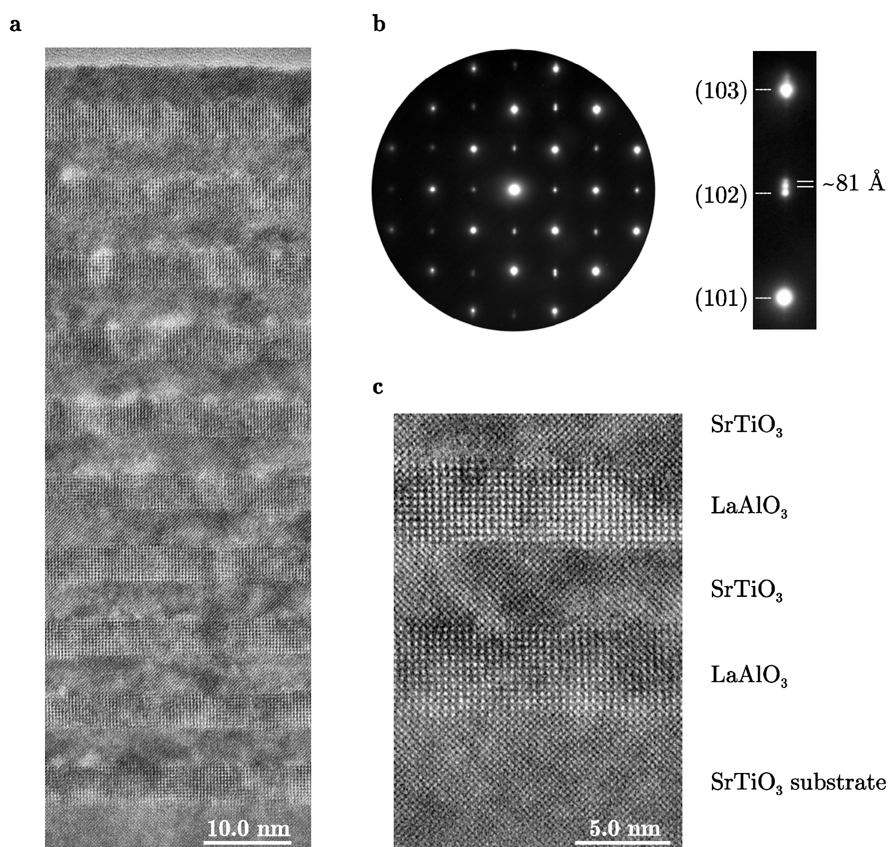

Figure 6.16 Transmission electron microscopy analysis of a $[(LaAlO_3)_{10}/(SrTiO_3)_{11}]_{10}$ superlattice. **(a)** Overview TEM image of the total superlattice. **(b)** Selected area electron diffraction pattern of the structure as shown in Figure 6.16a with a close-up near the (102) reflection of the $SrTiO_3$ substrate displaying some superlattice satellite peaks. **(c)** Detailed analysis of the first superlattice layers at the $SrTiO_3$ substrate.

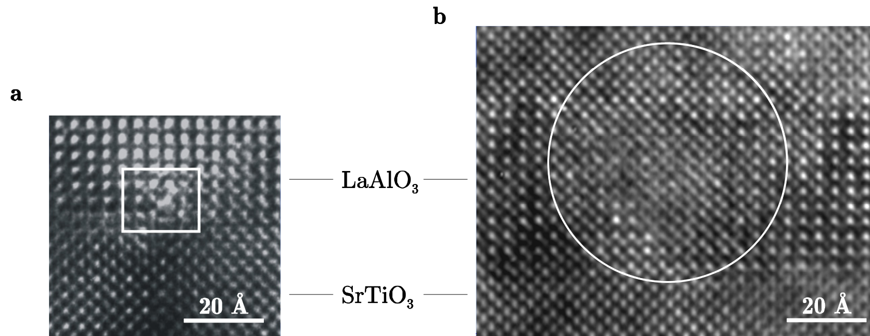

Figure 6.17 High-resolution transmission electron microscopy analysis of a $[(LaAlO_3)_{10}/(SrTiO_3)_{11}]_{10}$ superlattice. **(a)** Misfit dislocation at the TiO_2/LaO-interface. **(b)** Abrupt structural variation suggesting possible intermixing of superlattice layers.

the dynamical image formation process when using HRTEM. To determine the sequence of the atomic layers at an interface, high-angle annular dark field imaging by scanning transmission electron microscopy (HAADF-STEM)[III] is a far more beneficial technique. Using this technique, the electrons are focused to a very fine probe of 2.0 Å and after interaction with the sample, an annular detector is used to collect those electrons scattered under very large angles, starting from approximately 50 mrad. In this manner images are obtained in which the intensity is sensitive to the atomic number Z [124,131-135]:

$$I_{atom} \propto Z^n, \tag{6.5}$$

which is correct in the high angle limit ($1<n<2$) with an atomic number Z of 57, 38, 22, 13 and 8 for respectively La, Sr, Ti, Al and O. Figure 6.18a shows a HAADF-STEM image, taken along the (100) zone axis. It can be seen that the different layers are clearly separated and the $LaAlO_3$ appears with a higher intensity compared to the $SrTiO_3$ layers. This can be expected because of the higher average Z value for $LaAlO_3$ compared to $SrTiO_3$. No large outgrowth of one material into the other is observed, as was suggested by the structure variations in Figure 6.17b. An image taken at a larger magnification is presented as well in Figure 6.18b. It must be noted that this image represents the raw data, which is in contrast to most publications found in literature, where mostly Wiener filtered HAADF-STEM images are presented. In the image, the La and Sr atoms are most apparent, whereas it is more difficult to visualize and distinguish the Ti and the Al atoms. The expected differences in intensity between all the individual atoms are displayed in the simulated TEM-image in Figure 6.19a. The positions of the atoms in the heteroepitaxial structure were calculated by using the bulk lattice parameters. An ideal perovskite structure (ABO_3) was taken without the influence of in-plane strain and any resulting unit cell deformation. The weaker Al- and Ti-atoms are positioned

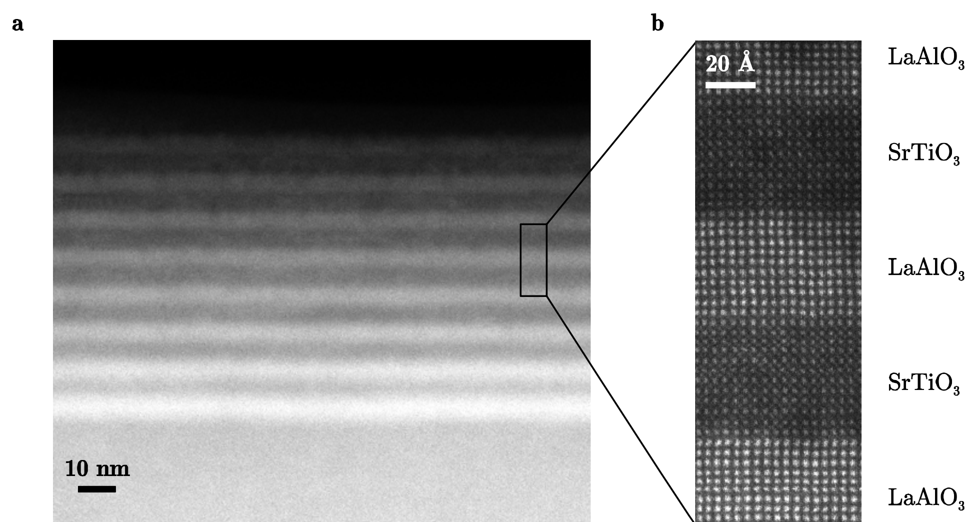

Figure 6.18 High-angle annular dark field image acquired by scanning transmission electron microscopy of a $[(LaAlO_3)_{10}/(SrTiO_3)_{11}]_{10}$ superlattice. **(a)** Clear intensity differences between separate $LaAlO_3$ and $SrTiO_3$ layers. **(b)** Close-up showing distinctly the individual La and Sr atoms.

in the center between respectively the brighter La- and Sr-atoms. Horizontal rows of atoms in crystallographic identical positions are shown in Figure 6.19b. The top scan displays the intensity of the atoms on the A-site, while in the bottom scan the B-site atoms are given. Although, the difference in intensity between the La- and Sr-atoms is rather large, which was already observed in Figure 6.18, the difference in intensity between the Al- and Ti-atoms is already difficult to detect in the ideal case. This makes it difficult to distinguish the conducting LaO-TiO_2 interface (X_A) from the insulating SrO-AlO_2 interface (X_B). To improve the analysis of the atomic stacking sequences at the interfaces, as shown in Figure 6.18, the signal-to-noise ratio was increased by averaging over a larger area in the TEM-image. However, due to some drift during acquisition this procedure wasn't successful.

Therefore, the superlattice was analyzed by HAADF-STEM in a state-of–the-art Titan microscope[IV], which holds a point-resolution of 0.7 Å and a very high stability. This stability results in a large reduction of drift, see Figure 6.20a. The atomic stacking sequences at the interfaces were investigated by averaging over the area indicated by the white rectangle in Figure 6.20a. This part of the image was divided into smaller sub-sections, which were added after cross correlation in Figure 6.20b. To quantitatively evaluate the peak heights and positions of the atom columns,

[IV] HAADF-STEM at the Titan 80-300 microscope was performed at FEI company (Eindhoven, The Netherlands).

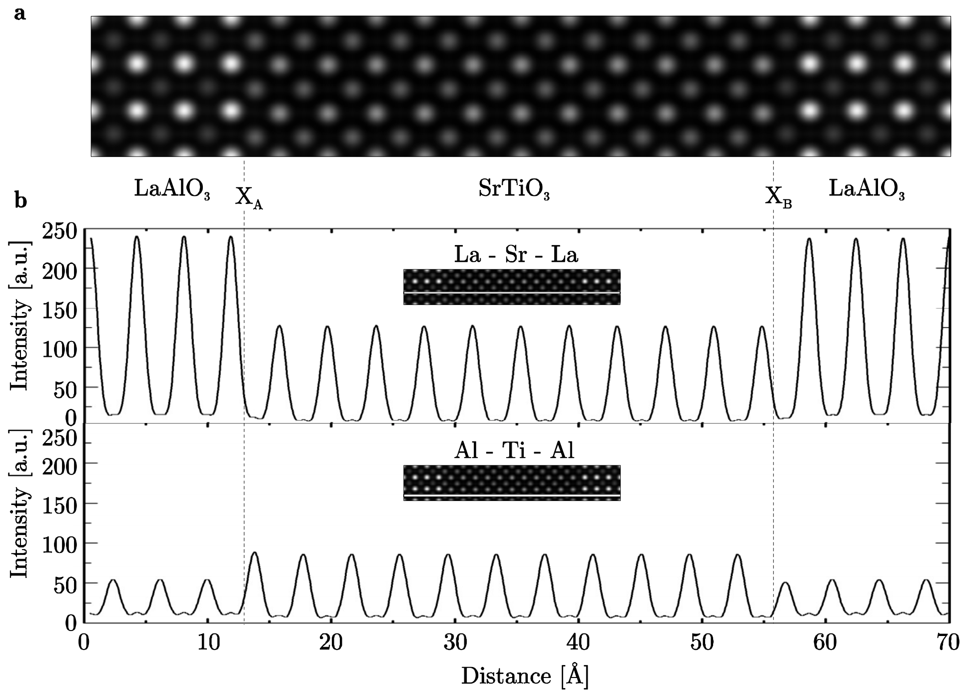

Figure 6.19 Simulated HAADF-STEM analysis of a $[(LaAlO_3)_{10}/(SrTiO_3)_{11}]_{10}$ superlattice. **(a)** Ordering of the atoms in an ideal heteroepitaxial perovskite structure. **(b)** Horizontal line-scans of the La- and Sr-atoms on the A-site in the perovskite structure (top) as well as the Al- and Ti-atoms on the B-site (bottom).

statistical parameter estimation was used, in which a parametric model of Gaussian peaks was fitted to Figure 6.20b in the least-squares sense[V]. This model can be described by the following function:

$$f_{kl}(\tau) = \zeta + \sum_{i=1}^{5} \sum_{m_i=1}^{M_l} \alpha_i \exp\left(\frac{-(x_k - \beta^x_{m_i})^2 - (y_l - \beta^y_{m_i})^2}{2\rho_i^2}\right), \tag{6.6}$$

with ζ the constant background, α_i the peak height, ρ_i the width of the Gaussian peak and $(\beta^x_{m_i}, \beta^y_{m_i})$ the atom position, which had to be determined for each type of atom (i corresponds to La, Sr, Al, Ti and X_A/X_B). The estimated parameters, corresponding to the minimum of the least squares sum of the applied model, were used to construct calculated HAADF-STEM images of both interfaces.

[V] Quantitative analysis of the HAADF-STEM images by statistical parameter estimation was performed at the EMAT research centre (University of Antwerp, Belgium).

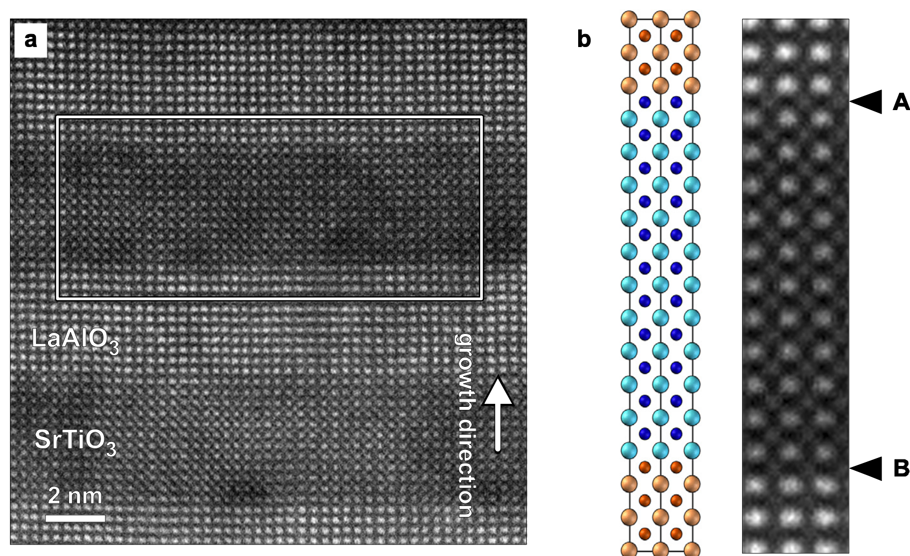

Figure 6.20 High-resolution, high-stability scanning transmission electron microscopy analysis of the atomic stacking sequences at the interfaces. **(a)** HAADF-STEM image of the $[(LaAlO_3)_{10}/(SrTiO_3)_{11}]_{10}$ superlattice. The area of the image indicated by the white rectangle is used for averaging. **(b)** Image showing the result of the averaging procedure, together with the atomic representation of the structure. The interfaces are indicated with A and B.

These models of the atomic ordering are shown in Figure 6.21 next to the results of the averaged measurements for interfaces A and B, as indicated in Figure 6.20b. To evaluate the calculated atom positions, both images are combined by overlaying circles, which indicated the calculated atom positions, on the measured intensities. This results in a close fit between the model and the measurements, although the estimated positions of the Al-atoms for interface B are shifted towards the tails of the heavier La-atoms. This is most likely a small discrepancy in the fitting procedure, due to the high intensity and large width of the La-peaks. The in-plane distances between the cations seemed to be constant throughout the superlattice ($a_{STO} \approx a_{LAO}$), while the average value for the out-of-plane distance between the Sr-atoms (c_{STO}/a_{STO}) was determined to be 1.00±0.01. This value was also observed for the average distance between the Ti-atoms. However, the average value for the distance between the La-atoms (c_{LAO}/a_{LAO}) was 0.96±0.01, which agrees rather well with the observed shortening of the c-axis in each $LaAlO_3$ layer in the superlattice by x-ray diffraction. An accurate value for the distances between the Al-atoms could not be determined, due to the strong influence of the nearby heavier La-atoms, which intensities are much larger.

To determine the atomic stacking sequence at each interface to be either AlO_2-SrO or LaO-TiO_2, the estimated peak heights for atom columns X_A and X_B were compared to the peak heights of the known atom columns of La, Sr, TiO and AlO,

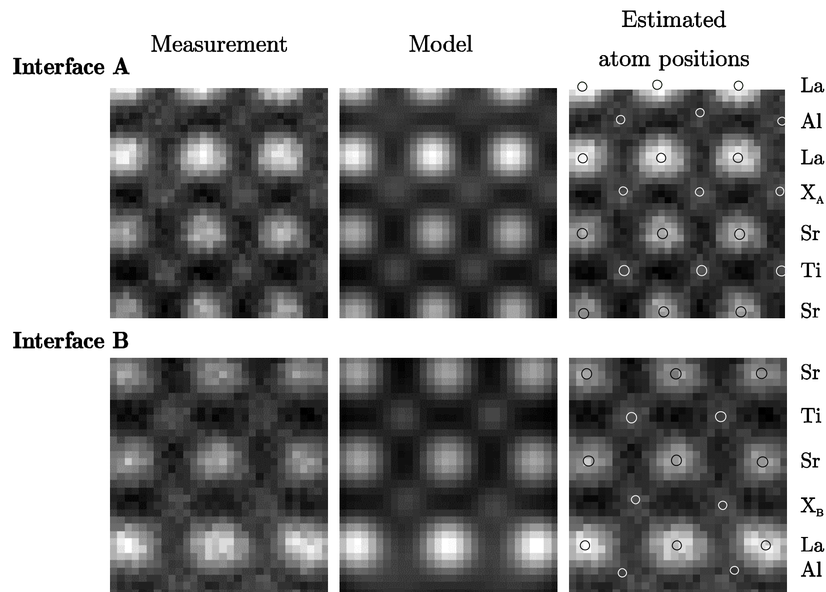

Figure 6.21 Quantitative analysis of the atomic ordering at interfaces A and B, as indicated in Figure 6.20b, by comparing the averaged result of the HAADF-STEM measurements (left) with the calculated parametric model of Gaussian peaks (middle) for the correctness of the estimated atom positions (right).

see Figure 6.22. The 90% confidence intervals, which have been computed using the so-called Cramér-Rao lower bound [136,137], are also given. By comparing the confidence intervals corresponding to the peak height of the atom columns at the interfaces (X_A and X_B) with those of the surrounding TiO/AlO peaks, it can be concluded that the interface on top of every $SrTiO_3$ layer (interface A) is TiO_2-LaO, whereas at the bottom (interface B) it is AlO_2-SrO.

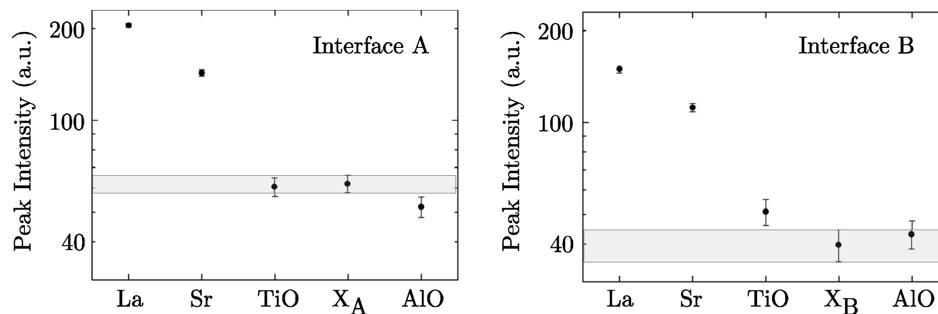

Figure 6.22 Quantitative analysis of the atomic stacking sequences at interfaces A and B, as indicated in Figure 6.20b, by comparing the estimated peak heights of the known La, Sr, TiO and AlO atom columns with the unknown atom columns at the interfaces (X_A and X_B). The corresponding 90% confidence intervals are also shown and intensified by colored bands for the atom columns at the interfaces (X_A and X_B).

These configurations were also expected from the deposition parameters, in which the superlattice growth was started on a TiO_2-terminated $SrTiO_3$ substrate and ideal BO_2-AO-BO_2-AO perovskite layering was suggested by the 2-dimensional growth mode.

6.5.4 Controlled growth of multilayers with variable thicknesses

Controlling the interface termination layer provides the possibility to tune the 2-dimensional electronic properties between an insulator and a conductor. This control on the atomic scale of the electronic reconstruction at the interface gives the opportunity to improve the performance of existing oxide devices and could even result in new types of devices. However, to study the nature and length scales of these space charge layers at $LaAlO_3/SrTiO_3$ interfaces, multilayer structures have to be fabricated with atomically abrupt interfaces, while the thicknesses of the individual layers are controlled. Using RHEED during pulsed laser deposition, the layer growth could be monitored on a sub-unit cell scale, which provides the control to tune the thickness of each individual layer with a unit cell precision. The quality of the final multilayer was investigated by scanning transmission electron microscopy[III] to define the chemical abruptness of the interfaces. Figure 6.23a shows the high-angle annular dark field image of a $LaAlO_3/SrTiO_3$ multilayer with various

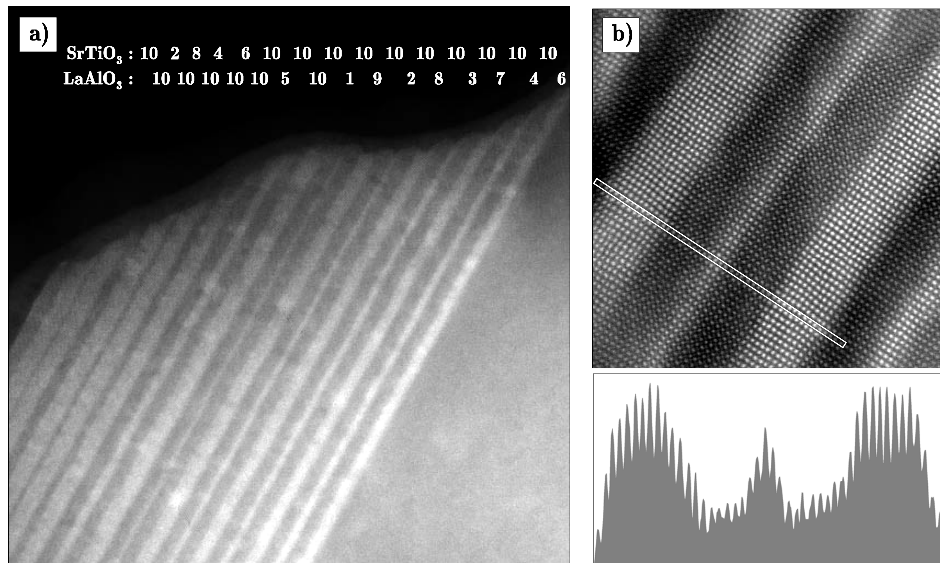

Figure 6.23 High-angle annular dark field image acquired by scanning transmission electron microscopy of a $LaAlO_3/SrTiO_3$ multilayer with various thicknesses of the individual layers. **(a)** Overview of the total heterostructure showing the separate $LaAlO_3$ (bright) and $SrTiO_3$ layers. The thicknesses of the individual layers are indicated in unit cells. **(b)** Detailed analysis of the $LaAlO_3$ layer with a thickness of only one unit cell.

thicknesses for the individual layers. The brightest features are columns of La-atoms, while the weaker features correspond to the Sr-atoms. The total multilayer displays epitaxial formation of the crystal structures and the quality of the interfaces does not degrade with continued deposition. The magnified view in Figure 6.23b shows a higher-resolution image, which visibly demonstrates the ability to control the thicknesses on a unit-cell scale.

6.6 Conclusions

The electronic properties of the heteroepitaxial interfaces between $LaAlO_3$ and $SrTiO_3$ were found to be very sensitive to the atomic stacking sequence. An accurate control of the atomic configuration at the interface can tune the conductivity of the 2-dimensional system between metallic and insulating. Whereas $SrTiO_3$ and $LaAlO_3$ are seemingly similar, the $Sr^{2+}O^{2-}$ and $Ti^{4+}O^{2-}_2$ layers are charge-neutral, while in the ionic limit the charge states in the $LaAlO_3$ are positive for $La^{3+}O^{2-}$ and negative for $Al^{3+}O^{2-}_2$. The polarity discontinuity at the interfaces leads to a metallic conductivity for the 'n-type' LaO-TiO_2 interface, where by electronic reconstruction through mixed valence Ti states extra electrons are placed in the $SrTiO_3$ conduction band. In the other case, the AlO_2-SrO interface was found to be insulating. Still 'p-charging' is conceivable, which results most likely in an atomic reconstruction by the introduction of oxygen vacancies.

To grow both types of interfaces with an atomic control, the surfaces of the $SrTiO_3$ substrates have to be single terminated by either TiO_2 or SrO. The first can be achieved by a chemical and thermal treatment, while the latter can be obtained by the deposition of an extra monolayer. In both cases the subsequent growth of $LaAlO_3$ is perfectly similar and results in a highly crystalline thin film with a surface of smooth terraces separated by unit cell steps. Due to the in-plane tensile strain in the thin $LaAlO_3$ film, the c-axis parameters are shorter than the bulk values.

The atomic ordering at the heteroepitaxial interface was investigated in-situ directly after growth to obtain structural information at high deposition temperatures without the influences of possible strain relaxation and impurity incorporation. A single unit cell of $LaAlO_3$ on a TiO_2-terminated $SrTiO_3$ substrate was found to adapt to the cubic bulk structure of the substrate at high deposition temperatures, while for lower temperatures the atoms in the $LaAlO_3$ unit cell are displaced from their bulk positions.

Due to the low misfit (~3%) between $LaAlO_3$ and $SrTiO_3$, the epitaxial relation can be used to grow superlattices, which are composed of alternating 'n-type' and 'p-type' interfaces. The observed oscillations in the RHEED monitoring during growth are used to accurately control the thicknesses of the individual layers. Structural analysis indicates a high quality ordering, in both the crystallinity of the total structure as well as the imposed periodicity along the c-axis. The atoms in the

$SrTiO_3$ layers are found to be in their bulk positions, while the c-axis parameter of the $LaAlO_3$ unit cells is shortened due to strain. The expected atomic ordering at both the LaO-TiO_2 and the AlO_2-SrO interfaces was proven by high-quality scanning transmission electron microscopy.

In order to investigate the influence of the layer thicknesses on the abruptness of the interfaces, a multilayer was fabricated with variable thicknesses of the individual $LaAlO_3$ and $SrTiO_3$ layers. In this way, the thickness could be reduced down to a single unit cell of $LaAlO_3$, while maintaining a high-quality atomic ordering.

6.7 References

1. Lüth, H. (Ed.), *Solid Surfaces, Interfaces and Thin Films* (Springer-Verlag, New York, 2001).
2. Ando, T., Fowler, A.B. & Stern, F., *Rev. Mod. Phys.* **54**, 437 (1982).
3. Abrahams, E., Kravchenko, S.V. & Sarachik, M.P., *Rev. Mod. Phys.***73**, 251 (2001).
4. Heinzel, T. (Ed.), *Mesoscopic Electronics in Solid State Nanostructures* (Wiley-VCH, Weinheim, 2003).
5. Mönch, W. (Ed.), *Electronic Properties of Semiconductor Interfaces* (Springer-Verlag, Berlin, 2004).
6. Ihn, T. (Ed.), *Electronic Quantum Transport in Mesoscopic Semiconductor Structures* (Springer-Verlag, New York, 2004).
7. Dingle, R., Störmer, H.L., Gossard, A.C. & Wiegmann, W., *Appl. Phys. Lett.* **33**, 665 (1978).
8. Bao, J.M., Pfeiffer, L.N., West, K.W. & Merlin, R., *Phys. Rev. Lett.* **92**, 236601 (2004).
9. Störmer, H.L. & Tsang, W.-T., *Appl. Phys. Lett.* **36**, 685 (1980).
10. Manfra, M.J., Pfeiffer, L.N., West, K.W., De Picciotto, R. & Baldwin, K.W., *Appl. Phys. Lett.* **86**, 162106 (2005).
11. Gerl, C., Schmult, S., Tranitz, H.-P., Mitzkus, C. & Wegscheider, W., *Appl. Phys. Lett.* **86**, 252105 (2005).
12. Ohtomo, A. & Hwang, H.Y., *Nature* **427**, 423 (2004).
13. Ahn, C.H., Triscone, J.M. & Mannhart, J., *Nature* **424**, 1015 (2003).
14. Dagotto, E., *Science* **309**, 257 (2005).
15. Schooley, J.F., Hosler, W.R. & Cohen, M.L., *Phys. Rev. Lett.* **12**, 474 (1964).
16. Schooley, J.F., Hosler, W.R., Ambler, E., Becker, J.H., Cohen, M.L. & Koonce, C.S., *Phys. Rev. Lett.* **14**, 305 (1965).
17. Binnig, G., Baratoff, A., Hoenig, H.E. & Bednorz, J.G., *Phys. Rev. Lett.* **45**, 1352 (1980).
18. Bednorz, J.G. & Müller, K.A., *Z. Phys. B* **64**, 189 (1986).
19. Cava, R.J., Van Dover, R.B., Batlogg, B. & Rietman, E.A., *Phys. Rev. Lett.* **58**, 408 (1987).
20. Wu, M.K., Ashburn, J.R., Torng, C.J., Hor, P.H., Meng, R.L., Gao, L., Huang, Z.J., Wang, Y.Q. & Chu, C.W., *Phys. Rev. Lett.* **58**, 908 (1987).
21. Chaudhari, P., Koch, R.H., Laibowitz, R.B., McGuire, T.R. & Gambino, R.J., *Phys. Rev. Lett.* **58**, 2684 (1987).
22. Simon, R.W., Platt, C.E., Lee, A.E., Lee, G.S., Daly, K.P., Wire, M.S., Luine, J.A. & Urbanik, M., *Appl. Phys. Lett.* **53**, 2677 (1988).
23. Müller, K.A. & Burkard, H., *Phys. Rev. B* **19**, 3593 (1979).
24. Young, K.H., Negrete, G.V., Eddy, M.M., Sun, J.Z., James, T.W., Robinson, McD. & Smith, E.J., *Thin Solid Films* **206**, 116 (1991).
25. Kingon, A.I., Maria, J.-P. & Streiffer, S.K., *Nature* **406**, 1032 (2000).

26. Abramov, Y.A., Tsirelson, V.G., Zavodnik, V.E., Ivanov, S.A. & Brown, I.D., *Acta Cryst. B* **51**, 942 (1995).
27. Yamanaka, T., Hirai, N. & Komatsu, Y., *Am. Mineral.* **87**, 1183 (2002).
28. Cowley, R.A., *Phys. Rev.* **134**, A981 (1964).
29. Unoki, H. & Sakudo, T., *J. Phys. Soc. Jpn.* **23**, 546 (1967).
30. Müller, K.A., Berlinger, W. & Waldner, F., *Phys. Rev. Lett.* **21**, 814 (1968).
31. Shirane, G. & Yamada, Y., *Phys. Rev.* **177**, 858 (1969).
32. Lehnert, H., Boysen, H., Dreier, P. & Yu, Y., *Z. Kristallogr.* **215**, 145 (2000).
33. Lehnert, H., Boysen, H., Schneider, J., Frey, F., Hohlwein, D., Radaelli, P. & Ehrenberg, H., *Z. Kristallogr.* **215**, 536 (2000).
34. Geller, S. & Bala, V.B., *Acta Crystallogr.* **9**, 1019 (1956).
35. Scott, J.F., *Phys. Rev.* **183**, 823 (1969).
36. Geller, S. & Raccah, P.M., *Phys. Rev. B* **2**, 1167 (1970).
37. O'Bryan, H.M., Gallagher, P.K., Berkstresser, G.W. & Brandle, C.D., *J. Mater. Res.* **5**, 183 (1990).
38. Bueble, S., Knorr, K., Brecht, E. & Schamhl, W.W., *Surf. Sci.* **400**, 345 (1998).
39. Chakoumakos, B.C., Schlom, D.G., Urbanik, M. & Luine, J., *J. Appl. Phys.* **83**, 1979 (1998).
40. Howard, C.J., Kennedy, B.J. & Chakoumakos, B.C., *J. Phys.* **12**, 349 (2000).
41. Hayward, S.A., Morrison, F.D., Redfern, S.A.T., Salje, E.K.H., Scott, J.F., Knight, K.S., Tarantino, S., Glazer, A.M., Shuvaeva, V., Daniel, P., Zhang, M. & Carpenter, M.A., *Phys. Rev. B* **72**, 054110 (2005).
42. Rijnders, A.J.H.M., *The initial growth of complex oxides: study and manipulation*, Chapter 2, PhD thesis, University of Twente, The Netherlands (2001).
43. Kroemer, H., *J. Cryst. Growth* **81**, 193 (1987).
44. Baraff, G.A., Appelbaum, J.A. & Hamann, D.R., *Phys. Rev. Lett.* **38**, 237 (1977).
45. Harrison, W.A., Kraut, E.A., Waldrop, J.R. & Grant, R.W., *Phys. Rev. B* **18**, 4402 (1978).
46. Wang, T., Moll, N., Cho, K. & Joannopoulos, J.D., *Phys. Rev. Lett.* **82**, 3304 (1999).
47. Kawasaki, M., Takahashi, K., Maeda, T., Tsuchiya, R., Shinohara, M., Ishiyama, O., Yonezawa, T., Yoshimoto, M. & Koinuma, H., *Science* **266**, 1540 (1994).
48. Koster, G., Kropman, B.L., Rijnders, G.J.H.M., Blank, D.H.A. & Rogalla, H., *Appl. Phys. Lett.* **73**, 2920 (1998).
49. Koster, G., *Artificially layered oxides by pulsed laser deposition*, PhD thesis, University Twente, The Netherlands (1999).
50. Ohnishi, T., Shibuya, K., Lippmaa, M., Kobayashi, D., Kumigashira, H., Oshima, M. & Koinuma, H., *Appl. Phys. Lett.* **85**, 272 (2004).
51. Kobayashi, D., Kumigashira, H., Oshima, M., Ohnishi, T., Lippmaa, M., Ono, K., Kawasaki, M. & Koinuma, H., *J. Appl. Phys.* **96**, 7183 (2004).
52. Migita, S., Kasai, Y. & Sakai, S., *J. Low Temp. Phys.* **105**, 1337 (1996).
53. Takahashi, R., Matsumoto, Y., Ohsawa, T., Lippmaa, M., Kawasaki, M. & Koinuma, H., *J. Cryst. Growth* **234**, 505 (2002).

54. Koster, G., Rijnders, G.J.H.M., Blank, D.H.A. & Rogalla, H., *Appl. Phys. Lett.* **74**, 3729 (1999).
55. Koster, G., Rijnders, G., Blank, D.H.A. & Rogalla, H., *Physica C* **339**, 215 (2000).
56. Wang, Z.L. & Shapiro, A.J., *Surf. Sci.* **328**, 141 (1995).
57. Wang, Z.L. & Shapiro, A.J., *Surf. Sci.* **328**, 159 (1995).
58. Yao, J., Merrill, P.B., Perry, S.S., Marton, D. & Rabalais, J.W., *J. Chem. Phys.* **108**, 1645 (1998).
59. Kim, D.-W., Kim, D.-H., Kang, B.-S., Woh, T.W., Lee, D.R. & Lee, K.-B., *Appl. Phys. Lett.* **74**, 2176 (1999).
60. McKee, R.A., Walker, F.J. & Chisholm, M.F., *Phys. Rev. Lett.* **81**, 3014 (1998).
61. McKee, R.A., Walker, F.J. & Chisholm, M.F., *Science* **293**, 468 (2001).
62. Klenov, D.O., Schlom, D.G., Li, H. & Stemmer, S., *Jpn. J. Appl. Phys.* **44**, L617 (2005).
63. Först, C.J., Schwarz, K. & Blöchl, P.E., *Phys. Rev. Lett.* **95**, 137602 (2005).
64. Lippmaa, M., Nakagawa, N., Kawasaki, M., Ohashi, S. & Koinuma, H., *Appl. Phys. Lett.* **76**, 2439 (2000).
65. Lee, J.Y., Juang, J.Y., Ou, J.H., Chen, Y.F., Wu, K.H., Uen, T.M. & Gou, Y.S., *Physica B* **284-288**, 2099 (2000).
66. Eres, G., tischler, J.Z., Yoon, M., Larson, B.C., Rouleau, C.M., Lowndes, D.H. & Zschack, P., *Appl. Phys. Lett.* **80**, 3379 (2002).
67. Song, J.H. & Jeong, Y.H., *Sol. State. Comm.* **125**, 563 (2003).
68. Li, Y.R., Li, J.L., Zhang, Y., Wei, X.H., Deng, X.W. & Liu, X.Z., *J. Appl. Phys.* **96**, 1640 (2004).
69. Jia, Q.X., Findikoglu, A.T., Reagor, D. & Lu, P., *Appl. Phys. Lett.* **73**, 897 (1998).
70. Lu, P., Jia, Q.X. & Findikoglu, A.T., *Thin Solid Films* **348**, 38 (1999).
71. Treece, R.E., Thompson, J.B., Mueller, C.H., Rivkin, T. & Cromar, M.W., *IEEE Trans. Appl. Supercond.* **7**, 2363 (1997).
72. Van Keuls, F.W., Romanofsky, R.R., Bohman, D.Y., Winters, M.D., Miranda, F.A., Mueller, C.H., Treece, R.E., Rivkin, T.V. & Galt, D., *Appl. Phys. Lett.* **71**, 3075 (1997).
73. Dalberth, M.J., Stauber, R.E., Price, J.C., Rogers, C.T. & Galt, D., *Appl. Phys. Lett.* **72**, 507 (1998).
74. Petrov, P.K., Carlsson, E.F., Larsson, P., Friesel, M. & Ivanov, Z.G., *J. Appl. Phys.* **84**, 3134 (1998).
75. Bouzehouane, K., Woodall, P., Marcilhac, B., Khodan, A.N., Crété, D., Jacquet, E., Mage, J.C. & Contour, J.P., *Appl. Phys. Lett.* **80**, 109 (2002).
76. Yamada, T., Astafiev, K.F., Sherman, V.O., Tagantsev, A.K., Su, D., Muralt, P. & Setter, N., *J. Appl. Phys.* **98**, 054105 (2005).
77. Hwang, H.Y., Ohtomo, A., Nakagawa, N., Muller, D.A. & Grazul, J.L., *Physica E* **22**, 712 (2004).
78. Nishimura, J., Ohtomo, A., Ohkubo, A., Murakami, Y. & Kawasaki, M., *Jpn. J. Appl. Phys.* **43**, L1032 (2004).

79. Mukunoki, Y., Nakagawa, N., Susaki, T. & Hwang, H.Y., *Appl. Phys. Lett.* **86**, 171908 (2005).
80. Maurice, J.-L., Carretero, C., Casanove, M.-J., Bouzehouane, K., Guyard, S., Larquet, É. & Contour, J.-P., *condmat* 0511123 (2005).
81. Nakagawa, N., Hwang, H.Y. & Muller, D.A., *Nature Materials* **5**, 204 (2006)
82. Huijben, M., Rijnders, G., Blank, D.H.A., Bals, S., Van Aert, S., Verbeeck, J., Van Tendeloo, G., Brinkman, A. & Hilgenkamp, H., *cond-mat* 0603088 (2006).
83. Kalabukhov, A.S., Gunnarsson, R., Borjesson, J., Olsson, E., Claeson, T. & Winkler, D., *cond-mat* 0603501 (2006).
84. Siemons, W., Koster, G., Yamamoto, H., Harrison, W.A., Geballe, T.H., Blank, D.H.A. & Beasley, M.R., *cond-mat* 0603598 (2006).
85. Robinson, I.K., *Handbook on Synchrotron Radiation 3*, Chapter 7 (North-Holland, Amsterdam, 1991), pp. 221-266.
86. Vonk, V., Konings, S., Barthe, L., Gorges, B. & Graafsma, H., *J. Synchr. Rad.* **12**, 833 (2005).
87. Borsboom, M., Bras, W., Cerjak, I., Detollenaere, D., Van Loon, D.G., Goedtkindt, P., Konijnenberg, M., Lassing, P., Levine, Y.K., Munneke, B., Oversluizen, M., Van Tol, R. & Vlieg, E., *J. Synchr. Rad.* **5**, 518 (1998).
88. Vlieg, E., *J. Appl. Cryst.* **31**, 198 (1998).
89. Vonk, V., Konings, S., Van Hummel, G.J., Harkema, S. & Graafsma, H., *Surf. Sci.* **595**, 183 (2005).
90. Vlieg, E., *J. Appl. Cryst.* **33**, 401 (2000).
91. Ruddlesden, S.N., Popper, P., *Acta Cryst.* **11**, 54 (1958).
92. Cohen, R.E., *Nature* **358**, 136 (1992).
93. Haeni, J.H., Irvin, P., Chang, W., Uecker, R., Reiche, P., Li, Y.L., Choudhury, S., Tian, W., Hawley, M.E., Craigo, B., Tagantsev, A.K., Pan, X.Q., Streiffer, S.K., Chen, L.Q., Kirchoefer, S.W., Levy, J. & Schlom, D.G., *Nature* **430**, 758 (2004).
94. Choi, K.J., Biegalski, M., Li., Y.L., Sharan, A., Schubert, J., Uecker, R., Reiche, P., Chen, Y.B., Pan, X.Q., Gopalan, V., Chen, L.-Q., Chlom, D.G. & Eom, C.B., *Science* **306**, 1005 (2004).
95. Esaki, L. & Tsu, R., *IBM J. Res. Devel.* **14**, 61 (1970).
96. Blakeslee, A.E. & Aliotta, C.F., *IBM J. Res. Devel.* **14**, 686 (1970).
97. Esaki, L., Chang, L.L. & Tsu, R., *Proc. 11th Int. Conf. Phys. Semiconductors*, 431 (1972).
98. Tsu, R. (Ed.), *Superlattice to Nanoelectronics* (Elsevier Ltd., Oxford, 2005).
99. Rijnders, G. & Blank, D.H.A., *Nature* **433**, 369 (2005).
100. Norton, D.P., Chakoumakos, B.C., Budai, J.D., Lowndes, D.H., Sales, B.C., Thompson, J.R. & Christen, D.K., *Science* **265**, 2074 (1994).
101. Balestrino, G., Martellucci, S., Medaglia, P.G., Paoletti, A. & Petrocelli, G., *Physica C* **302**, 78 (1998).
102. Tabata, H., Tanaka, H. & Kawai, T., *Appl. Phys. Lett.* **65**, 1970 (1994).
103. Tabata, H. & Kawai, T., *Appl. Phys. Lett.* **70**, 321 (1997).

104. Wang, N., Lu, H.B., Chen, W.Z., Zhao, T., Chen, F., Peng, H.Y., Lee, S.T. & Yang, G.Z., *Appl. Phys. Lett.* **75**, 3464 (1999).
105. Kim, L., Jung, D., Kim, J., Kim, Y.S. & Lee, J., *Appl. Phys. Lett.* **82**, 2118 (2003).
106. Kanno, I., Hayashi, S., Takayama, R. & Hirao, T., *Appl. Phys. Lett.* **68**, 328 (1996).
107. Choi, T. & Lee, J., *Thin Solid Films* **475**, 283 (2005).
108. Jiang, J.C., Pan, X.Q., Tian, W., Theis, C.D. & Schlom, D.G., *Appl. Phys. Lett.* **74**, 2851 (1999).
109. Dawber, M., Lichtensteiger, C., Cantoni, M., Veithen, M., Ghosez, P., Johnston, K., Rabe, K.M. & Triscone, J.-M., *Phys. Rev. Lett.* **95**, 177601 (2005).
110. Christen, H.-M., Boatner, L.A., Budai, J.D., Chisholm, M.F., Géa, L.A., Marrero, P.J. & Norton, D.P., *Appl. Phys. Lett.* **68**, 1488 (1996).
111. Christen, H.-M., Specht, E.D., Norton, D.P., Chisholm, M.F. & Boatner, L.A., *Appl. Phys. Lett.* **72**, 2535 (1998).
112. Gong, G.Q., Gupta, A., Xiao, G., Lecoeur, P. & McGuire, T.R., *Phys. Rev. B* **54**, R3742 (1996).
113. Ueda, K., Tabata, H. & Kawai, T., *Science* **280**, 1064 (1998).
114. Izumi, M., Nakazawa, K., Bando, Y., Yoneda, Y. & Terauchi, H., *Solid State Ionics* **108**, 227 (1998).
115. Izumi, M., Murakami, Y., Konishi, Y., Manako, T., Kawasaki, M. & Tokura, Y., *Phys. Rev. B* **60**, 1211 (1999).
116. Takahashi, K.S., Kawasaki, M. & Tokura, Y., *Appl. Phys. Lett.* **79**, 1324 (2001).
117. Ueda, K., Saeki, H., Tabata, H. & Kawai, T., *Solid State Commun.* **116**, 221 (2000).
118. Murugavel, P., Saurel, D., Prellier, W., Simon, Ch. & Raveau, B., *Appl. Phys. Lett.* **85**, 4424 (2004).
119. Murugavel, P., Padhan, P. & Prellier, W., *Appl. Phys. Lett.* **85**, 4992 (2004).
120. Murugavel, P., Singh, M.P., Prellier, W., Mercey, B., Simon, Ch. & Raveau, B., *J. Appl. Phys.* **97**, 103914 (2005).
121. Singh, M.P., Prellier, W., Simon, Ch. & Raveau, B., *Appl. Phys. Lett.* **87**, 022505 (2005).
122. Warusawithana, M.P., Colla, E.V., Eckstein, J.N. & Weissman, M.B., *Phys. Rev. Lett.* **90**, 036802 (2003).
123. Lee, H.N., Christen, H.M., Chsiholm, M.F., Rouleau, C.M. & Lowndes, D.H., *Nature* **433**, 395 (2005).
124. Ohtomo, A., Muller, D.A., Grazul, J.L. & Hwang, H.Y., *Nature* **419**, 378 (2002).
125. Fuchs, D., Adam, M., Schweiss, P. & Schneider, R., *J. Appl. Phys.* **91**, 5288 (2002).
126. Keim, E.G., Bijker, M.D. & Lodder, J.C., *J. Vac. Sci Technol. A* **19**, 1191 (2001).
127. Amelinckx, S., Van Dyck, D., Van Landuyt, J. & Van Tendeloo, G. (Eds.), *Electron Microscopy: Principles and Fundamentals* (VCH, Weinheim, 1997).
128. Zhang, X.-F. & Zhang, Z. (Eds.), *Progress in Transmission Electron Microscopy 1: Concepts and Techniques* (Springer-Verlag, Berlin, 2001).
129. Spence, J.C.H. (Ed.), *High-Resolution Electron Microscopy* (Oxford University Press, New York, 2003).

130. De Graef, M. (Ed.), *Introduction to Conventional Transmission Electron Microscopy* (Cambridge University Press, Cambridge, 2003).
131. Pennycook, S.J. & Jesson, D.E., *Ultramicroscopy* **37**, 14 (1991).
132. Browning, N.D., Chisholm, M.F. & Pennycook, S.J., *Nature* **366**, 143 (1993).
133. James, E.M. & Browning, N.D., *Ultramicroscopy* **78**, 125 (1999).
134. Delby, N., Krivanek, O.L., Nellist, P.D., Batson, P.E. & Lupini, A.R., *J. Electron Microsc.* **50**, 177 (2001).
135. Muller, D.A., Nakagawa, N., Ohtomo, A., Grazul, J.L. & Hwang, H.Y., *Nature* **430**, 657 (2004).
136. Den Dekker, A.J., Van Aert, S., Van den Bos, A. & Van Dyck, D., *Ultramicroscopy* **104**, 83 (2005).
137. Van Aert, S., Den Dekker, A.J., Van den Bos, A., Van Dyck, D. & Chen, J.H., *Ultramicroscopy* **104**, 107 (2005).

Chapter 7

Electronic properties of single and coupled $LaAlO_3/SrTiO_3$ interfaces

Abstract

Studies on single epitaxial connections between the two wide-bandgap insulators $LaAlO_3$ and $SrTiO_3$ have revealed them to be either high-mobility electron conductors or insulating, depending on the atomic stacking sequences. In the latter case they are conceivably positively charged. In electronically coupled complementary interfaces in $SrTiO_3$-$LaAlO_3$ thin film multilayer structures, a critical separation distance was found of 6 perovskite unit cell layers, corresponding to approximately 23 Å, below which a decrease of the interface conductivity and carrier density occurs. Interestingly, the high carrier mobilities characterizing the separate electron doped interfaces are found to be maintained in coupled structures down to sub-nanometer interface spacing.

7.1 Introduction

Interface physics of strongly correlated oxides is a rapidly developing branch of materials science. In heterostructures of ultrathin correlated oxide films, charge and spin states are reconstructed at the interfaces and hence affect the electronic and magnetic properties of the entire system. The ability to control both the atomic structure and composition of these oxide layers as well as their interfaces is emerging as one of the major challenges for the development of oxide-based electronic devices with a range of functional properties. Recent studies on atomically controlled oxide heterostructures have shown that the fundamental limits for physical quantities can now be explored, such as the fundamental size limits for ferroelectricity in ultrathin perovskite films [1-3]. Other examples of the importance of atomic control at the

interface are the enhancements of ferroelectricity [4,5] and ferromagnetism [6] up to room temperature. It has also been demonstrated that space charge layers can be produced at artificial heteroepitaxial interfaces, which result in conducting interfaces with high carrier mobility in between two insulators [7,8]. The fundamental issue for these new phenomena of correlated electron behavior at the interfaces was proposed to be 'electronic reconstruction', where the spreading of charge across a polar/non-polar interface causes variations in the electron density [9].

In order to investigate the behavior of correlated electrons at such interfaces, heteroepitaxial interfaces between the band-insulators $LaAlO_3$ and $SrTiO_3$ were investigated. The fabrication procedure and structural properties of single interfaces, superlattices and multilayers of these two compounds are already mentioned in Chapter 6. In this chapter the analysis will be described of the electronic properties of single interfaces as well as several interfaces in $LaAlO_3/SrTiO_3$ heterostructures. A detailed analysis of the coupling between two complementary interfaces will provide new information on the transport properties, such as resistance, carrier density and mobility, as a function of the separation distance between the interfaces.

7.2 Electronic properties of single interfaces

The investigated materials, $LaAlO_3$ and $SrTiO_3$, belong to the perovskite structural family. Perovskite oxides are commonly described in terms of their cubic unit cells, with the generic formula ABO_3. It is also very instructive to describe the perovskites in terms of their constituting AO and BO_2 layering sequence in the three principal directions. For example, whereas $SrTiO_3$ and $LaAlO_3$ are seemingly similar, the $Sr^{2+}O^{2-}$ and $Ti^{4+}O^{2-}{}_2$ layers are charge-neutral, while in the ionic limit the charge states in the $LaAlO_3$ are positive for $La^{3+}O^{2-}$ and negative for $Al^{3+}O^{2-}{}_2$, see section 6.2 in Chapter 6.

In perovskite heterostructures the AO-BO_2 stacking sequence is maintained, and consequently a polarity discontinuity arises at the $LaAlO_3$-$SrTiO_3$ interface, see Figure 7.1. Unlike conventional semiconductors where each ion has a fixed valence, in complex oxides compositional roughening is not the only option for charge rearrangement, but mixed valence charge compensation can also occur if electrons can be redistributed al lower energy cost than redistributing ions. This results in the net transfer of electrons per two-dimensional unit cell from $LaAlO_3$ to $SrTiO_3$ across the interface. The extra electrons at the LaO-TiO_2 interface were confirmed by metallic conductivity and Hall measurements by Ohtomo and Hwang [8]. The induced interface charges at this 'n-type' interface are compensated by electronic reconstruction conceivably through mixed-valence Ti states (Ti^{4+} to Ti^{3+}) that place extra electrons in the $SrTiO_3$ conduction band. The analogous construction of the AlO_2-SrO interface must now acquire extra holes per two-dimensional unit cell to maintain charge neutrality. This interface is formally called 'p-type'. Electrically,

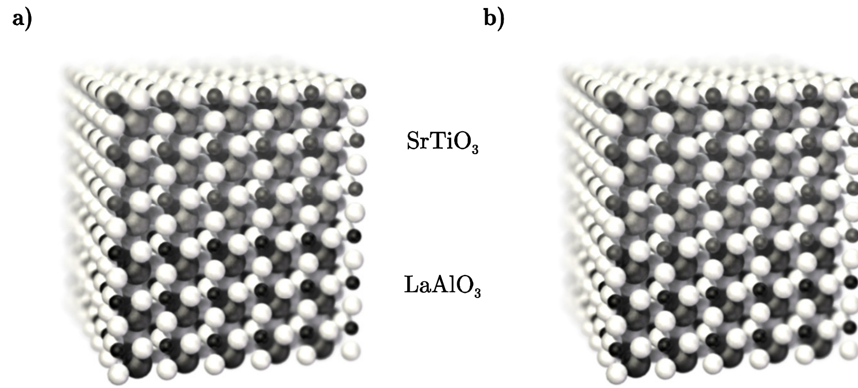

Figure 7.1 Schematic models of the two possible interfaces between $SrTiO_3$ and $LaAlO_3$ in the (001)-direction. The resulting $(LaO)^+/(TiO2)^0$ **(a)** and $(AlO2)^-/(SrO)^0$ interfaces **(b)**, showing the composition and the ionic charge state of each layer.

however, this interface was insulating [8]. As this p-charging is still conceivable and there are no available mixed valence states to compensate the holes, an atomic reconstruction is required and will most likely be formed by the introduction of oxygen vacancies.

7.2.1 Transport properties

The difference in the temperature dependent resistance between the two types of $LaAlO_3/SrTiO_3$ interfaces is very large, see Figure 6.8 in Chapter 6. A small change on the atomic scale in the termination of the $SrTiO_3$ substrate induces a transition from a metallic-like LaO-TiO_2 interface to an insulating AlO_2–SrO interface. The difference in resistance at 300 K is a factor of ~10^3 and goes to infinity for low temperatures. This distinct behavior, between the two interfaces, was already mentioned by Ohtomo and Hwang [8], but only the conducting LaO-TiO_2 interface was further investigated in their case. They noted that when a fraction of a monolayer of SrO was deposited on to the TiO_2-terminated $SrTiO_3$ substrate before $LaAlO_3$ growth, the carrier density decreased proportionally with increasing SrO coverage from 0 to 1 monolayer. This effect was investigated in more detail by Nishimura et al. [10], where they varied the interfacial layer sequence between the two extreme cases, as given above, by inserting various fractional layers of SrO through a sliding mask technique to integrate several samples in a single experimental run. By changing the SrO coverage from 0 to 1, the electron density was controlled from a value corresponding to 0.5 electrons per Ti site to zero. This decrease in carrier density with SrO coverage displayed a systematic increase in sheet resistance. However, no systematic change could be observed in the temperature dependence of the mobility. All samples showed similar scattering behavior and the conductivity was just determined by the carrier density. Still, an

abrupt change in the resistance could be observed when varying the SrO coverage from 0.83 to 1.0. The conductivity behavior changes dramatically from metallic-like to insulating and, therefore, no carrier density and mobility was determined for a SrO coverage of precisely 100%. This suggests that a very well controlled growth of precisely 1 monolayer of SrO is necessary to fabricate the insulating AlO_2–SrO interface. At 0.83 of a monolayer of SrO the probability of electrons to find a percolation path to induce conductivity is still too high.

To investigate in more detail the difference in transport properties between the conducting LaO-TiO_2 interface and the insulating AlO_2–SrO interface, single interfaces of these types were fabricated by pulsed laser deposition. The growth procedure as well as the structural properties, of such single interfaces, has been described already in section 6.3 of Chapter 6. These single interfaces were measured in a 4-wire configuration by wire-bonding contacts to unstructured 10 nm thick $LaAlO_3$ thin films with the voltage contacts only 200 μm apart. This contacting method induces locally some damage to the thin film and is therefore very useful for contacting the buried conducting layer at the interface. The IV-characteristics of these two interfaces are shown in Figure 7.2a, where a large difference is clearly visible in total current, which can be send through the interfaces. For the metallic-like LaO-TiO_2 interface a transition to a higher resistance is observed at a critical current of ~0.75 mA. Such a transition was not observed for the 'almost'-insulating AlO_2–SrO interface. Although, a detailed analysis of the dV/dI-characteristic still exhibited some irregularities, see Figure 7.2b and c. An increase in the voltage induces a decrease in the dV/dI-values with a minimum for ~3.3 V, which suggests

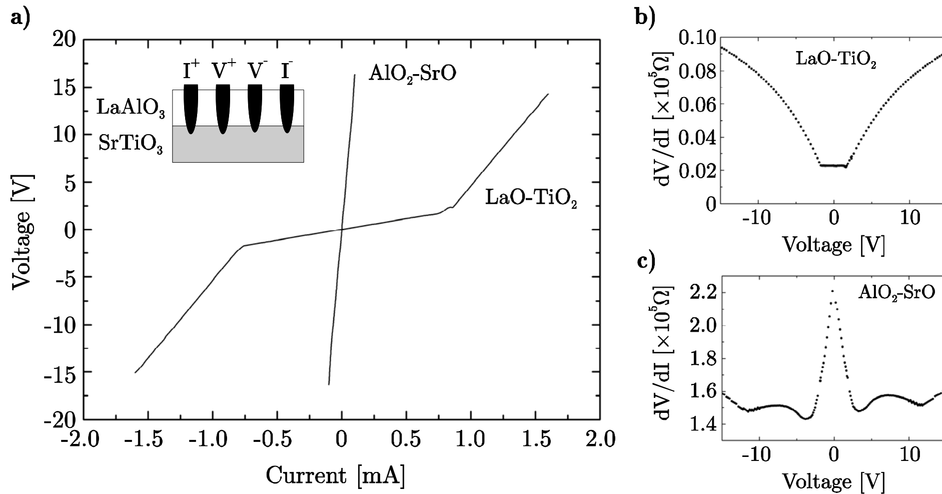

Figure 7.2 Transport properties of single $LaAlO_3$-$SrTiO_3$ interfaces at 300 K. **(a)** IV-characteristics of a conducting LaO-TiO_2 interface and an 'almost'-insulating AlO_2–SrO interface. Calculated dV/dI-values for the LaO-TiO_2 interface **(b)** and the AlO_2–SrO interface **(c)**.

the excitation of charge carriers from the valence band to the conduction band in $SrTiO_3$ [11].

Directional resistivity anisotropy

When the interface conductivity is truly 2-dimensional, terrace steps on the $SrTiO_3$ substrate of one unit cell height will have a large influence on the scattering process. Therefore, a 10 nm thick $LaAlO_3$ layer on a $SrTiO_3$ substrate with a conducting LaO-TiO_2 interface was investigated by structuring several transport geometries under different angles to the step edges, see Figure 7.3a. The geometries were created by a combination of photolithography and rotational argon ion etching, to produce a homogeneous measurement structure. The rotational argon ion etching was performed under an angle of 45 degrees and was optimized to remove locally the $LaAlO_3$ layer without etching to far into the $SrTiO_3$ substrate. This was important because the etching procedure will induce oxygen vacancies in the $SrTiO_3$ layer and create a conducting surface layer. Keeping the etch depth in the $SrTiO_3$ substrate below 5 nm prevented this effect and produced highly insulating $SrTiO_3$ surfaces[I].

The single TiO_2-terminated $SrTiO_3$ substrate had a miscut of ~0.21°, which implies an average distance between the individual terrace steps of ~100 nm. The quality of the initial substrate surface and the orientation of the terrace steps, also shown in Figure 7.3a, were determined by atomic force microscopy and x-ray diffraction. The surface of the 10 nm thick $LaAlO_3$ layer displayed atomically smooth terraces with unit cell steps, similar to the initial substrate. To make contacting of all the geometries possible, a 5nm thick Au layer was deposited on all contact paths by photolithography and sputter deposition. This is necessary, because it's very difficult to observe a structure with only 10 nm height differences under the microscopes of the wire-bonder and the cryogenic probestation.

To determine the resistance for all geometries, the individual IV-characteristics were measured by sweeping the bias current from +2 μA to –2 μA, while monitoring the voltage. All IV-measurements displayed a perfect straight line and no transition to another resistance value was observed. No clear anisotropy was observed in the measured sheet resistance with respect to the direction of the substrate terrace steps when the $LaAlO_3$ layers were grown on perfectly treated TiO_2-terminated $SrTiO_3$ substrates, see Figure 7.3b. This suggests a scattering behavior of the electrons, which is not perfectly 2-dimensional, but will extend over a layer thickness of at

[I] The induced surface conductivity, which is a result from the creation of oxygen vacancies in the $SrTiO_3$ substrate by argon ion etching over a large depth (> 5 nm), can be eliminated by either a thermal treatment for 1-2 hours at 450 °C in a flow of oxygen or a treatment by oxygen ion etching, which will remove slowly the top surface without the formation of oxygen vacancies.

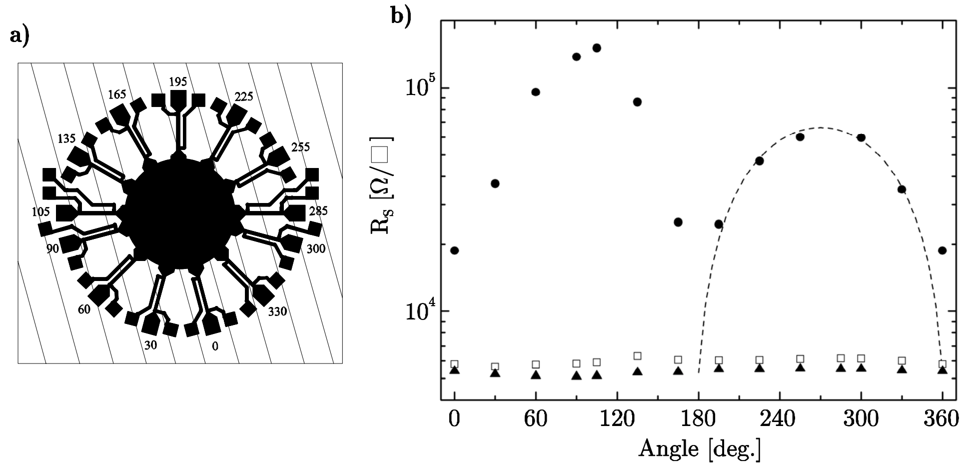

Figure 7.3 Resistivity anisotropy experiments on a LaO-TiO_2 interface at 300 K. **(a)** Schematic of the measurement geometries with a constant length of 500 μm and width of 50 μm. The values for the angle towards the terrace step direction (α) are also indicated. **(b)** The angle dependence of the sheet resistance is displayed for two samples with a $LaAlO_3$ layer on a perfectly single TiO_2-terminated $SrTiO_3$ substrate (□ and ▲) and one sample where the initial $SrTiO_3$ substrate was most likely double terminated with some SrO formed at the terrace steps (●). The dashed line gives a fit to the measured data.

least several unit cells. Only in case of a double terminated $SrTiO_3$ substrate, where most likely extra SrO was formed at the terrace steps, a clear angle dependence was observed in the sheet resistance. This angle dependence was partly fitted by the following equation:

$$R_S(\alpha) = R_0 + \frac{L_0 \sin(\alpha)\tan(\beta)}{c_{STO}} R_{STEP}, \tag{7.1}$$

with L_0 the length of all geometries (500 μm), α the angle between the geometry direction and the terrace step direction, β the miscut of the $SrTiO_3$ substrate (~ 0.21°) and c_{STO} the lattice parameter of the $SrTiO_3$ unit cell (3.905 Å). In this way the resistance contribution of each individual step (R_{STEP}) was determined, while taking the resistance of the terraces (R_0) like the measured values for the samples with the perfect TiO_2-terminated substrates. This results in a close fit to the measured data for R_0 and R_{STEP} values of respectively 5300 and 13 Ω/□. An anisotropy wasn't only observed with respect to the terrace step direction, but also in relation to the position of the geometries on the sample. The geometries with values for α between 0° and 180° showed higher sheet resistances than geometries on the other side. This is probably caused by some kind of inhomogeneity, which can result from the fabrication and structurization process. An effect from measuring up

or down the terrace steps can be excluded, because for every measurement the bias current was swept from negative to positive values and displayed no differences.

The geometries with α angles of 0°, 30°, 60° and 90° were analyzed in more detail by measuring the sheet resistance, while cooling down to low temperatures, see Figure 7.4. All structures displayed a decrease in the sheet resistance down to 100 K, but large differences in the temperature dependence were observed below this temperature. The measurement geometry, which was aligned parallel to the terraces steps (α=0°), shows a slow change in the sheet resistance to a constant value. This sheet resistance curve agrees very well with results from other groups for LaO-TiO_2 interfaces [8,10][II]. The other geometries display an increase in the sheet resistance at low temperatures. For larger α angles this increase in the sheet resistance is larger, but also starts at higher temperatures. This effect can possibly be caused by weak localization [12,13].

Hall effect measurements

One way to separate the carrier density and mobility in the expression for the electrical conductivity is to carry out a Hall effect measurement. The model Hall effect system consists of a uniform slab of electrically conducting material through which a uniform current density flows in the presence of a perpendicular applied magnetic field, see Figure 7.5a. The drift velocity of the moving charges q has

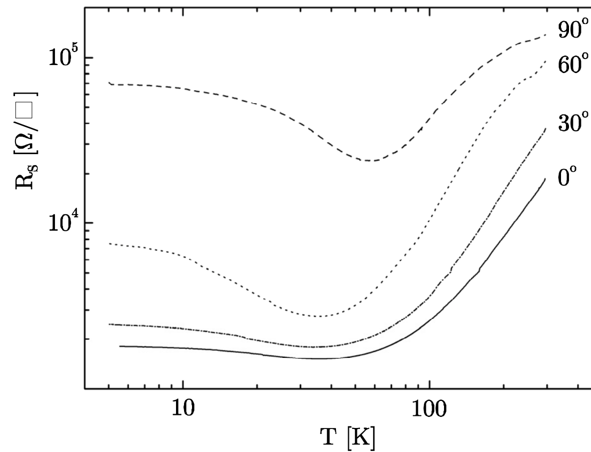

Figure 7.4 Temperature dependence of the sheet resistance for measurement geometries with different angles towards the substrate step direction, as indicated in Figure 7.2a.

[II] Ohtomo and Hwang have indicated that the unit for sheet resistance in their article, ref. 1, should be Ω/□ instead of mΩ/□.

magnitude v_d. The magnetic force ($F_y=|q|v_dB_z$) deflects the moving charge carriers to one side of the sample and generates an electric field perpendicular to both the current density and the applied magnetic field. If the charge carriers are electrons, as in Figure 7.5a, an excess negative charge accumulates at the upper edge of the strip, leaving an excess positive charge at its lower edge. This accumulation continues until the resulting electrostatic field becomes large enough to cause a force that is equal and opposite to the magnetic force. After that, there is no longer any net force to deflect the moving charges. This electric field causes a potential difference between opposite edges of the sample, called Hall voltage. The polarity depends on whether the moving charges are positive or negative. Experimentally the current density is determined by the bias current and the sample's geometry, while the electric field is determined by measuring voltage differences between electrical contacts on the sample. This leads to a determination of the carrier density n_S in a 2-dimensional system for a one-band model by the following equation:

$$n_S = \frac{IB_Z}{qV_H}, \tag{7.2}$$

with I the bias current, B_Z the magnetic field, q the charge magnitude and V_H the Hall voltage.

There are many intrinsic physical mechanisms that alter current density and electric field in a material and most of them relate to thermoelectric behavior, which can be minimized by controlling accurately the temperature of the sample's environment. In addition, most errors can be checked by reversing either the bias current or the magnetic field. Furthermore, if pairs of contacts used in a voltage measurement are not aligned properly perpendicular to the bias current, then the voltages measured will display an offset in the measurement. To minimize these geometrical problems, care must be taken with the size and position of the electrical contacts on the sample.

Hall effect measurements commonly use two types of sample geometries: long, narrow Hall bar structures and square Van der Pauw structures. Each type of geometry has advantages and disadvantages, but the most important difference is that a Hall bar has to be structurized in a sample, while for a Van der Pauw analysis a bare sample can be used. Due to the fact that structurization by argon ion etching can lead to oxygen vacancies in the $SrTiO_3$ substrate and conductivity over it's surface, the $LaAlO_3/SrTiO_3$ interfaces were investigated by using a Van der Pauw geometry. Figure 7.5b shows a Hall effect measurement of a LaO-TiO_2 interface, where the Hall voltage was measured while the magnetic field was swept from −1 Tesla to +1 Tesla for a constant bias current of 10 μA. By determining the slope of the Hall effect measurements, the carrier density was calculated to be 2.1×10^{13} cm^{-2} and 14.4×10^{13} cm^{-2} at respectively 5 K and 300 K. These values correspond to 0.03 and 0.22 charge carriers per unit cell area at respectively 5 K and

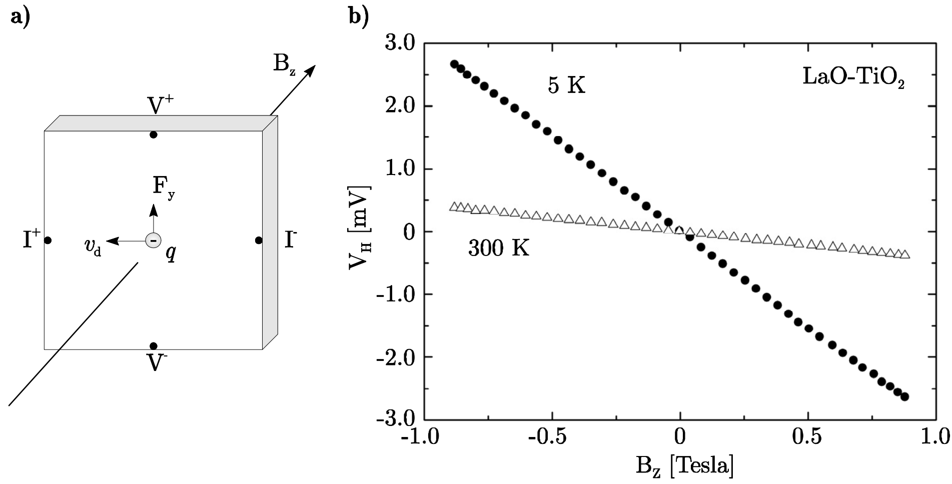

Figure 7.5 Hall effect measurement of the LaO-TiO_2 interface. **(a)** Schematic of the Van der Pauw measurement geometry. **(b)** Measured Hall voltage dependence on the applied magnetic field at 5 K and 300 K after subtraction of the offset voltages.

300 K. From the polarity of the Hall voltage dependence on the magnetic field variation could be determined that the charge carriers in this case are negatively charged and are therefore electrons.

The sheet resistance R_S of the LaO-TiO_2 interface can be measured by use of the Van der Pauw geometry. The four electrical contacts should be numbered clockwise in ascending order when the sample is viewed from above with the magnetic field perpendicular to the sample and pointing away from the observer. The sample should contain no holes and must be homogeneous and of uniform thickness. By measuring the voltages, while sweeping the bias currents from –10 μA to +10 μA, four different resistances $R_{23,14}(=V_{14}/I_{23})$, $R_{14,23}$, $R_{21,34}$ & $R_{34,21}$ were determined. In this way two characteristic resistances can be calculated ($R_A=(R_{23,14}+R_{14,23})/2$ and $R_B=(R_{21,34}+R_{34,21})/2$), which can be used by a numerical solution to calculate the sheet resistance R_S:

$$exp(-\pi \frac{R_A}{R_S}) + \exp(-\pi \frac{R_B}{R_S}) = 1, \tag{7.3}$$

For the LaO-TiO_2 interface the sheet resistance was determined to be ~300 and ~7000 Ω/☐ at respectively 5 K and 300 K. Placement of the electrical contacts in the Van der Pauw geometry at the corners of the sample, instead of the sample's sides, showed no change in the measurement results. Since the sheet resistance involves both the sheet carrier density and the mobility of the charge carriers, this mobility can be obtained from the equation:

$$\mu = \frac{1}{q n_S R_S}, \tag{7.4}$$

with q the charge magnitude and n_S, R_S the measured sheet carrier density and sheet resistance. This results in a carrier mobility μ for the LaO-TiO_2 interface of ~1000 and ~6 $cm^2 V^{-1} s^{-1}$ at respectively 5 K and 300 K.

The obtained values for n_S, R_S and μ for the conducting LaO-TiO_2 interface agree very well with results from other groups [8,10]. The 'almost'-insulating AlO_2–SrO interface had a sheet resistance of ~10^7 Ω/□ at 300 K, but this value increased dramatically at low temperatures. Therefore, it was not possible to determine the sheet resistance for this interface at 5 K. Still, the high resistance at room temperature made a Hall effect measurement impossible and the carrier density and mobility could, because of that, not be determined.

Seebeck effect measurements

Charge carriers in materials will diffuse when one end of a conductor is at a different temperature than the other. Electrons (or holes) will thermally diffuse from the hot end to the cold end, and carry their charge with them. This will create a higher density of carriers at one end of the material and produce a potential difference, the so-called thermoelectric voltage. This voltage developed is rather small, of the order of a few $\mu V K^{-1}$ for metals and $mV K^{-1}$ for semiconductors. When the current generated by this electric field cancels the flow due to thermal diffusion, equilibrium is reached. The Seebeck coefficient (also called the thermopower) is the ratio between the electric field and the temperature gradient or equivalently, the ratio between the voltage difference and the temperature difference between the ends of the sample. The sign of the Seebeck coefficient depends on the sign of the charge carriers (whether positive or negative charge builds up on the cold end). So measuring the Seebeck coefficient is a way to determine whether the charge carriers in a particular material are holes or electrons.

Therefore, Seebeck effect measurements were used to determine the sign of the charge carriers in both types of $LaAlO_3/SrTiO_3$ interfaces. Two electrical contacts were made to the interfaces by wire-bonding and the change in thermoelectric voltage was measured, while warming up only one electrical contact. The LaO-TiO_2 interface exhibited a decrease of 0.2 mV, when the negative voltage contact was warmed up, which was confirmed by numerous repeated measurements. Warming up the other positive voltage contact resulted in an expected 0.2 mV increase. This LaO-TiO_2 interface was already determined by Hall effect measurements to consist of electrons as charge carriers. The highly resistive AlO_2–SrO interface displayed a change of the thermoelectric voltage with temperature in the opposite direction. The voltage increased with 0.2 mV, when the negative voltage contact was warmed up, and decreased with 0.2 mV when the other positive voltage contact was warmed up.

These opposite changes in the thermoelectric voltage suggest holes as charge carriers for the AlO_2–SrO interface.

7.2.2 Photoelectronic properties

All single interface experiments showed some sensitivity to light. Many photoelectronic phenomena are the result of optical absorption by which free carriers are created, the so-called photogeneration of charge carriers [14]. Intrinsic optical absorption corresponds to the raising of an electron from the valence band to the conduction band. On the other hand, extrinsic optical absorption corresponds to the raising of an electron from an imperfection to the conduction band or the raising of an electron from the valence band to an imperfection. This optical absorption can be described quantitatively through the absorption constant α. In the simplest case, the intensity of the transmitted light through a material can be described by Beer's law:

$$I = I_0 \exp(-\alpha d), \qquad (7.5)$$

with I_0 the incident light intensity, α the absorption constant and d the thickness of the material. To investigate this effect in more detail, experiments were performed to determine the source of the photon absorption and as a result the origin of this photosensitivity.

Transmittance and reflectance measurements

Many transport properties can be explained by the assumption of an energy gap E_G between the valence band and the conduction band, the so-called direct bandgap. Each type of insulating material should be transparent for light of photon energies less than $\hbar\omega_e = E_G$, if the absorption of light is due only to the transfer of electrons from the valence band to the conduction band. To determine the absorption edges, the $LaAlO_3/SrTiO_3$ interfaces were measured by UV/VIS spectroscopy in which the transmittance was monitored in the ultraviolet/visible spectrum with wavelengths between 200 and 1100 nm. The fraction of light transmittance (I/I_0), which is usually expressed as a percentage transmittance, is shown in Figure 7.6a for the conducting LaO-TiO_2 interface as well as the insulating AlO_2–SrO interface. As a comparison, the transmittance curves for bare substrates of $SrTiO_3$, $LaAlO_3$ and TiO_2 are also given. From these measurements can be concluded that the absorption of both $LaAlO_3/SrTiO_3$ interfaces are determined by the $SrTiO_3$ substrate, because of similar absorption edges. These absorption edges are 406 nm (=3.05 eV), 386 nm (=3.21 eV) and 223 nm (5.55 eV) for respectively TiO_2, $SrTiO_3$ and $LaAlO_3$. These values agree very will with results from spectroscopy measurements by other groups [11,15,16].

To define the properties of the $LaAlO_3/SrTiO_3$ interfaces with a minimum influence of the $SrTiO_3$ substrates, the reflectance curves of the LaO-TiO_2 and the

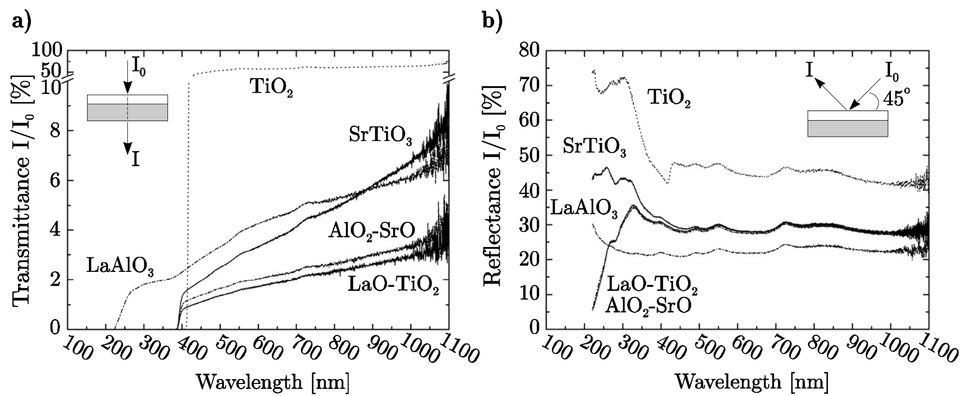

Figure 7.6 Measurement of the optical properties of the optical properties of LaO-TiO_2 and AlO_2-SrO interfaces as well as bare TiO_2, $SrTiO_3$ and $LaAlO_3$ substrates. **(a)** Transmittance analysis displaying clearly the absorption edges. **(b)** Reflectance analysis showing the large differences between the $LaAlO_3$/$SrTiO_3$ interfaces and the bare substrates for low wavelengths (or large energies).

AlO_2–SrO interfaces were also determined, see Figure 7.6b. The results of both types of interfaces are perfectly the same and no differences can be observed. However, the reflectance curves are similar to the $SrTiO_3$ substrate down to ~328 nm, but below this value the percentage reflectance decreases abruptly and all light is absorbed for this incident angle of 45°.

Photoconductivity measurements

Photoconductivity is an optical and electrical phenomenon in which a material becomes more conductive due to the absorption of electro-magnetic radiation such as light. This effect can be described by it's photosensitivity, spectral response and speed of response. To define the spectral response, a AlO_2-SrO interface was analyzed in the photospectrometer by measuring in a 4-wire configuration the variations in current at different wavelengths of incident light, while the bias voltage was kept constant at 10 V, see Figure 7.7a. To compare the effects of the different wavelengths correctly, the sample was illuminated for each individual measurement at a wavelength of 1100 nm to reach the same initial dark conductivity σ_0. For wavelengths down to ~380 nm no changes were observed in the measured current, which suggests that for energies below 3.2 eV no extra charge carriers were created. However, for wavelengths below ~380 nm the measured current is changing and the conductivity σ increases, see Figure 7.7b. This abrupt change of conductance at precisely the bandgap of $SrTiO_3$ suggests an intrinsic optical absorption, and as a result the raising of an electron from the valence band to the conduction band in the $SrTiO_3$ substrate without any influence of the AlO_2–SrO interface. Although, this badly-conducting interface is necessary to transport these extra charge carriers and

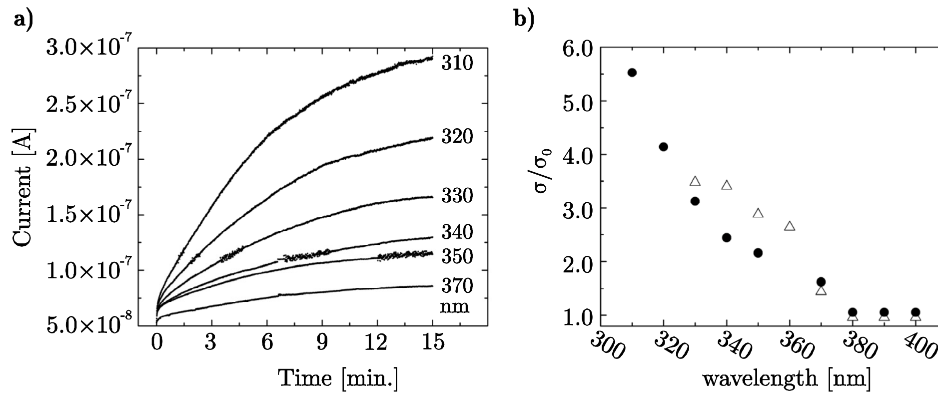

Figure 7.7 Photosensitivity analysis of the AlO_2-SrO interface. **(a)** Variations in the measured current for light illumination at different wavelengths. **(b)** Spectral response of the photoconductivity from the initial dark conductivity σ_0 after 15 min. for the AlO_2-SrO interface (●). As a comparison, the photoconductivity effects on a $SrTiO_{3-\delta}$ sample are also shown (△).

the low-conductivity of the AlO_2–SrO interface is only beneficial to determine the effect of photoconductivity, due to it's low initial amount of charge carriers.

The effect of photoconductivity can be clearly observed in Figure 7.7b, in which the change in conductivity σ/σ_0 is given after 15 min. To demonstrate that this abrupt increase in conductivity is resulting from the $SrTiO_3$ substrate, the surface of a bare substrate was transformed from highly-insulating to conducting by argon ion etching. The effect of photoconductivity on this reduced $SrTiO_{3-\delta}$ shows a similar transition at ~380 nm in good agreement with the photoenhancements of the electronic conductivity and dielectric constant observed recently by other groups [17-20]. The speed of the responses were determined by fitting a single exponential decay model to the measurements shown in Figure 7.7a. This resulted in a constant relaxation time for all wavelengths used of 7-8 min. for the AlO_2-SrO interface and 15-30 sec. for the reduced $SrTiO_{3-\delta}$. This difference in relaxation times suggests a much higher carrier mobility for the reduced $SrTiO_{3-\delta}$, where the extra generated charge carriers are much quicker transported to the conducting surface.

Experiments with high-intensity ultraviolet light illumination demonstrated also the large difference in photoconductivity between the conducting LaO-TiO_2 interface and the insulating AlO_2–SrO interface. In Figures 7.8a and b the results are shown for a sudden illumination by ultraviolet light (~365 nm) from an Hg-100 mercury lamp on both types of $LaAlO_3/SrTiO_3$ substrates. Both substrates were shielded from any light for 12 hours before these experiments. The AlO_2-SrO interface exhibits a much higher initial resistance than the LaO-TiO_2 interface, which is similar to earlier transport measurements. The transition to a lower resistance by light illumination is extremely fast for the AlO_2-SrO interface with a response time

less than ~0.1 sec., while the transition in the LaO-TiO_2 is much slower and reaches a constant resistance level after approximately ~120 seconds. Besides this large difference in response time, also the relative change in resistance is quite different between both interfaces. This is a direct result from the difference in the initial amount of charge carriers, which was already present in a dark environment. This initial amount of charge carriers was for the conducting LaO-TiO_2 interface estimated at 14.4×10^{13} cm^{-2} by Hall measurements. A change in the resistance of a factor of ~4 suggests an injection of about 43.2×10^{13} extra free electrons per cm^2 by this light illumination. For the AlO_2-SrO interface a very large change in the resistance of ~1.2×10^4 was observed, which suggests that the initial amount of free charge carriers before the light illumination had to be below 3.6×10^{10} cm^{-2}. This value can't be checked, because the Hall measurements provided no results for the insulating AlO_2-SrO interfaces.

Although the response speed for the light illumination is different between both interfaces, the relaxation times are still much smaller than the observed time scales,

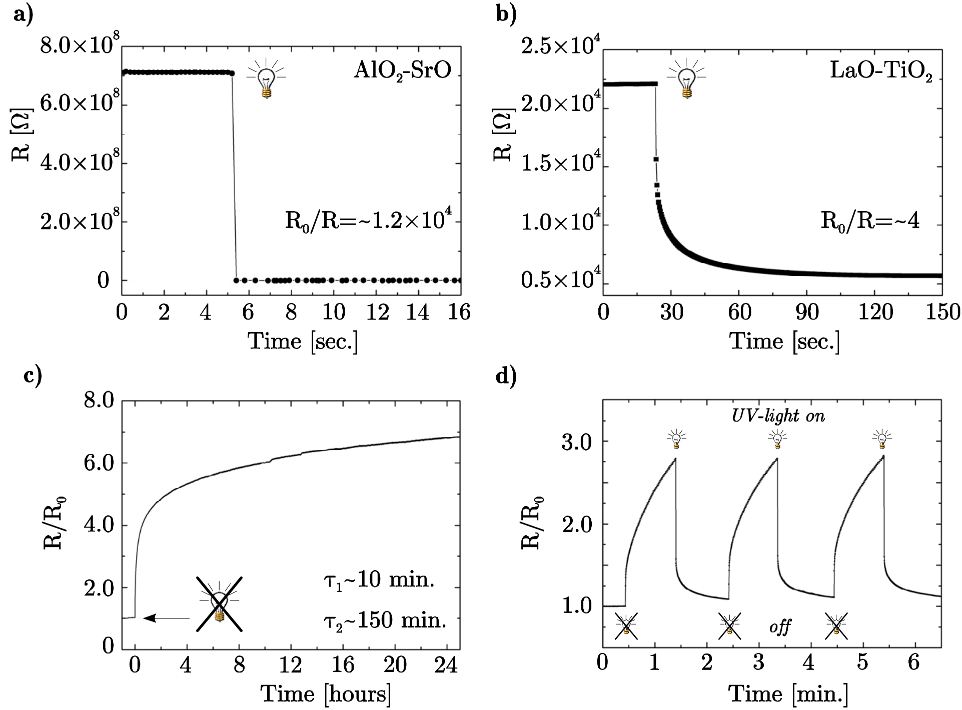

Figure 7.8 Photoconductivity analysis of the $LaAlO_3/SrTiO_3$ interfaces. Abrupt decreases in the resistances for ultraviolet light illumination of an AlO_2-SrO interface **(a)** and a LaO-TiO_2 interface **(b)**. **(c)** Slow increase in the resistance when the ultraviolet light illumination is removed, which can be fitted by a double exponential model with relaxation times τ_1 and τ_2. **(d)** Switching of the resistance by a factor of ~3 by successively turning the ultraviolet light on and off.

which are measured when the ultraviolet light is removed, see Figure 7.8c. The change back to higher resistance values is much slower for both types of interfaces and exhibits a continuous increase lasting for hours. This increase displays a relatively fast part followed by a relative slow part and can only be fitted by a double exponential decay model with relaxation times of τ_1~10 min and τ_2~150 min. A low level of impurities, which can act as trapping sites, can explain the long relaxation time for the extraction of the extra free charge carriers.

The phenomenon of photosensitivity in these $LaAlO_3/SrTiO_3$ interfaces can be used to switch the carrier density by successively turning the ultraviolet light on and off, see Figure 7.8d. The illumination by ultraviolet light will induce extra free electrons per cm^2 in the $SrTiO_3$ substrates, which will propagate to the conducting interface and increase the carrier density in this 2-dimensional electron system. As a result the resistance will decrease, although the level of this decrease depends on the amount of already present carriers at these interfaces. By subsequently turning off the ultraviolet light, the flow of extra carriers from the $SrTiO_3$ substrate is eliminated, which will bring the conducting interface to it's initial conductivity level. Switching between two resistance levels, with a relative difference in resistance of a factor of ~3, can be done every two minutes. However, much faster switching can be performed for smaller differences between the resistance levels. This photoconductivity phenomenon can be an additional possibility to tune the carrier density in these $LaAlO_3/SrTiO_3$ interfaces, when they are used in electronic devices [21-24]. However, to enable a careful analysis of the intrinsic interface properties, the effects of photocarrier injection are suppressed by shielding all samples from any light during the experiments and the 24 hours before.

7.3 Electronically coupled complementary interfaces

Until now the investigations on the $LaAlO_3$-$SrTiO_3$ interface conduction effects have concentrated on individual interfaces [8]. To study the electronic coupling of the complementary interfaces between these insulators, high-quality multilayers were fabricated in which a variable number of $LaAlO_3$ unit cell layers were stacked between $SrTiO_3$, and vice versa. The $LaAlO_3$-$SrTiO_3$ heterostructures were grown by pulsed laser deposition, including in situ monitoring by RHEED as described in section 6.3 of Chapter 6.

The first type of heterostructure was deposited on TiO_2-terminated $SrTiO_3$ (100) substrates and consisted of a $LaAlO_3$ layer followed by a $SrTiO_3$ top layer, see Figure 7.9a. Unit-cell RHEED intensity oscillations were used to control the number of unit cell layers for both materials. The thickness of the $LaAlO_3$ layer was varied from 1 to 26 unit cells while the number of unit cells for the $SrTiO_3$ top layer was always kept constant at 10. As the internal polarization of the $LaAlO_3$ is the driver for the interface doping, a change of the $LaAlO_3$ layer thickness could possibly result

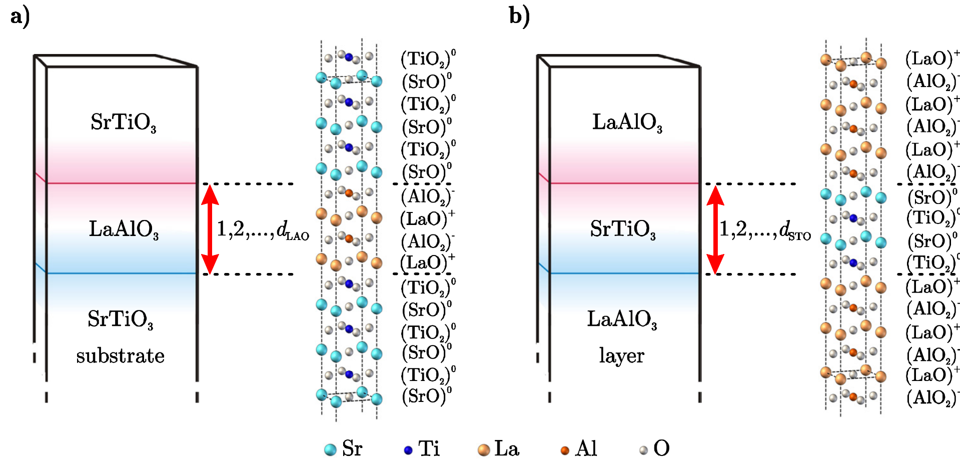

Figure 7.9 Representation of the investigated $LaAlO_3/SrTiO_3$ heterostructures. **(a)** Schematic view of a $SrTiO_3/LaAlO_3/SrTiO_3$ heterostructure: a (001)-oriented $LaAlO_3/SrTiO_3$ bilayer grown on top of a TiO_2-terminated $SrTiO_3$ substrate, where the thickness of the $LaAlO_3$ layer (d_{LAO}) is varied. Atomic representation of the structure, showing the composition and charge state of each layer for the case of d_{LAO}=2. **(b)** Schematic view of a $LaAlO_3/SrTiO_3/LaAlO_3$ heterostructure: a (001)-oriented $LaAlO_3/SrTiO_3/LaAlO_3$ trilayer grown on top of a SrO-terminated $SrTiO_3$ substrate, where the thickness of the $SrTiO_3$ layer (d_{STO}) is varied. Atomic representation of the structure, showing the composition and charge state of each layer for the case of d_{STO}=2.

in a modification of this polarization. For this reason heterostructures of a second type were also fabricated, in which a thin $SrTiO_3$ layer was sandwiched between sufficiently thick $LaAlO_3$ layers, see Figure 7.9b. For the fabrication of those heterostructures, the TiO_2-terminated $SrTiO_3$ (100) substrates were first covered with one monolayer of SrO by pulsed laser interval deposition at 50 Hz. Subsequently, a $LaAlO_3$ base-layer of 13 unit cells was deposited, followed by a $SrTiO_3$ layer, of which the thickness was varied from 2 to 11 unit cells, and finished by a $LaAlO_3$ top layer of 13 unit cells. Atomic force microscopy of the completed heterostructures showed atomically smooth terraces separated by unit cell steps, similar to the original substrate surface.

The electronic properties of the heterostructures were investigated by a four-point Van der Pauw method. For this, wire-bonded contacts were applied at the corners of the samples, connecting to the $(AlO_2)^-/(SrO)^0$ interface as well as to the $(LaO)^+/(TiO_2)^0$ interface. Measurements on individual interfaces using single $LaAlO_3$ layers on $SrTiO_3$ substrates confirmed the electron conduction of the $(LaO)^+/(TiO_2)^0$ interface with a sheet conductance of 1.4×10^{-4} $(\Omega/\square)^{-1}$ at room temperature, while the $(AlO_2)^-/(SrO)^0$ interface had a sheet conductance of ~10^{-7} $(\Omega/\square)^{-1}$. All single interface experiments showed photoconductivity due to photocarrier injection, see section 7.2.2. To enable a careful analysis of the intrinsic interface coupling, the

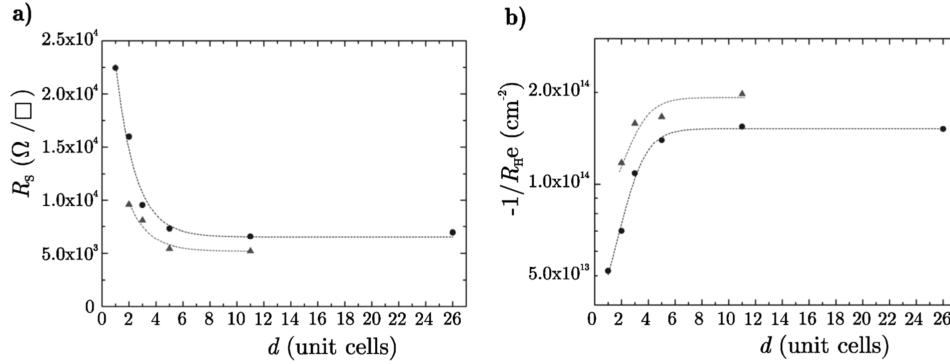

Figure 7.10 Electronic properties of the $LaAlO_3/SrTiO_3$ heterostructures at 300 K for different separation distances between the interfaces. **(a)** Dependence of the sheet resistance R_S on the separation distance *d*. **(b)** Dependence of $-1/R_He$ on the separation distance *d*. $SrTiO_3/LaAlO_3/SrTiO_3$ heterostructures and $LaAlO_3/SrTiO_3/LaAlO_3$ heterostructures are indicated by circles and triangles, respectively. The dashed lines are guides to the eye.

effects of photocarrier injection were suppressed in the multilayer studies by shielding the samples from any light during the experiments and the 24 hours before.

The sheet resistances R_S at room temperature, for both types of heterostructures, are presented in Figure 7.10a for different values of the separation distance (*d*) between the two interfaces. A decrease in *d* is found to be accompanied by an increase in R_S below a separation distance of six unit cells, corresponding to 23 Å. Interestingly, both types of heterostructures show a similar dependence on the interface separation distance, albeit with a difference of 20% in the absolute value of R_S. The sheet carrier densities n_S were deduced from measurements of the Hall-coefficient R_H, using n_S=$-1/R_He$. The room temperature results are shown in Figure 7.10b. Below a separation distance of six unit cells a decrease in sheet carrier density occurs for both types of heterostructures. The constant n_S for large *d* has a value of ~1.8×10^{14} cm^{-2}, corresponding to a charge density of ~29 μC cm^{-2}, which is ~0.27 electrons per unit cell area on the $(LaO)^+/(TiO2)^0$ interface. In this, the contribution by the $(AlO_2)^-/(SrO)^0$ interface to the carrier density is neglected, due to its much lower conductivity.

The change in n_S and R_S below a certain interface separation distance relates to the charge distribution in the heterostructure. There exists no theoretical modelling yet of the $SrTiO_3$–$LaAlO_3$ interface, but it is interesting to make the comparison with interfaces between the Mott insulator $LaTiO_3$ and the band insulator $SrTiO_3$ [7,9,25-27] Notably, for that system a characteristic distance of 6 unit cells was predicted, over which charge transfer and electronic reconstruction takes place [9,25-27]. The electronic reconstruction at a $SrTiO_3$-$LaTiO_3$ interface creates partially filled Ti-3d bands by band-bending effects and the symmetric confinement of charge leads to a suppression of n_S. An important difference with these experiments is the

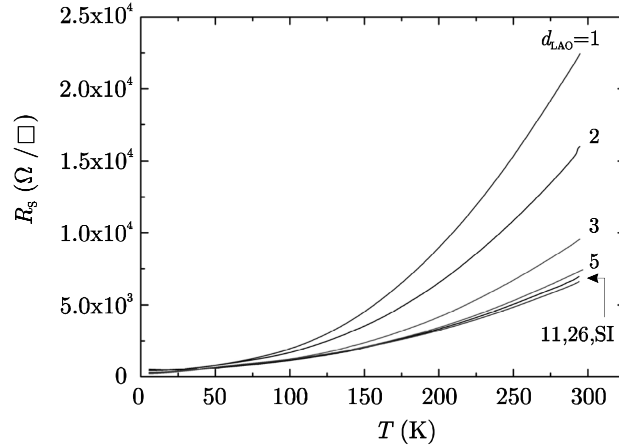

Figure 7.11 The temperature dependence of the sheet resistance $R_S(T)$ for different thicknesses of the $LaAlO_3$ layer (d_{LAO}) in $SrTiO_3/LaAlO_3/SrTiO_3$ heterostructures. A measurement on a single $(LaO)^+/(TiO_2)^0$ interface (SI) is also indicated.

absence of TiO_2 layers in parts of the here presented heterostructures. At the $LaAlO_3$ side, subbands are possibly created below the La-5d levels, in analogy with the Ti-3d levels at the $SrTiO_3$ side. The suppression of n_S, induced by the coupling between the interfaces, could then result from the constraint that the charge density at the $(AlO_2)^-/(SrO)^0$ interface is low.

The temperature dependence of the sheet resistance and the Hall coefficient provides further insight into the electronic properties of the interface electron gas. For the $SrTiO_3/LaAlO_3/SrTiO_3$ heterostructures the temperature dependence of the sheet resistance $R_S(T)$ is presented in Figure 7.11 for different values of the $LaAlO_3$ layer thickness (d_{LAO}) and Figure 7.12a shows the carrier density as determined from the Hall effect as function of temperature. The energy-scale over which charge

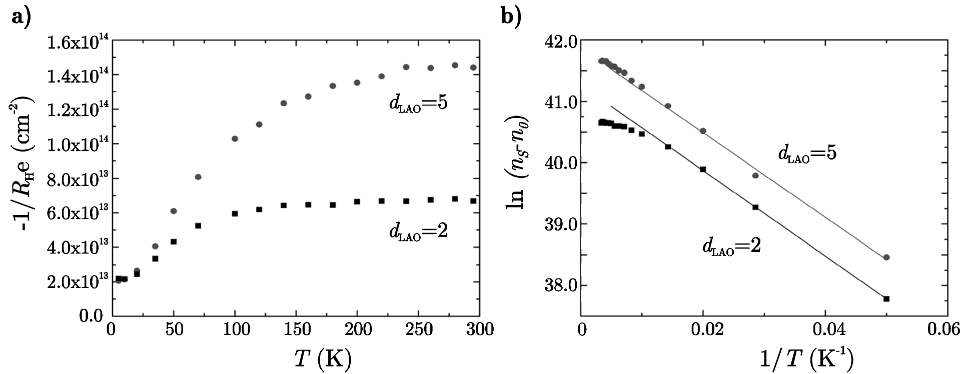

Figure 7.12 Temperature dependence of $-1/R_He(T)$ **(a)** and $\ln(n_S-n_0)$ **(b)** for $SrTiO_3/LaAlO_3/SrTiO_3$ heterostructures with separation distances of d_{LAO} = 2 (squares) and 5 (circles), where n_S is defined as $-1/R_He$ and n_0 is the low temperature limit of n_S.

carriers seem to be frozen out is 6.0 meV (Fig. 7.12b), which is comparable to observations in $SrTiO_3$ at low La-doping [28]. At temperatures above 100 K, the carrier density for $d_{LAO} = 2$ is approximately constant, for $d_{LAO} = 5$ the thermally activated increase continues.

The temperature dependence of the Hall mobility μ_H is given in Figure 7.13a. Above 50K the mobilities show a T^{-2} power law dependence, characteristic of Fermi-liquid behavior. Electron-phonon interactions are typically weak in $SrTiO_3$ (as is known from the poor heat conduction) and would give rise to a Bloch-Grüneisen temperature dependence of the resistance, which is not observed. Although electron-electron scattering is typically suppressed by screening and the Pauli exclusion principle, it is known to be relevant in transition metals with partially filled d-shells. At the n-type interface, this effect is expected to be important, when interface electronic reconstruction makes the Fermi surface intersect the Ti-3d subbands [9,25-27,29]. For all heterostructures, μ_H at room temperature is found to be constant at 6.0 ± 1.0 cm^2 V^{-1} s^{-1}, without any dependence on the separation distances (d_{LAO} and d_{STO}). This value corresponds with room temperature mobilities reported for single interfaces [8,30]. The very large mobilities in the zero-temperature limit provide an estimated electronic mean free path of 100 nm – 1 μm. This large electronic mean free path and the fact that μ_H does not decrease for decreasing interlayer thickness indicates that electron scattering at impurities or crystalline defects in the nearby interface are not dominating effects for the mobilities at room temperature.

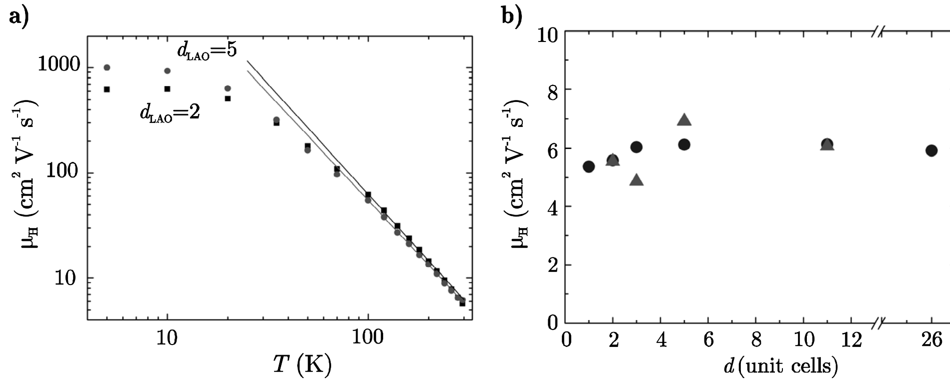

Figure 7.13 Transport properties of the $LaAlO_3/SrTiO_3$ heterostructures for different separation distances between the interfaces. **(a)** Temperature dependence of Hall mobility $\mu_H(T)$ for $SrTiO_3/LaAlO_3/SrTiO_3$ heterostructures with separation distances of $d_{LAO} = 2$ (squares) and 5 (circles). **(b)** The separation distance d dependence of μ_H at 300 K, where $SrTiO_3/LaAlO_3/SrTiO_3$ heterostructures and $LaAlO_3/SrTiO_3/LaAlO_3$ heterostructures are indicated by circles and triangles, respectively.

The studies on the $LaAlO_3$:$SrTiO_3$ heterostructures, presented above, prove the possibility to realize closely-spaced conducting sheets in these otherwise insulating oxide systems [31]. This provides a perspective for novel all-oxide electronic devices as well as for basic studies. In this respect it is interesting to note that the employed growth techniques can also be applied to the fabrication of multilayers with exclusively n-type interfaces, by combining the $SrTiO_3$ and $LaAlO_3$ layers with single layers of $LaTiO_3$ or TiO_2.

7.4 Conclusions

The heteroepitaxial interfaces between the band insulators $LaAlO_3$ and $SrTiO_3$ can be either metallic or insulating depending on the atomic stacking sequences. The charge carriers in these two-dimensional systems were determined to be electrons at the conducting LaO-TiO_2 interface with high carrier mobilities up to ~1000 cm^2 V^{-1} s^{-1} at low temperatures. The complementary AlO_2-SrO interface was found to be insulating, although p-charging is still conceivable.

In well-ordered interfaces the conductivity properties are independent of the orientation with respect to the terrace step direction of the substrate. The negligible influence of step heights of one unit cell suggested a thickness, over which the interface conductivity is taking place, of a couple of unit cells. However, large variations in the electronic properties with orientation are observed when the atomic ordering at the interfaces is not perfect.

All interface experiments showed photoconductivity due to photocarrier injection. Measurements of the transmittance and reflectance of the two types of interfaces at variable wavelengths resulted in a clear observation of the absorption edges for $LaAlO_3$ and $SrTiO_3$. However, no differences were observed between the metallic and the insulating interfaces. An abrupt increase in the conductance was observed for wavelengths below ~380 nm. This change at precisely the bandgap of $SrTiO_3$ suggests an intrinsic optical absorption, and as a result the raising of an electron from the valence band to the conduction band in the $SrTiO_3$ substrate without any influence of the $LaAlO_3$-$SrTiO_3$ interfaces. Photoconductivity measurements on a reduced $SrTiO_{3-\delta}$ substrate showed similar results. High-intensity ultraviolet light illumination on single $LaAlO_3$ layers on $SrTiO_3$ substrates increased the conductivity by factors of 4 and 12000 for the LaO-TiO_2 and AlO_2-SrO interfaces, respectively. The response times to a higher conductance, when the interfaces are illuminated, are extremely fast. In case of a AlO_2-SrO interface even below 0.1 second. Still, the response time to a lower conductance, when the ultraviolet is removed, is very slow. It takes hours before this process reaches equilibrium.

To study the electronic coupling of these complementary interfaces, high-quality heterostructures are fabricated in which a variable number of $LaAlO_3$ unit cell layers

are stacked between $SrTiO_3$, and vice versa. The sheet resistances and sheet carrier densities at room temperature, for both types of heterostructures, are found to change below a separation distance of six unit cells, corresponding to 23 Å. Interestingly, both types of heterostructures show a similar dependence on the interface separation distance, although there is a small difference in the absolute values.

The temperature dependence of the electronic properties provides further insight into coupled complementary interfaces. For the $SrTiO_3/LaAlO_3/SrTiO_3$ heterostructures, the energy-scale over which charge carriers seem to be frozen out is 6.0 meV, which is comparable to observations in $SrTiO_3$ at low La-doping. At temperatures above 100 K, the carrier density is approximately constant for a separation distance of 2 unit cells, while the thermally activated increase continues for a separation distance of 5 unit cells. The T^{-2} power law dependence in the carrier mobilities, observed above 50 K, suggests electron-electron scattering, which is known to be relevant in transition metals with partially filled d-shells. For all heterostructures, the carrier mobilities at room temperature are found to be constant at 6.0 $cm^2 V^{-1} s^{-1}$, without any dependence on the separation distances. Impurities or crystalline defects in the nearby interface are not dominating effects, because of the mean free path of 100 nm – 1 μm, which can be estimated from the very large mobilities in the zero-temperature limit.

7.5 References

1. Junquera, J. & Ghosez, P., *Nature* **422**, 506 (2003).
2. Ahn, C.H., Rabe, K.M. & Triscone, J.-M., *Science* **303**, 488 (2004).
3. Fong, D.D., Stephenson, G.B., Streiffer, S.K., Eastman, J.A., Auciello, O., Fuoss, P.H. & Thompson, C., *Science* **304**, 1650 (2004).
4. Haeni, J.H., Irvin, P., Chang, W., Uecker, R., Reiche, P., Li, Y.L., Choudhury, S., Tian, W., Hawley, M.E., Craigo, B., Tagantsev, A.K., Pan, X.Q., Streiffer, S.K., Chen, L.Q., Kirchoefer, S.W., Levy, J & Schlom, D.G., *Nature* **430**, 758 (2004).
5. Choi, K.J., Biegalski, M., Li, Y.L., Sharan, A., Schubert, J., Uecker, R., Reiche, P., Chen, Y.B., Pan, X.Q., Gopalan, V., Chen, L.Q., Schlom, D.G. & Eom, C.B., *Science* **306**, 1005 (2004).
6. Yamada, H., Ogawa, Y., Ishii, Y., Sato, H., Kawasaki, M., Akoh, H. & Tokura, Y., *Science* **305**, 646 (2004).
7. Ohtomo, A., Muller, D.A., Grazul, J.L. & Hwang, H.Y., *Nature* **419**, 378 (2002).
8. Ohtomo, A. & Hwang, H.Y., *Nature* **427**, 423 (2004).
9. Okamoto, S. & Millis, A.J., *Nature* **428**, 630 (2004).
10. Nishimura, J., Ohtomo, A., Ohkubo, A., Murakami, Y. & Kawasaki, M., *Jpn. J. Appl. Phys.* **43**, L1032 (2004).
11. Cardona, M., *Phys. Rev.* **140**, A 651 (1965).
12. Kramer, B. & MacKinnon, A., *Rep. Prog. Phys.* **56**, 1469 (1993).
13. Abrahams, E., Kravchenko, S.V. & Sarachik, M.P., *Rev. Mod. Phys.* **73**, 251 (2001).
14. Bube, R.H. (Ed.), *Photoelectronic Properties of Semiconductors* (Cambridge University Press, Cambridge, 1992).
15. Tang, H., Berger, H., Schmid, P.E. & Lévy, F., *Solid State Commun.* **92**, 267 (1994).
16. Lim, S.-G., Kriventsov, S., Jackson, T.N., Haeni, J.H., Schlom, D.G., Balhashov, A.M., Uecker, R., Reiche, P., Freeouf, J.L. & Lucovsky, G., *J. Appl. Phys.* **91**, 4500 (2002).
17. Katsu, H., Tanaka, H. & Kawai, T., *Jpn. J. Appl. Phys.* **39**, 2657 (2000).
18. Takesada, M., Yagi, T., Itoh, M. & Koshihara, S., *J. Phys. Soc. Jpn.* **72**, 37 (2003).
19. Hasegawa, T., Mouri, S., Yamada, Y. & Tanaka, K., *J. Phys. Soc. Jpn.* **72**, 41 (2003).
20. Qiu, Y., Wu, C.Q. & Nasu, K., *Phys. Rev. B* **72**, 224105 (2005).
21. Katsu, H., Tanaka, H. & Kawai, T., *Appl. Phys. Lett.* **76**, 3245 (2000).
22. Katsu, H., Tanaka, H. & Kawai, T., *J. Appl. Phys.* **90**, 4578 (2001).
23. Muraoka, Y., Muramatsu, T., Yamaura, J. & Hiroi, Z., *Appl. Phys. Lett.* **85**, 2950 (2004).
24. Muramatsu, T., Muraoka, Y. & Hiroi, Z., *Jpn. J. Appl. Phys.* **44**, 7367 (2005).
25. Okamoto, S. & Millis, A.J., *Phys. Rev. B* **70**, 075101 (2004).
26. Okamoto, S. & Millis, A.J., *Phys. Rev. B* **70**, 241104 (2004).
27. Okamoto, S. & Millis A.J., *Phys. Rev. B* **72**, 235108 (2005).
28. Okuda, T., Nakanishi, K., Miyasaka, S., Tokura, Y., *Phys. Rev. B* **63**, 113104 (2001).
29. Henrich, V.E., Dresselhaus, G. & Zeiger, H.J., *Phys. Rev. B* **17**, 4908 (1987).

30. Nishimura, J., Ohtomo, A., Ohkubo, A., Murakami, Y. & Kawasaki, M., *Jpn. J. Appl. Phys.* **43**, L1032 (2004).
31. Huijben, M., Rijnders, G., Blank, D.H.A., Bals, S., Van Aert, S., Verbeeck, J., Van Tendeloo, G., Brinkman, A. & Hilgenkamp, H., *cond-mat* 0603088 (2006).

Summary

Perovskite oxides and structurally related compounds are receiving much attention in present-day materials science research. They comprise of a broad range of interesting electronic phases such as superconductors, metals, semiconductors, insulators, ferromagnets, antiferromagnets, ferroelectrics, multiferroics, dielectrics and piezoelectrics. This diversity in material properties has led in the last decades to an extensive amount of research into 'oxide electronics'. In the last couple of years the focus of research has been directed into the fabrication of heteroepitaxial structures to explore new physical phenomena and new device concepts. This stacking of several different material compounds on top of each other is possible because of the close lattice-matching of the unit cells of the individual materials. Very small characteristic length scales of the order 0.1 - 1 nm determine the nature of the physical properties in oxide electronics. Therefore, a growth control with a precision on the atomic level is essential for novel epitaxial heterostructures.

For complex oxides, pulsed laser deposition (PLD) has proven to be a growth technique in which the deposited material can be controlled at the atomic scale. Stoichiometric transfer, high deposition rate and tunable energy of the arriving particles are properties, which make 2-dimensional layer-by-layer growth feasible for various complex oxides with a surface roughness of only one unit cell. This makes fabrication of thin films, heterostructures and superlattices possible with high quality surfaces and interfaces, which can be applied in electronic devices. However, the combination of pulsed laser deposition with reflection high-energy electron diffraction (RHEED), to monitor in-situ the thin film growth, is essential to obtain this high quality. Monitoring of the RHEED intensity provides information about the surface morphology as well as the diffusion and nucleation processes. This atomically controlled growth can only be fully exploited when the initial substrate crystals are prepared to have atomically flat surfaces and single unit cell steps. In this way atomically abrupt interfaces can be produced with a strong epitaxial relation between the two oxide layers.

The main aim of this thesis is to develop a controlled growth with atomic precision for the realization of artificial perovskite structures, to exploit the exceptional physical properties of complex oxide materials such as high-temperature superconductors and conducting interfaces between band insulators.

The superconducting $La_{2-x}Sr_xCuO_{4+\delta}$ compound was found to be an ideal material to study the influence of small variations in the stoichiometry on the electronic properties, because small alterations of the strontium and oxygen doping resulted in dramatic changes in the conductivity behavior. Variations in the strontium doping level (x=0, 0.05, 0.125, 0.15 and 0.25) and the background gas, oxygen ($\delta=0$) or ozone ($\delta>0$), provided the possibility to tune the electronic properties from insulating until superconducting, while maintaining the same tetragonal perovskite crystal structure.

The growth of $La_{2-x}Sr_xCuO_{4+\delta}$ thin films was dependent on the termination of the $SrTiO_3$ substrate surface. Experiments indicated that during the initial growth on the substrate surface the first atomic layers formed a rock-salt structure. In case of growth on a TiO_2-terminated surface, the film started with two (La,Sr)O layers, while for a SrO-terminated surface a single (La,Sr)O layer was formed first. Subsequent growth occurred in a layer-by-layer mode of half unit cell monolayers up to large thicknesses (~100 nm). The final surface roughness of the film remained comparable to the initial substrate surface with smooth terraces separated by half unit cell steps. For the case of a thin film on a SrO-terminated substrate however, the formation of very small precipitates on the surface was observed. The maximum superconducting transition temperature for optimum strontium doping, without extra oxygen doping, was found to be 26 K. This was lower than the bulk value of 38 K, due to the large tensile strain present in the thin films. However, when additional oxygen doping was used, the superconducting transition temperature was as high as the bulk value at optimum strontium doping and superconductivity was present in the underdoped region even down to the undoped case.

The ability to maintain the same crystal structure in the investigated doping region provided the possibility to fabricate multilayer structures of thin layers with variable doping levels. In this way a suppression of the superconducting transition temperature, due to the large epitaxial strain between the $La_{2-x}Sr_xCuO_{4+\delta}$ thin films and the $SrTiO_3$ substrate, was found to exist over thicknesses up to 30 unit cells. On the other hand, the multilayer structures were used to investigate ultrathin superconducting films, where a superconducting transition temperature of 7.5 K was observed for only 5 unit cells.

Various difficulties, connected with the sensitivity of $La_{2-x}Sr_xCuO_{4+\delta}$ to oxidation, complicated the fabrication of electronic devices. However, this sensitivity of the electronic properties on the carrier doping was used very successfully in the improvement of the fabrication process of electric field effect structures.

In the heteroepitaxial growth of the superconducting $YBa_2Cu_3O_{7-\delta}$ compound the atomic stacking sequence at the substrate–film interface played an essential role. During initial growth, the atomic interface configuration influenced the surface morphology and structural properties of the film, due to the formation of anti-phase

boundaries by coalescence of islands with different stacking sequences. The interface configuration was accurately controlled by both the terminating atomic layer of the $SrTiO_3$ substrate and the stoichiometry of the first unit cell layer. Using this capability the network of anti-phase boundaries and, therefore, the in-plane ordering was tuned, allowing the study of its influence on the structural and electrical properties of the $YBa_2Cu_3O_{7-\delta}$ film. The superconducting transition temperature was found to be reduced by improvement of the in-plane ordering, which indicated that the absence of anti-phase boundaries hampered the oxygen in-diffusion.

Due to the small lattice mismatch between $YBa_2Cu_3O_{7-\delta}$ and $SrTiO_3$ the first deposited atomic layers were strained to match the substrate. However, above a critical thickness for this strained pseudomorphic layer the strain relaxed by the introduction of defects. The initial defect density, which was already present at the substrate-film interface, determined the value for this critical thickness during subsequent growth, because the process of strain relaxation was improved by the number of antiphase boundaries. This engineering of the interface between $YBa_2Cu_3O_{7-\delta}$ and $SrTiO_3$ was analyzed in-situ during growth, besides reflection high-energy electron diffraction, by surface X-ray diffraction.

Sub-unit cell layer epitaxy was investigated as a novel growth technique for the artificial growth of perovskite structures. Using this technique new crystals were formed by sequentially depositing its sub-unit cell layers. Initial results demonstrated the fabrication of crystalline films with low roughness surfaces, while further investigations are necessary to improve the superconducting transition temperature.

The electronic properties of the heteroepitaxial interfaces between the band-insulators $LaAlO_3$ and $SrTiO_3$ were found to be very sensitive to the atomic stacking sequence. An accurate control of the atomic configuration at the interface tuned the conductivity of the 2-dimensional system between metallic and insulating. Whereas $SrTiO_3$ and $LaAlO_3$ are seemingly similar, the $Sr^{2+}O^{2-}$ and $Ti^{4+}O^{2-}_2$ layers were charge-neutral, while in the ionic limit the charge states in the $LaAlO_3$ were positive for $La^{3+}O^{2-}$ and negative for $Al^{3+}O^{2-}_2$. The polarity discontinuity at the interfaces led to a metallic conductivity for the ‘n-type’ LaO-TiO_2 interface, where by electronic reconstruction through mixed valence Ti states extra electrons were placed in the $SrTiO_3$ conduction band. In the other case, the AlO_2-SrO interface was found to be insulating. Still ‘p-charging’ is conceivable, which will result most likely in an atomic reconstruction by the introduction of oxygen vacancies.

To grow both types of interfaces with an atomic control, the surfaces of the $SrTiO_3$ substrates had to be single terminated by either TiO_2 or SrO. The first was achieved by a chemical and thermal treatment, while the latter was obtained by the deposition of an extra monolayer of SrO. In both cases the subsequent growth of $LaAlO_3$ was perfectly similar and resulted in a highly crystalline thin film with a

surface of smooth terraces separated by unit cell steps. The atomic ordering at the heteroepitaxial interface was investigated also in-situ directly after growth by surface X-ray diffraction to obtain structural information at high deposition temperatures without the influences of possible strain relaxation and impurity incorporation. A single unit cell of $LaAlO_3$ on a TiO_2-terminated $SrTiO_3$ substrate was found to adapt to the cubic bulk structure of the substrate at high deposition temperatures, while for lower temperatures the atoms in the $LaAlO_3$ unit cell are displaced from their bulk positions.

The strong epitaxial relation was used to grow superlattices, which were composed of alternating 'n-type' and 'p-type' interfaces. The observed oscillations in the RHEED monitoring during growth were used to accurately control the thicknesses of the individual layers. Structural analysis indicated a high quality ordering, in both the crystallinity of the total structure as well as the imposed periodicity along the c-axis. The atoms in the $SrTiO_3$ layers were found to be in their bulk positions, while the c-axis parameter of the $LaAlO_3$ unit cells was shortened due to strain. The expected atomic ordering at both the LaO-TiO_2 and the AlO_2-SrO interfaces was proven by high-quality scanning transmission electron microscopy. In order to investigate the influence of the layer thicknesses on the abruptness of the interfaces, a multilayer was fabricated with variable thicknesses of the individual $LaAlO_3$ and $SrTiO_3$ layers. In this way, the thickness was reduced down to a single unit cell, while maintaining a high-quality atomic ordering.

The heteroepitaxial interfaces between the band insulators $LaAlO_3$ and $SrTiO_3$ were either metallic or insulating depending on the atomic stacking sequences. The charge carriers in these two-dimensional systems were determined to be electrons at the conducting LaO-TiO_2 interface with high carrier mobilities up to ~1000 cm^2 V^{-1} s^{-1} at low temperatures. The complementary AlO_2-SrO interface was found to be insulating. The conductivity properties were found to be independent of the orientation with respect to the terrace step direction of the substrate. The negligible influence of step heights of one unit cell suggested a thickness for the interface conductivity of a couple of unit cells. However, large variations in the electronic properties with orientation were observed when the atomic ordering at the interfaces was not perfect.

All heteroepitaxial $LaAlO_3/SrTiO_3$ interfaces showed photoconductivity due to photo carrier injection. Measurements of the transmittance and reflectance of the two types of interfaces at variable wavelengths resulted in a clear observation of the absorption edges for $LaAlO_3$ and $SrTiO_3$. However, no differences were observed between the metallic and the insulating interfaces. An abrupt increase in the conductance was observed for wavelengths below ~380 nm. This change at precisely the bandgap of $SrTiO_3$ suggested an intrinsic optical absorption, and as a result the rising of an electron from the valence band to the conduction band in the $SrTiO_3$ substrate without any influence of the $LaAlO_3$-$SrTiO_3$ interfaces. High-intensity

ultraviolet light illumination on single $LaAlO_3$ layers on $SrTiO_3$ substrates increased the conductivity by factors of 4 and 12000 for the LaO-TiO_2 and AlO_2-SrO interfaces, respectively. The response times to a higher conductance, when the interfaces were illuminated, were very short. In case of a AlO_2-SrO interface even below 0.1 second. Still, the response time to a lower conductance, when the ultraviolet light was removed, was very long. It took hours before this process reached equilibrium.

To study the electronic coupling of these complementary interfaces, high-quality heterostructures were fabricated in which a variable number of $LaAlO_3$ unit cell layers were stacked between $SrTiO_3$, and vice versa. The sheet resistances and sheet carrier densities at room temperature, for both types of heterostructures, were found to change below a critical separation distance of 6 unit cells, corresponding to 23 Å. Both types of heterostructures showed a similar dependence on the interface separation distance, although there was a small difference in the absolute values.

The temperature dependence of the electronic properties provided further insight into coupled complementary interfaces. For the $SrTiO_3/LaAlO_3/SrTiO_3$ heterostructures, the energy-scale over which charge carriers seemed to be frozen out was 6.0 meV, which was comparable to observations in $SrTiO_3$ at low La-doping. At temperatures above 100 K, the carrier density was approximately constant for a separation distance of 2 unit cells, while the thermally activated increase continued for a separation distance of 5 unit cells. The T^{-2} power law dependence in the carrier mobilities, observed above 50 K, suggested electron-electron scattering, which was known to be relevant in transition metals with partially filled d-shells. For all heterostructures, the carrier mobilities at room temperature were found to be constant at 6.0 $cm^2\ V^{-1}\ s^{-1}$, without any dependence on the separation distances. Impurities or crystalline defects in the nearby interface were not dominating effects, because of the mean free path of 100 nm – 1 μm, which was estimated from the very large mobilities in the zero-temperature limit. Interestingly, these high carrier mobilities at low temperatures, characterizing the separate electron doped interfaces, were found to be maintained in coupled structures down to sub-nanometer interface spacing.

These different research topics demonstrate the importance of a controlled growth with an atomic level precision. To develop novel oxide electronic devices for future applications, the fundamental growth processes have to be studied down to the atomic level. This will be essential to reach the high-quality levels, which are needed for the implementation of 'oxide electronics' in daily life. An important advantage of such a highly controllable growth is the fact that it opens the door to a world of new fascinating phenomena.

Samenvatting (Summary in Dutch)

Oxidische materialen met een perovskiet of gerelateerde structuur krijgen veel aandacht in het hedendaags materiaalkundig onderzoek. Ze bestaan namelijk uit een ongelooflijk breed scala van interessante elektronische fasen, zoals supergeleiders, metalen, halfgeleiders, isolatoren, ferromagneten, anti-ferromagneten, ferroelectrica, multiferroica, dielectrica en piezoelectrica. Deze diversiteit in materiaaleigenschappen heeft in de laatste tientallen jaren geleid tot een uitgebreide hoeveelheid onderzoek naar 'oxidische elektronica'. In de laatste jaren is de focus van het onderzoek gericht op de fabricage van hetero-epitaxiale structuren om nieuwe fysische fenomenen en nieuwe toepassingsconcepten te verkennen. Deze stapeling van een aantal verschillende materialen op elkaar is mogelijk doordat de eenheidscellen van de individuele materialen sterk overeenkomen. Zeer kleine lengteschalen in de orde van $0.1 - 1$ nm bepalen de aard van de fysische eigenschappen in deze elektronica. Daarom is een gecontroleerde groei met een precisie op het atomaire niveau essentieel voor nieuwe epitaxiale heterostructuren.

Voor complexe oxidische materialen heeft gepulste laserdepositie (PLD) bewezen een groeitechniek te zijn waarbij het gedeponeerde materiaal gecontroleerd kan worden op een atomaire schaal. Stoichiometrische overbrenging, hoge depositie snelheid en regelbare energie van de aankomende deeltjes zijn eigenschappen die 2-dimensionale laag-voor-laag groei mogelijk maken voor verschillende oxidische materialen met een oppervlakte ruwheid van slechts één enkele eenheidscel. Dit maakt fabricage van dunne lagen, heterostructuren en 'superlattices' mogelijk met een hoge kwaliteit van de oppervlaktes en grensvlakken, welke gebruikt kunnen worden in elektronische toepassingen. De combinatie van gepulste laserdepositie met reflectie hoge-energie elektron diffractie (RHEED), om direct de groei van de dunne laag te bestuderen, is echter essentieel om de hoge kwaliteit te behalen. Analyse van de RHEED intensiteit geeft informatie over zowel de oppervlakteruwheid als de diffusie- en nucleatie processen. Deze atomair gecontroleerde groei kan alleen optimaal worden benut als de initiële substraatkristallen behandeld zijn om atomair gladde oppervlaktes te verkrijgen met terrasstappen van slechts één eenheidscel. Op deze manier kunnen atomair abrupte grensvlakken worden gemaakt met een sterke epitaxiale relatie tussen de twee aangrenzende oxidische lagen.

Het hoofddoel van dit proefschrift is om een gecontroleerde groei met atomaire precisie te ontwikkelen om kunstmatige perovskiet structuren te realiseren, waarmee de exceptionele fysische eigenschappen van complexe oxidische materialen, zoals hoge temperatuur supergeleiders en geleidende grensvlakken tussen band isolatoren, optimaal benut kunnen worden.

De supergeleidende $La_{2-x}Sr_xCuO_{4+\delta}$ samenstelling blijkt een ideaal materiaal om de invloed van kleine veranderingen in de stoichiometrie op de elektronische eigenschappen te bestuderen, omdat kleine wijzigingen in het strontium en zuurstof niveau resulteren in grote veranderingen in het geleidingsgedrag. Variaties in het strontium niveau (x=0, 0.05, 0.125, 0.15 en 0.25) en het achtergrondgas, zuurstof (δ=0) of ozon (δ>0), geven de mogelijkheid om de elektronische eigenschappen af te regelen van isolerend tot supergeleidend, terwijl de tetragonale perovskiet kristalstructuur behouden blijft.

De groei van dunne $La_{2-x}Sr_xCuO_{4+\delta}$ lagen is afhankelijk van het eindvlak van het $SrTiO_3$ substraat. Experimenten tonen aan dat tijdens de beginfase van de groei de eerste atomaire lagen een 'rock-salt' structuur vormen op het substraat oppervlak. In het geval van groei op een TiO_2 eindvlak vormen zich eerst twee (La,Sr)O lagen, terwijl in het geval van een SrO eindvlak slechts één enkele (La,Sr)O laag aanwezig is. De daaropvolgende groei vindt plaats in een laag-voor-laag wijze van steeds halve eenheidscellen tot diktes van ~100 nm. De uiteindelijke oppervlakteruwheid van de dunne laag blijft vergelijkbaar met dat van het substraat met gladde terrassen gescheiden door stappen van een halve eenheidscel hoog. Voor een dunne laag op een SrO eindvlak wordt echter ook de vorming van kleine clusters op het oppervlak waargenomen. De maximale supergeleidende overgangstemperatuur bij optimaal strontium niveau, zonder extra zuurstof toevoeging, is 26 K. Dit is lager dan de 38 K in enkelvoudige kristallen door de grote spanning die aanwezig is in de dunne laag. Echter bij extra toevoeging van zuurstof neemt de supergeleidende overgangstemperatuur toe bij een optimaal strontium niveau en is ook supergeleiding aanwezig voor een laag strontium niveau zelfs tot het geval waar geen enkel strontium aanwezig is.

De mogelijkheid om dezelfde kristalstructuur te behouden met alle variaties in de stoichiometrie zorgt ervoor dat structuren bestaande uit meerdere dunne lagen kunnen worden gefabriceerd, terwijl voor iedere laag het strontium niveau wordt gevarieerd. Op deze manier is een onderdrukking van de supergeleidende overgangstemperatuur, door de grote epitaxiale spanning tussen dunne $La_{2-x}Sr_xCuO_{4+\delta}$ lagen en het $SrTiO_3$ substraat, gevonden voor diktes tot 30 eenheidscellen. Anderzijds kunnen deze uit meerdere lagen bestaande structuren worden gebruikt om ultradunne supergeleidende lagen te maken, waarbij een supergeleidende overgangstemperatuur van 7.5 K is waargenomen voor een dikte van slechts 5 eenheidscellen.

Verschillende moeilijkheden, veroorzaakt door de gevoeligheid van $La_{2-x}Sr_xCuO_{4+\delta}$ ten opzichte van oxidatie, hebben de toepassing in elektronica verhinderd. Deze oxidatiegevoeligheid van de elektronische eigenschappen is echter wel succesvol toegepast om het fabricageproces van elektrische-veld-effect structuren te verbeteren.

In de hetero-epitaxiale groei van de supergeleidende $YBa_2Cu_3O_{7-\delta}$ samenstelling speelt de atomaire stapelingsvolgorde op het grensvlak tussen het substraat en de dunne laag een essentiële rol. Tijdens de beginfase van de groei beïnvloedt de atomaire configuratie op het grensvlak de oppervlakteruwheid en de structurele eigenschappen van de dunne laag door de vorming van anti-fase grensvlakken. Dit wordt veroorzaakt door de vergroeiing van eilanden met verschillende stapelingsvolgordes. De configuratie van het grensvlak kan worden afgeregeld door het eindvlak van het substraat en de stoichiometrie van de eerste eenheidscel te controleren. Door deze optie toe te passen kan het netwerk van anti-fase grensvlakken, en daardoor de ordening in het vlak, worden afgestemd. Dit maakt bestudering van de invloed daarvan op de structurele en elektronische eigenschappen mogelijk. De supergeleidende overgangstemperatuur neemt af als de ordening in het vlak toeneemt. Dit geeft duidelijk aan dat de afwezigheid van anti-fase grensvlakken de indiffusie van zuurstof bemoeilijkt.

Door het kleine verschil in kristalstructuur in het vlak tussen $YBa_2Cu_3O_{7-\delta}$ en $SrTiO_3$ groeien de eerste atomaire lagen met veel interne spanning. Boven een kritische dikte verdwijnt deze spanning echter door de introductie van defecten. De initiële dichtheid van de defecten, die al aanwezig zijn op het grensvlak tussen het substraat en de dunne laag, bepaalt de waarde voor de kritische dikte tijdens de daaropvolgende groei, omdat dit het proces van ontspanning kan bevorderen door de vorming van anti-fase grensvlakken. Deze beheersing van het grensvlak tussen $YBa_2Cu_3O_{7-\delta}$ en $SrTiO_3$ is, naast reflectie hoge-energie elektron diffractie, ook bestudeerd met oppervlakte röntgendiffractie.

Ook een nieuwe groeitechniek voor het kunstmatig fabriceren van perovskiet structuren is onderzocht waarbij nieuwe kristallen worden gemaakt door afwisselend sub-eenheidscellagen te deponeren. De eerste resultaten tonen aan dat kristallijne lagen met lage oppervlakteruwheden kunnen worden geproduceerd, maar verder onderzoek is nodig om een toename van de supergeleidende overgangstemperatuur te verwezenlijken.

De elektronische eigenschappen van de hetero-epitaxiale grensvlakken tussen de band-isolatoren $LaAlO_3$ en $SrTiO_3$ zijn erg gevoelig voor de atomaire stapelingsvolgorde. Een nauwkeurige controle van de atomaire configuratie op het grensvlak maakt een afregeling van de geleiding van dit 2-dimensionale systeem mogelijk tussen metallisch en isolerend. Alhoewel de kristalstructuren van $SrTiO_3$ en

$LaAlO_3$ er bijna hetzelfde uitzien, zijn de $Sr^{2+}O^{2-}$ en $Ti^{4+}O^{2-}{}_2$ lagen ladingsneutraal, terwijl voor de ionische limiet de lagen in $LaAlO_3$ positief voor $La^{3+}O^{2-}$ en negatief voor $Al^{3+}O^{2-}{}_2$ zijn. De discontinuïteit van de polariteit op de grensvlakken zorgt voor een metallische geleiding voor het 'n-type' LaO-TiO_2 grensvlak, waar extra elektronen in de geleidingsband van $SrTiO_3$ zijn geplaatst door elektronische reconstructie met gemengde Ti toestanden. In het andere geval is het AlO_2-SrO grensvlak isolerend, alhoewel 'p-oplading' wel denkbaar is. Dit moet dan waarschijnlijk resulteren in atomaire reconstructie door middel van de introductie van zuurstofvacatures.

Om beide grensvlakken met een atomaire controle te kunnen groeien moeten de oppervlakken van de $SrTiO_3$ substraten één enkel eindvlak hebben van TiO_2 of SrO. De eerste kan worden bereikt door een chemische en thermische behandeling, terwijl voor de tweede daarna nog een extra monolaag van SrO moet worden gedeponeerd. In beide gevallen is de daaropvolgende groei van $LaAlO_3$ perfect hetzelfde en resulteert het in een kristallijne dunne laag met een oppervlak van gladde terrassen gescheiden door stappen van één eenheidscel hoogte.

De atomaire ordening op het hetero-epitaxiale grensvlak is ook direct na de groei onderzocht met behulp van oppervlakte röntgendiffractie om structurele informatie te verkrijgen bij hoge temperaturen, zonder de invloed van mogelijke afname van de spanning in de kristalstructuur en toename van vervuilingen. Eén enkel eenheidscel van $LaAlO_3$ op een $SrTiO_3$ substraat met een TiO_2 eindvlak past zich aan naar de kubische structuur van het substraat bij hoge temperaturen, terwijl voor lage temperaturen de atomen in de $LaAlO_3$ eenheidscel verschuiven van de kubische posities.

De sterke epitaxiale relatie kan gebruikt worden om 'superlattices' te fabriceren bestaande uit afwisselend 'n-type' en 'p-type' grensvlakken. De waargenomen oscillaties in de RHEED analyse tijdens de groei zijn gebruikt om de diktes van de individuele lagen te bepalen. Structurele analyse geeft aan dat er een hoge kwaliteit in ordening aanwezig is zowel in de kristalliniteit van de totale structuur als in de periodiciteit langs de c-as. De atomen in de $SrTiO_3$ lagen blijken in hun standaard posities te zitten, terwijl de c-as lengte van de $LaAlO_3$ eenheidscellen verkort is door de interne spanning. De verwachte atomaire ordening op zowel het LaO-TiO_2 als het AlO_2-SrO grensvlak is bevestigd door middel van scanning transmissie elektronen microscopie. Om de invloed van de laagdiktes op de abruptheid van de grensvlakken te bepalen is een structuur gemaakt bestaande uit meerdere lagen met variabele diktes van de individuele $LaAlO_3$ en $SrTiO_3$ lagen. Op deze manier is het mogelijk om de dikte terug te brengen tot één enkele eenheidscel, terwijl de hoge kwaliteit van de atomaire ordening behouden blijft.

De hetero-epitaxiale grensvlakken tussen de band isolatoren $LaAlO_3$ en $SrTiO_3$ zijn metallisch of isolerend afhankelijk van de atomaire stapelingsvolgorde. De ladingsdragers in deze 2-dimensionale systemen blijken elektronen te zijn voor het

$LaO-TiO_2$ grensvlak met hoge mobiliteiten van ~1000 cm^2 V^{-1} s^{-1} bij lage temperaturen. Het complementaire AlO_2-SrO grensvlak is isolerend. De geleidingseigenschappen blijken onafhankelijk te zijn van de richting ten opzichte van de terrasstappen in het substraat. Door deze verwaarloosbare invloed van eenheidscel hoogteverschillen kan de geleiding aan het grensvlak niet werkelijk 2-dimensionaal zijn. Grote richtingsafhankelijke variaties in de elektronische eigenschappen zijn echter waargenomen wanneer de atomaire ordening op het grensvlak niet perfect is.

Alle hetero-epitaxiale $LaAlO_3/SrTiO_3$ grensvlakken tonen 'photo'-geleiding door het inbrengen van extra ladingsdragers met behulp van licht. Metingen van de transmissie en de reflectie van de twee typen grensvlakken bij verschillende golflengtes, resulteren in een duidelijke waarneming van de absorptie grenzen voor $LaAlO_3$ en $SrTiO_3$. Er zijn echter geen verschillen gezien tussen de metallische en isolerende grensvlakken. Golflengtes onder ~380 nm veroorzaken een abrupte toename in de geleiding. Deze verandering op precies de 'bandgap' van $SrTiO_3$ suggereert een intrinsieke optische absorptie en daardoor de verhoging van een elektron van de valentieband naar de conductieband in het $SrTiO_3$ substraat zonder enige invloed van de $LaAlO_3$-$SrTiO_3$ grensvlakken. Belichting van $LaAlO_3$ lagen op $SrTiO_3$ substraten met behulp van zeer intens ultraviolet licht verhoogt de geleiding in de $LaO-TiO_2$ en AlO_2-SrO grensvlakken met respectievelijk een factor 4 en 12000. De responstijd naar een betere geleiding, wanneer de grensvlakken worden belicht, is zeer kort. In het geval van een AlO_2-SrO grensvlak zelfs minder dan 0.1 seconde. Toch is de responstijd naar een slechtere geleiding, als het ultraviolet licht is verwijderd, zeer lang. Het duurt uren voor dit proces een evenwicht bereikt.

Om de elektronische koppeling tussen deze complementaire grensvlakken te bestuderen zijn heterostructuren van hoge kwaliteit gemaakt waarbij een variabele hoeveelheid $LaAlO_3$ eenheidscellen gestapeld is tussen $SrTiO_3$ lagen en vice versa. De weerstanden en de ladingsdragerdichtheden blijken voor beide typen heterostructuren bij kamertemperatuur te veranderen onder een kritische scheidingsafstand van 6 eenheidscellen (~23 Å). Beide typen heterostructuren vertonen hetzelfde gedrag bij verandering van de scheidingsafstand, hoewel er een klein verschil in de absolute waarden is.

De temperatuursafhankelijkheid van de elektronische eigenschappen geeft verder inzicht in de koppeling van de complementaire grensvlakken. De energieschaal waarover de ladingsdragers lijken te worden geactiveerd is 6.0 meV voor de $SrTiO_3/LaAlO_3/SrTiO_3$ heterostructuren. Dit is vergelijkbaar met experimenten aan La-gedoteerd $SrTiO_3$. Voor temperaturen boven de 100 K is de ladingsdrager-dichtheid constant bij een scheidingsafstand tussen de twee typen grensvlakken van 2 eenheidscellen, terwijl de thermisch geactiveerde toename doorgaat voor een scheidingsafstand van 5 eenheidscellen. De T^{-2} afhankelijkheid van de mobiliteiten voor temperaturen boven de 50 K suggereert elektron-elektron verstrooiing. Het is

bekend dat dit relevant is voor transitie metalen met gedeeltelijk gevulde d-schillen. Voor alle heterostructuren is de mobiliteit bij kamertemperatuur constant op 6.0 cm^2 V^{-1} s^{-1} zonder enige afhankelijkheid van de scheidingsafstand. Uit de vrije weglengtes van 100 nm tot 1 μm, afgeschat met behulp van de hoge mobiliteiten bij lage temperaturen, kan geconcludeerd worden dat onzuiverheden en kristallijne defecten in het nabije grensvlak niet dominerend zijn. Interessant is het verschijnsel dat de hoge mobiliteiten bij lage temperaturen, die de individuele 'n-type' grensvlakken karakteriseren, in stand blijven in gekoppelde heterostructuren zelfs met sub-nanometer scheidingsafstanden tussen de grensvlakken.

Deze verschillende onderzoeksonderwerpen demonstreren het belang van een gecontroleerde groei met atomaire precisie. Om nieuwe oxidische elektronica te ontwikkelen voor toekomstige toepassingen moeten de fundamentele groeiprocessen worden bestudeerd tot op atomair niveau. Dit zal essentieel zijn om de hoge kwaliteit te behalen die nodig is om oxidische elektronica in het dagelijks leven te implementeren. Een belangrijk voordeel van zo'n zeer gecontroleerde groei is het feit dat het de deur opent naar een wereld van nieuwe fascinerende fenomenen.

Dankwoord

Na vier fantastische jaren van onderzoek is de voltooiing van het proefschrift een feit. Het moment is dan ook aangebroken om nog eens met veel plezier terug te kijken op die periode en terug te denken aan alle mensen die daarin een grote rol hebben gespeeld. Graag wil ik dan ook alle mensen bedanken die dit mogelijk hebben gemaakt en die mij alle jaren geholpen en geïnspireerd hebben tijdens het onderzoek.

Allereerst wil ik Hans en Dave bedanken dat ze mij de mogelijk hebben gegeven om promotie-onderzoek te doen op een zeer fascinerend gebied. Jullie hebben mij al die jaren zeer veel vrijheid gegeven om mijn eigen ideeën te ontplooien en naar eigen inzicht keuzes te maken. De zeer inspirerende manier van begeleiding heeft mijn interesse in het materiaalkundig onderzoek voortdurend vergroot, terwijl het mijn benadering van materialen heeft verkleind tot op het atomaire niveau. Het heeft mij dan ook niet verbaasd dat jullie beiden in deze periode hoogleraar zijn geworden. Mijn begeleiding was compleet met de rol die Guus daarin had. Jij hebt mij wegwijs gemaakt in de wereld van gepulste laserdepositie en reflectie hoge-energie elektronen diffractie. Jouw opmerkingen houden een onderzoeker voortdurend scherp en kritisch op alle punten. Ik heb al die jaren altijd met zeer veel plezier uitgekeken naar de conferentiebezoeken over de hele wereld, omdat dit in het gezelschap van jullie drieën altijd garant stond voor veel gezelligheid.

In de beginperiode van mijn promotie heb ik veel kunnen leren van de toenmalige promovendi in de groep. Ik ben dan ook erg blij dat ik toen van Henk-Jan, Lianne, Alexander en Victor heb kunnen afkijken hoe goed onderzoek gedaan dient te worden.

Graag wil ik Frank en Dick bedanken. Uiteraard voor het altijd maar weer oplossen van de technische problemen in de laboratoria, maar nog veel meer voor de prettige werksfeer die voor een groot deel door jullie wordt gecreëerd. Het plezier in het werk dat jullie voortdurend uitstralen naar alle promovendi en studenten met jullie eeuwige humor zorgt ervoor dat het werk niet altijd even serieus wordt genomen en dat er genoeg wordt gelachen.

Sybolt en Gerrit wil ik bedanken voor alle uitleg over kristalstructuren en hun hulp in het begrijpen van röntgendiffractie. Ook wil ik Sybolt bedanken voor de kans die ik gekregen heb om mee te werken aan experimenten bij het ESRF. Het heeft

voor mij duidelijk gemaakt dat er een minimum aan slaap is dat een mens nodig heeft, maar dat het wel persoonsafhankelijk is.

Daarnaast wil ik Ans, Inke, Harrie en Jan bedanken. Wetenschap is natuurlijk niet mogelijk zonder administratieve en technische ondersteuning.

Het onderzoek in dit proefschrift had niet tot stand kunnen komen zonder de samenwerking met een aantal personen. Joska en Wolter hebben tijdens hun afstudeerperiodes een belangrijk deel van het onderzoek naar elektrische-veld-effect structuren gedaan. Ik heb altijd met veel plezier met jullie samengewerkt en ik zal ook in de komende jaren jullie promotie-onderzoek met veel interesse blijven volgen. De studie naar de initiële groei van $YBa_2Cu_3O_{7-\delta}$ heb ik samen met Seve gedaan. Het was een mooie samenwerking waarin ik veel van hem heb kunnen leren. Nog steeds is het voor mij niet te bevatten dat hij ons zo plotseling ontvallen is. De verschillende experimenten met behulp van oppervlakte röntgendiffractie zijn uitgevoerd op het ESRF in Grenoble samen met Vedran, Kurt, Sybolt, Paul en Heinz. Die verschillende weken zijn erg interessant en gezellig geweest en ik ben blij dat ik zelfs een keer de binnenstad heb mogen bekijken. De gedetailleerde hoge-resolutie elektronen microscopie en scanning transmissie elektronen microscopie zijn gedaan op de Universiteit van Antwerpen door Sara Bals. De studie naar de ordening van vortices door middel van scanning tunneling microscopie en spectroscopie is uitgevoerd op de Universiteit Leiden door Gertjan van Baarle.

Ik kijk met veel plezier terug op alle lol die ik heb gehad tijdens allerlei feesten, borrels en conferenties met een grote groep van promovendi en studenten. Het was en is nog steeds vrij duidelijk of de groep uit Twente aanwezig is en waar ze ergens staan. Ik wens dan ook Aico, Joska, Maarten, Jeroen, Vedran, Kurt, Matthijn, Frank!, Christian, Paul, Arjen M., Koray, Arjen J., Mercy, Gabriella, Kees, Gerwin, Karthi, Hans en Ariando veel succes met hun onderzoek in de komende jaren.

Een speciaal woord van dank gaat naar mijn broer Jeroen die iedere keer weer gedreven mijn verzoeken voor 3-dimensionale plaatjes en animaties inwilligde. Meerdere van dat soort afbeeldingen zijn dankbaar gebruikt bij het maken van dit proefschrift om sommige dingen te verduidelijken. De onverwachte vakantiebezoekjes van mijn broer Rob waren erg gezellig en zorgden ervoor dat hij met de laatste nieuwtjes huiswaarts ging.

Mijn ouders, Tiny en Rick, wil ik graag bedanken voor alle mogelijkheden die zij mij altijd geboden hebben om te doen wat ik leuk en interessant vond. Jullie eeuwige steun, om uit alle dingen die ik doe altijd alles uit te halen, heeft mij vaak gestimuleerd.

Tot slot wil ik Janke bedanken voor haar liefde en geduld in de afgelopen periode. De toekomst ligt open voor ons samen, hoewel het nog afwachten is waar naartoe het ons zal brengen.

Mark